

Using computational models to understand CO_2-rich fluid behaviour, photochemical reactions and high-temperature water reactions.

Christopher Wiseall

Thesis submitted to the University of Nottingham for the degree of Engineering Doctorate

December 2019

Dedicated to my Dad

Thesis Abstract

This Thesis uses computational model development throughout to aid with the understanding of experimental results in two general areas: understanding phase behaviour of CO_2-rich fluids and modelling of novel chemical reactions.

Chapter 1 the introduces experimental measurements that were carried out to measure the solubility of water in a 10% H_2 + CO_2 fluid mixture at 40 °C and above 8 MPa. The experimental results showed a continuation of the trend observed previously with pure CO_2, 5% N_2 + CO_2 and 10% N_2 + CO_2, where the solubility of water was dependent on the density of the mixture. The experimental results carried out in this work, along with the previously reported results, including at 25 °C, were compared to those predicted by both the Advanced Peng-Robinson 1978 and SAFT-γ Mie Equations of State. The predicted water solubility was generally underestimated compared to experimental results, which was considered to be safer than an overestimation for any future pipeline network.

The minimal saturation limit was *ca.* 1500 ppm, which with a safety multiplier of 60%, suggested that water solubility limits of 1000 ppm lay above the previously suggested limits of 500 ppm. To be surer of this, experiments would need to be continued at lower temperatures, such as 10 °C, which are more likely to be found as pipeline operating conditions, especially in the UK.

A computational model of a pipeline was then used to investigate the effect of impurities on pipeline behaviours, such as pressure drop, which is a crucial measure in the development of a pipeline network. The presence of impurities was shown to have an effect on the pressure drop of a pipeline, with the identity of the impurity exhibiting a much less pronounced effect.

The pipeline model was then adapted to a smaller size to support a technique previously developed within the group to measure the phase behaviour of reactive mixtures, using an increased in pressure drop to indicate a phase change.

Within Chapter 2 both photochemistry and high-temperature water reactions are introduced before the process modelling and the mathematical techniques used throughout this Thesis are introduced in Chapter 3.

The models developed for photochemical reactions and photochemical reactors are introduced in Chapter 4. Although previously reported models of photochemical reactions were limited, the model developed in this work was shown to agree well. Maximum likelihood estimation was then used with the model to estimate the quantum yield of a number of reactions, assuming the lamp manufacturer's light intensity was accurate. The quantum yields were then used to accurately predict further experimental results, outside of the experimental space used in the estimation.

The photochemical reactor models were then developed for the FEP tubular reactor and Vortex reactors, which were much more complex than the excimer flow and batch reactors. The Vortex reactor process model matched the Computational Fluid Dynamics model well, with the ability to predict the performance of reactions in the Vortex reactor.

Within Chapter 5 a high-temperature water reactor model was developed and used to model a multi-step reaction in two different reactors; a large-scale and small-scale reactor. Maximum likelihood estimation was used to estimate the kinetic parameters of the reactions, with a reparameterization of the Arrhenius equation and an optimisation algorithm used to reduce the correlation and uncertainty of parameters. The estimated kinetic parameters from the smaller reactor were then used to predict the performance of the larger reactor, which was a key aim of the model development.

The thermal reaction modelled in Chapter 5 was the second stage of a reaction modelled in the photochemical chapter. The *daisy-chaining* of these two reactions was then modelled with a possible equivalence of 2.5 kg per day being possible if the laboratory equipment was available. A future reactor was then designed using the reaction's kinetics to optimise the yield, while reducing energy and material use.

Acknowledgements

I would firstly like to pay thanks to both Professor Mike George and Professor Sir Martyn Poliakoff for their advice, support and discussions throughout my time at Nottingham. I would like to especially thank for them for their guidance when my work needed to refocus. I would also like to thank them, along with Professor Colin Snape and the CCSCFE CDT, for supporting my application for the policy placement at the National Assembly for Wales.

I would like to thank Dr. Medhat Sharabi as well as Dr. Jie Ke and Dr. Rowena Howie for their discussions regarding the model development. Also, the nature of the modelling part of my research also relied on the experimental data collected by colleagues and I would like to pass thanks on to Dr. Darren Lee, Dr. Rowena Howie, Dr. Erica DeLaney, Bryan Tambosco, Toby Waldron-Clarke, Jonny Hunter, Adam Lee and Dr. Gurbuz Comak for this. A special thanks is also needed for Melissa Richardson whose organisational and logistical work has ensured all aspects of the Photoelectro project work has ran as smoothly as possible.

For the water solubility experimental work, I would like to thank Dr. Stephanie Foltran and Dr. Thomas Murphy for their guidance.

I would also like to thank Dr. Katy Orford and the National Assembly for Wales for giving me the opportunity of working for the Climate Change, Environment and Rural Affairs Committee at the National Assembly for Wales. The placement gave me a wide range of skills outside of a typical PhD experience of which I am grateful for.

A special thanks for the workshop and technical staff at the University of Nottingham is also needed. Mark Guyler's help and advice with the CCS work was invaluable as well as the workshop's development of the reactors which I modelled.

I wish to show wider appreciation of all the members of the Poliakoff and George group, I will miss waiting to see what cake had been made on Monday mornings and the walks around the lake.

Declaration

I declare the work presented in this Thesis is an account of my own research from the Period October 2015 – December 2019. Due to the nature of the work, a number of experiments have been carried out through collaboration, with the relevant researchers acknowledged. This Thesis has not been accepted in part or whole for the fulfilment of any other degree or personal qualification.

Christopher Wiseall, 6th December 2019

Preface

The Engineering Doctorate (EngD) Thesis was originally closely tied with my industrial sponsor, Process Systems Enterprise (PSE). PSE is a leading supplier of advanced process modelling software and digital design and operation services to the process industries. The EngD also contained multiple modules to understand the broader aspects of research within the Carbon Capture and Storage and Cleaner Fossil Energy (CCSCFE) Centre for Doctoral Training (CDT). As suggested by the name of the CDT, the aim of associated research is to push forward the understanding around CCS and cleaner fuels.

The key objectives of the Thesis originally were to develop the equation of state for multicomponent mixtures relevant to CCS. Within this development there was a specific focus on the development of understanding surrounding the water solubility in CCS mixtures. The experimental results were then planned to be used to benchmark PSE's software's predictive capabilities.

Unfortunately, the UK Government decided to withdraw £1 billion worth of funding for CCS in the November 2015 budget. This decision had a direct impact with my sponsor company, who closed their CCS division, requiring a change in focus.

The area which this Thesis then focussed on was the modelling of chemical reactors, especially those used for flow photochemistry. The modelling of chemical reactors was well aligned with PSE, as they are a process modelling company.

Due to this change in focus, the Thesis is largely presented in two separate parts: the first part (Chapter 1) is based on understanding the complex phase behaviour of CCS relevant mixtures and the second part (Chapters 3, 4 and 5) introduces the modelling of photochemical and high-temperature water reactions. There is also an explanation of the modelling and statistical techniques common throughout the Thesis in Chapter 2.

Table of contents

1. Water solubility and pressure drop for Carbon Capture and Storage 1

1.1. Chapter Overview 2

1.2. Chapter aims 3

1.3. Climate change and mitigation 3

1.3.1. Negative Emissions 4

1.4. What is Carbon Capture and Sequestration (CCS)? 5

1.4.1. When will CCS be used? 6

1.4.2. Capture Technologies 6

1.4.3. CCS Exhaust Stream Composition 9

1.5. Why is water solubility important? 10

1.5.1. Impurities' effect on phase behaviour 11

1.5.2. Water solubility measurements 12

1.5.3. Experimental work that forms the basis of initial investigations 17

1.5.4. Experimental measurement of water solubility 19

1.5.5. Density used for calculations 24

1.5.6. Molar Fraction and Concentration calculation 26

1.5.7. Water solubility comparison with Equations of State (EoS) 29

1.5.8. Proposed safety limits 33

1.5.9. Summary of water solubility measurements and EoS comparisons 35

1.6. Pressure drop modelling of CCS pipelines 36

1.6.1. Literature comparison of equations of states for CCS relevant mixtures 36

1.6.2. Density comparisons 37

1.6.3. Viscosity comparisons 40

1.6.4. Pipeline model 44

1.6.5. Effect of impurities on pressure drop in pipeline 45

1.6.6. Effect of conditions on pressure drop in pipelines 48

1.6.7. Summary of pressure drop modelling 50

1.7. Pressure drop for predicting phase behaviour 52

1.7.1. Experimental set-up 52

1.7.2. Modelling set-up 54

1.7.3. Experimental results and model comparison 55

1.8. Chapter summary 60

1.9. Future work 60

2. Introduction to relevant chemical reactions 62

2.1. Chapter Overview 63
2.2. Introduction to green and sustainable chemistry 63
2.2.1. The 12 Principles of Green chemistry 64
2.2.2. The 12 Principles of sustainable engineering 65
2.2.3. Quantitative measures of sustainability 66
2.2.4. Consequences of green and sustainable chemistry 67
2.3. Continuous flow chemistry 68
2.3.1. Advantages of flow chemistry 69
2.3.2. Disadvantages of flow chemistry 69
2.4. Introduction to photochemistry 70
2.4.1. Benefits of photochemistry 71
2.4.2. Limitations of photochemistry 72
2.4.3. Principles of Green Chemistry and Engineering relevant to Photochemistry 72
2.4.4. Photochemical processes 73
2.4.5. Photochemical reactions 75
2.4.6. Quantum yield 76
2.4.7. Emission of light 77
2.4.8. Absorption of Light 78
2.4.9. Kinetic models for photochemistry 82
2.5. Photochemical reactions in flow 84
2.5.1. Photoreactor design 84
2.5.2. Photoreactors used in this work 87
2.6. Introduction to high temperature water reactions 93
2.6.1. What is high temperature water (HTW)? 93
2.6.2. High temperature water with organic reactions 94
2.6.3. High temperature water reactors used in this work 95
2.7. Multi-step reaction processes 97
2.7.1. Benefits of modelling multi-step processes 98
2.8. Aims of reaction modelling 99
2.8.1. Aims of photochemical research section 99
2.8.2. Aims of HTW research section 100
2.8.3. Audience for modelling development 100
3. Chemical process modelling and mathematical techniques 101
3.1. Chapter Overview 102
3.2. Introduction to process modelling 102
3.3. Modelling approaches 103
3.3.1. Empirical models 104

3.3.2. First principle approach 104
3.3.3. Hybrid approach 104
3.4. Modelling of processes 105
3.4.1. Types of equations used in chemical engineering 105
3.4.2. Discretisation 108
3.4.3. Coordinate systems 109
3.4.4. Physical properties 110
3.5. Computational Fluid Dynamics 117
3.6. Conservation equations 117
3.6.1. Mass balance 118
3.6.2. Energy balance 119
3.6.3. Momentum balance 121
3.6.4. Dynamic vs steady state 125
3.7. Solving differential equations numerically 125
3.7.1. Approaches for solving for differential equations 126
3.7.2. Truncation errors 127
3.7.3. Runge-Kutta methods 127
3.7.4. Newton's method 130
3.8. Parameter estimation 131
3.8.1. Parameter estimation methods 132
3.8.2. Parameter correlation 136
3.8.3. Uncertainty of sensors 138
3.9. Model validation 138
3.9.1. Estimated parameter validation 139
3.9.2. Model output validation 140
3.10. Process optimisation 143
3.11. Sensitivity analysis 144
3.11.1. Sensitivity analysis 144
3.12. Numerical methods used in this work 148
3.12.1. Solvers used within gPROMS ProcessBuilder 148
4. Modelling photochemical reactions and reactors 150
4.1. Chapter Overview 151
4.2. Introduction to photochemical chapter 152
4.3. Aims of photochemical research section 153
4.4. Initial model development 153
4.4.1. Modelling the absorption of light 154
4.4.2. Rate of photoreaction 154

4.4.3. Quantum Yield 155
4.4.4. Reactor model design and assumptions 155
4.4.5. Example reaction – Paternó-Büchi 156
4.5. Comparison with CFD 162
4.6. Introduction to excimer reactor models 163
4.6.1. Radiative transfer equation for annular reactors 164
4.6.2. Comparison of two-flux method with previous Beer-Lambert law 165
4.6.3. Lamp power and actinometry 168
4.6.4. Excimer flow reactor 168
4.6.5. Excimer batch reactor 171
4.7. Excimer flow results 171
4.7.1. 2-Pyridone Isomerisation 172
4.7.2. Photodecarboxylative cyclisation of potassium *N*-phthalimidobutanoate 187
4.7.3. Reaction of Cookson's dione 196
4.8. Use of photosensitisers 203
4.8.1. Photosensitisers in kinetic schemes 203
4.8.2. Cis-/trans-cyclooctene with photosensitiser 204
4.8.3. Photocyclisation of THPAA and propargyl alcohol 212
4.9. Vortex Model Development 218
4.9.1. Model proposal 219
4.9.2. Idealised model based on Paternò–Büchi reaction 220
4.9.3. Vortex reactor experimental results for Cookson's dione 224
4.10. FEP tubular reactor model development 230
4.10.1. Simplified FEP tubular reactor 233
4.11. Chapter summary 235
4.12. Future work 236
5. Modelling reactions in a high-temperature water reactor 238
5.1. Chapter Overview 239
5.2. Thermal chapter introduction 240
5.3. Aims of HTW research section 241
5.4. High temperature water reactor model development 242
5.4.1. Model description 242
5.4.2. Mass balance 243
5.4.3. Energy balance 244
5.4.4. Effect of Dispersion 245
5.5. Ring opening step in larger reactor 248
5.5.1. Model input for larger reactor 248

5.5.2. Experimental results 249
5.5.3. Kinetic parameter estimations for the ring-opening step in larger reactor 251
5.6. Hydrolysis followed by ring-opening step in larger reactor 262
5.6.1. Model input 262
5.6.2. Experimental results 262
5.6.3. Kinetic parameter estimation for multi-step reactions 263
5.6.4. Combination of reactions 265
5.7. Summary of the larger reactor experiments 267
5.8. Hydrolysis followed by ring-opening step in smaller reactor 268
5.8.1. Model input 268
5.8.2. Experimental results 269
5.8.3. Kinetic parameter estimations 270
5.9. Sensitivity analysis for the estimated parameters 275
5.9.1. Variance based sensitivity analysis at set temperature 276
5.10. Prediction of larger reactor from smaller reactor's estimated parameters 280
5.10.1. Prediction of the hydrolysis and ring-opening steps in the larger reactor 280
5.10.2. Prediction of the ring-opening step in the larger reactor 281
5.11. Daisy-chain with Photoreactor 283
Prediction of performance with 60 ml·min^{-1} 283
5.12. Chapter Summary 285
5.13. Future work 287
6. Thesis summary 288
7. References 298
8. Appendix 318
8.1. Appendix I – Introduction to photochemistry and HTW 318
8.1.1. Definitions of quantum yield 318
8.1.2. RTE section 320
8.2. Appendix II – Photochemical chapter 326
8.2.1. Decarboxylative cyclisation 326
8.2.2. Cookson's dione Aillet calculations 330
8.2.3. Bodenstein-like assumption for quantum yield 331
8.2.4. Experimental results for the THPAA cyclisation 332
8.3. Appendix III – High temperature water chapter 334
8.3.1. Enthalpy of reaction and temperature change in reactor 334
8.3.2. Effect of dispersion 335
8.3.3. Raman method for calculating yield of smaller reactor yields 337

Acronyms

Acronym	Description
AAD	Absolute average deviation
ATR-IR	Attenuated total reflectance infra-red
BIP	Binary interaction parameter
BPR	Back-pressure regulator
CCS	Carbon capture and storage
CCUS	Carbon capture, utilisation and storage
CFD	Computational Fluid Dynamics
CSTR	Continuous stirred tank reactor
DPs	Discretisation points
EE	Elementary effects
EOR	Enhanced oil recovery
EoS	Equation of State
FEP	Fluorinated ethylene propylene
FID	Flame ionisation detector
FTIR	Fourier-transformed infra-red
GC	Gas chromatography
GDP	Gross domestic product
GUI	Graphical user interface
HPC	High-performance computer
HTW	High-temperature water
hv	Energy of a photon
IEAGHG	International Energy Agency Greenhouse Gases
IoT	Internet of Things
IPCC	International Panel on Climate Change
LVRPA	Local volumetric rate of photon absorption
MLE	Maximum likelihood estimation
NIR	Near-infra-red
NMR	Nuclear Magnetic Resonance
PDE	Partial differential equation
PR	Peng Robinson Equation of State
PR-A	Advanced Peng Robinson Equation of State
PS	Photosensitiser
RMSE	Root mean squared error
RTD	Residence time distribution
RTE	Radiative transfer equation
SAFT	Statistical associating fluid theory
SD	Standard deviation
SRK	Soave-Redlick-Kwong Equation of State
TCD	Thermal conductivity detector
VLE	Vapour-liquid equilibrium

Parameters and variable symbols

Symbol	Definition
a	Intermolecular energy parameter of van der Waals equation
A	Surface area of external wall of reactor
Ã	Reparameterised Arrhenius parameter
A_0	Arrhenius equation's pre-exponential factor
A_{BL}	The absorbance of a medium as defined in the Beer-Lambert law
b	Hard sphere parameter for van der Waals equation
B	Reparameterised Arrhenius B parameter
B_0	Aillet normalised conversion parameter defined in Section 2.4.9
c	Aillet normalised distance parameter defined in Section 2.4.9
C_A	Concentration of compound A
c_p	Specific heat capacity of fluid
D	Dispersion coefficient of fluid
d_c	Diameter of the coil used in the coiled reactors
De	Dean number is a dimensionless number used to understand the centripetal forces when a fluid flows through a curved pipe
D_H	Hydrodynamic diameter of the fluid flow
D_{mol}	Molecular diffusion coefficient
D_s	Effective dispersion coefficient from combination of molecular diffusion and other dispersive effects, such as fluid flow through a curved pipe
d_t	Diameter of the tube that fluid flows through
E	Total energy balance of the system in questions
E_p	Energy of a photon
E_A	Activation energy of a thermal chemical reaction
E_θ	Residence time distribution value which describes how much time different fluid elements have spent in the reactor
F	F-statistic is a value used to compare the means of two different samples
f_D	Darcy friction factor used in the calculation of the pressure drop within the Darcy-Weisbach equation
f_D	Fanning friction factor can be used in the calculation of the pressure drop of a fluid flow and is equal to the ratio between local shear stress and local kinetic energy density
F_τ	Total force balance within the momentum equation
$g(\Theta)$	Function used to describe the calculation of a parameter from its previously estimated value
G	Np x Np matrix of the first derivatives of $g(\Theta)$ with respect to each parameter
h	The Helmholtz free energy is thermodynamic potential that measures the useful work obtainable from a closed thermodynamic system at constant temperature and volume
H	Mass specific enthalpy
I	Irradiance of light
I_T	Total amount of light absorbed by the whole system used in the Beer-Lambert derived radiative transfer equation
k	Kinetic constant of a thermal reaction

k_H	The collimation factor for the light at the emitting surface
k_{HT}	Heat transfer coefficient between the pipe wall and fluid
k_T	Thermal conductivity of the fluid
L	Length of pipe
M_i	The mass of compound i within mass balance equation
M_F	Mass flux used within the pipeline model
n	Degree of collimation of the light where n = 0 is the isotropic case and n = ∞ is the fully collimated case
N_d	Number of directions of light used in the discrete ordinate method
n_{df}	Number of degrees of freedom used in the statistical analysis
N_E	Number of experimental points used in the statistical analysis
N_θ	Number of parameters used in the statistical analysis
N_{hv}	Number of moles of photons
P	The system pressure
P_c	Pressure at the critical point of a fluid
p_i	Fraction of population of type i asserted by null hypothesis
Q	Measure of the heat transfer
q	Energy flux within the pipe
q_w	Heat flux from the wall into the fluid
r	Radial position used within the cylindrical coordinates
R	Size of radius
Re	Reynolds number which is the ratio of inertial forces to viscous forces within a fluid
s	Distance along the dimension used in the discrete ordinates method and two-flux approximation
s^2	The unbiased estimator of the variance of a sample
Sc	Schmidt number is the ratio of kinematic viscosity and mass diffusivity
S_i	First order effect index is used to measure the contributions of a single parameter to the output variance
S_{Ti}	Total effect index is used to measure the total contributions (value + interactions) of a parameter to the output variance
T	Temperature
t	Time
Ta	Taylor number is a dimensionless number that characterises the inertial forces from a fluid rotating around an axis
T_c	Temperature at the fluid's critical point
T_r	Reduced temperature is the actual temperature of a fluid divided by its critical point
T_w	Temperature of the reactor wall
u	Unit vector for light used in the discrete ordinates method and two-flux approximation
$\tilde{u}$	The volumetric energy holdup of the pipeline
v	Velocity of fluid through the reactor
V	Variance-covariance matrix of parameters calculated in the parameter estimation method
V_c	The volume occupied by a unit mass of a fluid at its critical point
X	Conversion of the starting material

$\overline{X}$	Sample mean
x_i	Molar fraction of component i
Y_i	Reference t-value statistic used within the t-test
z	Axial position along the reactor
Z_c	Critical compressibility used in the van der Waals equation

Greek Letter	Definition
α	Napierian absorption coefficient
β	Competing absorption factor between two absorbing species
β_T	Total extinction coefficient including scattering and absorption of light
γ	The angle made between the light unit vector and the radial axis
∇	Differential operator
∇^2	Laplacian operator giving the divergence of the gradient of Euclidean space
δ	Thermal diffusivity of a fluid
ϵ	Surface roughness of the pipe used within the Haaland equation
ε	Decadic linear absorption coefficient
ħ	Planck's constant relates the energy carried by a photon to its frequency
ζ	Dimensionless scaling factor used in the van der Waals equation
θ	Estimated parameter value
θ	Azimuthal angle used in cylindrical coordinates
κ	Dispersion ratio used to calculate the effective dispersion coefficient of fluid flow through a coiled tube
λ	Wavelength of light
μ	Dynamic viscosity is a measure of a fluid's internal resistance to flow
μ_0	Specified mean used in the t-test
μ_{EE}	Mean value of elementary effects used to measure the effect a parameter's value has on the output of a model
ν	Kinematic viscosity is the ratio of dynamic viscosity to density and is also known as the 'momentum diffusivity'
ξ	Scattering coefficient
ρ	Density of a fluid
σ	Standard deviation
τ	Local shear stress
ϕ	Quantum yield
ϕ'	Quantum kinetic parameter
ϑ	The 'albedo' which describes how absorbing or reflective a medium is
χ^2	Chi-squared value used within statistical analysis
ψ	Value depends on coordinates system used (ψ = 0 for cartesian coordinates and ψ = 1 for cylindrical coordinates)
ω	Acentric factor is a measure of the non-sphericity of a molecule
$\omega_{i,j}$	Correlation between parameters
Ω	Angular velocity

1. Water solubility and pressure drop for Carbon Capture and Storage

1.1. Chapter Overview

This chapter introduces Carbon Capture and Storage (CCS) as a technological response to climate change as it aims to remove carbon dioxide from the atmosphere.[1] One of the remaining challenges of CCS is the understanding of impure-dense-phase CO_2, as the carbon dioxide is unlikely to be of high-purity. The effect of impurities on the solubility of water in dense-phase CO_2 needs to be clearly understood to enable the large-scale development of CCS pipeline networks, due to the effect it can have on corrosion rates and the corresponding safety considerations.[2–4] A number of methods are discussed for measuring water solubility, before experimental work is carried out using an Fourier-Transformed Infra-Red (FTIR) spectroscopic method previously developed at the University of Nottingham.[5]

The FTIR method was used to measure the water-solubility limits of 10 % H_2 + CO_2 at 40 °C, with the results showing a continuation of the trend of reducing solubility with the reduction in density of the fluid. The results of the spectroscopic method, along with the previously measured values for 5 % and 10 % N_2 + CO_2, are then compared with the predictions of different equations of state (EoSs).

The EoSs generally overestimated the water solubility limits at 40 °C, which was considered to be safer than the underestimation. The experimental values for the water solubility at 25 °C were also compared to EoSs, which also showed an underestimation for the majority of mixtures. The only mixture where the comparison was overestimated by the EoSs was the 10 % H_2 + CO_2 mixture. The chance of 10 % H_2 + CO_2 occurring within CCS pipelines was considered low, hence the difference between the prediction and experiment was less problematic.

Experimental results for both the density and viscosity of CO_2 rich mixtures, found in literature, were then compared to EoS predictions, with *ca*. 5 % difference shown for the majority of conditions. The accuracy of the EoSs for both density and viscosity meant that the EoSs were used to predict the pressure-drop of CCS pipelines at a variety of conditions and pipeline shapes.

Finally, the model used for the prediction of pressure drop with CCS relevant mixtures was used to support a method developed to measure phase-behaviour of mixtures. Experimental values, collected by Dr. Gurbuz Comak, showed an increase in pressure drop when a fluid flowed through conditions which caused a change in phase. The model supported the theory that the increase in pressure drop indicated a phase change. The defined model was able to accurately predict the pressure drop of a reactive mixture which is traditionally difficult to measure the phase behaviour due to the reactivity.

1.2. Chapter aims

As mentioned in the Preface, the work related to CCS was truncated due to the change of UK Government's CCS policy decision and subsequent closing of the CCS division in PSE. The original objectives for the CCS work were modified from the development of PSE's Equation of State with experimental results to:

Aim 1.1 - To carry out experimental work for determining the phase behaviour of tertiary systems of CO_2, H_2 and H_2O relevant to CCS pipeline operation

Aim 1.2 - To compare the experimental work on phase behaviour with the predictive capabilities of PSE's Equation of State

Aim 1.3 - To use PSE's software to understand the effect impurities with CO_2 has on the operation of pipelines, especially the pressure drop of a pipeline

Aim 1.4 - Undertake a training exercise modelling existing experimental work on the pressure drop and phase behaviour of a CH_3CN mixture at elevated temperatures

1.3. Climate change and mitigation

An Intergovernmental Panel on Climate Change (IPCC) report found a 98 % chance that anthropogenic CO_2 emissions have caused climate change.[6] There has been an increase in general awareness of this issue, however, this has not always lead to tougher regulations on high emissions industries. There

are a number of reasons for this; lobbying powers of carbon rich industries, energy security of alternatives and ethical arguments such as 'why should less economically developed countries not take advantage of cheap fossil fuels, like countries such as the USA and the UK have for the best part of two centuries?', among others.[7] However, there have been some successes such as the introduction of the UKs Climate Change Act 2008, the first legally binding emissions targets set by any government. This will be achieved by introducing five year carbon budgets that follow the most cost efficient path to achieve the 2050 carbon dioxide emission targets.[8] The UK Government has also recently legislated for net-zero carbon emissions by 2050.[9]

It is widely assumed that most of the carbon dioxide emissions are emitted from power stations and that efforts should be focussed on improving power stations efficiencies and emissions.[10] However. the power sector accounts for just 24 % of CO_2 emissions in the UK, and are run as efficiently as possible using the technologies installed due to the strong economic drivers for efficiency in the power sector.[11] In order to improve emissions of fossil-fuel plants, significant investment would be required to improve the efficiency of older sites, which is economically unfavourable, or new cleaner plants would need to be built, such as using supercritical (sc) boilers.[12] There is a reduced focus on commercial industries (17 % of UK Emissions), as manufacturing plants also burn their own fossil fuels as well as the carbon emissions from transport.[11] One method to reduce emissions would be to electrify these processes and take advantage of the large economies of scale that power plants benefit from.[13] Although methods such as electrification would help to reduce overall emissions, it would not achieve net zero carbon emissions. In order to achieve 'zero' emissions a carbon mitigation technology is required, with CCS being the most developed.

1.3.1. Negative Emissions

Negative emissions are seen as a crucial technology requirement for all feasible plans to reach the +1.5 °C target agreed at COP21.[14,15] The possibility of negative emissions have been proposed through the use of carbon capture and sequestration in combination with biofuels, known as BECCS.[16] Biofuels

are considered 'carbon neutral' by some as the carbon fixed during growth is then re-released into the atmosphere, hence the balance is equal. However, considering biofuels as carbon neutral is not strictly valid as there is a fuel and energy cost in the processing of the biofuel, as well as the production of any fertiliser (if used), however biofuels are certainly a vast improvement on fossil fuels.[17] Also, there are more recent concerns of the destruction of soil in biomass processing, which some estimate holds up to 40 % of the carbon of a forest.[18]

If the carbon from the combustion of these biofuels is captured and stored underground, the carbon is removed from the atmosphere and could be considered to have negative emissions. It is thought that if the world is to meet the +1.5 °C 2050 target, negative emissions will be required as emissions are expected to peak in the 2030s.[19]

1.4. What is Carbon Capture and Sequestration (CCS)?

CCS is considered one of the major carbon mitigation technologies currently available for deployment.[20] The general concept is to capture and transport the carbon dioxide produced during fuel combustion to a suitable storage site rather than allowing it to be released to the atmosphere as shown in Figure 1. The carbon dioxide is then stored and therefore taken out of the 'carbon cycle'.[21]

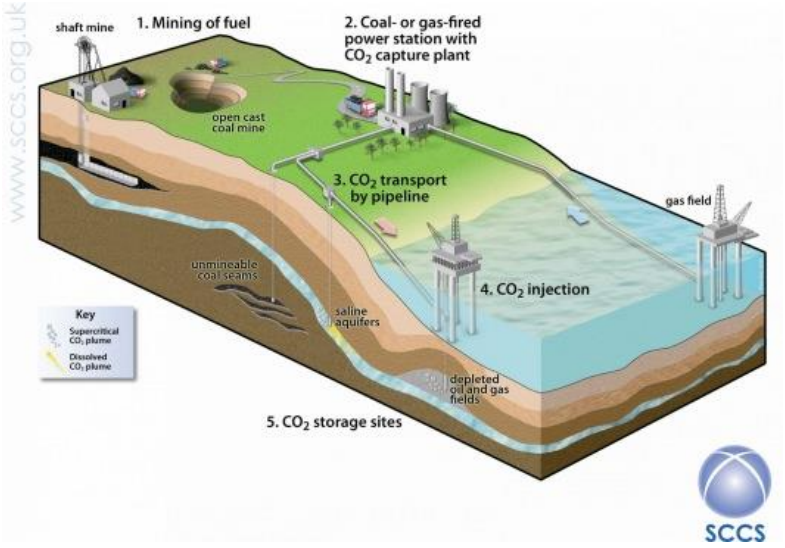


Figure 1 - Schematic describing the CCS process for a power plant, where a carbon-based fuel is burnt in a power plant, with the CO2 captured and transported through pipelines to off-shore depleted oil and gas fields or on-shore depleted goal seams where it is stored.[22] More recently CCS is being seen as a possible route for carbon-intensive industries, such as steel works, to decarbonise rather than the more traditional idea of it being used to decarbonise power plants.

There are a number of stages in the CCS process; Capture, Transportation and Storage. Historically there has been great interest in both capture and storage and hence a wealth of research has been conducted in these areas.[23] Until recently the large-scale transport of carbon dioxide was relatively less understood. There are three different established capture technologies currently available, each offering their own advantages and disadvantages as well as affecting the subsequent stages.

1.4.1. When will CCS be used?

Traditionally CCS was viewed as a technology to decarbonise fossil-fuel power plants, however, more recently this view has changed to either re-use the captured carbon or decarbonise industries that in the past have been considered difficult to decarbonise due to a number of factors.[24]

CCS is sometimes reformulated as Carbon Capture, Utilisation and Storage (CCUS), where the CO_2 is utilised as a feedstock for chemical or agricultural processes.[25] By finding methods to use the CO_2 as a feedstock it is hoped that demand for CO_2 will increase. This increased demand will increase the price of CO_2 which will drive further investment in CCUS technologies. The second driver behind this change to CCUS is the rapid reduction in price for renewable power, with offshore wind in the UK being able to supply 5.8 GW power at £39 $MW{\cdot}h^{-1}$, which is below the wholesale price at the time of writing.[26] Finally, some industries such as the cement industry, which emit CO_2 as an unavoidable part of the process would not be able to decarbonise without a way to capture the carbon.[27]

1.4.2. Capture Technologies

The capture technology selection depends on a number of criteria such as fuel type and whether the plant can be retrofitted with CCS. The type of technology selected will have an impact on the composition of the flue gas; which in turn impacts purification and compression costs before the gas is ready to be transported.[28] The three separate technologies are summarised in Figure 2 and explained below.

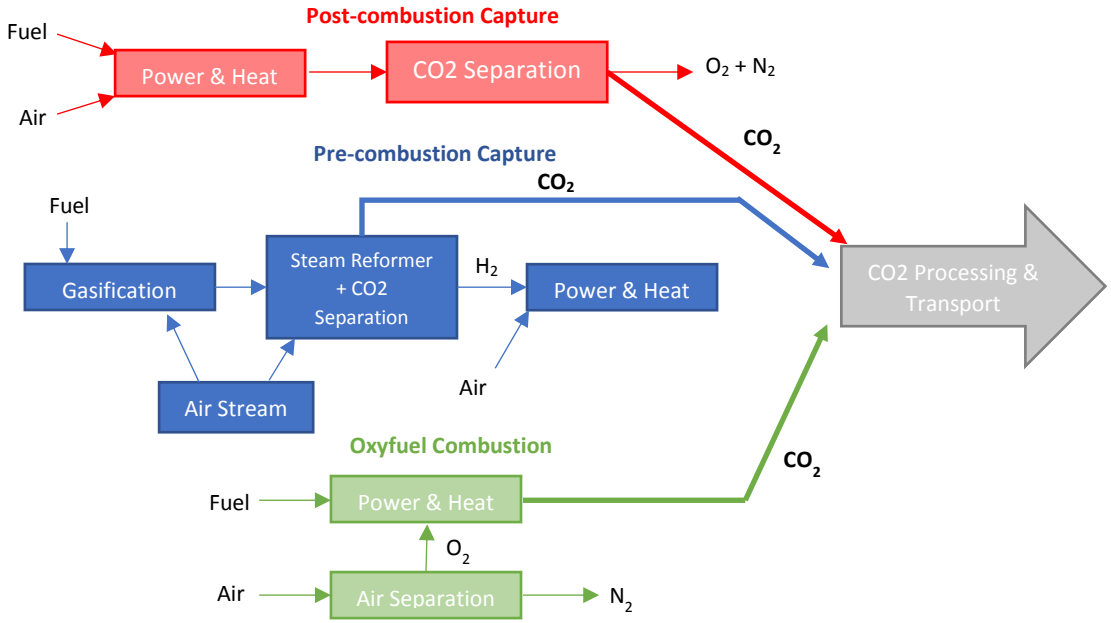


Figure 2 – A schematic of the three most common technologies used within CCS. Post-combustion capture uses solvents or adsorbents after the fuel has been burnt to capture the CO_2 and is the most widely developed technology in CCS. Pre-combustion removes the carbon before the fuel is burnt through the gas-shift reaction and oxyfuel combustion burns the fuel in a high-oxygen environment to create a high CO_2 concentration in the exhaust stream.[17]

Post-combustion capture

Post-combustion capture technology removes carbon from the emissions after the fossil fuel has been combusted. This technology relies on the selective adsorption of CO_2 into a solvent or adsorbent, before the CO_2 is stripped out of the solvent and independently pumped away to be stored. Traditionally the solvent of choice has been amine based although more recently alternative solvents and techniques such as membrane separation have been developed due to environmental issues and energy concerns.[29] The amine solvents absorb the CO_2 at *ca.* 50 °C and is heated to *ca.* 130 °C to release the CO_2. This presents a dilemma for the solvent technology; the increased absorption properties and selectivity for CO_2 often leads to a more energy intensive process being required to release the CO_2 from the solvent.[30]

Post-combustion technology is currently seen as the most developed technolgoy with the SaskPower Boundary Dam plant currently the largest scale CCS Power Plant in operation, designed to capture 1 $MtCO_2 \cdot year^{-1}$.[31] The main concerns with post-combustion technology is the thermal efficiency cost

of this process; the majority of reported figures are around a 10 % reduction in total power plant efficiency.[1] Pulverised coal plants currently run at an efficiency close to 40 %, the addition of CCS to therefore poses a significant difference. This is a concern as pulverised coal plants are the most prevalent power plant globally.[1]

Pre-combustion capture

Pre-combustion capture removes the carbon from the fuel before it enters the combustion chamber. This is achieved by gasification of the fuel followed by the water gas shift reaction, yielding carbon dioxide and hydrogen, shown below.[32] The carbon dioxide is then separated from this mixture and pumped for storage; the hydrogen is then burnt in the combustion chamber.

$$CH_4 + 2\ H_2O \rightarrow CO_2 + 4\ H_2$$

Due to the extra technical requirements of this method the systems have to be specifically designed and built for this purpose, it is currently challenging to retrofit existing plants. The technologies required have been proven in other industries such as gasification and natural gas processing. However, until recently the technologies have not been proven when combined together. Kemper County energy facility was completed in July 2016 at a cost of $6.6 billion and is capable of capturing 3 $MtCO_2 \cdot year^{-1}$ which is expected to be used for Enhanced Oil Recovery (EOR). This project was $4.4 billion over budget and took 2 years longer than expected which highlights the difficulties new large-scale technologies face.[33] Pilot scale plants fitted with pre combustion capture technologies have shown an overall efficiency penalty of 7-8 % which is lower than post combustion, however still relatively high.[32]

Oxyfuel Combustion

In oxyfuel combustion the fuel is burnt in an oxygen rich gas mixture rather than being combusted in air. A pure oxygen stream is not used as this would lead to high flame temperatures which would be too high for current materials to withstand.[34] Instead, recycled flue gas is mixed with the oxygen or the fuel is burnt via staged combustion. This recycling leads to a high percentage of CO_2 in the exhaust

gases and less purification is required before being pumped for storage or utilisation compared to the previously mentioned technologies.[34]

1.4.3. CCS Exhaust Stream Composition

For the most efficient transport of CO_2 a supercritical phase is suggested, this offers the best properties for both density and gas flow behaviour.[4] The critical point of pure CO_2 is 31.1 °C and 7.38 MPa, so the conditions need to be kept above this point, although impurities will have an effect on this.[35] A single phase flow is preferred as multi-phase flow is much more complex to model and will encourage the condensation of liquid water leading to corrosion issues.[36]

The composition of the CO_2 stream for transport after processing is dependent on the capture technology used, as well as fuel type. Table 1 shows an example composition of three different technologies taken from pilot plants after purification; the exact compositions can differ depending on the efficiency of each process which can fluctuate between plants.[37]

Table 1 - Typical molar percentages for different components found in CCS exhaust streams, for the different capture technologies after purification.[37]

3 Pilot Plant CO_2 Stream Gas Composition (% mol.)

Component	Post-combustion capture	Pre-Combustion Capture	Oxy Fuel Combustion (wet)
CO_2	94.4	98.21	93.82
H_2O	5.6	1.79	4.16
H_2	0	0	0
CO	0	0	0
N_2	Traces	0	0.28
O_2	Traces	0	1.38
Ar	0	0	0.35

The fuel differences predominantly effect the trace gases. Coal naturally contains higher amounts of sulphur, hence why it produces more H_2S than natural gas combustion. The presence of these impurities will also affect the physical behaviour of the CO_2 rich gas mixture and need to be understood further.[3]

Table 2 shows the current suggested safety limits for a range of gases expected to be found in CCS exhaust mixtures, including a suggested water concentration limit. These safety limits were calculated using binary mixtures of CO_2 + x, rather than more likely multi component mixtures. In order to create revised safety limits a deeper understanding is needed regarding the phase behaviour of these mixtures.

Table 2 – The DYNAMIS CCS Proposed Safety Limits for different components commonly found in CCS exhaust streams.[4]

Component	Concentration
H_2O	500 ppm
H_2S	200 ppm
CO	2000 ppm
CH_4	Aquifer < 4 vol.%, EOR <2vol.%
N_2	< 4 vol.% (all non-condensable gases)
Ar	< 4 vol.% (all non-condensable gases)
H_2	< 4 vol.% (all non-condensable gases)
CO_2	> 95.5 %

Understanding the behaviour of CO_2-rich fluids, especially the role of impurities, is crucial for reducing costs for the large-scale adoption of CCS. This is important for water solubility limits, which need to be measured as the presence of liquid water within a pipeline increases the rate of corrosion causing safety concerns and increased operating expenditure.

1.5. Why is water solubility important?

Water solubility is a major interest area due to the environmental, safety and economic implications of the presence of water in pipelines.[38] If liquid water forms inside the pipeline, gases are able to dissolve into it; with CO_2 able to form carbonic acid and SO_2 available to form sulfurous acid. This carbonic acid causes 'sweet' corrosion while sulfuric acid causes 'sour' corrosion, with both being a cause for concern.[39]

One example of an environmental concern is if CO_2 leaks offshore, the pH of the surrounding water would be lowered affecting very sensitive marine ecosystems.[40] CO_2 leaks on land tend to have less severe consequences because the ecosystems are generally more robust. However if the

concentrations are high enough (over 3 %), CO_2 can impact the health of humans, animals and vegetation and if concentrations reach critical levels (>10 %) for extended periods of time the effects can be fatal.[41,42] Another particularly concerning property of CO_2 leaks is the ability to displace oxygen in valleys and confined spaces, resulting in asphyxiation and possible casualties. The concern for health effects would be amplified if H_2S, SO_2 or CO are also present in the pipeline, even in small quantities these compounds can cause serious harm to life.[43]

These risks can be easily minimised by careful monitoring of the pipeline network and wells where the gas is stored. For example, in Dakota, USA, further preventative measures have been taken by installing a series of regularly spaced valves along the pipeline so that in the event of a breach the valves close, thus restricting the CO_2 flow and preventing further CO_2 loss.[43] In general, the probability of these events occurring is low and there are few recorded cases. Product failure and corrosion have been the cause of most incidents, rather than human error, therefore with further research and development, these risks could be reduced significantly.[43] The pressure required to keep the fluid in the supercritical region is large, so any faults in the pipeline could be exposed, potentially leading to a large explosion.[43,44]

The economic effects also need to be considered, when a project is commissioned the costs are calculated with an assumed corrosion rate of pipelines, some estimates suggest corrosion costs the global economy billions of dollars per year.[45] An increase in corrosion rates leads to higher replacement and repair costs. This could mean the pipeline is uneconomical, especially in an industry where keeping costs low is a key issue with the current 'carbon price' being low.[46] Another economic question companies will want to answer is that of the minimum amount of energy and money required for purification and compression while also ensuring the safety of the pipeline.

1.5.1. Impurities' effect on phase behaviour

In order for a cost effective and safe CO_2 distribution network, a key stage in CCS development, water solubility in supercritical CO_2 needs to be studied and understood, especially for CO_2 containing

impurities. For example, the critical point is reduced with the introduction of impurities, with the critical temperature for 5 % N_2 + CO_2 expected to be 27.1 °C and 22.5 °C for 10 % N_2 + CO_2.[47]

The phase behaviour differences are then expected to have an effect on the water solubility. Understanding water solubility will then help create a model for the operational composition, temperature and pressure range of the proposed pipelines.

1.5.2. Water solubility measurements

Due to economic reasons it is most likely that future CCS pipelines will be constructed using carbon steel.[3] Keeping the water present in a single phase is important as this would avoid increased corrosion rates.

Current water limits are set on previous work with natural gas pipelines and does not use experimental data to inform CCS-specific limits.[4] The water solubility is expected to be dependent on impurities present in the CO_2 and hence water safety limits need to be better understood.[5,48] One of the issues of measuring the water content of the CCS-relevant system is the high pressure required, which is unsuitable for most standard techniques. To measure there are generally two approaches:

- Analytical methods – CO_2 is allowed to become saturated with H_2O before being measured;
- Synthetic methods – A known composition of mixture is made before being measured.[49]

Analytical methods for water solubility

Most analytical methods for water solubility measurements involve allowing the vapour and water to mix and reach equilibrium before the fluid is analysed for water content compared to CO_2.

Wiebe and Gaddy – Expanded Gas Method

One of the first experiments regarding CO_2 as the solvent followed on from work in 1939 where both Wiebe and Gaddy were investigating water as the solvent, and CO_2 the solute. They investigated water solubility and noticed a large increase in solubility at pressures above 71 MPa, shown by large amounts of water in the expanded gas.[50]

The expanded gas method involved saturating the water with CO_2 at a set temperature and pressure in an apparatus before expanding the fluid so the quantity of gas and quantity of liquid water could be measured at 25°C and atmospheric pressure.[51] The gas was measured by a Shepherd manometric gas analysis apparatus with the water measured by a Burette system. This experiment gave a value of CO_2 and water and therefore allowed the amount of CO_2 dissolved per gram of water to be calculated and compared. It was noted that above 71 MPa the amount of water dissolved was significant, and the formation of a single completely miscible phase was observed; this was one of the first observations of the effects on solubility of supercritical CO_2.[50]

Improved Expanded Gas Method - Sabirzyanov

Sabirzyanov improved the accuracy of the expanded gas method. The saturation of water was achieved through the introduction of carbon dioxide to a sealed cylinder containing water.[52] This cylinder was then agitated by being rocked twice a minute, for two hours, through 160° with a perforated ball to improve phase mixing. The gas is then expanded into weighed graduated flasks and the volume measured at normal conditions. As with the Wiebe and Gaddy method, the solubility was determined from the volume of the gas and the weight of the liquid achieving an error of 3 %.

Chromatography method

Another method for determining the composition of a sample is through gas chromatography (GC); it is a commonly used analytical method, for phase behaviour studies. Small samples are taken from a supercritical cell such that the equilibrium is not disturbed, and then analysed.[53] The components are eluted through a GC column using an inert gas such as helium. The components are then separated over the length of the column by the differing strengths of interaction between analyte and column. There are a number of methods of detecting the amount of each component, such as a flame ionisation detector (FID) or thermal conductivity detector (TCD). The detectors all work on a similar principle of detector output being relative to the amount of analyte present. The SINTEF group based in Trondheim, Norway use a TCD as the components are relatively unreactive.[54] Flame ionisation

detectors are often used for separating organics because they are combustible. However, water solubility studies would be near-impossible with FID as the water would extinguish the flame.

Synthetic methods for water solubility

The synthetic methods regarding water solubility start with a known amount of water and a known composition of gas. The synthetic method allows the mixture to equilibrate at a defined pressure and temperature before being analysed.[49] There have been a variety of synthetic-type techniques developed to measure the amount of water present in the supercritical phase.

Although not explicitly developed for water solubility there have been a number of methods developed for studying phase behaviour of all fluids. The phase change is detected by observing an obvious change in signal moving from above the critical point to below, which could suggest the condensation point. For these methods to succeed a known composition and set of conditions where the water is guaranteed to be in phase are required.

Human observation

Using a pressure cell with observation windows allows human observation and was the traditional method of studying phase behaviour. The pressure, temperature or volume of the cell is changed allowing people to observe the formation of bubbles or condensation.[55] The conditions of the cell at the transition point are then noted down as the equilibrium conditions between the phases. A similar approach could be used for the solubility of water as the formation of bubbles or condensation would indicate the solubility limits. One concern regarding human observation would be that near the critical point the phases can become opaque and impair judgement[56].

An example of a semi-automated observation method is the chilled mirror dew point hygrometer; where a gas mixture with an unknown concentration of water is allowed to condense on an inert, polished, chilled mirror surface.[57] A beam of light is then reflected off this surface and connected to a photodetector.[58] The mirror temperature is then altered at the point where the rate of condensation is equal to that of the dew layer evaporation, this is termed the dew point.

Over time the traditional method has become more and more automated. The automated method is the preferred method to obtain physical measurements as it is objective and more-easily comparable. However this does not mean that view cells are defunct; they have been used to confirm the existence of previously unknown phase behaviour predicted by the measurements of other techniques.[59]

Spectroscopic Methods

Spectroscopic methods can be used to measure the concentrations of water in fluids through the use of the Beer-Lambert Law which relates concentration and absorbance value. The spectroscopic method offers a direct measurement of the optical properties of the fluid rather than analytical methods which could disturb the dissolution equilibrium before a measurement is taken.[5,60] In order to study water concentration an absorbance band that is caused by water needs to be selected. There have been two main options for this in recent literature; near-IR absorbance and IR absorbance.

Near Infra-red Absorbance (NIR)

Due to the strong absorbance of CO_2 in water's vibrational 3500 – 4000 cm^{-1} region as well as the possibility of interference of the H-O-H bending mode around 1600 cm-1. Wang decided to use the absorbance bands in the 7100 – 7500 cm^{-1} region which relates to a water overtone band ($2v_3$) at 7208 cm^{-1} as shown in Figure 3.[60] An amount of water was added to the cell before being pressurised with $scCO_2$; the cell is then allowed to equilibrate and the NIR spectra measured.

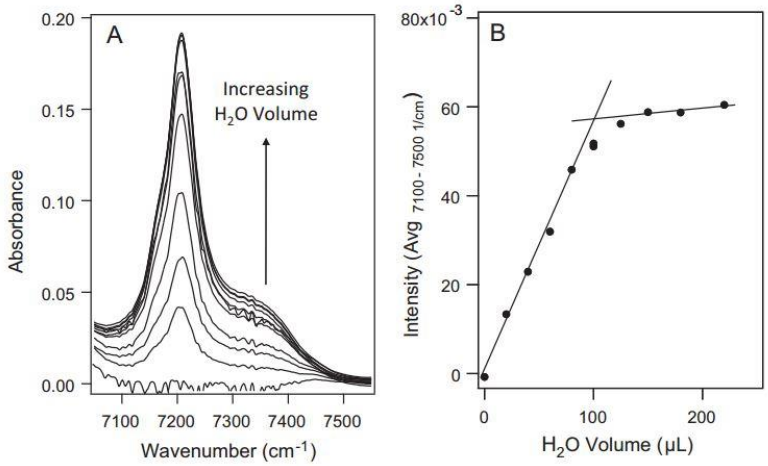


Figure 3 – The Near-IR method for calculating the solubility of water in CO_2, following the increase of water's $2\nu_3$ overtone band around 7200 cm^{-1}. Saturation is reached when the band stops increasing with amount of water added. [60]

This process is repeated with an increased amount of water and the average absorbance between 7100 – 7500 cm^{-1} is plotted against volume of water. The average absorbance increases with volume of water before reaching a plateau which indicates the solubility limit has been reached. This band was analogous to the 10,500 cm^{-1} $2\nu_1 + \nu_3$ band observed by Jackson et al.[61] Wang's work appears to agree with other groups' findings, although it should be noted a verified set of data is not currently available for this system.

Attenuated Total Reflection Infra-Red method

Unlike the high-pressure IR cell mentioned earlier, Attenuated Total Reflectance (ATR)-Infra-Red (IR) only requires a single window into a cell which can be diamond and thus provides a more chemically and physically stable apparatus. The ATR-IR cell used in the Poliakoff/George group was developed in conjunction with Alexander Novitskiy from Moscow State University and is based on the Specac Golden Gate SCFs analyser incorporating modifications to both the top plate geometry and heating system.[62] This gives the apparatus the uniformity and stability required for phase equilibrium measurements up to 650 K and 250 bar.

The IR beam travels through the diamond surface and penetrates into the medium in contact with the diamond by half the wavelength of the IR beam. Therefore, this method is a surface sensitive method

and hence can only give information about the medium in direct contact with the diamond surface. The penetration depth increases as the wavenumber increases and hence is useful for the IR fingerprint region.[63] This method is surface sensitive as the difference in absorbance between a vapour and liquid can be detected. It also gives spectroscopic data regarding the fluid in contact with the sensor, hence a better understanding of the system can now be developed.

The ATR-IR method has currently been used for EtOH, MeOH and H_2O as well as a binary system of EtOH + H_2O. This method, if able to be used with CO_2, could be extremely useful as the phase changes could be detected as well as understanding the amount of water present in each phase.

1.5.3. Experimental work that forms the basis of initial investigations

A technique was developed in the group to measure the water solubility of water into CO_2, which has been reported in literature and explained below.[5] The method was validated with pure CO_2 and matched previous experiments well. The water solubility limits for 5 % and 10 % N_2 + CO_2 have previously been measured in the group and published. [5] The previously published results for molar fraction of water (xH_2O) and concentration of water in the CO_2-rich phase are shown in Figure 4 (a) and (b), respectively.

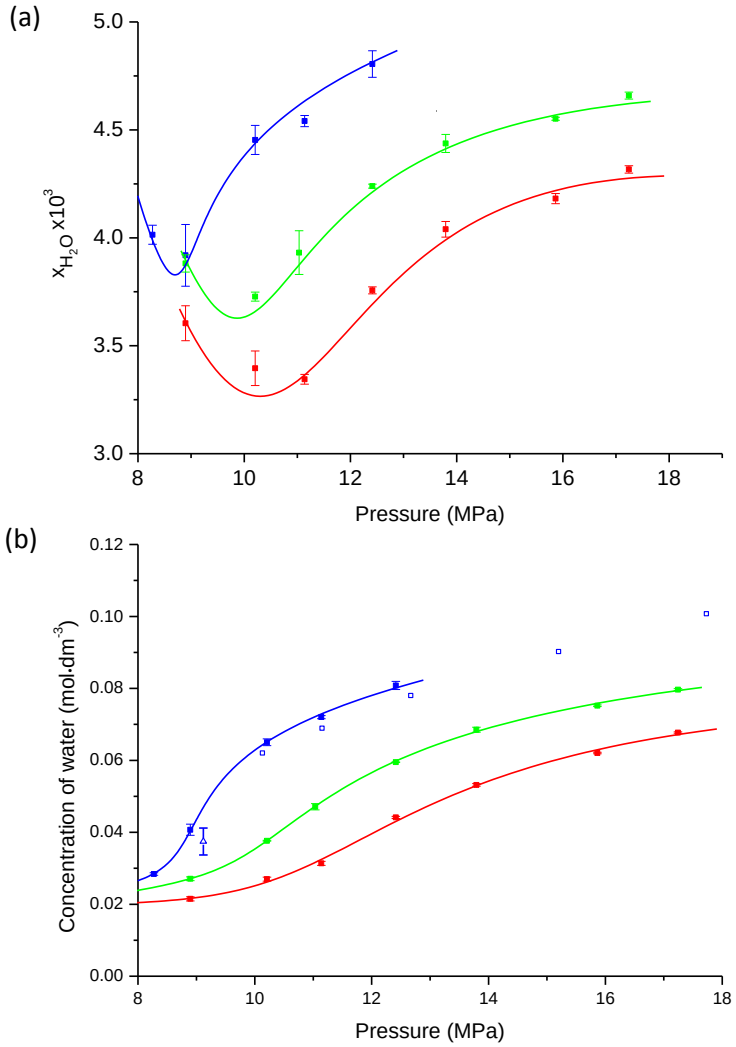


Figure 4 – The evolution at 40 °C of (a) molar fraction and (b) concentration of H_2O in Pure CO_2 from Foltran et al. (2015) (■), Pure CO_2 from King et al. (1992) (□), Pure CO_2 from Wang et al. (2013) (△), 5 % N_2 + CO_2 from Foltran et al. (2015) (■) and 10 % N_2 + CO_2 from Foltran et al. (2015) (■); lines are drawn to guide the eye.[5,60,64]

As can be seen in Figure 4 the increasing concentration of N_2 in CO_2 decreased the solubility of water into the CO_2-rich phase. The decrease in solubility was largely thought to be due to the decreasing density, as can be seen in Figure 5 where the solubility limits for both mixtures seem to follow a trend. The densities of the N_2 + CO_2 mixture were calculated using REFPROP and were previously reported.[5]

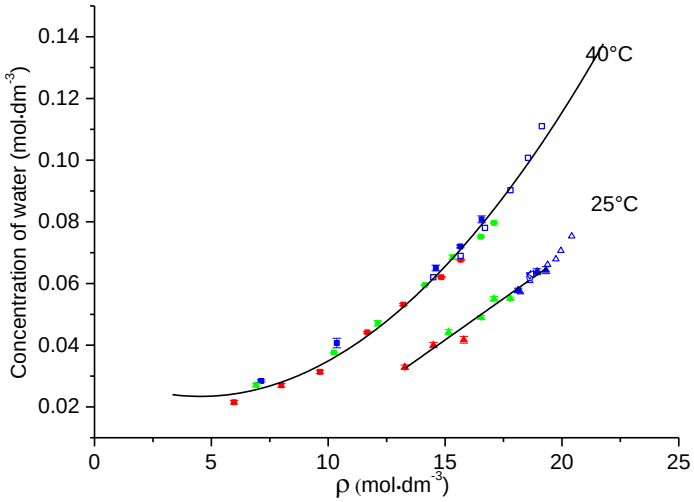


Figure 5 – Evolution of the molar concentration of water as a function of density for H_2O in Pure CO_2 at 40°C (■), Pure CO_2 at 40°C from King et al. (□), 5 % N_2 + CO_2 at 40 °C (■), 10 % N_2 + CO_2 at 40 °C (■), (▲) 25 °C in pure CO_2 from this work; (△) 25 °C in pure CO_2 from King et al. (1992); (▽) 25 °C in pure CO_2 from Wiebe (1940); (○) 25 °C in pure CO_2 from Gillespie and Wilson (1982); (◁) 25 °C in pure CO_2 from Song and Kobayashi (1986); (▲) 25 °C in CO_2 + 5 % N_2; (▲) 25 °C in CO_2 + 10 % N_2; lines are drawn to guide the eye.[5,50,64–66]

As the water solubility had largely been found to be density dependent with N_2 as an impurity, it was important to see if this trend continued for other gases. Hydrogen was chosen to investigate this as it has unique properties due to its small molecular size and would be expected to be most likely to exhibit unusual behaviour.[67] The experimental set up was then used within this work to understand the water solubility for 10 % H_2 + CO_2.

1.5.4. Experimental measurement of water solubility

The method developed was a spectroscopic method that used specialised-custom-built equipment due to the high-pressure conditions. The experimental set-up, known as the rig, contained two major components; a high-pressure IR cell to measure and a sample mixer to prepare the mixture, as shown in Figure 6. The rig also contained a number of safety measures, including pressure and temperature trips to ensure the operator's safety.

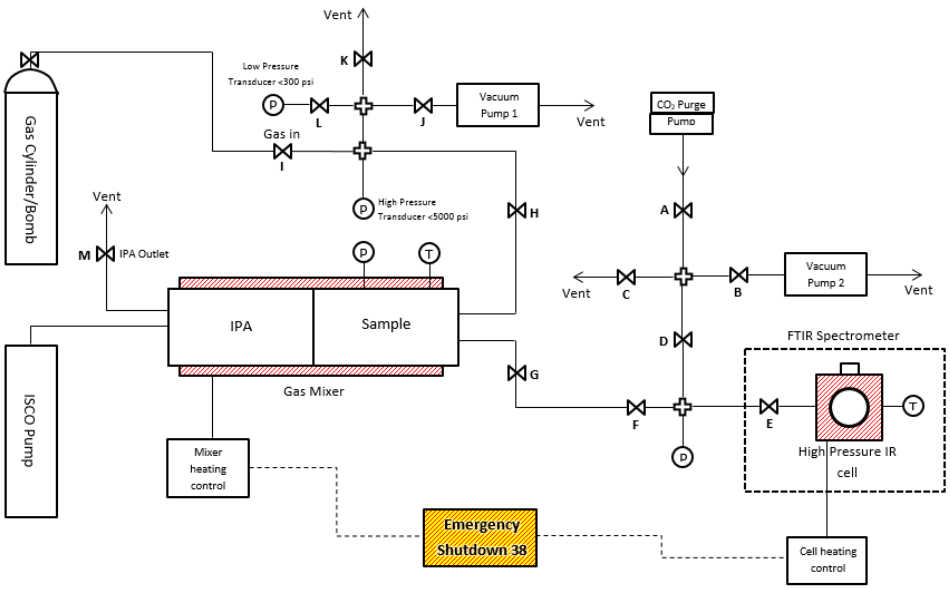


Figure 6 - Schematic of the rig diagram for high pressure FTIR measurement with the gas mixer pressurised with IPA as the hydraulic liquid with the heating jacket indicated by the hashed red area. The high pressure FTIR cell was also temperature controlled as indicated by the hashed red area. The encircled Ts and Ps indicate thermocouples and pressure transducers, respectively.

High-pressure FTIR cell

The method used for the high pressure Fourier Transformed Infra-Red (FTIR) measurements takes advantage of a high-pressure IR cell; the stainless-steel cell contains a small aperture with two CaF_2 windows giving an optical path length of 3mm, sealed by a Teflon O-ring and epoxy resin seal.[68] This is surrounded by a heating jacket which controls the temperature to within ±0.3 °C. The temperature and pressure inside the cell are measured by a K-type thermocouple and SuperTJE pressure transducer, respectively. The high-pressure cell was designed to be used with most FTIR spectrometers, with minimal alteration to the spectrometer. In this case, a Nicolet 380 spectrometer with a 4 cm^{-1} resolution was used, with the spectra obtained from a Fourier transformation of 32 interferograms.

Gas sample mixer

The high pressure FTIR cell was combined with a gas sample mixer that enabled custom gas compositions to be synthesised separately from the cell, as shown in Figure 6 and reported in literature.[5,69] The gas sample mixture was prepared using a custom-built mixer which is a variable

volume cylindrical cell with a built-in magnetic stirrer. The volume of cell was controlled by a hydraulic piston, using isopropryl alcohol (IPA) as the pressurising fluid and an ISCO pump. Inside the variable volume cell, a K-type thermocouple and a SuperTJE pressure transducer measure the temperature and pressure of the cell, respectively.

Initially, the sample cell was expanded to the maximum volume (120 cm^3), before H_2 was injected into the sample mixer to a known pressure. As the volume, pressure and temperature of the cell were known, the amount of H_2 was calculated using the known density of H_2 from the NIST webbook of chemistry database.[70] The amount of H_2 was then used to calculate the amount of CO_2 needed to produce a mixture of the required composition. The calculated amount of CO_2 was then injected, from a weighed gas bomb, into the mixer cell through a Bronkhorst CO_2 mass flow controller. The mass flow controller indicated when the required amount of CO_2 had been injected, before the mass of the empty bomb was measured for confirmation of the final amount. The mixer cell was then heated to 40 °C, and pressure increased using the hydraulic piston to *ca.* 10 MPa. The mixture was then left stirring for 2 hours to ensure homogeneity. Due to the small molecular size of H_2, and the possibility of leakage, the mixture was remade each day experiments were carried out. The process of making up the H_2 + CO_2 mixture led to slight differences in composition, with a range from 9.85 to 10.15 %mol. deemed acceptable.

Data collection and analysis

A small, known, volume of water was injected with a micro-syringe into the high pressure FTIR cell, before being pressurised with the 10 % H_2 + CO_2 mixture up to the required pressure. The cell was placed on a magnetic stirrer plate to ensure the water was well mixed with the CO_2-rich fluid mixture. After *ca.* 5 minutes the FTIR cell was removed from the stirrer plate and placed inside the spectrometer. An FTIR spectrum was then taken every 5 minutes until equilibrium was achieved. As the volume of water injected into the cell (< 2 µl) was small compared to the volume of cell

(0.877 cm^3), it was assumed that only the CO_2-rich phase appeared between the two IR windows. The region of interest for these measurements was the H_2O v_2 stretch around 1605 cm^{-1}.

Between each test, the cell was flushed with pure CO_2 three times, with an FTIR spectrum taken afterwards to ensure all water had been cleared.

The process of injecting a known volume of water into the FTIR cell before being pressurised with the 10 % H_2 + CO_2 mixture was repeated with increasing volumes of water. The absorbance of the 1605 cm^{-1} band increased with the volume of water injected, as can be seen in Figure 7. The absorbance of the 1605 cm^{-1} band reached a maximum, which was assumed to be when maximum saturation of water in the 10 % H_2 + CO_2 phase was reached.

The absorbance values are plotted against the volume of water injected into the cell, as shown in Figure 7. The blue circles, below the saturation limit, are known as the 'calibration' points with the red circles being the 'saturation' points.

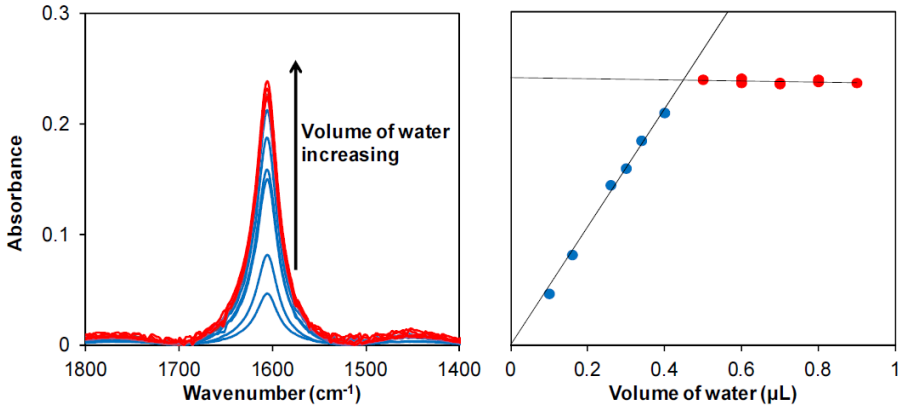


Figure 7 – Increase of the H_2O v_2 bending mode at 1605 cm^{-1} as a function of the volume of H_2O at 40 °C and 10.20 MPa, with corrections for the CO_2 spectra for the 5 % N_2 + CO_2 mixture. The blue spectra represent the calibration experiments and the red spectra represent the saturation experiments and (b) plot of the absorbance value of the H_2O band at 1605cm^{-1} as a function of the volume of water injected. Figure reproduced from Foltran et al. with permission.[5]

Calculation of saturation volume

To calculate the volume of water in the saturated phase, a number of calculations were needed to translate the FTIR absorbance value to the molar fraction and concentration. The process for the

calculation of the saturation volume at 9.72 MPa is presented below, before the saturation volume of the remaining pressures are presented.

The absorbance at 9.72 MPa and 40 °C is plotted against varying volumes of water in the 10 % H_2 + CO_2 phase in Figure 8. In Figure 8 the filled circles are the calibration points and the empty circles are the saturation points. A linear function for the calibration points was fitted with the gradient (0.372 μl^{-1}) and intercept (0.0136) and used in the subsequent calculations.

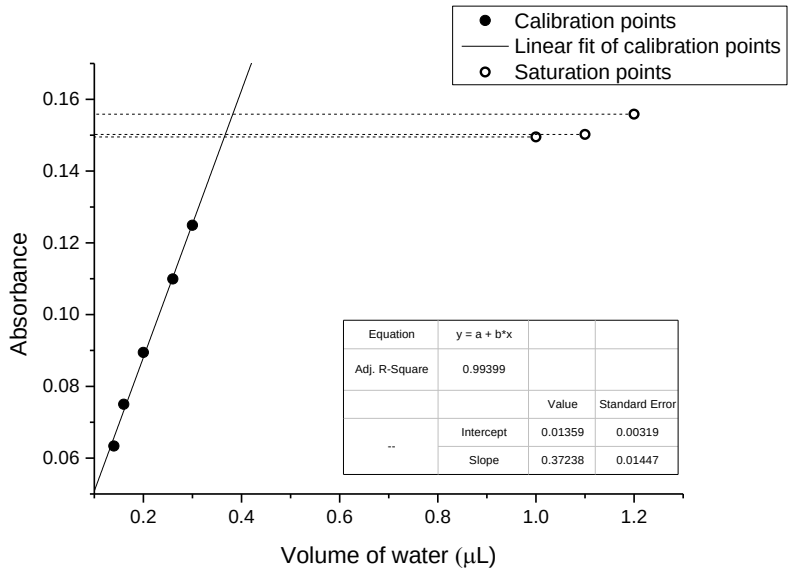


Figure 8 – The absorbance values for the 1605 cm^{-1} stretching band of H_2O as a function of the volume of water injected into the FTIR cell at 40 °C and 9.72 MPa for the 10 % H_2 + CO_2. The filled symbols (●) indicate the calibration experiments and the empty symbols (○) indicate the saturation experiments. The gradient and intercept are used to calculate the volume of water at saturation.

Due to the sensitivity of the equipment the pressure fluctuated inside the FTIR cell and hence the spectra were taken at slightly different pressures. The molar fraction of H_2O was calculated at each precise pressure before the values were averaged for the final data point. For the three saturation data points around 9.72 MPa shown in Figure 8, the volume of saturated water was calculated using the linear fitted function of the calibration points. For example, the value for 1.2 ml had an absorbance value of 0.156 which is equivalent to 0.381 µl as per the gradient and intercept calculated shown in Figure 8. The remaining calculated saturation volumes for the experiments around 9.72 MPa are shown in Table 3.

Table 3 - The volume of water injected into the FTIR cell and corresponding absorbance value of the saturation experiments for 10% H_2 + CO_2 at 9.72 MPa and 40 °C. The calculated volume of water at saturation calculated using the gradient and intercept of the calibration points is also presented.

Volume of water injected (µl)	Absorbance value	Saturated volume of water (µl)
1	0.150	0.364
1.1	0.150	0.366
1.2	0.156	0.381

1.5.5. Density used for calculations

For the molar fraction and concentration of water at saturation to be calculated, the density of the H_2 + CO_2 fluid was required. Due to the sensitivity of the mixture to small fluctuations in temperature and pressure, especially around the critical point, the pressure and temperature were recorded at the moment the FTIR spectra was taken. The pressure and temperature were then used to estimate the density of the 10 % H_2 + CO_2 mixture, which has previously been measured in the group and reported in literature.[35] The density measurements for 10 % H_2 + CO_2 at 40.05 °C at increasing pressures are shown in **Error! Reference source not found.**.

Fitting of function to experimental density data

The pressures recorded when the FTIR spectra was taken often varied slightly between measurements, hence a function was fitted so more accurate densities could be used. Initially, a global function was fitted to all of the data, however upon closer inspection a difference was observed between the globally fitted function and the experimental data. To overcome this, a locally fitted function was used from the two data points above and below the pressure in question. A comparison of the globally and locally fitted functions is shown in Figure 10, showing much greater agreement for the locally fitted function. The density here is shown in mol·dm^{-3}, which is converted from the measured kg·m^{-3} by dividing by the molecular weight of the fluid (39.81 g·mol^{-1}).

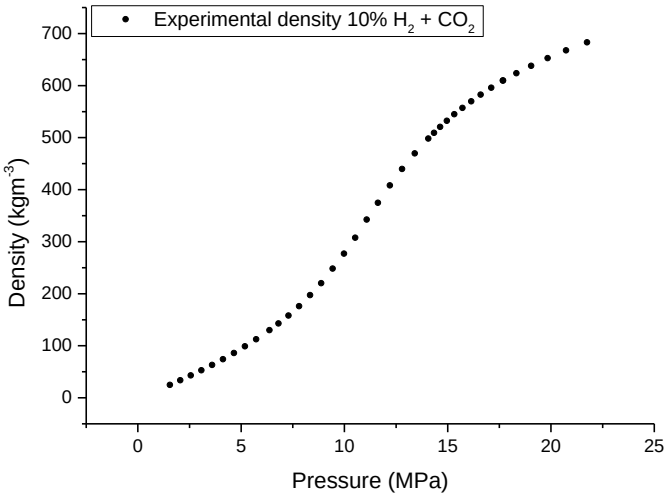


Figure 9 - The experimental density of 10 % H_2 + CO_2 at 40 °C at increasing pressures measured using the Anton-Paar densitometer technique.[35]

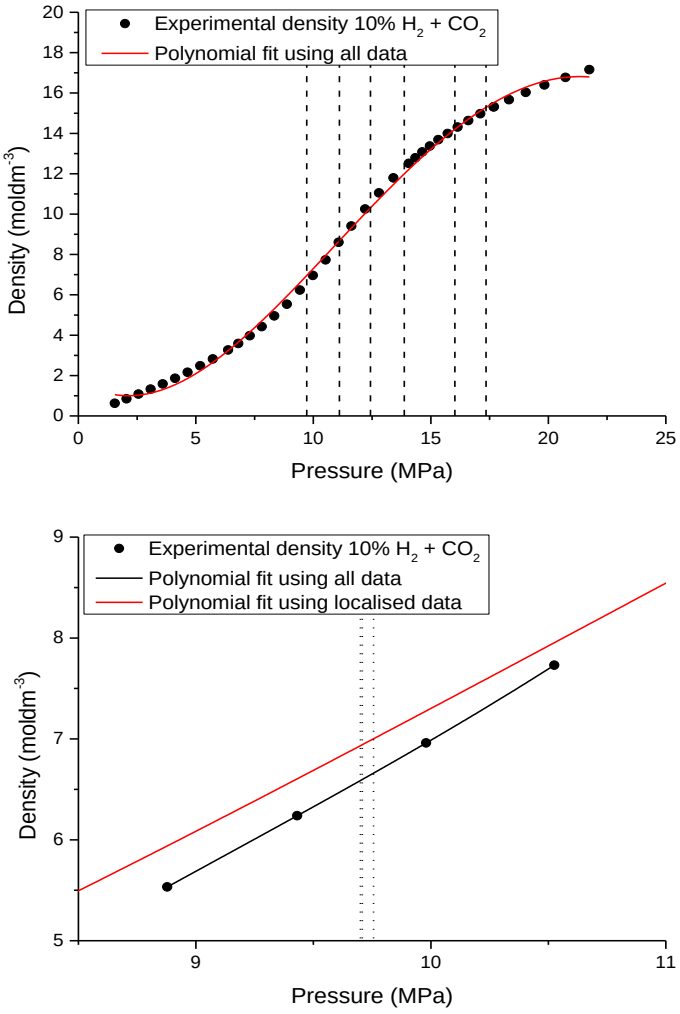


Figure 10 - The experimental density of 10 % H_2 + CO_2 at 40 °C at increasing pressures measured using the Anton-Paar densitometer technique fitted with a function using all data points indicated by a red line (–). (b) The globally fitted function (–) compared with the locally fitted function (–) with the locally fitted function showing much greater fit. The dashed lines indicate the pressures where measurements were taken.[35] **The R2 values for the global and local function were 0.998 and 1, respectively, showing the need for a visual comparison.**

1.5.6. Molar Fraction and Concentration calculation

The density of the mixture including water was assumed to be the same as the binary mixture because the volume of water solubilised into the CO_2-rich fluid was negligible. This number of moles of water at saturation, mol_{H2O}^{sat}, in the 0.877 cm^3 FTIR cell was used for the calculation of the concentration of water at saturation, $Conc_{H2O}^{sat}$, as shown in Equation 1.

$$Conc_{H2O}^{sat} = \frac{mol_{H2O}^{sat}}{0.000877} \quad (1)$$

The mole fraction of water at saturation, x_{H2O}^{sat}, was calculated using the molar density of the binary mixture, ρ_{mol}, at the recorded conditions, as shown in Equation 2.

$$x_{H2O}^{sat} = \frac{mol_{H2O}^{sat}}{0.000877 \times \rho_{mol}} \quad (2)$$

The mole fraction and concentration of water was calculated for each saturation point and plotted at the average pressure. The calculated values for each step in the water solubility calculation are shown in Table 4 for 10 % H_2 + CO_2 mixture at 9.72 MPa.

Table 4 - A table of the values used in the calculation of the molar fraction and concentration of H2O at the saturation limit at 9.72 MPa and 40 °C for 10% H_2 + CO_2.

Vol. of water injected (µL)	Temp (°C)	Pressure (MPa)	Density of mixture (mol·dm^{-3})	Amount of CO_2 + H_2 (x10^{-3} mol)	Vol. of H_2O sat.(µl)	Mol. of H_2O in sat. (x10^{-5} mol)	Mol. Fraction H_2O x10^{-3}	Conc H_2O (mol·dm^{-3})
1	40.44	9.708	6.622	5.807	0.364	2.01	3.445	0.0229
1.1	40.44	9.700	6.611	5.798	0.366	2.02	3.468	0.0230
1.2	40.54	9.756	6.689	5.866	0.381	2.10	3.569	0.0240

Remaining conditions for 10% H_2 + CO_2

The experimental values for the calibration and saturation are shown in Figure 11; the average value for saturation is shown to simplify the figure. The conditions recorded at the time of measurement were used in the calculations, as outlined above.

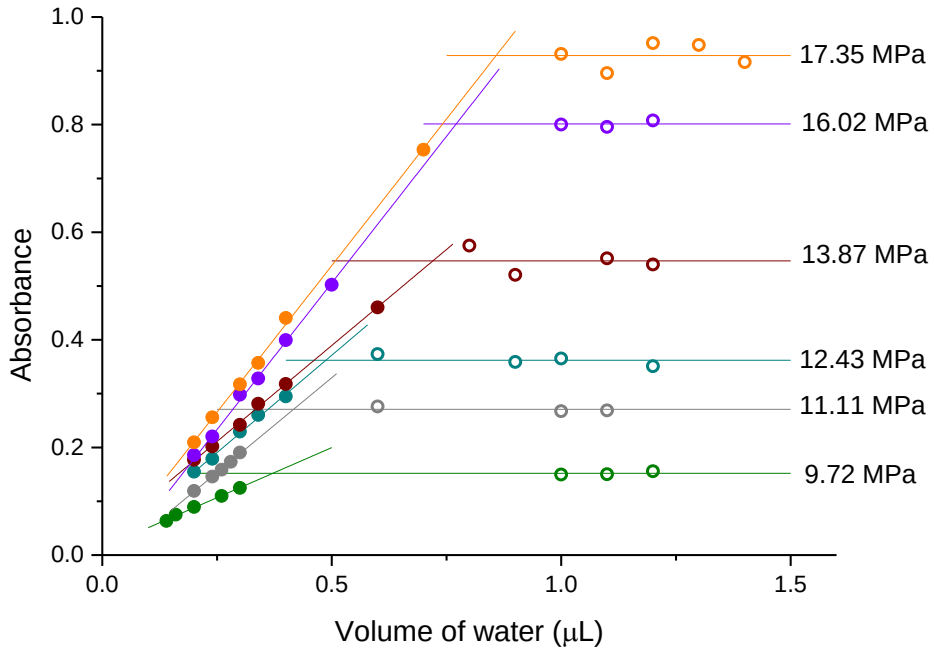


Figure 11 - The calibration (●) and saturation (○) absorbance values plotted against volume of water injected into the FTIR cell at different pressures, indicated by different colours and shown on the right of the figure.

The values in Table 5 for the molar fraction and the concentration were then plotted against the pressure and are shown in Figure 12 (a) and (b), respectively, where the error bars are a standard deviation each way.

Table 5 - The calculated molar fraction (xH_2O) and concentration of H_2O at the saturation point, with the standard deviation shown in brackets.

Average pressure (MPa)	Average density ($mol \cdot dm^{-3}$)	Average xH_2O (±SD, $x10^{-3}$)	Average conc. H_2O (±SD, $mol \cdot dm^{-3}$)
9.72	6.47	3.494 (0.067)	0.0232 (0.0006)
11.11	8.29	3.144 (0.052)	0.0261 (0.0004)
12.43	10.01	3.072 (0.103)	0.0307 (0.0008)
13.87	11.57	3.780 (0.152)	0.0438 (0.0015)
16.02	13.40	3.511 (0.039)	0.0502 (0.0004)
17.35	14.29	3.724 (0.033)	0.0534 (0.0011)

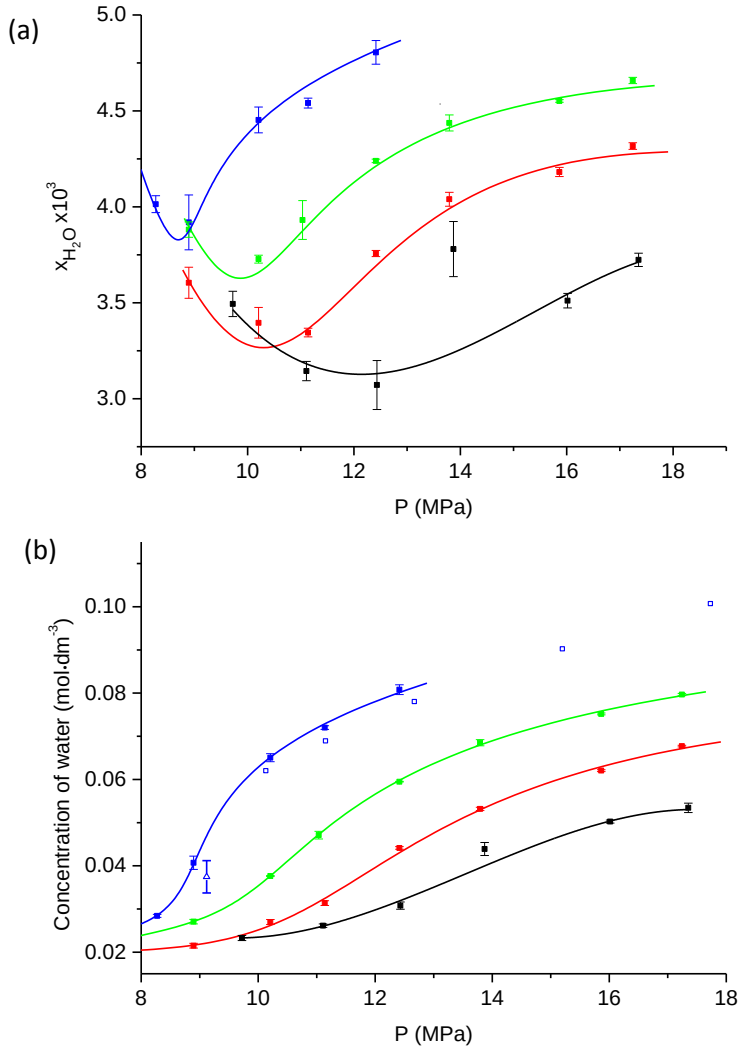


Figure 12 - Evolution of (a) molar fraction and (b) concentration of H_2O in Pure CO_2 (■) from Foltran et al. (2015), Pure CO_2 from King et al. (1992) (□), Pure CO_2 from Wang et al. (2013) (△), 5 % N_2 + CO_2 from Foltran et al. (2015) (■), 10 % N_2 + CO_2 from Foltran et al. (2015) (■) and 10 % H_2 + CO_2 from this work (■) at 40 °C; lines are drawn to guide the eye.[5,60,64]

The water saturation values for 10 % H_2 + CO_2 was below that of both N_2 + CO_2 binary mixtures. The values continued the trend of reducing water solubility with decreasing density, which was expected. The value for the molar fraction of water in 10 % H_2 + CO_2 at 13.87 MPa was greater than the expected values as shown by the black line in Figure 12. The experiments for this pressure were repeated and showed no change, which suggested either this was an accurate value or a possible secondary effect that was not considered. When the concentration of water was calculated and plotted where the difference between the indicative line and experimental value did not appear as obvious.

The concentration of the water was then plotted against the density, shown in Figure 13, where the values for 10 % H_2 + CO_2 match previous experiments depending on density. The continuation of the trend showed that the water solubility was likely to be largely reliant on the density of the mixture, rather than the components of the mixture. This relationship with density is expected to make the prediction and control of water solubility easier for future CCS pipelines, as the components of the fluid does not appear to be influential.

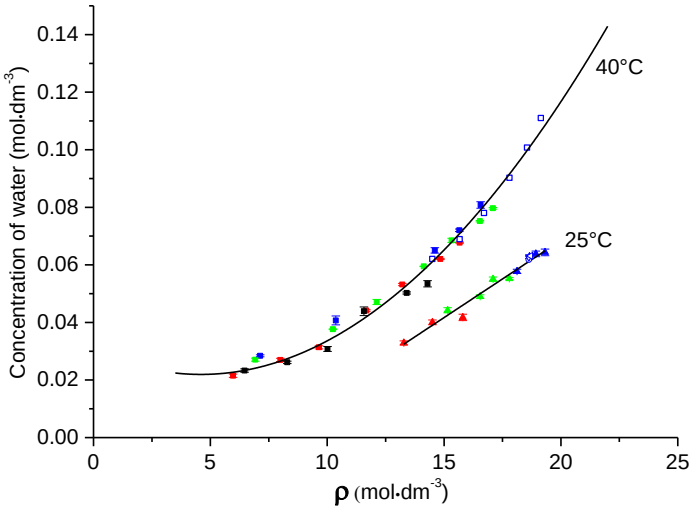


Figure 13 - Evolution of the molar concentration of water as a function of density for H_2O in Pure CO_2 at 40°C (■), Pure CO_2 at 40°C King et al. (□), 5 % N_2 + CO_2 at 40 °C from Foltran et al. (2015) (■), 10 % N_2 + CO_2 at 40 °C from Foltran et al. (2015) (■), 10 % H_2 + CO_2 at 40 °C from this work(■), (▲) pure CO_2 at 25 °C from Foltran et al. (2015); (△) pure CO_2 at 25 °C King et al. (1992); (▽) pure CO_2 at pure CO_2 at 25 °C from Wiebe (1941); (○) pure CO_2 at pure CO_2 at 25 °C Gillespie and Wilson (1982); (◁) pure CO_2 at 25 °C Song and Kobayashi (1986); (▲) CO_2 + 5 % N_2 at 25 °C from Foltran et al. (2015); (▲) CO_2 + 10 % N_2 at 25 °C from Foltran et al. (2015); lines are drawn to guide the eye.[5,50,64–66]

1.5.7. Water solubility comparison with Equations of State (EoS)

For the large-scale deployment of a CCS network, the water solubility needs to be predictable by EoSs as consistent online measurement of pipeline composition is not currently carried out.[71] The water solubility limits can be predicted using an Equation of State (EoS). In this Thesis, the Advanced Peng-Robinson (PR-A) and gSAFT-γ Mie EoS are used.[72–74]

Equations of state used in this work

The Advanced Peng-Robinson (PR-A) EoS is a cubic equation of state based on the original Peng-Robinson equation developed for the oil and gas industries. The 'advanced' version incorporates a predictive term within the parameter considering the attractive potential and has been shown to be more accurate for mixtures of fluids.

The SAFT-γ Mie EoS takes a bottom up approach to predicting macro fluid properties through estimating the interaction between molecules, namely the Helmholtz free energy. It allows for novel molecules to be defined and their properties to be predicted by understanding the additional effect to the Helmholtz free energy of different functional groups.

Further details on the development of both EoSs are provided in Chapter 3.

Method for EoS prediction of water solubility

A water content limit for CCS pipelines of 500 ppm has been proposed for CCS specific mixtures, with this figure based on previous work, without supporting measurements.[3,4,75] As mentioned previously, the limit for water is likely to have a safety factor to ensure water does not condense inside the pipelines; with 60 % of the experimental limits also previously suggested.[4]

There has been a literature precedent for measuring mutual solubility of water and CO_2, using custom alpha functions and custom binary interaction parameters, achieving an absolute average relative difference of 0.07 % for the CO_2 + H_2O binary mixture.[76] For these experiments, there was limited data available for ternary mixtures, especially for mixtures with CO_2 as the major component, hence why the standard EoS was used without customising the alpha function or BIPs was used.

The saturation point was predicted by incrementally increasing the mole fraction of water by 0.025×10^{-6} within the mixture, which was below the standard deviation of all experimental measurements. The software was then able to use the EoS to predict when two phases form, with this point recorded as the saturation limit. The molar fraction was then converted into a concentration

using the predicted density of the EoS. The EoS predicted molar fraction and concentrations are shown in Figure 14 and Figure 15, respectively. This method was then repeated at all conditions used in the experimental method. At 40 °C the binary mixtures of 10 % H_2 + CO_2 were predicted by all EoSs to be single phases at the beginning.

Comparison of EoS water solubility prediction

The results from the EoS prediction for both the molar fraction and concentration of water is shown in Figure 14 and Figure 15 respectively. Generally, there is a good agreement between the predicted and experimental values as discussed below.

The predicted water solubility limits for pure CO_2, 5 % and 10 % N_2 + CO_2 were lower than the experimental values for both gSAFT and PR-A EoSs. The difference between PR-A and gSAFT was that PR-A predicted a higher water solubility limit than gSAFT, apart from with pure CO_2 where PR-A was marginally higher. It should be noted that for all, but 10% H_2 + CO_2, both EoS were similar to each other. For 10% H_2 + CO_2 the PR-A overestimated the water solubility at higher pressures, whereas gSAFT underestimated the water solubility across all pressures. This general underestimation was considered safer than an overestimation as the EoSs would predict water condensation before the experimental results suggest water condensation. For 10 % H_2 + CO_2, the overestimation is at pressures above the standard operating pressures of pipelines.[23] The safety limits for pipelines are also likely to have a safety limit of 60% of the experimental limits.[3]

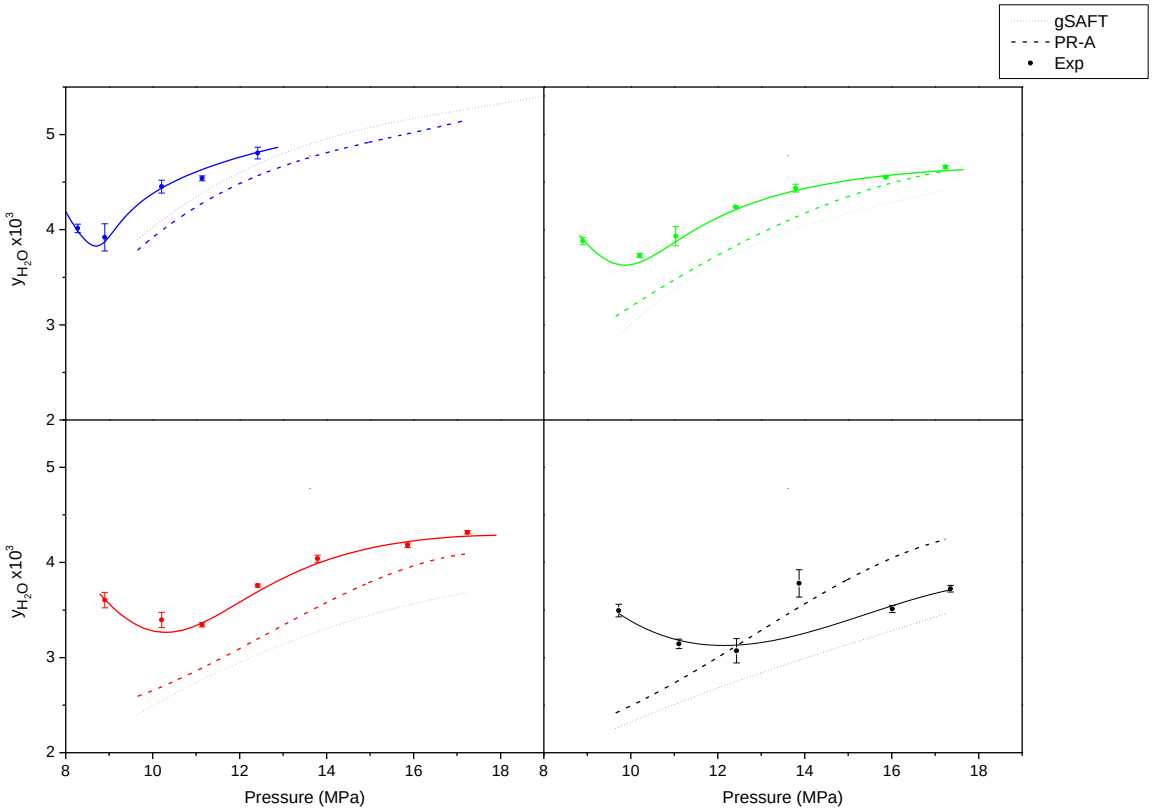


Figure 14 - A comparison of the experimental molar fraction of water at saturation with the predicted values using the PR-A (- - -) and gSAFT (···) EoSs; pure CO_2 is shown in blue, 5 % N_2 + CO_2 is shown in green, 10 % N_2 + CO_2 is shown in red and 10 % H_2 + CO_2 is shown in black.[5,72–74]

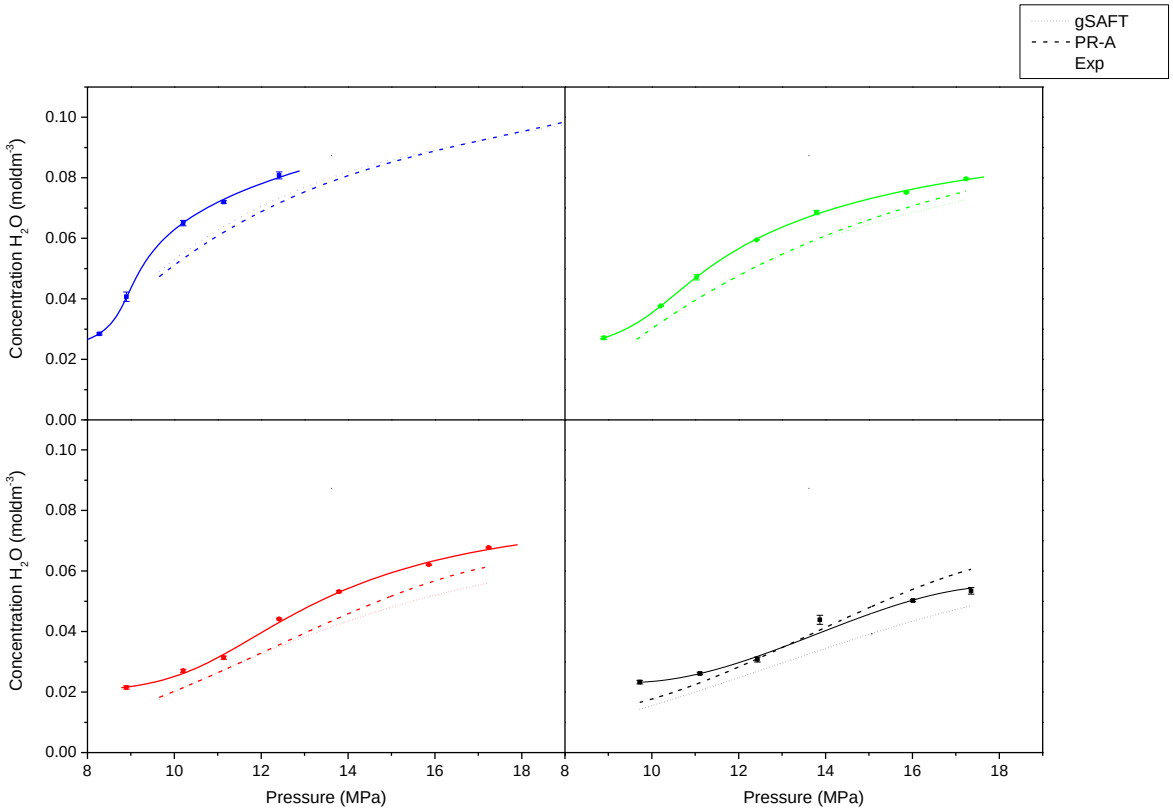


Figure 15 - A comparison of the experimental saturation concentration of water with the predicted values using the PR-A (- - -) and gSAFT (···) EoSs; pure CO_2 is shown in blue, 5 % N_2 + CO_2 is shown in green, 10 % N_2 + CO_2 is shown in red and 10 % H_2 + CO_2 is shown in black. [5,72–74]

1.5.8. Proposed safety limits

For the proposed safety limits the molar fractions previously shown will be discussed in terms of ppm as this is what is generally used for pipeline safety limits.[4] Table 6 shows the experimental values for the water saturation limit at 8.90 MPa (unless otherwise stated), along with the safety limits predicted by PR-A and gSAFT EoSs, at 40 °C and 25 °C. The EoS was also used to predict the water solubility limits at 8.90 MPa at 10 °C, where there was no experimental data, as this is a typical UK temperature. The pressure used was chosen because it would be a typical pressure found in CCS pipelines and was towards the lowest experimental values found for the water solubility.

Table 6 - A comparison of the experimental water saturation limits for CO_2-rich mixtures at 8.90 MPa (unless otherwise stated) 40 and 25 °C with predicted limits using the PR-A EoS and gSAFT, showing a general underestimation by the EoSs, with greater disparity compared to experimental values for 25 °C. For 10 °C, experimental values were unknown, so the predicted values are shown which are still above the previously suggested 500 ppm safety limit.[75] † - measured at 9.72 MPa and • - 10 % starting fluid predicted to be biphasic, so limit shown when 3 phases formed.

		H_2O saturation limit (ppm)		
Temperature	**Mixture**	**Experimental**	**PR-A**	**gSAFT-γ Mie**
40 °C	Pure CO_2	3920	3200	3350
	5% N_2 + CO_2	3880	2525	2550
	10% N_2 + CO_2	3600	2325	2250
	10% H_2 + CO_2	3490†	2425†	2150†
25 °C	Pure CO_2	3180	3025	3650
	5% N_2 + CO_2	2970	2425	2775
	10% N_2 + CO_2	3180	1625	1825
	10% H_2 + CO_2	-	1550•	1675•
10 °C	Pure CO_2	-	2175	3100
	5% N_2 + CO_2	-	1875	2500
	10% N_2 + CO_2	-	1550	1950
	10% H_2 + CO_2	-	1675•	2125•

As can be seen in Table 6, both EoSs underestimate the water solubility compared to experimental values for 40 and 25 °C. The predicted values for 10 °C mostly continue the trend of a reduction in water solubility with temperature for each mixture.

However, the 10 % H_2 + CO_2 at 10 °C results showed a change in trend with the predicted values above those for 10% N_2 + CO_2. As these values were for the transition from biphasic to triphasic, there was greater uncertainty as to assigning these points as the water saturation limits. This was thought to be due to the fact that the 10 % H_2 + CO_2 fluid at 10 °C and 8.90 MPa was predicted to be biphasic by both EoSs before water was introduced. For these, the water solubility limit was defined when the fluid became triphasic. For gSAFT, the 10 % H_2 + CO_2 mixture was also predicted to be biphasic at 25 °C and 8.90 MPa, so the point where it became triphasic was again assumed to be the water solubility limits. In future, a large volume view cell could be used to investigate the phase separation at these conditions to check the prediction of the EoSs.

All of the predicted values were above the previously suggested water solubility limits of 500 ppm. The suggestion of a safety limit of 60% of the water solubility limit would be *ca.* 1000 to 1370 ppm for 10 °C, depending on composition. This work suggests a limit of 1000 ppm would therefore be sensible

for any mixtures above 90 % CO_2, which could reduce costs in the purification and drying stage. To be sure of this recommendation, further experiments would need to be carried out at the reduced temperatures.

1.5.9. Summary of water solubility measurements and EoS comparisons

The water solubility experiments carried out in this work on the 10 % H_2 + CO_2 mixture showed a continuation of the trend of decreasing water solubility with decreasing density. This trend of decreasing water solubility was shown on the water concentration-density graph, where the results were on the same trend line observed for previously reported mixtures at 40 °C.

The water solubility limits were then estimated using the Advanced Peng-Robinson and gSAFT EoS, showing a slight underestimation by the EoS at 40 °C for all EoS apart from gSAFT with 10 % H_2 + CO_2. The experimental values and EoS predictions were then compared using ppm, to understand the currently proposed safety limits for CCS pipelines. The experimental and predicted values generally showed good agreement and were at least double the previously proposed water safety limit of 500 ppm for 25 °C and 40 °C. This suggested that the safety limits could perhaps be increased, although further tests would be needed at lower temperatures, such as 10 °C, as these conditions are much more likely to be found in the UK and Europe.

1.6. Pressure drop modelling of CCS pipelines

For future CCS pipeline networks, the wider effects of impurities on the pipeline and fluids needs to be understood, not just the effect on water saturation limits. For example, investment decisions will need to be made for the pipeline diameter, amount and location of recompression pumps, which will also be affected by fluid properties and expected flowrates. To understand the changes, a pipeline model was needed as large-scale pipeline networks are unsuitable for experiments.

The physical properties for the fluid were calculated using PR-A EoS with the superTRAPP algorithm to predict transport properties. The scales and flowrates of the pipeline used were of the scale expected with CCS pipeline networks, the details of which are discussed below.[23]

Before the pipeline model and predictions are discussed, a comparison of predicted and experimental values of density and viscosity are discussed, as these are the major physical properties affecting pressure drop.[77]

There are a number of equations that have been proposed to calculate pressure drop in literature, with a variety of assumptions. Often these calculations ignored the viscosity of the fluid, whereas in this Thesis, the viscosity of the fluid was used within the pipeline model.[2,78,79]

1.6.1. Literature comparison of equations of states for CCS relevant mixtures

An evaluation of the accuracy of the vapour-liquid equilibria for different EoS, on CCS relevant mixtures, has been performed by Diamantonis *et al*.[80] They found that Perturbed Chain – SAFT EoS was, on average, the most accurate EoS studied when compared to the limited experimental data available. When a single temperature-independent binary interaction parameter was used with Cubic EoSs, that had been correlated to experimental data, the SRK, PR, SAFT and PC-SAFT EoS were all comparable with errors in the range 3-6 %. The method also produced accurate results for a tertiary mixture by using binary interaction parameters for the corresponding binary mixtures. Another study,

by Mazzoccolia et al. found the PR EoS to be the most accurate among the cubic EoS for predicting the density of binary CO_2 mixtures.[81]

1.6.2. Density comparisons

Although Diamantonis et al. showed that a number of EoS were within 3-6 % accuracy for predicting vapour-liquid equilibria, similar comparisons were needed for the density and viscosity.[80] Colleagues at Nottingham have previously measured the density of CCS relevant mixtures, as presented below.

Density experiments

The density of 5 % and 10 % H_2 + CO_2, at relevant pressures, has previously been reported and published within the group at Nottingham.[35] The method measured the density of the mixtures using an Anton-Paar Densitometer which observes the vibrational resonance frequency of a small tube, which is affected by the density. The method allowed the change in density to be measured over time, with a small volume of fluid vented through a computationally controlled vent after equilibrium was reached. This method of releasing small amounts of the mixture allowed the density to be measured at decreasing pressures; it was initially validated using pure CO_2, before mixtures were measured.[82]

Density prediction

The density of mixtures can be predicted using EoSs, with the values predicted by the PR-A and gSAFT-γ Mie EoS compared to experimental values.[72–74] A comparison of the experimental results and predicted values for pure CO_2, 5 % H_2 + CO_2 and 10 % H_2 + CO_2 for each EoS is shown in Figure 16, Figure 17 and Figure 18, respectively.

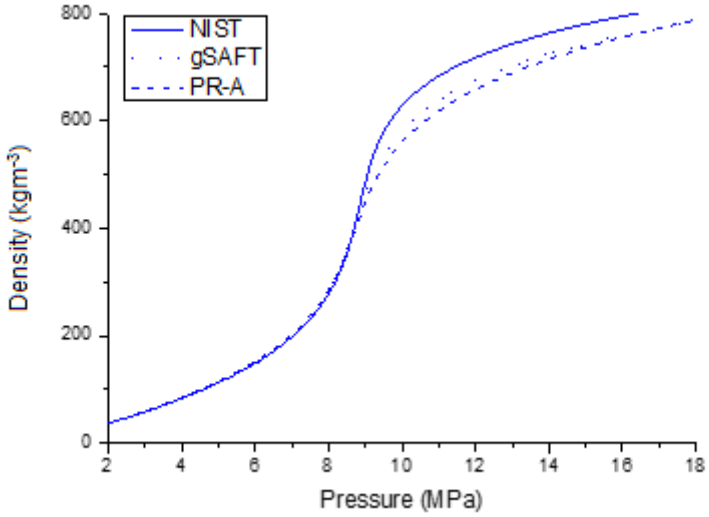


Figure 16 - A comparison of the density of pure CO_2 at 40 °C from the NIST chemistry webbook (—) with the predicted density from PR-A (- - -) and gSAFT (⋯) EoS. [70,72–74]

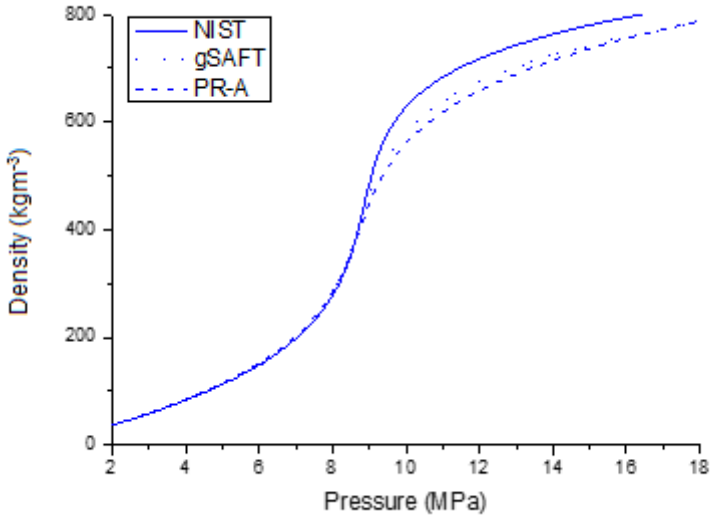


Figure 17 - A comparison of experimental density of 5 % H_2 + CO_2 at 40 °C (●) with the predicted density from PR-A (- - -) and gSAFT (⋯) EoS. [35,72–74]

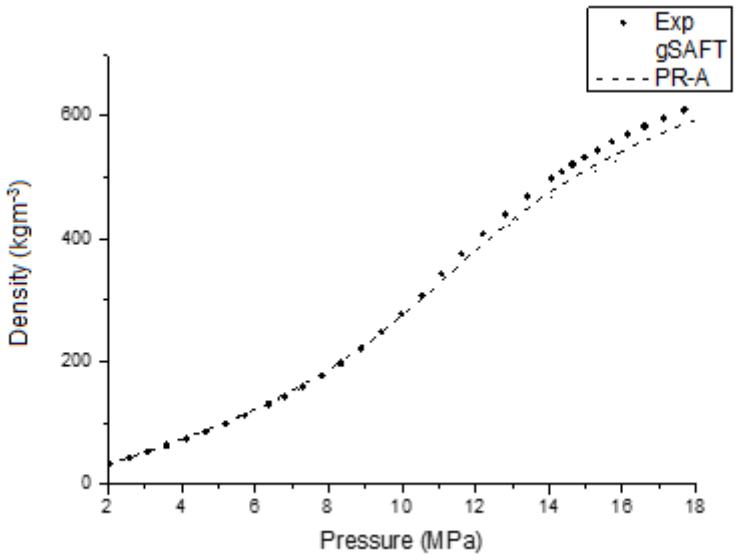


Figure 18 - A comparison of experimental density of 10 % H_2 + CO_2 at 40 °C (●) with the predicted density from PR-A (- - -) and gSAFT (⋯) EoS. [35,72–74]

Comparison of predicted values

For the mixtures shown in Figure 16 to Figure 18, the percentage difference from the experimental results, ρ_{exp}, compared to the reference results, ρ_{ref}, predicted using PR-A and gSAFT, are shown in Figure 19 (a) and (b), respectively. For both of the EoS above the critical point, the predicted values for the mixtures is *ca.* 5 % above the experimental value, which was considered reasonably accurate for the subsequent calculations.

With PR-A, the greatest difference between experimental and predicted values was for the pure CO_2, especially around the critical point, with 10 % H_2 + CO_2 being the most similar across all the pressures. For gSAFT, the greatest difference between experimental and predicted values was also for pure CO_2, especially around the critical point, with 10 % H_2 + CO_2 the most accurately predicted across all experiments.

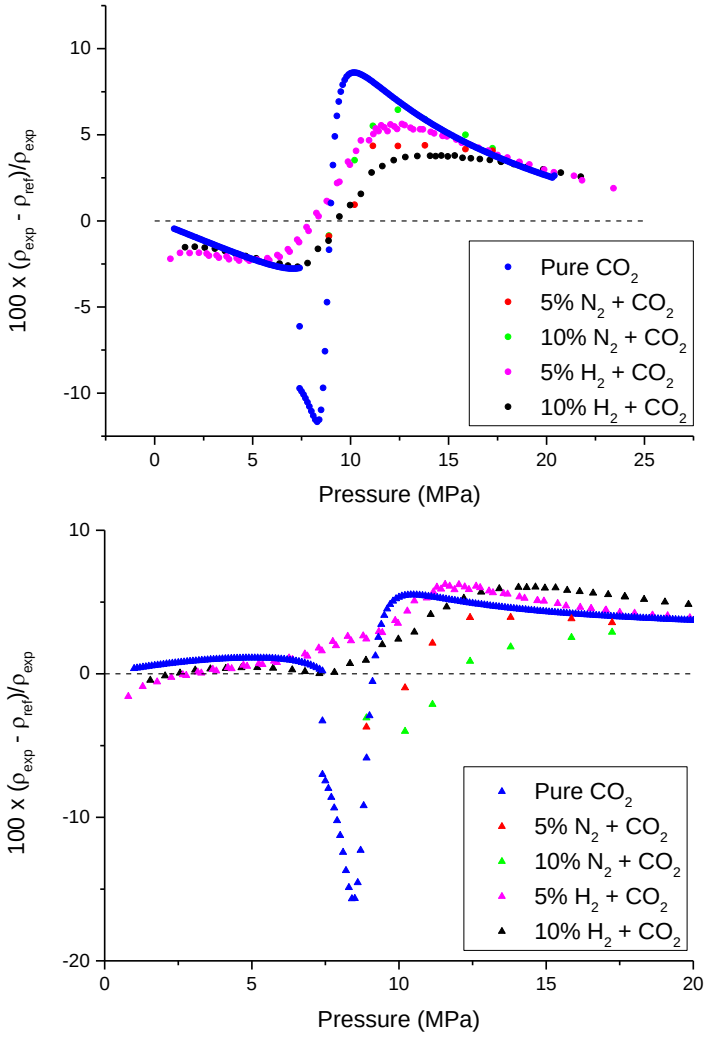


Figure 19 – The percentage difference experimental density (ρ_{exp}) from the reference density (ρ_{ref}). The reference density was calculated using PR-A (●) EoS in (a) and using the gSAFT (▲) EoS in (b), with pure CO2 shown in blue, 5 % N_2 + CO_2 in red, 10% N_2 + CO_2 in green, 5 % H_2 + CO_2 in pink and 10 % H_2 + CO_2 in black. The biggest difference for both EoSs is with pure CO_2, with a general overestimation of density of *ca.* 5 % above CO2's critical point pressure (7.39 MPa).[5,35,72–74]

1.6.3. Viscosity comparisons

In addition to density, the viscosity is a contributing factor to the pressure drop along pipelines. For the initial comparisons, the viscosity predicted by the PR-A EoS was compared to literature values.[72] The superTRAPP algorithm was used to calculate viscosity, which is a function of density.[83] Unfortunately, gSAFT was unable to predict viscosity within gPROMS ProcessBuilder due to current incompatibility with external algorithms such as superTRAPP.[84]

No literature data was discovered for the viscosity of binary mixtures of 5 % and 10 % N_2 or H_2 + CO_2. However, viscosity data has been measured at relevant conditions for mixtures of 94.9 % and 89.8 % CO_2 + *impurities* (Mixture 1 and 2 respectively), where the impurities were a mixture of non-condensable gases (CH_4, N_2, H_2, O_2, Ar and CO) expected to be found in CCS-related mixtures. The components of the Mixtures 1 and 2 are shown in Table 7.

Table 7 - The composition of Mixtures 1 and 2 used in the literature for viscosity measurements.[85]

Components	Mixture 1 (mol%)	Mixture 2 (mol%)
CO_2	94.9	89.8
CH_4	0.626	5.05
N_2	1.41	0
H_2	0.818	3.07
O_2	0.801	2.05
Ar	1.21	0
CO	0.213	0

The predicted viscosities of Mixtures 1 and 2 were compared with the experimental values for 5 and 10 % N_2 or H_2 + CO_2 mixtures. The different compounds were expected to have an effect on the viscosity compared to N_2 or H_2, however were expected to lie within the error from the EoS predictions.

Viscosity prediction comparison of pure CO_2

The experimental values for the viscosity of pure CO_2, μ_{exp}, was compared with the predictions provided from PR-A with superTRAPP algorithm.[72,83,85–87] The percentage change between μ_{exp} and μ_{ref} presented in Figure 20 show the EoSs predictive capability within ±4 % for pure CO_2, which were comparable to the literature predictions discussed in Section 1.6.1.

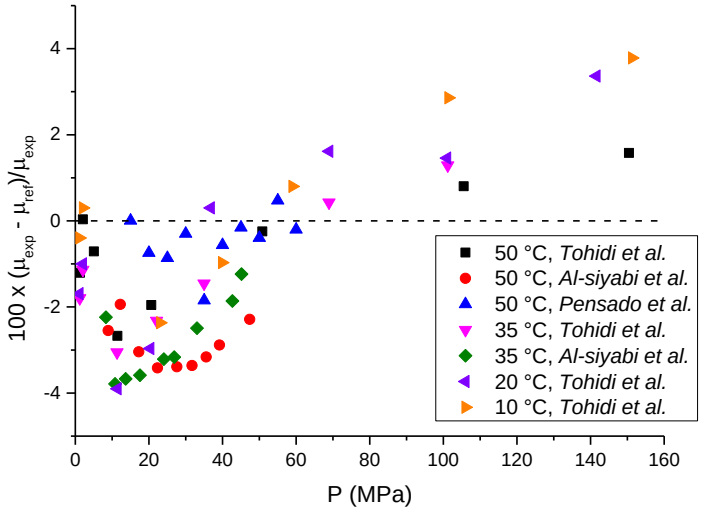


Figure 20 - The percentage difference experimental viscosity (μ_{exp}) from the reference viscosity (μ_{ref}) for pure CO_2. The reference density was calculated using PR-A with superTRAPP algorithm for transport properties. The experimental viscosities were collated from three literature sources at 4 different temperatures: 50, 35, 20 and 10 °C. The percentage difference had an absolute maximum difference of 4 %.[72,83,85–87]

Viscosity prediction of CO_2 with impurities

As mentioned above, the experimental data for CO_2-rich systems containing impurities was limited for the region of interest. The predicted viscosity of binary mixtures 5 % and 10 % N_2 and H_2 and Mixtures 1 and 2 was therefore compared to the experimental data of Mixtures 1 and 2, with the % difference between EoS and experimental values shown in Figure 21.

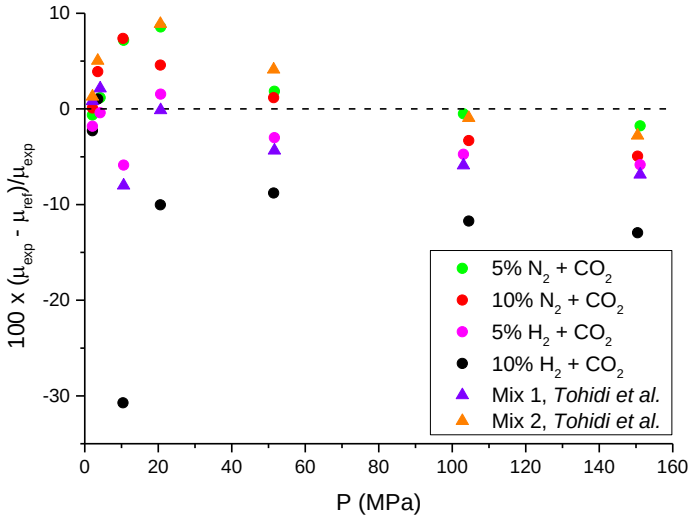


Figure 21 - The percentage difference experimental viscosity (μ_{exp}) from the reference viscosity (μ_{ref}) for 5 % N_2 + CO_2 (●), 10% N_2 + CO_2 (●), 5 % H_2 + CO_2 (●), 10% H_2 + CO_2 (●), Mixture 1 (▲) and Mixture 2 (▲) at 25 °C using PR-A with superTRAPP algorithm for the reference viscosity. The experimental viscosities used for the comparison was the measured values for Mixtures 1 and 2 for the 5 % and 10 % impurity mixtures.[72,83,85]

The points plotted in Figure 21 are also summarised in Table 8 and Table 9, where the absolute average deviation (AAD, %) differences are also shown. The % difference for both N_2 + CO_2 mixtures as well as the 5 % H_2 + CO_2 mixtures are similar to the predicted value for the composition of Mixtures 1 and 2, respectively. This data supports the previous assumption that the error in the EoSs outweighs the error caused by the difference in compositions.

For 10 % H_2 + CO_2 the increased error with an increased amount of H_2 was not unexpected. H_2 has a lower viscosity than N_2 and the other impurities in the mixtures, so the high H_2 concentration mixtures were disproportionately affected.

Table 8 – The experimental viscosities of Mixture 1 from literature with the % difference from the predicted values using PR-A with superTRAPP algorithm for Mixture 1, 5 % N_2 + CO_2 and 5 % H_2 + CO_2. [72,83,85]

		Predicted viscosity % difference		
Pressure (MPa)	**Experimental Viscosity (µPa·s)**	**Mixture 1**	**5 % N_2 + CO_2**	**5 % H_2 + CO_2**
2.08	15.3	+1%	-1%	-2%
4.18	15.9	+2%	+1%	0%
10.59	59.8	-8%	+7%	-6%
20.66	81	0%	+9%	+2%
51.60	124.2	-4%	+2%	-3%
103.07	173	-6%	-1%	-5%
151.12	213.2	-7%	-2%	-6%
	AAD:	**4.0%**	**3.1%**	**3.3%**

Table 9 - The experimental viscosities of Mixture 2 from literature with the % difference from the predicted values using PR-A with superTRAPP algorithm for Mixture 2, 10% N2 + CO2 and 10% H2 + CO2. [72,83,85]

		Predicted viscosity % difference		
Pressure (MPa)	**Experimental Viscosity (µPa·s)**	**Mixture 2**	**10 % N_2 + CO_2**	**10 % H_2 + CO_2**
2.08	15.3	+1%	0%	-2%
3.53	15.2	+5%	+4%	+1%
10.42	43.1	+18%	+7%	-31%
20.57	73.8	+9%	+5%	-10%
51.42	114.8	+4%	+1%	-9%
104.49	167.4	-1%	-3%	-12%
150.46	206.4	-3%	-5%	-13%
	AAD:	**5.9%**	**3.63%**	**11.1%**

1.6.4. Pipeline model

Both the density and viscosity could be predicted to a reasonable degree of accuracy, therefore the effect of impurities and conditions on future CCS pipelines could be explored in more detail. The pipeline model used was a pre-defined model provided by gPROMS, which allowed the conditions, components and dimensions of the pipeline to be inputted. As the model was proprietary, alteration of the underlying equations and methods was forbidden.

Although the customisation of the pipeline model equations was forbidden, the basic equations for the pipeline were provided. The pipeline was a plug-flow model with the mass balance for the pipeline shown below, where $\tilde{m}$ is the mass hold up, M_F is the mass flux through the volume, t is time and z is the axial coordinate.

$$\frac{\partial \tilde{m}}{\partial t} + \frac{\partial M_F}{\partial z} = 0 \tag{3}$$

The momentum balance for the pipeline model is shown in Equation 4, where v is the linear velocity, P is the pressure and f_τ is the force balance.

$$\frac{\partial \tilde{m}}{\partial t} v + \frac{\partial \tilde{m}}{\partial z} v^2 + \frac{\partial P}{\partial z} = f_\tau \tag{4}$$

The pressure drop, $\frac{dP}{dz}$, along the length of the pipeline was calculated using the Darcy-Weisbach equation where f_D is the Darcy friction factor, ρ is the density, D_H is the hydrodynamic diameter and v is the fluid velocity.[88] Literature calculations had shown that the Darcy-Weisbach equation, shown in Equation 5, provided a simple method with which to predict pipeline pressure drop.[89]

$$\frac{dp}{dz} = f_D \frac{\rho}{2} \frac{\langle v \rangle^2}{D_H} \tag{5}$$

The Haaland equation, shown in Equation 6, was used to calculate the Darcy friction factor f_D.[90]

$$\frac{1}{\sqrt{f_D}} = -1.8 \, log \left[\left(\frac{1}{3.7} \frac{\epsilon}{D_H} \right)^{1.11} + \frac{6.9}{Re} \right] \tag{6}$$

The advanced Peng–Robinson (PR-A) equation of state was used with the superTRAPP algorithm for transport properties.[72,83] A surface roughness of 0.015 mm was assumed for stainless steel.[91] The pipeline was considered to be parallel to the ground and adiabatic across the whole length; both of these assumptions are highly idealised but gave insight for initial investigations.

For the pipeline model, an input pressure of 10 MPa was used as this was considered a reasonable expectation by and International Energy Agency Greenhouse Gases (IEAGHG) study on Greenhouse Gas (GHG) pipeline infrastructure.[23] To keep the CO_2-rich mixture in the dense phase a minimum pressure of 8 MPa would be expected, along with an industry standard for the pressure drop along a pipeline of 0.02 MPa·km^{-1}.[75]

1.6.5. Effect of impurities on pressure drop in pipeline

As experiments for multi-kilometre pipelines were unrealistic for this project, the calculations for the pressure drop would require accurate values for the parameters. As shown above, the density and viscosity of the mixtures can be predicted within *ca.* 5 % error of experimental values using the PR-A EoS with superTRAPP algorithm for transport properties.

This EoS was then used for initial calculations of the pressure drop of pipelines with 5 % and 10 % mol. impurities of either N_2 or H_2. Again, both of these were chosen as N_2 and H_2 have considerably different properties and is consistent with the work presented in this Thesis. The pipe dimensions were chosen as the mid-range of the large study undertaken by IEAGHG in 2014 with the 150 kg·s^{-1} flowrate being chosen as equivalent to *ca.* 5 million tonnes CO_2 per year, the equivalent of a 0.8 GW average power station.[23]

The pressure drops for both 5 % and 10 % impurities were not significantly different from that of pure CO_2, as shown in Figure 22 where the flowrate was 150 kg·s^{-1} at 20 °C. The predicted values were all above the industry standard of 0.02 MPa·km^{-1} and take *ca*. 200 km to reach the dense phase limit of 8 MPa. Figure 23 compares the effect of impurity concentration on the pressure drop, as well as the effect of reducing the internal diameter of the pipeline to 0.4 m with a fixed flowrate of 150 kgs^{-1} at

20 °C. The reduced pipeline diameter led to a much greater pressure drop, with the dense phase limit being reached at 60 km and 75 km for 10 % N_2 + CO_2 and 10 % H_2 + CO_2, respectively.

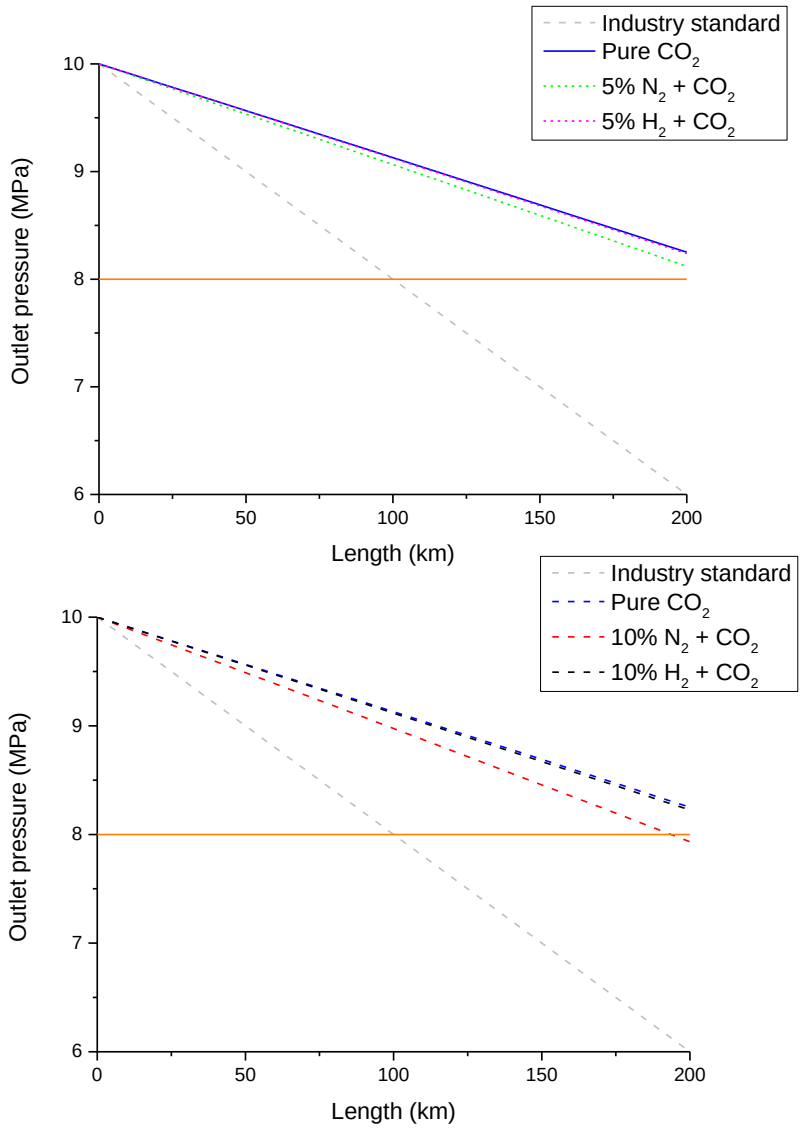


Figure 22 – The pressure drop along a pipeline with a flowrate of 150kg·s^{-1} with an internal diameter of 0.5 m and ambient temperature of 20 °C. (a) The pressure drop for pure CO_2 (—), 5 % N_2 + CO_2 (···) and 5 % H_2 + CO_2 (···); (b) The pressure drop for pure CO_2 (—), 10 % N_2 + CO_2 (- - -) and 10% H_2 + CO_2 (- - -). Both examples show the pressure drop to be well above the industry standard (- - -) of 0.02 MPa per km and above the dense phase limit (—) for *ca.* 200 km. [72,75,83,84]

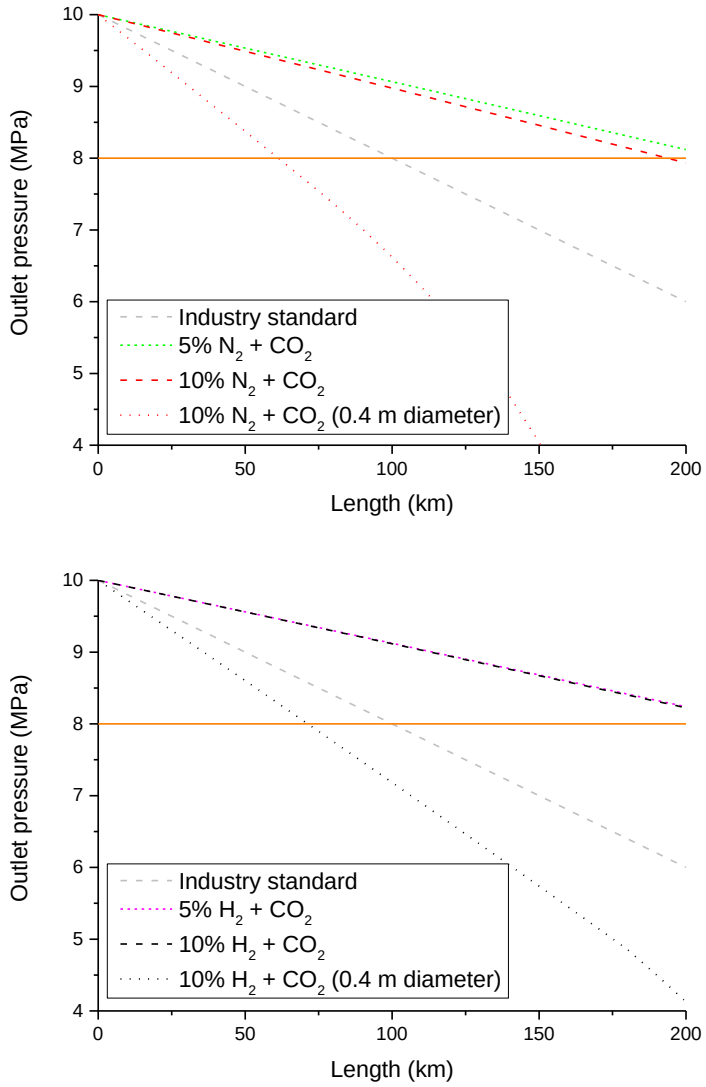


Figure 23 - The pressure drop along a pipeline with a flowrate of 150kgs^{-1} with an internal diameter of 0.5 m and ambient temperature of 20 °C. (a) The pressure drop for 5 % N_2 + CO_2 (···), 10 % N_2 + CO_2 (- - -) and 10% N_2 + CO_2 with a 0.4 m internal pipeline diameter (···); (b) The pressure drop for 5 % H_2 + CO_2 (···), 10 % H_2 + CO_2 (- - -) and 10 % H_2 + CO_2 with a 0.4 m internal pipeline diameter (···). For the 0.5 m internal diameter the pressure drop was well above the industry standard (- - -) of 0.02 MPa·km^{-1} and above the dense phase limit (—) for *ca.* 200 km. The 0.4 m internal diameter had a large effect on pressure drop and went below the industry standard. [72,75,83,84]

As can be seen in Figure 21, for 10 % H_2 + CO_2, the viscosity of the fluid is underestimated between 30 % and 10 % in the region of interest. The large underestimation in the viscosity, combined with the overestimation of the density of pure CO_2, was thought to be the reason for the negligble difference in pressure drop between pure CO_2 and 10 % H_2 + CO_2 fluids.

The pipeline model was then used to investigate the expected pressure drop for Mixtures 1 and 2, which are similar to those expected in CCS pipelines. As shown in Figure 24, the pressure drop is similar

to the binary mixtures presented above. This was expected as the viscosities and densities were shown to be similar. The pressure drop for both mixtures was well above the industry standard and shows that dense-phase CO_2-rich mixtures can be expected to transport over large distances without the need for repressurisation, with 0.5 m diameter pipelines.

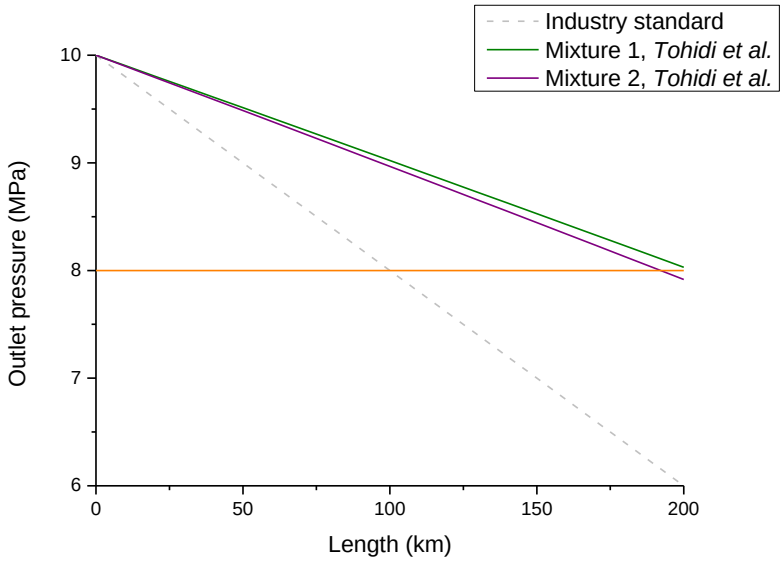


Figure 24 – The pressure drop of Mixture 1 (—) and 2 (—) at 150 kgs^{-1} and 20 °C with an internal diameter of 0.5 m. As expected, the pressure drop was similar to the values shown above for N_2 and H_2 + CO_2 and was well above the industry standard pressure drop (- - -) and dense phase limit (—). [72,75,83–85]

1.6.6. Effect of conditions on pressure drop in pipelines

For future CCS pipelines it is not just the composition of the mixture that is expected to change. Both the inlet pressure, temperature, size and flowrate of the pipeline would be variable, this is discussed below.

In Figure 25, the inlet pressure is changed along with the ambient temperature of a 200 km pipeline while fixing the inlet flowrate at 150 kg·s^{-1} and internal diameter of 0.5 m; which shows the large increase in pressure drop for higher temperatures. Although the ambient temperatures are rarely expected to exceed temperatures of 30 °C for prolonged periods of time, especially in the UK, understanding this effect will be crucial for operators as ambient temperatures are expected to change along the pipe route.

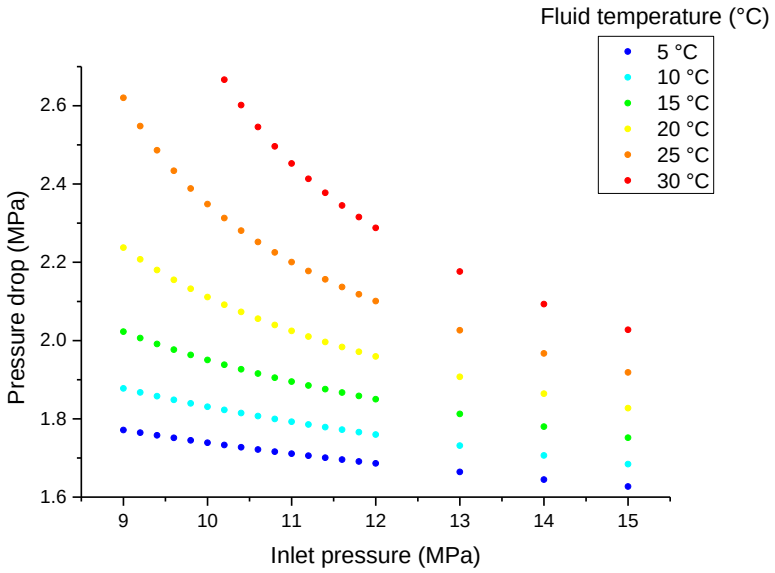


Figure 25 – The predicted pressure drop for 10 % N_2 + CO_2 at 150 kg·s^{-1} and 0.5 m internal diameter, 200 km pipeline at six different temperatures: 5 °C (●), 10 °C (●), 15 °C (●), 20 °C (●), 25 °C (●) and 30 °C (●) and increasing inlet pressure.[72,83,84]

As CCS is up scaled within the UK, through clustering of CO_2 sources, the pipelines used to transport the CO_2 will change in dimensions and flowrates depending on demand. The effect of mass flowrate and internal pipeline diameter, when the ambient temperature is fixed to 20 °C and inlet pressure of 10 MPa, is shown in Figure 26. This showed that a large range of flowrates can be kept below the dense-phase limit of 8 MPa by varying the pipe diameter. For example, a flowrate of 350 kg·s^{-1} is equivalent to 11 million tonnes per year which could be kept below the pressure drop by using a 0.75 m diameter pipeline.

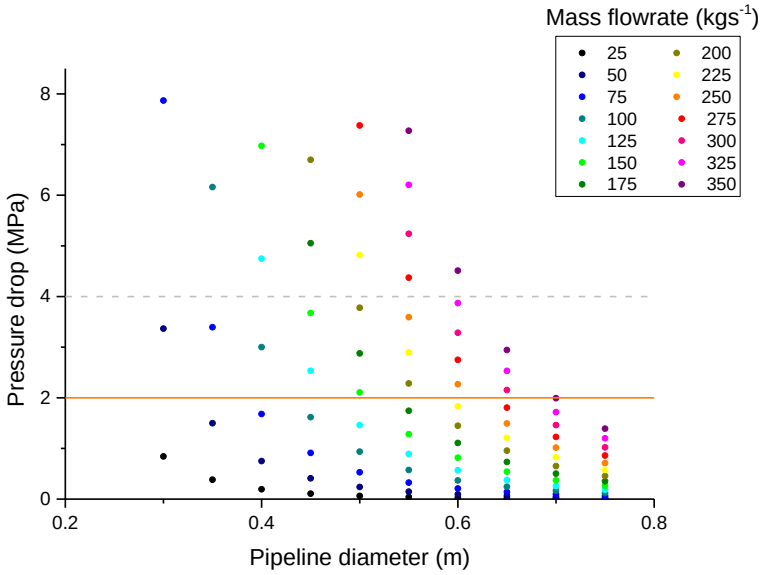


Figure 26 - The predicted pressure drop for 10 % N_2 + CO_2 at 150 kg·s^{-1} at 20 °C with an inlet pressure of 10 MPa at increasing mass flowrates from 25 to 350 kg·s^{-1} for different internal pipeline diameter. The dense phase limit (—) and industry standard pressure drop (- - -) is shown. [72,75,83,84]

1.6.7. Summary of pressure drop modelling

Understanding the pressure drop of a pipeline is crucial for the development of a pipeline network, as the need for distance between recompression points can affect both the capital and operating expenditure. A pipeline model was used to predict the pressure drop of CCS relevant mixtures.

However, before any pressure drop modelling took place, the density and viscosity of different relevant mixtures were compared to the predicted value using both the Advanced Peng-Robinson and gSAFT EoS. The predicted values for both density and viscosity were within *ca.* 5 % of the experimental values which, considering the compositional difference, was accurate for the modelling of the pressure drop of pipelines.

For the initial tests, a flowrate of 150 kg·s^{-1} and a pipeline diameter of 0.5 m was used as this was the equivalent of a 0.8 GW power station, with the pipeline diameter towards the middle of those studied in an IEAGHG report on CCS.[23] The pressure drop predicted under these conditions lay well above the industry standard pressure drop of 0.2 MPa·km^{-1}, with little difference shown between the different impurities and the pure CO_2. When the pipeline diameter was decreased to 0.4 m, a more significant pressure drop was observed, below the industry standard pressure drop.

Further investigations were carried out on the effect of temperature and inlet pressure, showing a greater increase in pressure drop for higher temperatures. The effect of pipeline diameter and flowrate was also investigated, showing that mass flowrates of 350 $kg \cdot s^{-1}$, equivalent of 12 million tonnes per year, could be kept in the dense phase using a pipe with a diameter of 0.75 m.

1.7. Pressure drop for predicting phase behaviour

The predictions of the density and viscosity shown in the previous section enabled the modelling of the pressure drop for mixtures in possible future CCS pipelines. This procedure led to the possibility of using the pressure drop in a tube to measure the properties, such as phase transitions, of other fluid mixtures.[92]

When a fluid changes from a liquid to a gas there is a rapid expansion such that inside a fixed volume tube there will be an acceleration of the fluid along the pipe. This increase in velocity would increase the pressure drop, as per the Darcy-Weisbach equation.[88] The experimental work had been previously carried out in Nottingham and a modified version of the pipeline model presented in the previous section was used to support the validity of the method. This need for computational validation was needed as there was limited literature data available for the conditions in question.

1.7.1. Experimental set-up

The measurement method was based on monitoring the pressure difference between the inlet and outlet pressure transducers, separated by a three metre stainless-steel tube. The stainless-steel tube was coiled around an aluminium heating block and surrounded by a heating jacket. Automated sampling, with a high-pressure sample loop, was used to analyse the composition of potentially reactive mixtures of CH_3CN + H_2O at high temperatures and pressures. A high-pressure liquid chromatography (HPLC) pump (Jasco PU-980) and a back-pressure regulator (BPR, Jasco BP-1580-81) were used to deliver fluid samples at a controlled flow rate and pressure. A schematic of the experimental setup is shown in Figure 27.

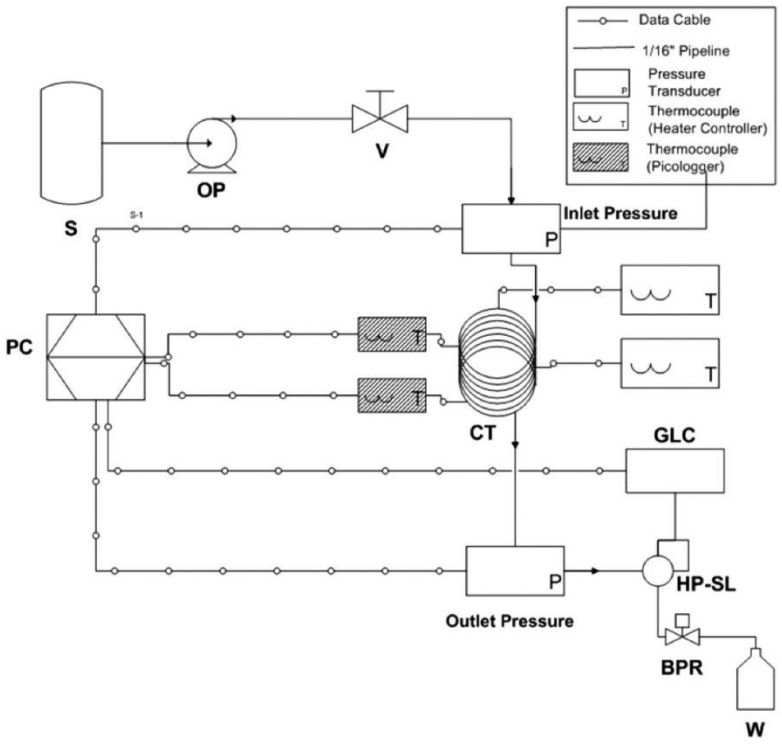


Figure 27 - Schematic of the automated high-pressure fluid continuous flow apparatus. The components are labeled as follows: BPR, back pressure regulator; CT, capillary tube; GLC, gas–liquid chromatography; HP-SL, high-pressure sample loop; OP, organic pump; P, pressure transducer; PC, computer; S, sample reservoir; T, thermocouple (shaded for logging temperature); V, check valve; and W, waste container. Dotted lines indicate data flow.[92]

The key component was the coil of stainless-steel capillary tubing across which the pressure drop occurs. The specifications of the tube are 1.59 mm outer diameter, 0.10 mm inner diameter, and 3 m length.

The general procedure used to record pressure-drop values was as follows. A sample of known composition was pumped through the rig, as shown in Figure 27. The pump and BPR were set to the elevated flow rate and pressures. The temperature controller was set to a temperature lower than the expected transition temperature. The rig was allowed to equilibrate, and a temperature ramp of 0.5 or 1 °C·min^{-1} was applied for the collection of transition points. The pressure readings between the inlet and outlet of the stainless-steel tube were recorded and plotted as a function of temperature. The pressure drop depends, to a great extent, on the velocity of the fluid, therefore, several flow rates in the range from 0.02 ml·min^{-1} to 1 ml·min^{-1} were tested to establish the effect of fluid flow rate on

the pressure-drop values. The flow rates were chosen to minimize fluctuations caused by the BPR. As explained below, transition points were identified by a distinct change in pressure-drop values.

1.7.2. Modelling set-up

The model used for the estimation of the pressure drop in CCS pipelines was adapted to mirror the experimental dimensions used with these experiments. The advanced Peng–Robinson (PR-A) equation of state was used with the superTRAPP algorithm for transport properties.[72,83] The computational model was based on an empty tube using the Haaland equation to calculate the Fanning friction factor.[90] A surface roughness of 0.015 mm was assumed for stainless steel.[91] The pressure-drop model ignored the heat-up stage of the process and assumed that the tube was adiabatic, with the fluid pumped at the experimental pressure and temperature. The adiabatic assumption was made to simplify the model because initial tests where the fluid was heated from ambient led to an unstable model. This unstable model often led to computational failures, which were thought to be due to the large gradient of heating as the fluid entered the reactor.

For the initial validation of the method and model, the phase behaviour of IPA was measured. The maximum pressure drop calculated was matched to the pressure drop observed for the pure IPA system using an adjustment factor of 0.2. The adjustment factor was a linear multiplier of the friction factor and was needed as the initial predictions overestimated the pressure drop. This model, defined by the IPA pressure drop, was then used for all subsequent calculations. The adjustment factor could have been due to a number of reasons such as; higher surface roughness or the pressure transducer being set further along from the pipe outlet, in an expanded Swagelok T-piece.

Heated pipe model

The model of the heated pipe used was similar to the pipeline model described above. However, due to the heating of the pipe an energy balance equation was used as described below.

The energy balance for the pipe is shown in Equation 7, where $\tilde{u}$ is the volumetric energy holdup in the pipe, q is the pipe energy flux, q_w is the heat flux from the wall, $A^w_{surface}$ the internal surface area of the pipe, A_{cross} is the cross-sectional area of the pipe and L is the length of the pipe.

$$\frac{\partial \tilde{u}}{\partial t} + \frac{\partial q}{\partial t} = \frac{q_w \, A^w_{surface}}{L \, A_{cross}} \tag{7}$$

The volumetric energy holdup ($\tilde{u}$) and pipe energy flux (q) was calculated as shown In Equations 8 and 9 respectively, where $\tilde{m}$ is the volumetric mass holdup, H is the mass specific enthalpy and M_F is the mass flux.

$$\tilde{u} = \tilde{m}H - P \tag{8}$$

$$q = M_F H \tag{9}$$

The heat flux (q_w) from the wall of the pipe to the fluid was calculated as shown in Equation 10, where k_{HT} is the pipe fluid to wall heat transfer coefficient, T is the temperature of the fluid and T_w is the temperature of the wall.

$$q_w = k_{HT}(T - T_w) \tag{10}$$

1.7.3. Experimental results and model comparison

Both the experimental and computational prediction will be presented and compared throughout. The results used to define the model with pure IPA are shown in Figure 28, comparing the experimental values and previous literature values, both showing good agreement.

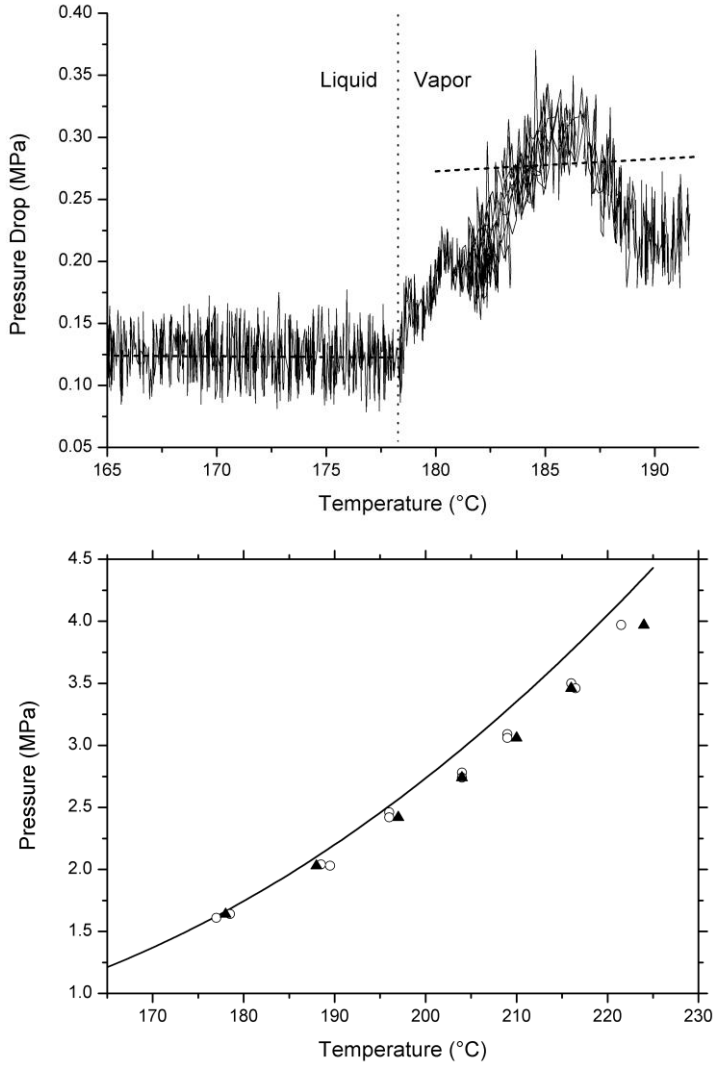


Figure 28 - (a) Pressure-drop measurements in pure IPA with a flow rate of 0.07 ml·min^{-1} at 1.64 MPa. The continuous black line shows the experimental recording, the black dashed line shows the computational prediction, and the black arrow indicates the transition point from the liquid to the vapour phase determined experimentally. (b) Measured P–T diagram of IPA from a range of isobars (○, experimental value; ▲, computer model) compared to the literature data (–). A ramp of temperature at a rate of 1 °C·min^{-1} was used for each isobaric measurement.[92]

The noise in the experimental data was largely thought to be due to the back-pressure regulator, however it could also have been due to thermal expansion or the enthalpy of vaporization. Considering this noise there is still an obvious increase in the pressure drop at the phase boundary, which was defined as the phase change location.

Acetonitrile and water mixture

Following on from the model defined with the pure IPA, the reactive mixture of acetonitrile and water was studied, with the results from both the experimental and computational pressure drop values shown in Figure 29. The experimental and model-predicted values show good agreement across all inlet pressure values.

As $CH_3CN + H_2O$ is a reactive mixture, there was concern that the two components would react and form a multi-component mixture. To check if the reaction occurred, a gas chromatogram of the mixture at the end of the experiments is shown in Figure 30, highlighting the lack of reaction between the two species.

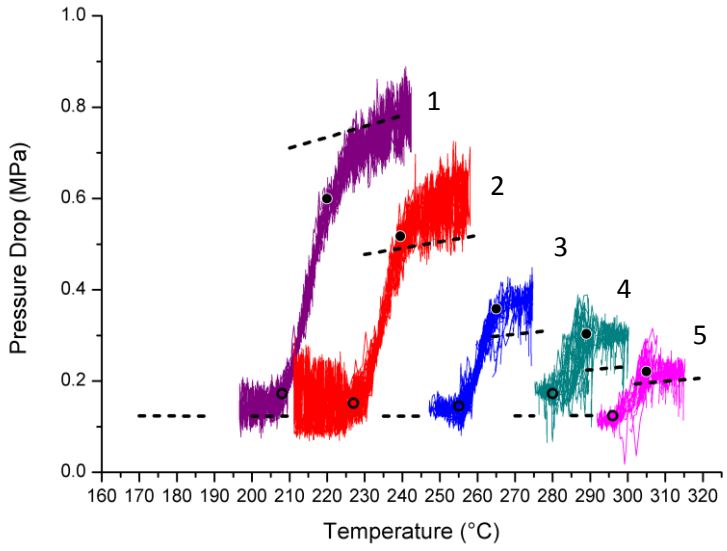


Figure 29 - Pressure-drop variation with temperature for $CH_3CN + H_2O$ with $xCH_3CN = 0.1$ at various pressures and a flow rate of 0.06 ml·min^{-1} for each isobar: (1) 2.12 MPa, (2) 3.14 MPa, (3) 5.61 MPa, (4) 8.35 MPa, (5) 10.29 MPa with ○ and ● representing the bubble and dew points, respectively. The temperature ramp rate is 1 °C·min^{-1}. The dashed lines represent the computational prediction for the pressure drop for each isobar.

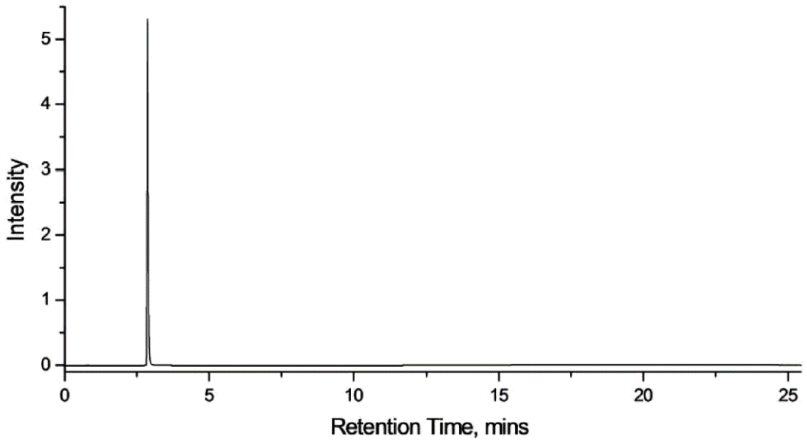


Figure 30 - GLC chromatogram of the outlet at 8.35 MPa. Two injections were made automatically for each pressure, in which the temperature for a specific injection was between the initial and end point of the ramp temperature.

The values found from the experimental and computational methods for the $CH_3CN + H_2O$ mixture are summarised and compared to literature values in Figure 31.[42] The combination of the experimental results and the computational model show that the method developed was valid for measuring the phase behaviour of fluids. The advantages of this method, with its short residence time, allowed the phase behaviour of reactive mixtures to be measured.

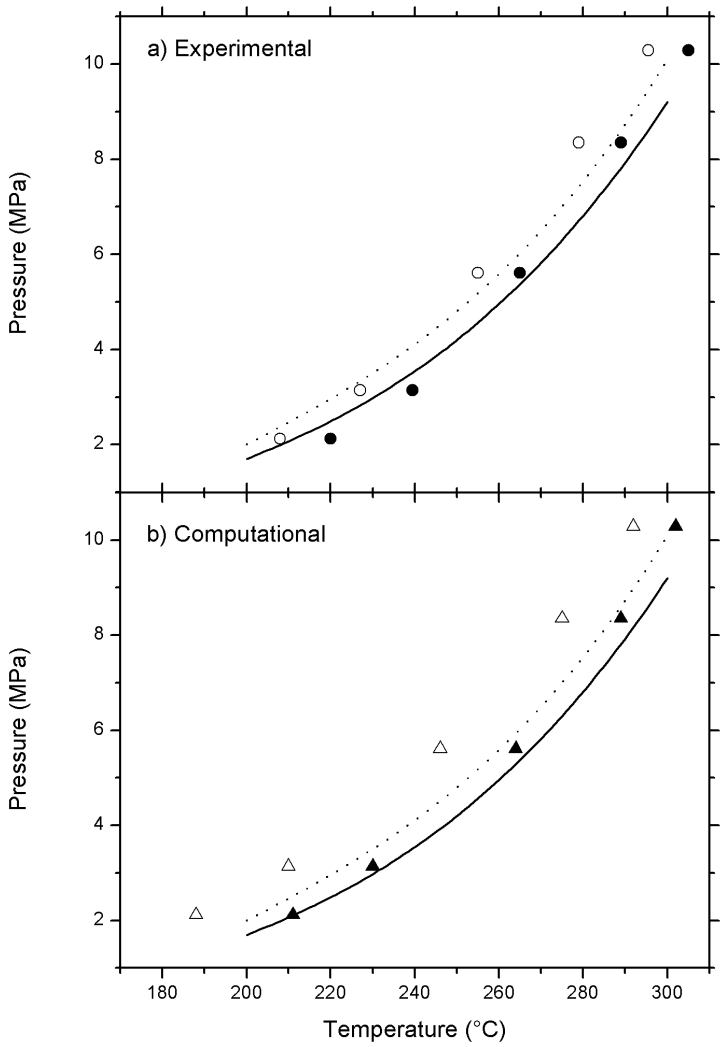


Figure 31 - (a) Plot of the bubble (○) and dew points (●) obtained for CH_3CN + H_2O with xCH_3CN = 0.10 using the experimental pressure-drop method. (b) Plot of the bubble (△) and dew points (▲) with xCH_3CN = 0.10 obtained using the computational pressure-drop method. The dashed and solid black lines represent smoothed curves which join the four reported data points for either bubble or dew points.[42]

1.8. Chapter summary

The solubility of water in supercritical 10 % H_2 + CO_2 was successfully measured, which continued the trend of reducing water solubility with density. The experimental water solubility limit was found to be *ca.* 1000 ppm across all of the different mixtures; with the PR-A EoS able to estimate the limit within an accuracy of *ca.* 5 %. The experimental values suggested that a safety limit greater than the previously proposed water concentration limit of 500 ppm could be used, which would be beneficial for the pre-transmission processing. However, further experiments would need to be carried out at lower temperatures because the pipeline conditions are unlikely to be >25 °C, especially in the UK.

The effect of impurities was shown to have little effect on the pressure drop of CCS pipelines of 0.5 m internal diameter for CO_2 mol% >90 %, with all calculations above the industry standard pressure drop. The conditions expected for pipelines in the UK (<30 °C) showed that the pressure drop was expected to be below 2.5 MPa, which would keep the CO_2-rich fluid in the dense phase. The flowrate and internal diameter of the pipeline were shown to have a large effect on pressure drop, which was expected. As the design of the pipeline would be expected to change along the route from source to sink, especially with the clustering of CO_2 sources in the UK, more detailed modelling would be required with expected impurities to have an optimally designed system.

Finally, a novel method for predicting the phase behaviour of reactive mixtures was presented. The model developed in this Thesis helped to validate the method as there was a lack of literature data available. The pressure-drop method was shown to be able to measure the phase behaviour of reactive mixtures, which other previous methods were unable to.[92]

1.9. Future work

The measurement of fluid composition, especially the presence of water, would be useful for pipeline monitoring. The phase behaviour of fluids has previously been measured within the group using ATR; the development of this into a miniaturised ATR monitor could be useful for pipeline monitoring,

especially if these could be connected to an Internet of Things (IoT) system to give real time updates of pipeline composition.

It would also be interesting to include possible economic impact of impurities for the CCS process. However, there is limited data available from current CCS projects along with a reluctance from companies to reveal economic data. Furthermore, even though the effect of impurities on pipeline behaviour for >90% CO2 mixtures only showed small differences with impurities, the effect on recompression processes would be more pronounced. For the accurate prediction of these processes, further experiments would be needed to improve EoSs relevant to CCS.

2. Introduction to relevant chemical reactions

2.1. Chapter Overview

This chapter acts as an introduction for the Chapters 3 and 4 which are related to modelling novel chemical reactions and reactors. The concept of green and sustainable chemistry is introduced including a number of metrics that allow the green 'credentials' and sustainability of a process to be measured. The idea of flow chemistry is also discussed, with a brief explanation as to how continuous flow processes can address some of the challenges of green and sustainable chemistry. This chapter then introduces concepts that are crucial for understanding the research areas of the remaining work, which are; (i) photochemistry, (ii) high-temperature water chemistry and (iii) multi-step reaction processes.

With photochemistry, a brief explanation is given as to its development as a synthetic technique along with an understanding of the underlying physical processes which occur on the absorption of a photon. This is followed by explaining the way photochemical transformations are carried out in the laboratory along with a brief introduction to the concepts required for the modelling of photochemical reactions.

A similar approach is taken for high-temperature water (HTW), where an initial introduction is given explaining what HTW is and the origin of its use in chemical processes. The effects of HTW with chemical reactions are discussed, before the equipment used within the laboratories are introduced.

Finally, multi-step chemical processes are introduced, including the benefits that the combination of multiple steps can bring. Following this, the modelling of both these processes is introduced, with possible benefits and potential issues discussed.

2.2. Introduction to green and sustainable chemistry

The chemical industry plays a large part in the global economy and will be key for future developments and innovations across a wide range of sectors, from healthcare to climate change.[93,94] Within the UK, the chemicals sector accounted for £12.1 billion of the UK economy's Gross Value Added and directly

supported 99,000 jobs in 2017.[95,96] Despite this success, there are a number of pressures on the global chemical sector to improve, especially regarding the sustainability and toxicity of its processes.[97] The concept of 'sustainable chemistry' and 'green chemistry' have been growing concepts in recent decades and they are now becoming more commonplace.[98]

The terms 'green chemistry' and 'sustainable chemistry' are often used interchangeably. Both terms are responses to the need to produce chemicals in a more efficient and environmentally-friendly way. Green Chemistry, as defined by Sheldon, is shown below:

> ***"Green chemistry efficiently utilises (preferably renewable) raw materials, eliminates waste and avoids the use of toxic and/or hazardous reagents and solvents in the application of chemical products." – Sheldon*** [99]

Sustainable chemistry is defined by Scheringer et al. below:

> ***"Sustainable chemistry is … chemical research aiming at the optimization of chemical processes and products with respect to energy and material consumption, inherent safety, toxicity, environmental degradability" – Scheringer et al.***[100]

2.2.1. The 12 Principles of Green chemistry

The '12 Principles of Green Chemistry' are another way of understanding the green credentials of a process. They are often thought of as ideals to be aimed for, and were proposed by Warner and Anastas, shown in Table 10.[101]

Table 10 – The 12 Principles of Green Chemistry as developed by Anastas and Warner.[102,103]

1. Prevention	Preventing waste is better than treating or cleaning up waste after it is created.
2. Atom economy	Synthetic methods should try to maximize the incorporation of all materials used in the process into the final product.
3. Less hazardous chemical syntheses	Synthetic methods should avoid using or generating substances toxic to humans and/or the environment.
4. Designing safer chemicals	Chemical products should be designed to preserve efficacy of function while reducing toxicity.
5. Safer solvents and auxiliaries	Auxiliary substances should be avoided wherever possible, and as non-hazardous as possible when they must be used.
6. Design for energy efficiency	Energy requirements should be minimized, and processes should be conducted at ambient temperature and pressure whenever possible.
7. Use of renewable feedstocks	Whenever it is practical to do so, renewable feedstocks or raw materials are preferable to non-renewable ones.
8. Reduce derivatives	Unnecessary generation of derivatives—such as the use of protecting groups—should be minimized or avoided if possible; such steps require additional reagents and may generate additional waste.
9. Catalysis	Catalytic reagents that can be used in small quantities to repeat a reaction are superior to stoichiometric reagents (ones that are consumed in a reaction).
10. Design for degradation	Chemical products should be designed so that they do not pollute the environment; when their function is complete, they should break down into non-harmful products.
11. Real-time analysis for pollution prevention	Analytical methodologies need to be further developed to permit real-time, in-process monitoring and control before hazardous substances form.
12. Inherently safer chemistry for accident prevention	Whenever possible, the substances in a process, and the forms of those substances, should be chosen to minimize risks such as explosions, fires, and accidental releases.

2.2.2. The 12 Principles of sustainable engineering

Further to the principles of green chemistry, the '12 Principles of Green Engineering' have been developed by Anastas and Zimmerman for the development of larger-scale processes, as shown in Table 11.[104]

Table 11 – The 12 Principles of Green Engineering as proposed by Anastas and Zimmerman.[104]

1. Inherent rather than circumstantial	Designers need to strive to ensure that all material and energy inputs and outputs are as inherently non-hazardous as possible.
2. Prevention instead of treatment	It is better to prevent waste than to treat or clean up waste after it is formed.
3. Design for separation	Separation and purification operations should be designed to minimize energy consumption and materials use.
4. Maximize efficiency	Products, processes and systems should be designed to maximize mass, energy, space and time efficiency.
5. Output-Pulled versus Input-Pushed	Products, processes and systems should be 'output pulled' rather than 'input pushed' through the use of energy and materials.
6. Conserve complexity	Embedded entropy and complexity must be viewed as an investment when making design choices on recycle, reuse, or beneficial disposition.
7. Durability rather than immortality	Targeted durability, not immortality, should be a design goal.
8. Meet need, minimise excess	Design for unnecessary capacity or capability (eg. 'one size fits all') solutions should be considered a design flaw.
9. Minimise material diversity	Material diversity in multi-component products should be minimized to promote disassembly and value retention.
10. Integrate material and energy flows	Design of products, processes and systems must include integration and interconnectivity with available energy and material flows.
11. Design for commercial 'afterlife'	Products, processes and systems should be designed for performance in a commercial 'afterlife'.
12. Renewable rather than depleting	Material and energy inputs should be renewable rather than depleting.

It should be noted that both the 12 Principles of Green Chemistry and Engineering should be considered as a checklist for a process to be checked against, with as many as possible to be considered with the development of a process. It is unlikely that all the principles could be met with a single process.

2.2.3. Quantitative measures of sustainability

Further to the qualitative definitions provided above, there are a number of quantitative measures for the sustainability of a chemical process, as defined below.

Atom economy

Atom economy is a common measure of the sustainability of a chemical reaction. It is a measure of the number of atoms of the starting material are found in the final desired product, as defined in Equation 11.[105]

$$Atomeconomy = \frac{Molecular\ weight\ of\ desired\ product}{Molecular\ weight\ of\ all\ reagents} \times 100\% \quad (11)$$

E-factor

The E-factor is a simple ratio of the mass of waste produced during a process over the mass of product produced during a process, as defined in Equation 12. Originally water was not counted as a waste but it is now common to be counted within the E-factor calculation.[99,106] It is a popular measure for understanding a processes sustainability due to its simplicity, as shown below.[107] A typical pharmaceutical process has an E-factor of 25-100.[108]

$$E-factor = \frac{Mass\ of\ waste}{Mass\ of\ product} \quad (12)$$

GREEN MOTION™

GREEN MOTION™ is a recently developed metric for green chemistry which assesses the health, safety and environmental impacts of manufactured compounds, giving a number between 0-100.[109] The safer and less impactful the process, the higher the rating. The calculations consider: the origin of the raw material, the solvent selection, the toxicity of the solvent and material, the reaction efficiency and process efficiency. By considering all of these factors, GREEN MOTION ™ is thought to be a quantitative measure of the degree to which a process adheres to the 12 principles of green chemistry.

2.2.4. Consequences of green and sustainable chemistry

The requirements of doing more with less has driven chemists to explore sometimes overlooked methods for producing chemicals; leading to the further exploration of processes such as photochemistry or unusual conditions such as High-temperature Water (HTW). The use of

photochemistry, carrying out reactions in water and daisy-chaining reactors can have inherently green credentials as they can reduce solvent-use and increase atom efficiency.

2.3. Continuous flow chemistry

Continuous flow chemistry is the process of performing chemical reactions, with the reactive starting material fluid continuously flowing through a typically small reaction volume. Flow chemistry is a growing area of research that is being used to address the principles of green chemistry and engineering.[110] The understanding of flow chemistry lies at the interface of chemistry and chemical engineering and an understanding of both fields is often required to optimise processes.[101,104,111] The use of flow set-ups have become more commonplace as groups have developed their own in-house reactors or as commercially available reactors have become available.[112–115] Flow processes also lend themselves to novel energy inputs, such as light, due to the often small volume that is exposed to the energy input at one time.

There are a number of fundamental differences between batch and flow processes with respect to production time and yield.[116] The reaction time, and hence production rate, of a batch reaction is how long the flask is held at a set temperature. Whereas within flow processes it is defined as the flowrate and volume of the reactor. The stoichiometry of a reaction in a flow process is defined by the concentration of the reagents as well as the flow rates of each component.

In 2007 the ACS Green Chemistry Institute and global pharmaceutical companies recommended continuous flow processing as the 'number one key green research area to promote green and sustainable manufacturing'.[111]

There are a number of other advantages of flow chemistry, however, there are also a number of disadvantages compared to traditional batch reactions, as outlined below. In industry, large-scale processes such as oil refining are all continuous.[117]

2.3.1. Advantages of flow chemistry

Flow chemistry allows for the relatively simple scalability of processes from laboratory scale to industrial process scale as the principles for the reactors are more similar compared to industrial processes.[118] It can also offer safety benefits due to the smaller volumes of reagents that are exposed to the energy input compared to batch chemistry where large volumes of organic solvents could be heated.[116,119,120] The reduction in heated volume of thermal processes allows for more accurate heating control and a reduction in energy use for the overall process.[111,121] Multiple flow reactors can also be used in series for multi-step reactions, with the added benefit of being able to introduce additional reagents chemicals into the process when required. Multiple reactors can also be used in parallel to 'scale out' the production rate of a process.

2.3.2. Disadvantages of flow chemistry

One major disadvantage of flow chemistry is the requirement of specialised equipment and operator knowledge that is not currently commonplace in chemical laboratories.[110] The adoption of flow chemistry within the pharmaceutical industry, due to the regulatory environment, has also been slow however is starting to now improve, with the US Food and Drug Administration (FDA) actively encouraging the technique.[122,123] Furthermore, with the possibility of multiple reaction steps integrated into one process, a change in one step, such as solvent choice, needs to be considered for the subsequent steps.[123]

2.4. Introduction to photochemistry

Although photochemistry has been studied for many years there has been a recent increase in interest and research due to its potential for sustainable and efficient production of chemicals.[124] The use of photons can also give higher selectivity, as well as a reduction in expensive and hazardous materials.[125] Chemical reactors have been historically designed for thermal chemistry, so if the potential of photochemistry is to be realised there needs to be a focus on developing reactors optimised for the absorption of photons.[126] It is thought that a number of current industrial processes use photochemical conversions, although commercial information is often kept confidential.[126] Of those disclosed, some of the most commonly known industrial processes involving photochemistry are the synthesis of the synthesis of rose oxide and the manufacture of artemisinin.[127–129] It should be noted that the research group within Nottingham has a historical interest in the photochemical synthesis of artemisin.[130,131]

Previously, most industrial uses of photoreactors have been largely focussed on either heterogeneous photocatalysis or microfluidics.[132] There have been a number of reasons for this; heterogeneous reactors are widely used in industry for processes such as waste water treatment and hence there has been an industrial need to optimise them.[133] For microfluidics, the dimensions can simplify the calculations due to the high proportions of light that is absorbed within the small path length.[134]

More recently there has been an increased interest in larger scale homogeneous photoreactors, which have the potential to transform the chemical and pharmaceutical industry and hence also need to be optimised.[135–137] Ideally, the reactor design and use should be optimised before the manufacture and scale up of reactors to maximise desired outcomes, with minimal design iterations.

By incorporating a process model into the design of processes and reactors it was hoped to predict the best operating conditions before large amounts of solvents and chemicals are used, compared to traditional manual optimisation procedures.[138]

2.4.1. Benefits of photochemistry

Photochemistry has been exploited by nature through photosynthesis using photons from the sun to convert CO_2 and H_2O into glucose.[139] Over recent years, the development of new photochemical reactions has given researchers novel pathways within organic synthesis and access to compounds unsuitable for thermal chemistry.[140,141] For example, the use of photochemistry can offer a unique pathway to products not available *via* traditional thermal chemical routes, such as with the electrocyclic cyclisation as shown in Figure 32.[142]

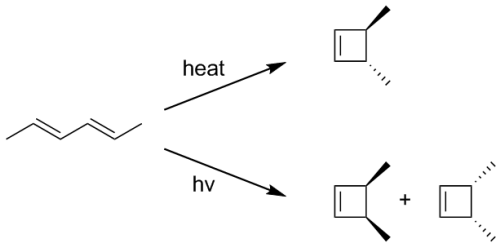


Figure 32 - An electrocyclic ring-forming reaction with the choice of either thermal or photoreactions deciding which product is formed. [142]

Different products can be formed as the absorption of a photon leads to an excited state with a different electronic configuration than the ground state, such that the reactivity of excited molecules is different to ground state molecules.[143–146] The formation of different products can also be wavelength dependent as shown in Figure 33.[147]

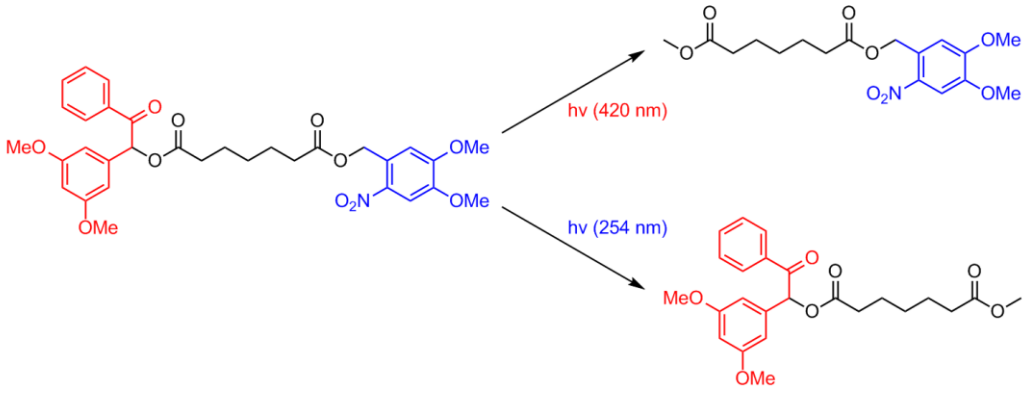


Figure 33 - An example of the wavelength dependence of reactions, with different bonds becoming reactive depending on the wavelength used to initiate the photochemical reaction. [147]

2.4.2. Limitations of photochemistry

A large number of the limitations for photochemistry are related to the equipment and technology available to researchers.[126] Traditionally typical photoreactors that are found in laboratories use broad-wavelength emitting light sources, such as mercury arc lamps, along with a large reservoir of reagents. The large reservoir often dictates that the concentration of reagents should be low due to the attenuation of light into the reactive medium. However, this has evolved in recent years due to the development of reactors by a number of groups specifically designed for high-throughput-high-productivity reactions.[126] Companies have also started to develop commercially available reactors for scale-up, such as the Vapourtec UV-150, Corning® G1 Photo Reactor or the Heraeus Noblelight.[148–150]

2.4.3. Principles of Green Chemistry and Engineering relevant to Photochemistry

Due to the breadth of photochemistry, there could be arguments put forward for all of the principles of green chemistry and engineering. However, there is likely to be a number of principles common between all photochemical processes which are presented in Table 12.

Table 12 - The principles of Green Chemistry and Engineering relevant to Photochemistry

Relevant Principles for Photochemistry	
Green Chemistry	**Green Engineering**
2. Atom efficiency – Photons can be considered as reagents, leading to highly atom efficient conversions.	**4. Maximise efficiency** – Use of photochemistry can lead to highly efficient reactors of a small size.
3. Less hazardous chemical syntheses – Photons are considered non-toxic reagents.	**10. Integrate material and energy flow** – The energy flow of the reactor is used directly within the material flow.
6. Energy efficiency – Photon energy is used to directly excite the molecules of interest rather than thermal heating of solvents.	**12. Renewable rather than depleting** – Photons can be considered as renewable as they can easily be generated without using a material.
8. Reduced derivatives – Photochemical reactions can give access to transformations that would typically require protecting groups.	
12. Inherently safer chemistry for accident prevention – Using photons can avoid the requirements for heating and therefore reduce risk. (Although caution should be taken with UV and high-powered lights)	

2.4.4. Photochemical processes

To understand a photochemical process, there are a number of first principles of photochemistry that first need to be defined. The absorption of a photon can lead to a number of different subsequent processes which are outlined in Figure 34 and explained below.[151]

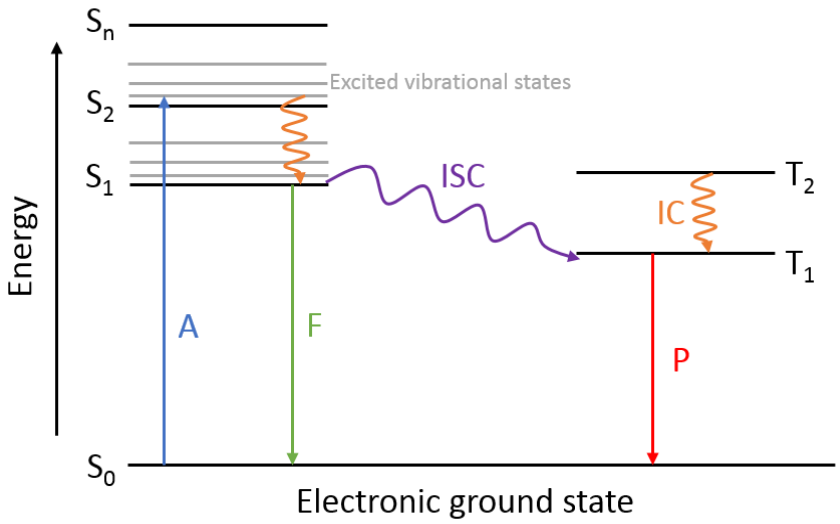


Figure 34 - A Jablonski diagram showing the different processes associated with photon absorption; where S_0 – singlet electronic ground state, S_1 – first singlet excited ground state, S_2 – second singlet excited ground state, T_1 – first triplet excited state, T_2 – second triplet excited state, A – absorption, F - fluorescence, P – phosphorescence, ISC – intersystem crossing and IC – internal conversion. (Rotational excited states are not shown). Adapted from [152].

Photophysical Phenomena

The absorption of photons can lead to a number of different excitations, from the electronic and vibrational ground state to an excited state with a higher vibrational and electronic excitation level.[151]

Rotational excitation (λ ≈ 0.3 mm – 3 mm)

Near-IR absorption with conventional intensities of light does not generally lead to photo induced reactions.[151]

Vibrational excitation (λ ≈ 700 nm – 1 mm)

Near-IR and IR absorption. The distance between the nuclei changes and although photoreactions are uncommon with vibrational excitation, isomerisations can occur.[151]

Electronic excitation (λ ≈ 190 nm – 750 nm)

UV and visible absorption. The electronic energy of the molecule is altered, this may also affect the vibrational and rotational levels too. This leads to isomeric molecule with different physical properties which can lead to photo induced reactions.

The different processes associated with electronic excitation are as follows, where **A** is the absorbing molecule:

General Excitation A + hv → A* The absorption of a photon into an excited electronic and vibrational state.

Thermal relaxation A* → A'. As A* is considered to be 'hot' compared to its environment it can equilibrate its *temperature* and hence moves to the lowest vibrational state of its electronic state (A').

Fluorescence A' → A + hv'. The A' excited electronic state returns to the ground state through the emission of a photon.

Radiationless decay A' → A. The A' excited state can return to the ground state through a non-radiative pathway.

Intersystem crossing A' → A''. Intersystem crossing occurs when the, often, singlet excited state (**A'**) lies close to a triplet state (**A''**) which cannot be reached from the direct excitation of the ground state, due to a forbidden transition.

Phosphorescence A'' → A + hν''. Although the triplet states are often slightly more stable than singlet state with a lifetime of 10^{-4} to 1 s compared to 10^{-9} to 10^{-7} s, respectively; they still deactivate to the ground state through the emission of a photon.[153]

If energy difference between A'' and A' is less than 40 kJ, the molecule can have sufficient thermal energy to cross back to A' – if it then goes on to emit a photon to return to the ground state (fluoresces), this is called high temperature or α-phosphorescence or delayed fluorescence.[151]

Energy transfer to acceptor molecule

$A^{exc} + B \rightarrow B^{exc} + A$

Rather than the deactivation of the excited state through unimolecular mechanisms, deactivation is also possible through the transfer of energy to a secondary molecule, and is often the process used by photocatalysts.[154] The energy transfer has to take place within the lifetime of either the singlet or triplet excited state.

2.4.5. Photochemical reactions

In addition to the mechanisms above, molecules that have absorbed light can then go on to react with other molecules. This photoreaction can happen at a number of different stages when the molecule is excited (e.g. either A*, A' or A''). For the purpose of the following explanations this shall be characterised as A^{exc}.[151]

Dissociation

Into radicals – $A^{exc} \rightarrow B^{\bullet} + C^{\bullet}$. Instead of relaxing back into the ground state, the photo-excited state molecule splits apart into two separate radical species.

Into other instable molecules $R\text{-}CHN_2^{exc} \rightarrow N_2 + R\ddot{C}H$ Similar to the radical mechanism, the photo-excited state can form other instable molecules such as carbenes.[155]

Into ions – $A^{exc} \rightarrow B^{+} + C^{-}$ Rather than the separation of electron pairs into radical species they can be ejected from the separate species and form ions.

Into a positive ion and an electron – $A^{exc} \rightarrow A^{+} + e^{-}$. The absorption of high energy photons is able to cause the emission of electrons from the molecule, also known as the photoelectric effect.[151]

Formation of stable molecules – $A^{exc} \rightarrow B + C$. The excited state can also cause the molecule to split apart and form two stable molecules.

Photoisomerisation – $A^{exc} \rightarrow B$. Photoisomerisation is a relatively common effect where the excited state can relax back into a ground state with a different conformation to the molecule that was excited.

2.4.6. Quantum yield

Further to the absorption of photons, an additional term is required to describe the rate of a photoreaction. The quantum yield, ϕ, of a reaction is a measure of the efficiency of the reaction as compared to the number of photons it has absorbed. A number of different more-specific definitions can be used for the quantum yield (see Appendix I) depending on whether it is specific to the direct photochemical process or the overall process.[151] A simple definition for understanding is the 'ratio between the molar flux of molecules reacting during the photochemical reaction and the flux photons absorbed by the molecule'. [126] For a large number of reactions, ϕ is often <1, signifying a deactivation process has occurred and not every photon causes the reaction to proceed. The value of ϕ can also be >1, signifying the photochemical step is an activating step, triggering the whole process.[126]

Methods for measuring Quantum yield

Modern techniques for measuring the quantum yield of reactions were largely developed for the understanding of biological processes, to further understand photosynthesis, however it is increasingly being considered for synthetic chemistry.[139,156] There are generally two approaches for measuring quantum yield: via actinometry or through comparison of compounds with known quantum yields. Single photon quantum yield determination can also only be defined for monochromatic light, which is unlike typical experimental conditions.[157]

Actinometry measures the radiant flux of a light via measuring the yield of a photochemical reaction with a known reference quantum yield.[158] Once the radiant flux is known, the quantum yield of the reaction in question can then be calculated.[159] Actinometry provides the most fundamental measurement of the number of photons absorbed. However, actinometry can become complex for comparisons when the light used is a broadband emitter and/or the chromophore absorbs at different wavelengths to differing amounts.

The comparison method also uses a compound that reacts with a known quantum yield, however, the illumination of the starting material and known reference compound is carried out simultaneously. It can be considered more straightforward to calculate the quantum yield as there is reduced processing of experiments. However, differing spectral properties can again introduce added complexity.[160]

2.4.7. Emission of light

Understanding the emission of light and its intensity is crucial for the development of a model handling photoreactions and photoreactors. The number of photons present is the driving force behind the reactions and hence needs to be understood. The light sources that are used in a wide range of industries have slight differences in both nomenclature and understanding.

For example, light power is often widely confused between disciplines due to the variety of needs for lighting.[161] Light power is often quoted in candela which is nominally the light given off by one candle. This relativity to a candela is not suitable due to both the use of UV lamps and the understanding of

absorbance, as set out below.[162] For photoreactors it is more useful to speak in terms of power output per unit area. The power output can then be translated into the number of photons per second per unit area through use of the Planck-Einstein relationship, defined in Equation 13, where E_p is the energy of the photon, $\hbar$ is Planck's constant, c is the speed of light and λ is the wavelength of the photon.[163]

$$E_p = \frac{\hbar c}{\lambda} \tag{13}$$

One area of caution to take note of is the uncertainty between the manufacturer's specification and number of photons entering the reactor volume. This uncertainty can be due to a number of reasons such as: geometry, light diffraction at the reactor surface or the age of the lamp.

For simple modelling, an assumption of monochromatic light is widely used as this allows for the conversion of light power to photon output. This assumption leads to another source of uncertainty surrounding light intensity as lamps are often not monochromatic sources and molecules absorb at different strength over a range of wavelengths.

2.4.8.Absorption of Light

Understanding the absorption of light is an important aspect of the photochemical process, with the approach taken outlined below. The part of the molecule that absorbs light is known as the chromophore and can lead to a variety in both the wavelength and strength of absorbance, depending on the associated transitions. For example, highly conjugated molecules often absorb light, with the degree of conjugation leading to a change in wavelength.[164]

Local volumetric rate of photon absorption (LVRPA)

The local volumetric rate of photon absorption represents the number of photons absorbed by an absorbing species per unit time and per unit of reactor volume. The calculation of LVRPA requires a radiative transfer equation (RTE) to calculate the irradiance first.

Radiative transfer equation

Radiative transfer equations (RTE) model the distribution of light throughout a field. There are a number of possible equations that could be used, with three described below. Further explanations for RTEs relevant to the models developed in this work are discussed within the Photochemical chapter.

The Beer-Lambert law, defined in Equation 14, could be considered the simplest RTE as it relates the measured irradiance, I, of an electromagnetic beam to the length, L, it has travelled through an absorbing medium of known concentration, C. The absorbance, A, is a logarithmic relationship of the initial irradiance, I_0, and is often quoted in the literature due to its self-referential nature.[165] In the Beer-Lambert law, the decadic molar absorption coefficient, ε, describes how *absorbing* a medium is in the linear direction.

$$A_{BL} = -\log_{10}\left(\frac{I}{I_0}\right) = \varepsilon LC \qquad (14)$$

This Beer-Lambert derived RTE is only valid for linear light such that the absorption coefficient is per linear distance, as it has been derived from a single-dimension differential equation. For more complicated geometries, more complex RTEs are required; there are generally two approaches that can be used for more complex geometries: discrete-ordinates method or the two-flux approximation.

Discrete ordinates method

The discrete ordinates method (DOM) discretises the angular space into a finite number, $\boldsymbol{N_d}$, of directions, $\boldsymbol{u_i}$. The RTE is a system of partial differentials and integrals that are solved with computational Partial Differential Equation (PDE) solvers. The integrals become a weighted summation of the light over $\boldsymbol{N_d}$ directions. [166,167]

For simplicity, the derivation of an absorbing only medium is shown here as this was assumed for the homogeneous reaction mixture. For a medium that only absorbs, the RTE is defined in Equation 15 where s is the dimension distance:

$$\frac{dI}{ds} = -\alpha I(s, \boldsymbol{u}) \tag{15}$$

The angular space is discretised in N_d directions and for purely absorbing mediums the RTE can be solved using a finite volume method.[168] The irradiance can be obtained by summing the irradiance from each direction and multiplying it by the weight (w_j) of the associated light as defined in Equations 16.

$$RTE = \int_{\Omega'=4\pi} I(s, \boldsymbol{u}) d\Omega = \sum_{j=1}^{\boldsymbol{N_d}} w_j I\left(s, \boldsymbol{u_j}\right) \tag{16}$$

A more in-depth explanation of the derivation of the full RTE for all mediums using the DOM is shown in Appendix I. These calculations require heavy pre-calculation which limits its ability to be coupled with other equations, such as mass balance.[168] There are a number of disadvantages associated with the DOM method:

- False diffusion due to the spatial approximation of the irradiance, although this can be improved by decreasing the mesh size it can cause large increases in computational requirements
- The 'ray effect' which is specific to discretised RTEs, where the light is only considered for each direction.[169] Again, a reduction in mesh size can improve this but leads to an increased computational requirement.

Two-flux approximation

The two-flux approximation overcomes the 'ray effect' by approximating the light to a function, known as a phase function, which can then be differentiated over the angular space.[170,171] This phase function is differentiated by splitting the local environment into two hemispheres. The approximation was first developed for heat transfer problems and used the following assumptions:

- rectangular 1D geometry;
- isotropic phase function; and

- irradiance independent of the incident angle.[172]

These approximations have since been extended for cylindrical and spherical coordinate systems as well as for anisotropic radiation fields.[173] Similarly to the DOM method, the derivation for just an absorbing medium is shown below, while a more detailed discussion of the full RTE shown in the Appendix I. As defined previously in Equation 15, a homogeneous absorbing medium with no scattering was assumed.

$$\frac{dI}{ds} = -\alpha I(s, \boldsymbol{u}) \tag{15}$$

This was then adapted by Van Noort et al. to become a simplified one-dimensional operator of the RTE independent of the azimuth (θ), shown in Equation 17, where γ is the angle measured between the unit vector ($\boldsymbol{u}$) and the r axis, as shown in Figure 35.[173]

$$\frac{dI}{ds} = \frac{dI}{ds_1}\cos\gamma \tag{17}$$

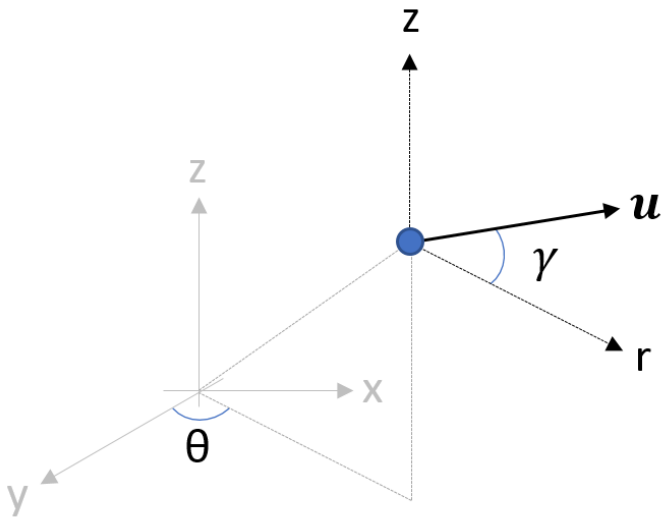


Figure 35 – The frame of reference used for the one-dimensional radiative transfer equation used with the two-flux approximation, where θ is the azimuth of which the RTE is independent, γ is the angle the unit vector (u) makes with the r axis, which used within the phase function.

The first equation can be analytically solved if it is separated into two hemispheres, which is well known as the two-flux method.[172] This was extended for collimated radiation before being adapted to

the function defined in Equation 18 for the general angular dependence for each hemisphere, where n is the degree of collimation (n=0 is the isotropic case and n=∞ is the collimated case).[174]

$$I^{\pm}(\gamma) = I^{\pm}|\cos^{n}\gamma| \tag{18}$$

Using this definition within Equations 15 and 17 and then integrating over each hemisphere (positive and negative values of $\cos\gamma$) with the help of summation rules for the nth moment equations obtained, a first independent relation for the intensities is obtained, shown in Equation 19.

$$\frac{d(I^{+} + I^{-})}{ds_1} = -k_h\alpha(I^{+} - I^{-}) \tag{19}$$

In which the collimation factor (k_h) is defined in Equation 20.

$$k_h = \frac{n+2}{n+1} \tag{20}$$

A second independent equation was required for curvilinear systems of coordinates to ensure the obtained solutions verify the energy balance on the photonic phase, which is defined in Equation 21.[172,175]

$$\frac{d(I^{+} - I^{-})}{ds_1} + \frac{\psi}{s_1}(I^{+} - I^{-}) = -k_h\alpha(I^{+} + I^{-}) \tag{21}$$

In which the parameter ψ depends on the coordinate system used, with cylindrical coordinates ψ = 1. Differentiating (19) and combining with (21) led to this one-dimensional two-flux approximate RTE in any geometry, defined in Equation 22.

$$\frac{d^2(I^{+} + I^{-})}{ds_1^2} + \frac{\psi}{s_1}\frac{d(I^{+} + I^{-})}{ds_1} - k_h^2\alpha^2(I^{+} + I^{-}) = 0 \tag{22}$$

2.4.9. Kinetic models for photochemistry

Major developments of photochemical reaction process models have either been for heterogeneous photocatalysis or for the decontamination of streams such as for cleaning water.[150,154,176] The kinetic

models developed for these cases were useful for guidance, although were not directly applicable to the work presented in this Thesis; homogeneous chemical reactions.

For integration into the reactor models, a new coupling of equations needs to be considered, compared to thermal reactor engineering; the coupling of the radiative transfer equation and the conservation equations. This has two main consequences: assuming the reactor is perfectly mixed or plug flow which is often used in thermal engineering will lead to a heterogeneous field of reaction rates and concentrations due to either mixing or light attenuation.[126]

To the author's knowledge, just one model is capable of understanding the kinetics and predicting the performance of homogeneous photochemical transformations. Aillet at al. developed a model that used experimental results to predict the quantum yield of photoreactions, which is discussed below.[156]

Aillet's photoreaction model

The method chosen was developed by Aillet et al. and uses the following assumptions to simplify the behaviour so a quantum yield can be calculated, assuming there is:

- plug flow with no variation in concentration across the diameter;
- single wavelength; and
- a known lamp intensity at the reactor wall. [156]

The experimental values used for the estimation were inputted into the equation derived by Aillet et al., as shown in Equation 23. The value shown in red in Equation 23, named the 'Aillet Value' from this point onwards, was plotted against the residence time, with the gradient of this graph equal to $\Phi \frac{I^{W,photon}}{\Delta c}$, where $B_0 = C_{A0}\varepsilon_A(R_w - R_L)\, ln(10)$.

The gradient can be used to calculate the quantum yield as the photon irradiance at the wall, $I^{W,photon}$ is known where $\Delta c = \frac{R_L^2 - R_W^2}{2R_W}$.

$$C_{A0}\left(X + \frac{1}{B_0} ln\left[\frac{1 - e^{-B_0}}{1 - e^{-B_0(1-X)}}\right]\right) = \Phi \frac{I^{W,photon}}{\Delta c} t \quad (23)$$

The use of the Aillet value to calculate the quantum yield is used in Chapter 4 and compared to the method developed in this work with a number of examples.

Future model possibilities

For the scale-up of photochemical processes from typical laboratory scale (mg to g) to larger scales (kg to tonnes), a number of processes need to be further understood, as suggested by Loubière et al.:

- Photocatalysis;
- Competitive photoreactions; and
- Consecutive photoreactions.[126]

Loubière et al. recognised the need for "interconnecting photochemistry and chemical engineering from the beginning of a study in order to identify reaction and process limitations as soon as possible, and to develop a strategy to overcome these".[126]

2.5. Photochemical reactions in flow

Carrying out photochemical reactions in flow can address a number of the issues traditionally found with batch photochemistry. Flow set-ups are generally designed for a small optical path length that combined with high powered light sources, allow for high concentrations of starting materials to be used.[177,178] These high concentrations ensure a high efficiency for photon absorption while keeping conversion high and reducing solvent requirements.[177] The tunability of conditions allows for much more flexible optimisations compared to batch methods as well as improving safety credentials.

2.5.1. Photoreactor design

This combination of lamp choice and reactor design has led to a number of innovations to optimise photochemical processes. For example, visible light photochemistry has rapidly grown over the last

decade due to the availability of inexpensive, long-lived and narrow-banded LEDs in the visible region. More recently, the advent of UV LEDs has driven similar innovations for UV reactions.[179]

Light sources

For photochemical reactions to proceed, a light source is needed to initiate the reaction. The light source can range from sunlight to highly specialised lamps designed for photochemical transformations. The choice of the light's wavelength and power can have a large effect on the overall performance of the reaction.[180]

Mercury lamps

Mercury lamps are readily available at a range of powers, with the output wavelengths depending on the type of mercury lamp used. Low-pressure mercury lamps convert *ca.* 30% of the power drawn into UV photons, of which 90% are of 254 nm, as shown in Figure 36.[177,181,182]

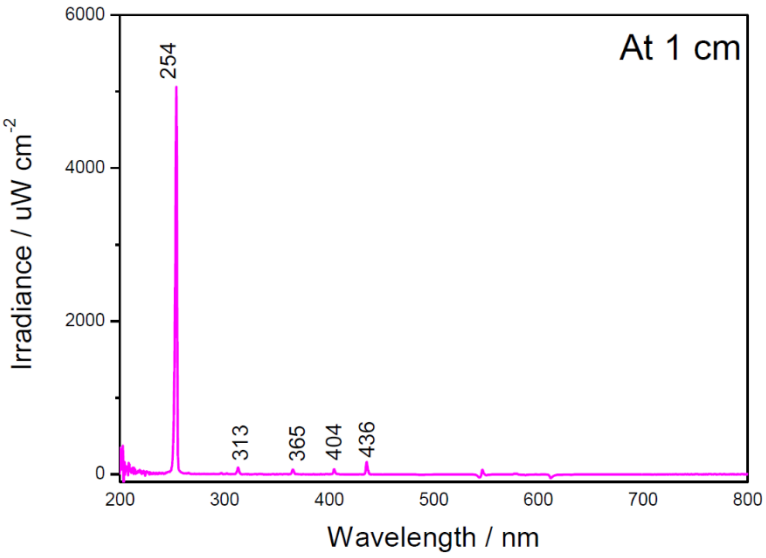


Figure 36 - The irradiance emission spectrum of a low-pressure mercury arc lamp measured 1 cm away from the lamp, showing the large proportion of photons at 254 nm. Recorded by Dr. Charlotte Clark using an Ocean Optics UV-VisUSB 2000+ spectrometer. Reproduced with permission.

Medium and high-pressure mercury lamps convert a higher percentage of power into photons, and hence much high-power lamps are commercially available. The photons emitted by medium and high-pressure mercury lamps are at a wider set of wavelengths, these are considered 'broadband' emitters,

as shown in Figure 37.[177,181] This is due to the fact that although mercury emits strongly emits at 254 nm it also absorbs light at 254 nm and hence the energy is re-absorbed and emitted at higher wavelengths in a process known as 'imprisonment of radiation'.[183]

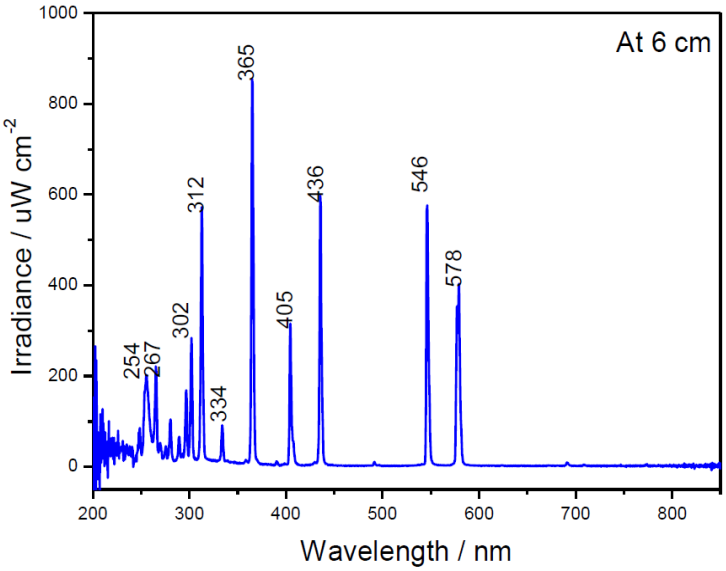


Figure 37 - The irradiance emission spectrum of a high-pressure mercury arc lamp measured 6 cm away from the lamp, showing the broad range of wavelengths emitted. Recorded by Dr. Charlotte Clark using an Ocean Optics UV-VisUSB 2000+ spectrometer. Reproduced with permission.

From a practical point of view, medium and high-pressure mercury lamps emit photons at a variety of wavelengths which are then able to excite a variety of chromophores within a reactive system. The advantage of higher lamp powers then needs to be balanced against the reduced selectivity for reactions and the possible of formation of unwanted side products.[140]

Light Emitting Diodes

Light emitting diode (LED) technology has undergone large amounts of innovation recently, largely due to the advances of LED TVs and need for efficient lighting. LEDs are now largely seen as inexpensive, efficient and safe replacements for filament- and discharge-based lighting. There is a wide range of LEDs available depending on needs, with just the LEDs used in this work being discussed below.

Excimer lamps

The excimer reactors take advantage of the excitation of rare-gas dimers, rare gas-halogen dimers or rare gas-halogen exciplexes to generate near-monochromatic light. The choice of the combination of gases/halogens leads to different wavelengths and can be tuned to create light at certain wavelengths.[184] The gas acts as a dielectric medium between two electrodes such that when a sufficient voltage is applied across the plates, an electrical breakdown of the gas occurs which allows the formation of the excimer complex, which decay to give near-monochromatic photons.[185]

2.5.2. Photoreactors used in this work

The design of the reactors can have a large effect on the overall performance of the process. Due to the need for absorption of light by the fluids, typical reactor designs are often unsuitable. There are a number of different possible designs in the literature, which often vary by group and reaction. The reactors used in this work are described below.

Excimer flow reactor

The excimer flow reactor consists of a cylindrical vessel, with a 'cold finger' placed inside of the vessel. This cold finger is made of three concentric pipes, as shown in Figure 38. The inner pipe allows the reactive material to be pumped to the end of the reactor, while the remaining two pipes allow a coolant to be pumped through the reactor to regulate temperature. The cold finger is placed inside of a quartz tube, which is able to be inserted into the excimer lamp.

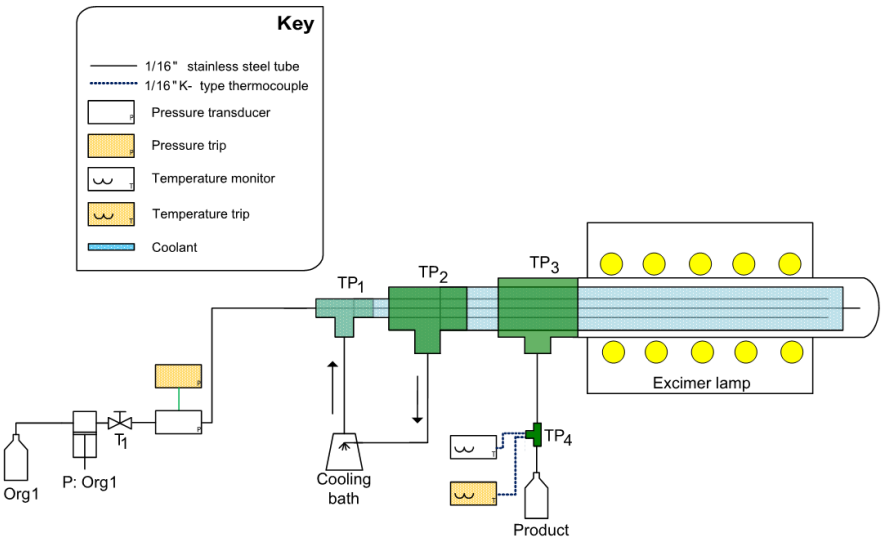


Figure 38 - A schematic of the excimer flow reactor set up, with the different T-pieces (TP) used for the separation of the reagent and coolant flows. Schematic produced from literature with permissions.[186]

The outer diameter of the stainless-steel pipe is 12 mm and sits inside a quartz tube with an external diameter of 15.6 mm. Considering the thickness of the quartz tube, the gap between the two, in which the reactive fluid flows is 120 µm. This reactor system has a total volume of *ca.* 10 mL and an irradiated volume of 1.37 mL, both of which were determined mathematically by previous members of the group.[186] Reagent solutions can be flowed through the irradiated volume at a variety of flow rates as a thin film ensuring all the solution can absorb light. The Excilamps can be easily interchanged so that the desired radiation wavelength can be selected.

Excimer flow reactor lamps

Four lamps have been manufactured for use with the Excimer flow reactor, which have a smaller diameter than the Excimer batch reactor. The Excimer lamp discharge tubes are cylindrical so the reactor can be placed inside the lamps, such that the surface of the reactor can be irradiated from all directions, as shown in Figure 39.

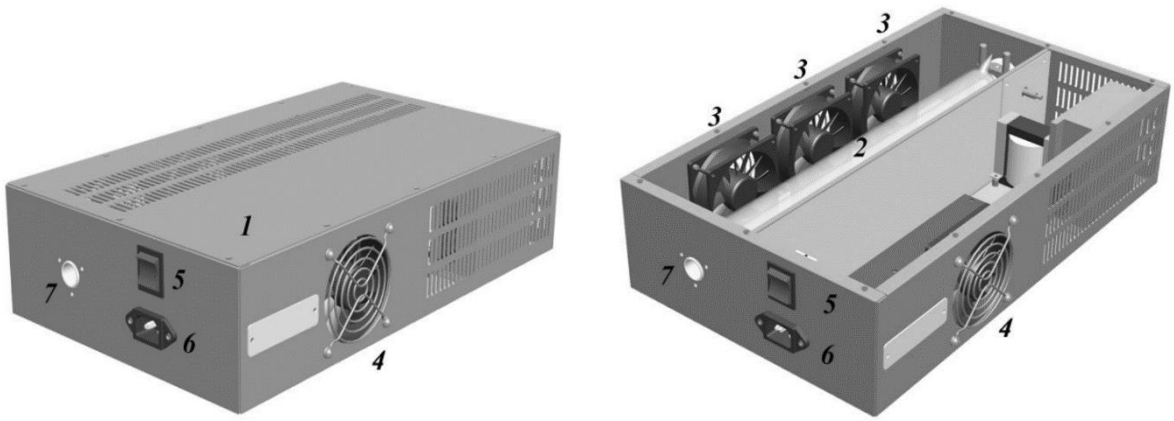


Figure 39 - The design of the excimer flow lamps, where 1 is the external casing, 2 is the discharge tube, 3 and 4 are the cooling fans, 5 is the power switch, 6 is the power supply plug and 7 is the hole in which the reactor is inserted.[187]

In the group at Nottingham there are a number of different excimer lamps, with varying powers for both the Excimer flow and batch reactor setups. The Excilamps used with these reactors were obtained from the Institute of High Current Electronics (Tomsk, Russia).[187]

The different wavelengths, the excimers used, power drawn and irradiance at the lamp surface for each lamp is shown in Table 13. The irradiance at the lamp surface is provided by the lamp manufacturer and was used for the modelling of the Excimer reactors.

Table 13 - Table of the wavelengths and equivalent irradiances supplied by the manufacturer for the excimer flow lamps.[187]

Emission wavelength (nm)	Excimer used	Power drawn (W)	Irradiance at lamp surface ($W \cdot m^{-2}$)
207	KrBr	180	100
222	KrCl	113	210
282	XeBr	113	360
308	XeCl	113	490

Excimer batch reactor

The batch reactor is a jacketed quartz vessel, with the outer jacket containing coolant. The reaction mixture is stored in the central cavity, which has a radius of 1.27 cm, length *ca.* 36 cm and a maximum irradiatable volume of *ca.* 150 mL. Coolant can flow into the outer jacket through one of the side arms and out through the other side arm, as shown in Figure 40. The selection of a coolant fluid has to be considered in terms of the absorption of light as it is between the lamp and the reactive mixture. The

excimer batch reactor is then placed into the excimer lamp in a vertical orientation, compared to a horizontal orientation with the excimer flow reactors. As it is a batch reactor, there is a mechanical stirrer inserted into the top of the reactor; the effectiveness of this stirrer is discussed in the photochemical modelling chapter.

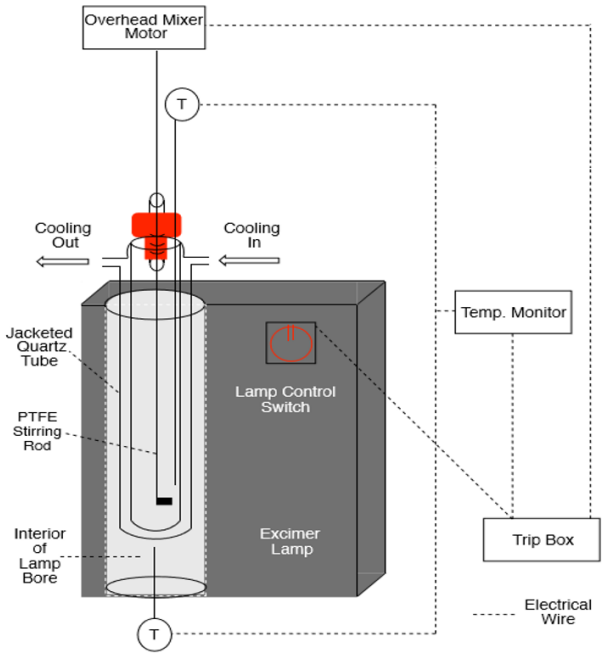


Figure 40 - A schematic of the excimer batch reactor with the excimer lamp in a vertical orientation and the coolant pumped through the reactor in between the reactive mixture and the irradiated wall. Schematic produced by Toby Waldron-Clarke and reproduced with permission.

Excimer batch reactor lamps

As mentioned above, the Excimer batch reactor has a wider diameter which is used for the wider batch reactors. The lamps operate on the same principle, with the wavelength, composition, power and irradiance values provided by the manufacturer shown in Table 14.

Table 14 - Table of the wavelengths and equivalent irradiances supplied by the manufacturer for the excimer batch lamps.[187]

Emission wavelength (nm)	Excimer used	Power drawn (W)	Irradiance at lamp surface ($W \cdot m^{-2}$)
222	KrCl	269	180
253	XeI	283	170
282	XeBr	229	270
308	XeCl	229	330

FEP tubular reactor

The design of UV continuous flow photoreactor that has achieved the most prominence is the 'FEP reactor' initially designed by Booker-Milburn and co-workers in 2005.[112] This type of reactor consists of a water-cooled medium-pressure mercury lamp with fluorinated ethylene propylene (FEP) tubing wrapped directly around the cooling jacket of the lamp. Reagent solutions are flowed through the reactor via an HPLC pump and product is collected at the outlet. A schematic and photograph of this reactor set-up can be seen in Figure 41. The photo of the FEP tubular reactor is a model case, as the dimensions of the FEP tubing and coil diameter can change depending on the conditions required.

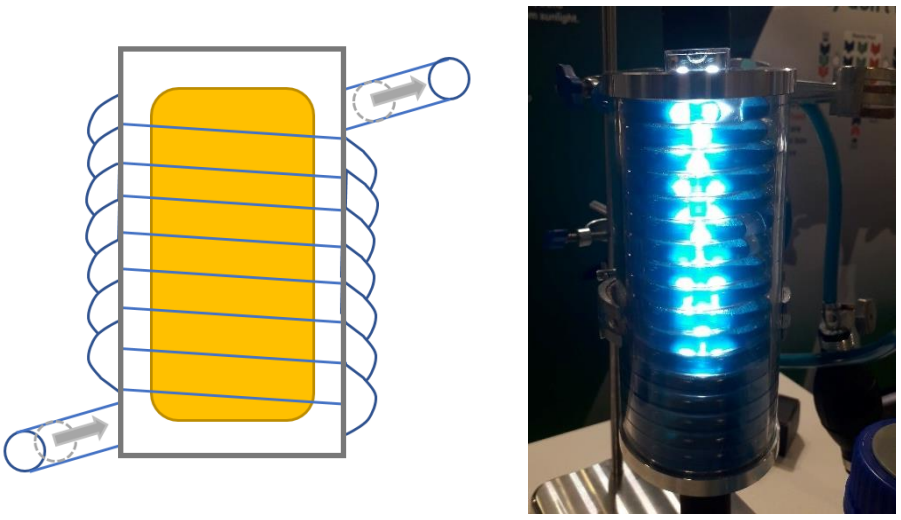


Figure 41 - A schematic of the FEP tubular reactor and a photo of a model set up, with the lamp in the centre and the FEP tubing wrapped around it in a coil. Please note that the dimensions of the tube and coil can change depending on the conditions required. This photo was taken by Amy Flinn.

An updated FEP tubular reactor, known as the Firefly, has been developed by colleagues in Bristol to increase the scale of production for photoreactions.[136] The Firefly reactor was proposed to be used with a high temperature water reactor able to produce over 1 kg per day in a 'daisy-chained' process, as discussed in the Chapter 5.

Vortex reactor

The vortex reactor was designed to take advantage of a phenomena known as Taylor vortices, which occur when a rotating cylinder is placed inside a cylinder. The Taylor vortices increase the mass

transfer of new reagents to the irradiated wall to overcome an inherent issue with photochemical reactors.[126,188,189] The reactor itself consists of a transparent Pyrex jacketed tube with an internal diameter of 22 mm that contains a stainless-steel cylinder with a bore running through the centre to allow for the reactive mixture to be continuously pumped through the reactor, as shown in Figure 42.

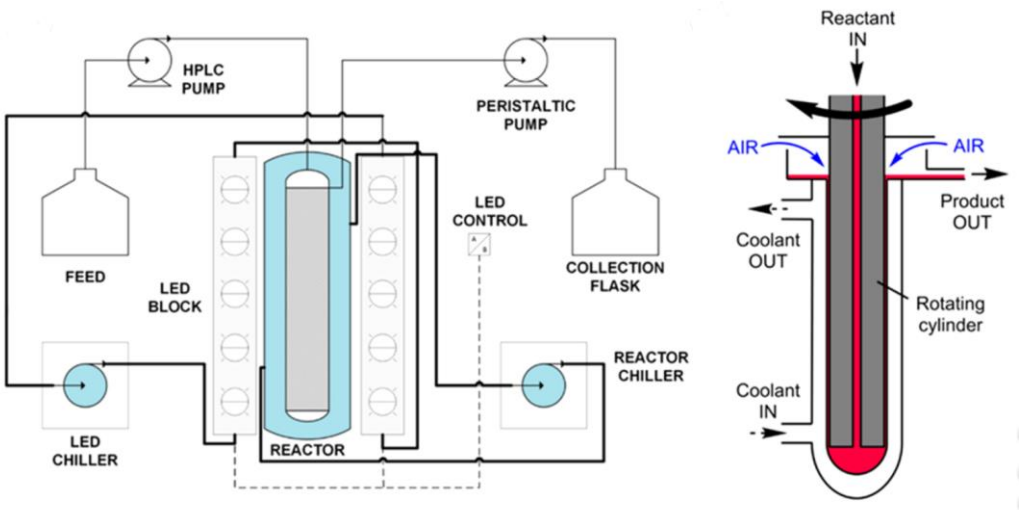


Figure 42 - A schematic of the Vortex reactor used in this work, where a rotating cylinder is placed inside a cooled reaction vessel, which is exposed to LED blocks. Pumps are used to control the flow of both the reagents and coolant. Reproduced from literature with permission.[135]

The gap size between the irradiated wall and the rotating cylinder can be changed by using cylinders of different diameters, with gap sizes of 1, 2, 3 and 4 mm used in this work. The choice of this gap size has to be considered when comparing results due to the increased volume of the reactor. The rotating cylinder is 15 cm tall, giving an overall reactor volume of 9.89 cm^3 for the 1 mm gap.

The light source can be easily interchanged with the Vortex reactor depending on requirements. For this work, blocks of visible LEDs were used consisting of 5 x 1400 lm chips built by Citizen Electronics. The light emitted was quoted in lumens and therefore not applicable for the modelling of photoreactors as lumens are a measure of visible light and not wavelength-specific irradiance.

The rotation of the block could also be controlled, so the strength of the Taylor vortices could be altered. The strength of Taylor vortices can be measured using the Taylor number, Ta, which is calculated, as shown below where Ω is the angular velocity, R_1 is the external radius, R_2 is the internal

radius and ν is the kinematic viscosity. The rotation speed required for Taylor vortices with the reactor set up used in this work is discussed in the photochemical modelling chapter. The strength of Taylor vortices is measured using the Taylor number, defined in Equation 24, where Ω is the rotational velocity, R_1 is the internal diameter, R_2 is the external diameter and ν is the kinematic viscosity.[190]

$$Ta = \frac{\Omega^2 R_1 (R_2 - R_1)^3}{\nu^2} \quad (24)$$

2.6. Introduction to high temperature water reactions

Water is the most abundant natural solvent on Earth and has been used for numerous biological and geological processes for millions of years.[191] It has inherently 'green' properties as it is non-toxic and non-flammable. Ambient water also has a number of unusual properties, including the hydrogen-bonding effect. It also has a high heat capacity, which makes it an excellent heat buffer for exothermic reactions.[191] The use of water can also eliminate the protection-deprotection processes of functional groups and hence increase the efficiency of reactions.[192]

The properties of ambient water can also change when heated at pressure until it forms 'High Temperature Water', which is discussed in detail below.

2.6.1. What is high temperature water (HTW)?

High temperature water (HTW) has a broad definition of liquid water above 200 °C and supercritical water, where the critical point of water is 374 °C and 22.06 MPa.[193] Often geochemical reactions occur in HTW, with the conversion of kerogen into petroleum occurring in HTW in the presence of clay minerals.[194–196] HTW has also long been used in chemical processes for material synthesis, waste destruction, recycling and biomass processing. It is also increasingly being used within organic synthesis due to its unusual properties.[197–201]

At standard conditions water's anomalous properties are due to the strong hydrogen bonds between water molecules, which break down at higher temperatures. The breakdown of the hydrogen bonding network leads to water becoming less polar, with a polarity more like methanol or ethanol.[202] This

change in solvation properties can be useful for the separation of product *post*-reaction when the water cools and some organic compounds become insoluble. HTW also becomes both more acidic and basic as the water self-ionises into H_3O^+ and OH^-.[203,204] The heat capacity of HTW also increases up to a maximum *ca.* 380 °C.[205]

The properties can also vary widely within the definition of HTW used above and should be considered when comparing conditions. In order to access these conditions for chemical reactions, custom built equipment is needed, along with the suitable safety controls.

2.6.2. High temperature water with organic reactions

As the physical properties of HTW can vary with the conditions, a wide range of chemical reactions can be supported in HTW, including ionic, polar non-ionic and free radical reactions.[193] HTW does not just act as a solvent, it can also act as a reagent or disassociate and act as both an acid and base catalyst.[206] Water molecules can also catalyse a reaction through interacting with the transition state to reduce its energy. This transition state catalysis mechanism is important for intramolecular hydrogen transfer and isomerisation as the water molecules act as a proton relay to make the transition state less strained.[207–209]

Challenges of HTW reactions

The major challenges with HTW are the elevated temperatures and pressures required, with equipment found in traditional chemistry laboratories unsuitable. Flow conditions can be used to alleviate some issues as a small volume can be kept at the elevated conditions, rather than a larger volume batch reactor, which could pose serious safety issues.[110]

Principles of Green Chemistry and Engineering relevant to HTW reactions

There are a number of Green Chemistry and Engineering principles that can be considered for HTW reactions, as shown in Table 15.

Table 15 - The principles of Green Chemistry and Engineering relevant to reactions in high-temperature water.

Relevant Principles for high-temperature water reactions	
Green Chemistry	**Green Engineering**
3. Less hazardous chemical syntheses – Water is non-toxic.	**4. Maximise efficiency** – Use of high-temperature water allows for rapid conversion of products on a small scale.
5. Safer solvents and auxiliaries – Water is non-toxic and can be used to replace the use of both bases and acids, due to their unusual properties.	**3. Design for separation** – When cooled, water, returns to being non-solubilising for a large number of organic compounds.
7. Use of renewable feedstocks – Water is a renewable resource.	**12. Renewable rather than depleting** – Water is a renewable resource.
8. Reduced derivatives – The properties of high-temperature water can allow non-standard reactions, that typically require protecting groups.	

2.6.3. High temperature water reactors used in this work

The high temperature and pressures needed for HTW often requires specialised equipment. The reactors used in this work are custom-built and consist of a stainless-steel coiled pipe. The coiled pipe is wrapped around a heated block that is again surrounded by an insulated jacket.

Reactors used in this work

There were two different reactor sizes used in this work, a larger and smaller reactor, which were used in a modular set up where the two reactors could be interchanged. The larger reactor was used initially, before a smaller reactor was designed to allow for further understanding of the reaction while reducing material and energy use. A simplified schematic of the experimental set up is shown in Figure 43. It should be noted that there were a number of safety systems in place for the experimental work that have been omitted from the diagram for simplicity.

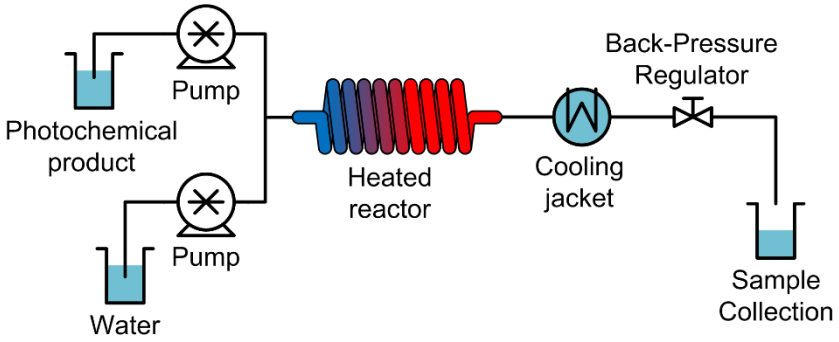


Figure 43 - A simplified schematic of the high-temperature water reactor built for this work where pumps control the flow of reagents entering the reactor and a back-pressure regulator regulates the pressure before the product are collected. It should be noted there are a number of safety measures in place, including pressure and temperature trips, that have been omitted for simplicity. Produced by Dr. Rowena Howie and used with permission.

Reactor sizes for the larger and smaller reactor

Two sizes of reactors were used in the development of this method; the larger reactor was used initially to carry out the reactions as it had been built previously.[210] The smaller reactor was built to reduce material use in the optimisation and understanding stage of the development. A photo of the larger and smaller reactors used in this work are shown in Figure 44 (a) and (b), respectively.

Both reactors consisted of a coiled pipe wrapped around a heating block that is used to control the temperature. The larger reactor consisted of a 6 m long stainless-steel pipe with an internal diameter of 0.152 cm, giving a reactor volume of *ca.* 44 cm^3. The smaller reactor consisted of a 3 m long stainless-steel pipe with an internal diameter of 0.0285 cm, giving a reactor volume of *ca.* 0.77 cm^3.

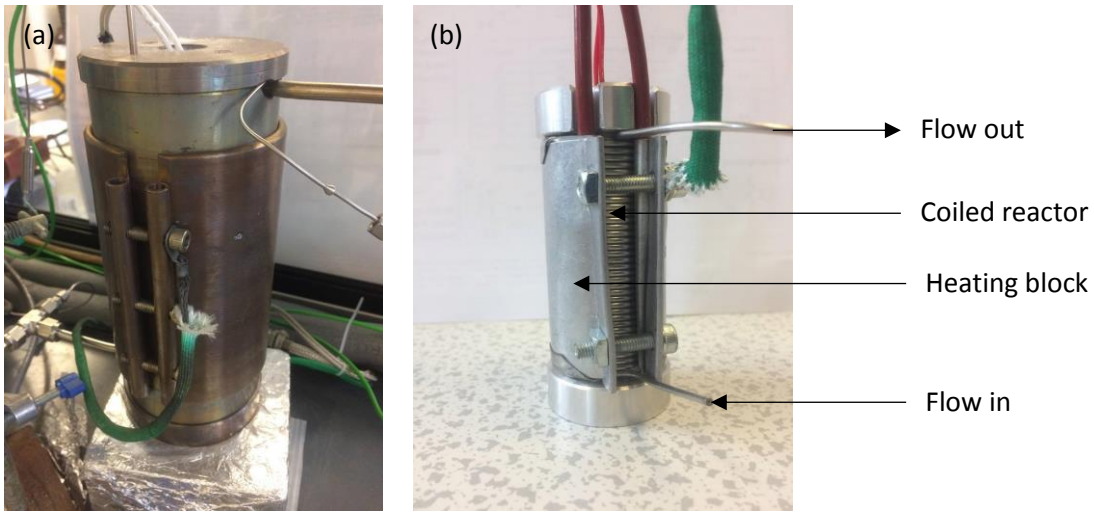


Figure 44 - Photographs of (a) the larger reactor and (b) the smaller reactor used in this work, with the different components indicated for the smaller reactor. The larger reactor used the same design on a larger scale. Photos taken by Dr. Rowena Howie and used with permission.

2.7. Multi-step reaction processes

The combination of multiple reaction steps in series can take advantage of the specific advantages flow processes offer. By combining reaction steps, the intermediates do not have to be isolated and are directly transferred into the subsequent reactor; reducing costs and time. For practical reasons the combination of steps are sometimes separated so solvent swaps can occur. This technique is particularly useful with photochemistry where solvent choice can affect the absorption of light due to differing absorption behaviour.[211,212]

Typically, the optimisation of each flow process is carried out before combining of the steps which can lead to competing factors. For example, the optimal residence times for each reactor could suggest a different flowrate for each step. These competing factors mean that the overall process has to be considered when optimising each separate step.[116] This could be seen as the difference between local minima and global minima in a mathematical optimisation.[213]

Connecting reactors in series is often known as 'daisy-chaining' where the output of one reactor is the input of the next with minimal processing between the reactors. The daisy-chained process used in this work was the daisy-chaining of an FEP tubular photoreaction followed by a high-temperature reaction, as shown in Figure 45. The first reaction was carried out in acetonitrile, with the output of the first reaction diluted with water in flow, before being flowed through the high temperature reactor.

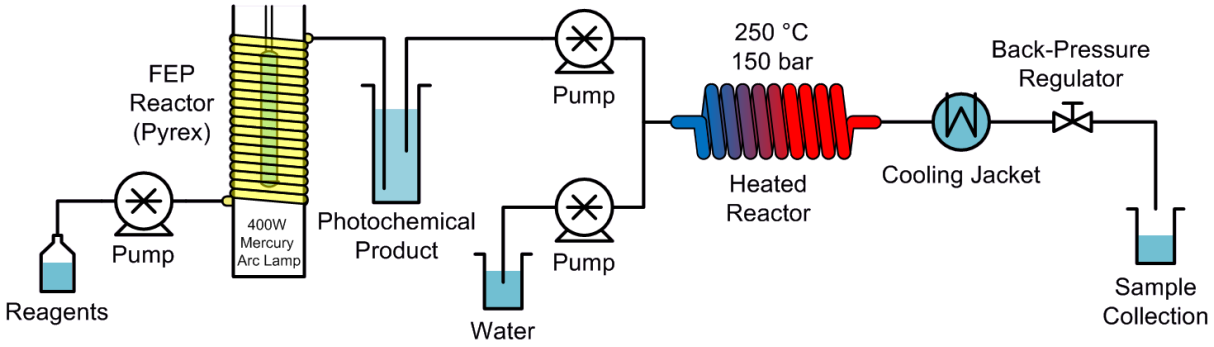


Figure 45 - A simplified schematic of the multi-reaction process used in this work, with a FEP tubular reactor followed by the high-temperature water reactor. Water was added after the photochemical step through pumping at the same flowrate as the photochemical step to create a 50%vol. solvent mixture. It should be noted there are a number of safety measures in place, including pressure and temperature trips, that have been omitted for simplicity. Produced by Rowena Howie and used with permission.

2.7.1. Benefits of modelling multi-step processes

As mentioned previously, the optimisation of a single step can lead to a decrease in the overall efficiency of the process. For example, using one solvent in the first stage may improve the yield of a single step, however may require the solvent to be swapped which requires additional energy and produces additional waste.[116,214]

Process models can be used to model the overall processes to understand interactions between different steps.[119,123,215] For example, a complete process model of the artemisinin process which has been used to reduce the E-factor values of the process by *ca.* 65%, from 65 to 22.5.[138]

2.8. Aims of reaction modelling

Considering the information presented above, there are a number of aims for the modelling of photochemical and high-temperature water reactions. A common aim for both sections is to ensure it is approachable from a typical chemist's point of view, such that the terms used are common terms used in chemistry rather than being chemical engineering focussed. The aims defined at the start of the reaction modelling part of the Thesis are laid out below, where the number is related to the Chapter in which they are addressed.

2.8.1. Aims of photochemical research section

Considering the discussion above, there were a number of aims set for the modelling of the photochemical reactions:

Aim 4.1 - Develop a process model of a photochemical reactor

Aim 4.2 - Use photochemical process model to understand photochemical reaction kinetics and compare outputs with experimental results

Aim 4.3 - Use kinetics to predict reactor performance of reactions for; unimolecular reactions, multi-component reactions with competing absorbances, photosensitised reactions and consecutive reactions

Aim 4.4 - Develop models of more complex photochemical reactors

Aim 4.5 - Use photochemical model in conjunction with the high-temperature water process model to predict performance of a daisy-chained process

2.8.2. Aims of HTW research section

Considering the discussion above, there were a number of aims set for the modelling of the high-temperature water reactions:

Aim 5.1 - Develop a process model for a high-temperature water reactor

Aim 5.2 - Use a high-temperature water process model to understand reaction kinetics and compare reactor performance prediction with experimental results

Aim 5.3 - Use kinetics to predict reactor performance for a variety of reactions

Aim 5.4 - Use a high-temperature water model in conjunction with the photochemical process model to predict performance of a daisy-chained process

Aim 5.5 - Optimise multi-step reaction process

2.8.3. Audience for modelling development

The main aim of the model development was so that the chemists within the laboratory can use a computational program to quickly understand and optimise reactions. One of the major differences the author found when developing the model was the different lexicon between chemistry and chemical engineering. One example of this is the use of "concentration"; chemists usually think of the units being $mol \cdot dm^{-3}$ whereas chemical engineering often considers this with $kg \cdot m^{-3}$. The difference in lexicon and units meant care was needed with using research from both fields within the model development.

3. Chemical process modelling and mathematical techniques

3.1. Chapter Overview

Within this chapter, the theories which govern the various modelling and mathematical techniques used throughout this Thesis are discussed. These techniques and ideas discussed are relevant across all of the different chapters, which is why this chapter is presented separately. Within this chapter, different modelling approaches are discussed, followed by methods and approaches typically used within the modelling of chemical processes. For the development of models, a practical point of view was taken rather than a theoretical approach, as the models were to be used to predict reactor performance rather than a purely theoretical approach.

The numerical methods for solving the equations used in process models are then discussed along with an introduction to Maximum Likelihood Estimation (MLE). The ideas and techniques behind model validation are then discussed, followed by sensitivity analysis. Finally, the specific numerical techniques used in this work are then introduced and briefly discussed.

The more specific points relevant to models of the pipes, photoreactors and high-temperature water reactors are discussed within each relevant chapter.

3.2. Introduction to process modelling

Chemical process models allow the user to understand an overall chemical transformation from the starting material to the product on a scale, typically, larger than the laboratory.[216] The modelling of a chemical process allows for the process to be optimised, monitored, and controlled safely. The simplest model for a chemical reaction could be considered as the typical Arrhenius equation, where the rate of formation of a product is calculated.[217] However, in real life situations the rate equations are often coupled to other processes such as mixing and heat transfer. The interaction of these processes also leads to the coupling of the equations which describe the processes.[218]

Traditionally, chemical processes were modelled using paper-based calculations.[219] More recently, with the development of increased computational power, chemical process models are often

modelled computationally. Using a computer allows for multiple equations to be solved simultaneously which would otherwise take a considerable amount of time manually.

"It is unworthy of excellent men to lose hours like slaves in the labour of calculation which could be safely relegated to anyone else if machines were used" – Gottfried Leibniz, 1685.[220]

The variety of processes that are observed in chemical reactors can lead to highly complex models. To overcome this, assumptions are often made to reduce the complexity and computational expense of calculation.

The process of modelling a chemical process covers four important aspects: [221]

- Model development;
- Parameter estimation using experimental data;
- Model validation; and
- Model predictions.

Before the different concepts behind process models are developed further it is also worth appreciating the idea that models are just descriptions of what is observed and should be taken as that, rather than an exact understanding of all processes.

"All models are wrong, but some are useful" – George Box, 1979.[222]

3.3. Modelling approaches

There are two general approaches for modelling of processes: empirical '*top down*' approach or the theoretical models built using first principles from the '*bottom up*'.[216]

3.3.1. Empirical models

Empirical models use observation and experimentation to develop relationships between process behaviours, considered to be a '*top down*' approach.[223] Empirical models are generally used when a correspondence between two or more variables has been observed within a process, with the relationship either too complex to understand, too complex to model or unnecessarily complex for the model needs.[224] The model can be developed through trial and error, computational approximation of analytic formula or could be a 'black-box' model that offers no understanding of the underlying process. These such models are often accurate at predicting outputs within the experimental space used to develop the model but can quickly become inaccurate outside of this experimental space.[224] An example of an empirical model is the Peng-Robinson equation of state described in Section 3.4.4.

3.3.2. First principle approach

The first-principles approach to process modelling is the opposite to empirical modelling, and typically uses physical principles to develop a model from the '*bottom up*'.[225] The use of first principles is hoped to be more robust across different conditions as they model the physical processes. However, they can also lead to inaccurate predictions as certain behaviours may not been considered within the model. There are generally two reasons why some behaviours are not considered in first-principle models: the behaviour being unexpected and hence overlooked or the behaviour being too complex to model, leading to expensive computational requirements.[226] The SAFT equation of state, described in Section 3.4.4, is considered a *bottom up* approach as it models the interaction between molecules to understand the behaviour.

3.3.3. Hybrid approach

The hybrid approach to process modelling uses a mixture of both first principles and experimentation to build an accurate model. The first principles allow for a greater understanding of the process while the use of experimentation allows for a greater accuracy for predicting experiments.[226] The hybrid

approach requires parameter estimation to predict parameter values such as activation energy or pre-exponential factor.[227] The parameter estimations will represent true values of the parameters if all behaviours observed have been accurately modelled. However, if some behaviours have not been accurately modelled, the estimated parameters may be inaccurate to their true definition, even though the parameters are valid within the context of the model and allow for predictive capabilities.[226]

3.4. Modelling of processes

As chemical engineering is a quantitative field, it requires accurate descriptions of, often, complex processes. There are a number of different types of equations that can be used to model the behaviours observed in chemical processes.[228]

3.4.1. Types of equations used in chemical engineering

There are a number of different types of equations used in modelling of chemical engineering processes, from simple algebraic equations to partial differential equations. A short introduction to differential equations is given below as the solving of them is key to model development.

Ordinary differential equations

Differential equations are used to model a variable that changes across the system. These equations form ordinary differential equations when all of the quantities are functions of a single independent variable. For example, the change in concentration of compound A, C_A, in a reactor system is described in Equation 25, where k is the kinetic constant.[229]

$$-\frac{dC_A}{dt} = kC_A \tag{25}$$

The solution to this equation gives the concentration-time profile of the reagent in the reactor which can be used to design an optimally shaped reactor.

Higher-order differential equations are also common with chemical reactor engineering, for example, to describe heat transfer within a pipe as shown in **Error! Reference source not found.** and defined in Equation 26. The temperature, T, depends on the radial position, r, and the heat transfer coefficient, k_{HT}, which is dependent on temperature. The solution to this equation gives the temperature profile across the pipe, which allows us to understand the heat loss to the surroundings.[77]

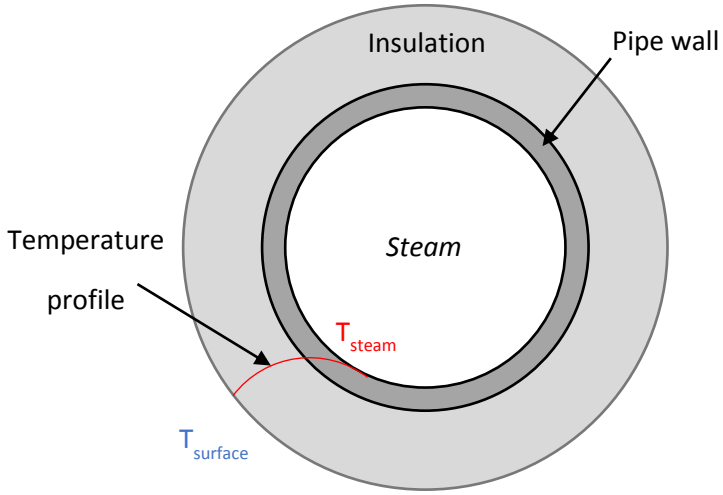


Figure 46 - A schematic of a steam pipe at temperature, T_{steam}, where the heat is transferred through the pipe wall and insulation, giving a temperature of $T_{surface}$. The differential equation describing this behaviour is shown below.

$$\frac{d}{dr}\left(k_{HT} r \frac{dT}{dr}\right) = 0 \tag{26}$$

Some differential equations can be solved analytically, by hand, however computers are often unable to carry out analytical solutions of differential equations and require numerical methods.[230] There are a number of methods for solving differential equations numerically, as shown Section 3.7, although higher-order differential equations can become computationally expensive. To solve the equations, the dependent variables at certain values of the independent variable needs to be defined, also known as *boundary conditions* for variables that change with directional coordinates, or *initial conditions* for variables that change with time. To be solved completely the number of boundary or initial conditions should be equal to the order of the differential equation.

The dimensions of the differential equations are then discretised into small distances for calculation, where the number of discretisation points chosen can have a considerable effect on the overall calculation, as shown in Section 3.4.2.

Partial differential equations

Equations that describe certain behaviours of systems are often functions of more than one independent variable. The equations can then be differentiated with respect to each independent variable and are known as partial differential equations and are indicated by a ∂. For example, molecular diffusion of a compound in a pipe can be in both the axial and radial directions, where D is the diffusion coefficient, as shown in Equation 27.[229]

$$\frac{\partial C}{\partial t} = D_{mol}\frac{\partial^2 C}{\partial z^2} + D_{mol}\frac{1}{r}\frac{\partial}{\partial r}\left(r\frac{\partial C}{\partial r}\right) \tag{27}$$

Integral equations

The differential equations described above and elsewhere in chemical engineering literature can be integrated, which leads to equations that describe the overall behaviour of the system. For example, the differential equation describing the reaction of compound A in Equation 28 is integrated, forming Equation 29 which describes the concentration of compound A with time, where $C_{A,0}$ is the initial concentration of A.[219]

$$\frac{dC_A}{dt} = -kC_A \tag{28}$$

$$\int \frac{dC_A}{dt} = -\int kC_A$$

$$\ln\frac{C_A}{C_{A,0}} = -kt;\ C_A = C_{A,0}exp^{-kt} \tag{29}$$

Often differential equations can be solved analytically, as above, forming algebraic or transcendental equations. However, analytical solutions are not always available, and a numerical approach is needed.

The modelling of chemical processes requires multiple differential equations that are coupled to each other, such as the temperature profile and rate of reaction. Equations that contain dependent variables that are functions of the same independent variable need to be solved simultaneously to describe the system in question.[231] PSE's software, gPROMS, contain numerical solvers which are considered world leading for solving multiple equations simultaneously.

3.4.2. Discretisation

With differential techniques there are generally two issues with computational methods: they often cannot calculate the analytical solution or sometimes analytical solutions do not exist. Discretisation involves separating the independent variable into discrete amounts so that the calculations can be made for each discrete point. At infinitesimally small separation, both the function and discretised solution are equal. However, infinitely small volumes are unable to be modelled computationally.[231]

In computational modelling the number of discretisation points are often known as the mesh size. The mesh size is ideally chosen so that the result is not significantly affected by changing the mesh size. The cells made from this mesh are assumed to be uniform in all variables relative to the differential equation being solved. Ideally, the size of an individual cell is small enough such that the calculation results do not change with further reducing the cell size. The size of the mesh should also be balanced with the computational time required, often simplified models can be used to check the sensitivity to the mesh before a full calculation is started.[232]

The idea of mesh size is illustrated in **Error! Reference source not found.**, with a single dimensional problem. Reactors often change across multiple dimensions, meaning problems can easily become computationally expensive.

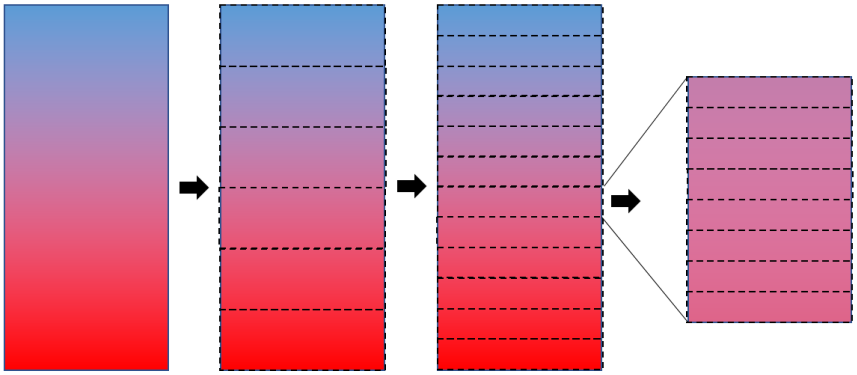


Figure 47 - A schematic of a temperature difference between a hot an cold side indicated by the colour. The dashed lines indicate different mesh sizes, with a decreasing mesh size showing how at a certain size the discretisation shows negligble difference across the mesh.

3.4.3. Coordinate systems

There are a number of different coordinate systems that can be used in the set-up of models. The most commonly found system is the Cartesian coordinate system with x, y and z axis that are pair-wise perpendicular to each other. Another relevant coordinate system is the cylindrical coordinate system that uses the radius ($\boldsymbol{r}$), polar angle ($\boldsymbol{\theta}$) and axial distance ($\boldsymbol{z}$) to define the position. Both the Cartesian and cylindrical coordinates are shown in **Error! Reference source not found.**.[233] The conversion between Cartesian and cylindrical coordinates is calculated as shown in Error! Reference source not found..[234]

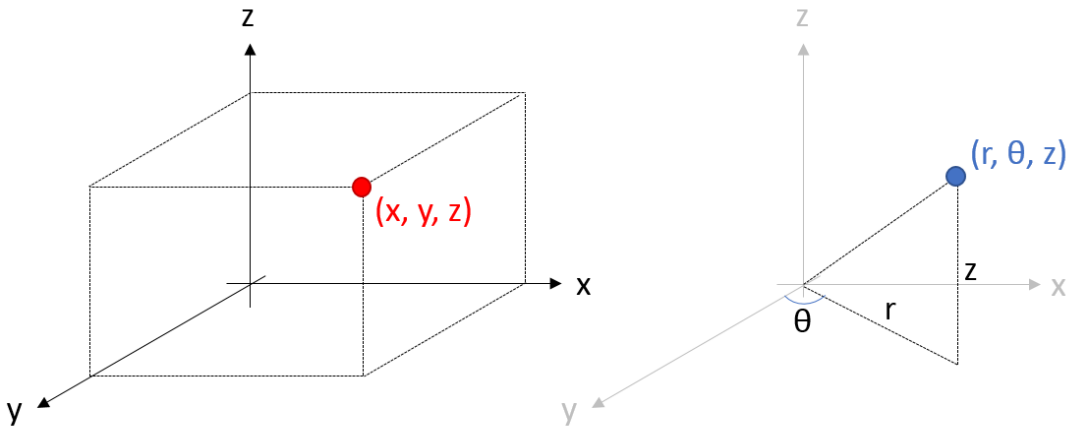


Figure 48 - A description of cartesian coordinates shown with (x,y,z) and cylindrical coordinates shown with (r, θ, z).

Table 16 – A table showing how to convert between cartesian and cylindrical coordinates.

		From	
		Cartesian	Cylindrical
To	Cartesian	$x = x$ $y = y$ $z = z$	$x = r\cos\theta$ $y = r\ \sin\theta$ $z = z$
	Cylindrical	$r = \sqrt{x^2 + y^2}$ $\theta = arctan\left(\frac{y}{x}\right)$ $z = z$	$r = r$ $\theta = \theta$ $z = z$

Laplacian

The Laplacian operator (∇^2) is a differential operator that gives the divergence of the gradient of Euclidean space. It is often used in the calculation of diffusion and has a useful form in both Cartesian and cylindrical coordinate systems. [233,235]

Laplacian in Cartesian coordinates

The Laplacian in a Cartesian coordinate system is the second derivative of each direction, as defined in Equation 30. [19]

$$\nabla^2 u = \frac{\partial^2 u}{\partial x^2} + \frac{\partial^2 u}{\partial y^2} + \frac{\partial^2 u}{\partial z^2} \tag{30}$$

Laplacian in cylindrical coordinates

The Laplacian in cylindrical coordinates is the second derivative of each direction as defined in Equation 31; with axisymmetric systems the final term for the angular derivation can be ignored. [19]

$$\nabla^2 u = \frac{\partial^2 u}{\partial z^2} + \frac{1}{r}\frac{\partial}{\partial r}\left(r\frac{\partial u}{\partial r}\right) + \frac{1}{\theta}\frac{\partial^2 u}{\partial \theta^2} \tag{31}$$

3.4.4. Physical properties

For the modelling of physical processes, an understanding of the physical properties of a fluid is needed. To simplify models, where the physical properties are not expected to change or have little

influence on the output, the properties can be assumed to be constant and defined by literature values at set conditions.[228]

However, a high proportion of processes, especially in the chemical and engineering industry can be affected by the physical properties. Physical properties also often change depending on localised conditions, such as the density of a fluid flowing through a heated pipe will change along the pipe.[236] The models developed need to consider these changes and a number of programs, known as Equations of State (EoS), have been developed to predict fluid properties.

Equations of state (EoS)

Equations of state (EoS) predict physical properties of fluids and fluid mixtures and have been developed from the ideal gas law. The ideal gas law, shown in Equation 32, could be considered the simplest EoS, where the pressure (p), volume (V), number of moles (n) and temperature (T) are all related using the ideal gas constant (R).[237]

$$pV = nRT \tag{32}$$

There are a number of assumptions for this model to be used; the collisions between the molecules and container are perfectly elastic, there are no intermolecular forces and the volume of the molecules is negligible compared to that of the container.

For most situations found in chemical processes, these assumptions are not valid, hence a number of EoSs have been developed to more accurately predict physical properties. They are generally split into two different approaches: *top-down* empirical relationships or *bottom-up* first principle approaches.

Cubic equation of states

One example of a model developed after the ideal gas law was published is the van der Waals equation of state (EoS) which has adapted the ideal gas law by adding terms for intermolecular forces (a) and molecular size (b), as shown in Equation 33.[238]

$$P = \frac{RT}{V - b} - \frac{a}{V^2} \tag{33}$$

The models based on this van der Waals EoS are often called 'cubic equation of states' as they can be rearranged into a cubic equation, shown in Equation 34, with the simplest example from the van der Waals equation.[239]

$$P = \frac{RT}{V-b} - \frac{a}{V^2} \quad \rightarrow \quad PV^2 = \frac{RTV^2}{V-b} - a \quad \rightarrow \quad pV^2(V-b) = RTV^2 - a(V-b)$$

$$\rightarrow PV^3 - (V^2P + RT)V^2 + aV - ab = 0 \tag{34}$$

This cubic equation can then be solved with known values for T_c, V_c and P_c, as at the critical point $\frac{\partial \mathrm{P}}{\partial \mathrm{T}}, \frac{\partial^2 P}{\partial \mathrm{T}^2} = 0$. This provides solutions for the parameters, a and b.

$$a = \frac{27R^2T_c^2}{64p_c}, \quad b = \frac{RT_c}{8p_c}$$

Peng Robinson Equation

The Peng Robinson (PR) equation has been shown to give accurate predictions of the volumetric behaviour for vapour-liquid equilibrium (VLE) calculations. By altering the attractive pressure term of the van der Waals equation so that the attractive energy parameter (a) becomes temperature dependent Peng and Robinson proposed an equation of the form as shown in Equation 65.[240]

$$P = \frac{RT}{v - \mathrm{b}} - \frac{a(T)}{(v+\mathrm{b}) + \mathrm{b}\cdot(v-\mathrm{b})} \tag{35}$$

The energy parameter, $a(T)$, is a function of temperature which at the critical point becomes a constant depending on T_c and P_c. At the critical point $\frac{\partial \mathrm{P}}{\partial V}, \frac{\partial^2 P}{\partial V^2} = 0$ which allows for the values of a and b to be calculated; by applying this to the PR equation the values become:

$$a(T_c) = 0.45724\frac{R^2T_c^2}{P_c}, \qquad b(T_c) = 0.07780\frac{RT_c}{P_c}, \qquad Z_c = 0.307$$

For temperatures other than the critical temperature the intermolecular energy parameter (a) is altered by a dimensionless scaling factor (ζ), which is a function of the reduced temperature (T_r) and the acentric factor (ω). The hard sphere parameter (b) is kept the same as at T_c as shown below.

$$a(T) = a(T_c)\,.\,\zeta(T_r, \omega), \quad b(T) = b(T_c)$$

$$T_r = \frac{T}{T_c}$$

An alteration to the Peng-Robinson EoS was made in 1978 to improve accuracy for mixtures for molecules with high acentric factors.[72] An *advanced* version (PR-A) was also used within this work where known values for liquid densities and vapour pressures are matched to literature values.

The advanced Peng-Robinson has a different scaling factor for the intermolecular energy parameter, as shown in Equation 36, where q_i is a term dependent on the acentric factor of the molecule (ω).

$$a(T_c) = 0.45724\frac{R^2T_c^2}{P_c}\left[1 + q_i\left(1 - \sqrt{T_r}\right)\right]^2 \tag{36}$$

$$\omega > 0.491, \quad q_i = 0.3796 + 1.485\omega - 0.1644\omega^2 + 0.01667\omega^3$$

$$\omega \leq 0.491, \quad q_i = 0.3746 + 1.542\omega - 0.2699\omega^2$$

Soave - Redlich - Kwong Equation

The Soave-Redlich-Kwong (SRK) equation is another cubic equation of state which is generally considered more accurate than the van der Waals equation. Originally the EoS was developed by Redlich and Kwong, with Soave providing an improvement, shown in Equation 37, that has become widely used.[241]

$$P = \frac{RT}{V - b} - \frac{a \cdot \zeta}{V(V + b)} \tag{37}$$

The values for both a and b can be calculated from the critical temperatures as before and are shown below, where ω is the acentric factor which is a measure of the *non-centricity* of a molecule.

$$\zeta = \left((1 + (0.480 + 1.574\omega - 0.176\omega^2)\left(1 - \sqrt{T_r}\right)\right)^2, \quad a = 0.42748\,\frac{R^2T_c^2}{P_c}, \quad b = 0.08664\,\frac{RT_c}{P_c}$$

First principles EoS

The previously introduced cubic EoS are often considered 'top-down' approaches as they have been developed from fitting equations to experimental data. More recent developments in EoS have attempted to take a '*bottom up'* approach, where the interactions between molecules give rise to the overall physical properties of the fluid.[242]

Statistical associating fluid theory

The Statistical Associating Fluid Theory (SAFT) EoS approach is a *bottom up* approach as it uses a statistical approach to predicting vapour-liquid equilibrium behaviour of mixtures through describing the interactions between components. This method has become more popular in recent years due to increased computational power at a relatively low price. This approach is based on the first-order perturbation theory of Wertheim.[243–246] With perturbation theory, the potential energy of a relative complex molecular fluid is described as the sum of the potential energy of a simple reference fluid and a perturbation term. One advantage of using a SAFT approach is that a limited number of parameters are needed for relatively accurate predicitons.[242]

SAFT was initially developed to estimate the Helmholtz free energy, a measure of the useful obtainable work from a closed thermodynamic system, by estimating the interactions between all the species. SAFT incorporates four distinct terms; the hard-sphere repulsive interactions, chain formation from covalent bonding between hard spheres, an associative term and a dispersion term. **Error! Reference source not found.** shows a schematic representation of the SAFT model.[242]

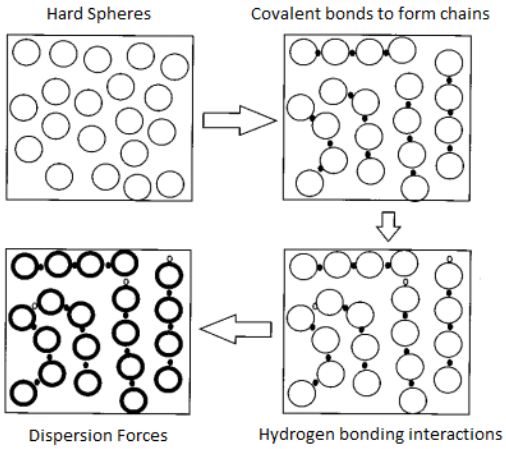


Figure 49 – Schematic representation of the physical basis of the SAFT model. The Helmholtz free energy is calculated for the hard spheres before terms to calculate the addition of covalent bonds, hydrogen bonding and dispersion forces are added.[242]

Mathematically, SAFT is defined in Equation 38 for the residual Helmholtz free energy per mole (h):

$$\frac{h^{res}(T,\rho)}{RT} = \frac{h^{hs}(T,\rho)}{RT} + \frac{h^{chain}(T,\rho)}{RT} + \frac{h^{assoc}(T,\rho)}{RT} + \frac{h^{disp}(T,\rho)}{RT} \quad (38)$$

gPROMS-proprietary SAFT EoS

gSAFT is the physical properties package utilised by Process Systems Enterprise, the sponsor of my studentship, and is an optional extra for the gPROMS process builder software.[84] There are currently two options available with gSAFT; SAFT-VR SW and SAFT-γ Mie. SAFT-VR SW uses attractive potentials of a variable range and takes the whole molecule as a shape with a certain polarity. SAFT-γ Mie is a group contribution model which assesses contributions from different functional groups within the molecule. The latter often gives more accurate results but is also more computationally expensive; another advantage of SAFT-γ Mie is that properties can often be predicted for mixtures with limited experimental data due to the consideration of functional groups rather than complete molecules.

Binary interaction parameters

Binary Interaction Parameters (BIP) are factors that are often used within EoSs to increase the accuracy of physical property predictions when two fluids are mixed.[247] The simplest BIPs account for deviations in predictions from simple mixing rules and have since been calculated using experimental data for a large number of binary mixtures.[248] There have been some generalised BIP correlations

developed, particularly by Gao et al., for cubic EoSs with mixtures containing CO_2, N_2 and H_2.[249] The BIPs used in this work came from the INFOBIPS data set, derived from the Dechema Chemistry Data Series.[250]

Transport properties

Typical EoSs are not able to predict physical properties such as viscosity or thermal conductivity for fluids.[251,252] Viscosity is an important variable in the prediction of physical processes, especially for understanding flow and pressure drop and the thermal conductivity is essential for understanding heat transfer within fluids. There have been a number of secondary methods developed to predict these properties using properties predicted by EoSs. The most common methods used in the industry are outlined below.

Viscosity

superTRAPP model

The superTRAPP algorithm is a function of density and was developed by NIST for predicting viscosity for non-polar hydrocarbon that are consistent over a wide range of conditions, using propane as a reference fluid.[253] It is an extended corresponding states model and is one of the most versatile and well-known algorithms for transport properties. The corresponding states theorem indicates that all fluids when compared at the same reduced temperature and reduced pressure have approximately the same compressibility factor.[236]

Pedersen model

The Pederesen algorithm is a predictive corresponding states model originally developed for oil and gas systems.[254] It is based on accurate correlations for the viscosity and density of the reference fluid, methane.

Lohrenz-Bray-Clarke (LBC) model

The LBC model is a predictive model which relates gas and liquid densities to a fourth-degree polynomial in reduced density.[255] The reduced densities are calculated initially by the EoS rather than the original correlations provided by Lohrenz.

Thermal conductivity

superTRAPP method

The superTRAPP method uses propane as a reference fluid and is applicable to both liquid and gas phases.[253] It is an extended corresponding states model where the thermal conductivity is defined as the sum of the internal and translational contributions.

3.5. Computational Fluid Dynamics

Within the photochemical reactor model development, the process models developed were often compared with Computational Fluid Dynamic (CFD) models developed by a colleague. CFD aims to solve the Navier-Stokes equations, which are discussed in Section 3.6.3, and give an understanding of how a fluid moves depending on the forces, physical properties and size of container.[256] CFD calculations are often highly computationally expensive due to the small mesh size used and number of equations that need to be balanced.[257,258]

Comparisons are made between the process models, which are less computationally expensive, and CFD predictions throughout this work to show the validity of both methods, especially for reactors with complex flow behaviour.[259]

3.6. Conservation equations

Conservation equations are used to balance equations within process modelling. The conservation equations are developed from a simple idea that a quantity entering into a system must leave the system, get used up or be generated by the system.[219] The relationships between these is simple and is explained below along with an equation to codify the relationships:

- The streams entering the system cause an increase of the substance in the system
- The streams leaving the system reduce the amount of the substance in the system
- The generation or consumption mechanisms, chemical reactions for example, can either increase or decrease the amount of substance in the system
- The remaining amount is what is left in the system

$$Accumulation = In - Out + Generation - Consumption$$

For chemical processes there are generally three equations that need to be balanced within a process model:

- Mass balance;
- Energy balance; and
- Momentum balance.

The balancing of these equations comes from thermodynamic principles. The equations used within each are decided within the development of the model. Some factors can be ignored if they are deemed either too complex or assumed to have negligible effect, with the model developer making these choices.[218]

3.6.1. Mass balance

The mass balance is derived from the law of the conservation of mass which states there is no generation of mass within a system.[219] This law creates a mass balance, shown in Equation 39, where M_{in} is the total mass into a system, M_{out} is the total mass leaving a system and $M_{accumulated}$ is the accumulated mass within a system.

$$M_{in} - M_{out} = M_{accumulated} \quad (39)$$

The conservation of mass applies to the total amount of mass within the system but does not apply to individual components within a system. For example, with chemical reactions, an input component

can be changed into a different component. The overall generation of mass, $\dot{m}_{gen}$, is equal to zero, whereas the generation of mass of a component i, $\dot{m}_{gen,i}$, does not necessarily have to be equal to zero. However, the total of all components is equal to zero, as shown in Equation 40.

$$\dot{m}_{gen} = \sum_{i=1}^{n} \dot{m}_{gen,i} = 0 \tag{40}$$

Diffusion

Diffusion is a second order relationship regarding the change in concentration of a compound and is often described using Fick's second law, defined in Equation 41, for the z dimension, where D is the diffusion coefficient.[260]

$$\frac{dC}{dt} = D\frac{\partial^2 y}{\partial z^2} \tag{41}$$

The direction of diffusion can be both parallel and perpendicular to the flow of a reactor. This would depend on the shape of the reactor, and can have an effect on the output of a chemical reactor.[219]

3.6.2. Energy balance

The energy balance is derived from the law of the conservation of energy which states there is no generation of energy within a system.[219] This law creates an energy balance, shown in Equation 42, where E_{in} is the total energy into a system, E_{out} is the total energy leaving a system and $E_{accumulated}$ is the accumulated energy within a system.

$$E_{in} - E_{out} = E_{accumulated} \tag{42}$$

There can be a range of types of energy that are typically found within chemical processes, such as:

- Kinetic energy if the system is moving;
- Potential energy, such as gravitational potential energy, if the system is moving upwards;
- Heat could enter the system via conduction, convection or radiation; and
- Work could be done on, or, by the system.

Adiabatic

An adiabatic system means no heat is gained or lost within the system. Assuming a system is adiabatic can simplify a model by removing the energy balance equation. Adiabatic assumptions can be used if the system is assumed to be a constant temperature.[261]

Heat transfer to surroundings

Different theories have been developed to model heat transfer into a fluid from its surroundings. Prandtl's theory for convective heat transfer uses a boundary layer in which all the resistance to heat transfer is located.[77] The rate of convective heat transfer, $\dot{Q}$, is defined in Equation 43, where k_{HT} is the heat transfer coefficient, A is the surface area of heat transfer, T_2 is the temperature of the surrounding fluid and T_1 is the temperature of the solid surface. The values of k_{HT} have been measured in a wide range of situations within literature and are used to calculate heat transfer.

$$\dot{Q} = -k_{HT}A(T_2 - T_1) \tag{43}$$

Constant energy flux

The constant heat flux assumes a known rate of energy is inputted into the system at the wall, using a Neumann boundary condition.[262] This can be used for electrical heaters where a known rate of energy is being produced, but the temperature is not directly known.

Constant temperature at system boundary

A constant temperature can also be defined within a model, using a Dirichlet boundary condition.[262] This can be used instead of a constant heat flux and is often used when a heater has been set to a defined temperature

Photochemical energy

Energy can also enter a system through the introduction of light, which can then be used to promote reactions. The equations used to describe the introduction of light energy to a system are presented

in Chapter 2 and 0 as they are generally less well understood than the thermal equations presented above.

3.6.3. Momentum balance

As momentum is equal to mass times velocity and hence is related to both the mass and energy balances and comes from Newton's second law of motion.[263] The conservation of linear momentum is defined in Equation 44, assuming a constant density, where m is the mass of the fluid, v is the fluid velocity and F_{sys} is the force balance for the system.

$$\frac{d}{dt}(mv) = \sum F_{sys} \tag{44}$$

Navier-Stokes equations

The Navier-Stokes equations describe the movement of viscous fluids and are derived from applying Newton's second law of motion to fluids. The Navier-Stokes equations are applicable to a wide range of scientific and engineering principles; from weather forecasting to fluid flow in a pipe. Assumptions are often made to simplify the equations as they can become complex, for example, there may not always be a solution for three-dimensional problems. Proving there are always solutions for three dimensions is a 'Millenium Prize Problem', with an award of $1 million.[264] One of the most-common simplifying assumptions is assuming the fluid is incompressible.

Incompressible fluid

A fluid is often considered incompressible when the effect of pressure on the fluid density is negligible.[265] It is often assumed that most liquids are incompressible, whereas gases can become compressible at heightened velocity. The compressibility of different fluids can be measured by the compressibility factor.

The simplified incompressible Navier-Stokes equation is shown in Equation 45 where $\mathbf{u}$ is the flow velocity, t is time, μ is the dynamic viscosity, ρ_0 is the initial density, w is the specific thermodynamic work carried out on the system and $\mathbf{g}$ is an external source of stress, such as gravity.

$$\frac{\partial \mathbf{u}}{\partial t} + (\mathbf{u} \cdot \nabla)\mathbf{u} - \frac{\mu}{\rho_0} \nabla^2 \mathbf{u} = -\nabla w + \mathbf{g} \tag{45}$$

Pressure drop

A major issue with large scale pipelines is the pressure drop along the length of the pipe.[266] Resistive interactions between the fluid and the pipe lead to frictional forces being developed, causing a pressure drop between two points. The relationship between the fluid and pipe properties is known as the Darcy-Weisbach equation, defined previously in Equation 5, where p = pressure, L= Length of pipe (m), f_D= Darcy friction factor, ρ = density (kgm^{-3}), $\langle v \rangle$ = mean flow velocity (ms^{-1}) and D_H = Diameter (m).[88]

$$\frac{dp}{dz} = f_D \frac{\rho}{2} \frac{\langle v \rangle^2}{D_H} \tag{5}$$

The two major contributing factors for pressure drop are the fluid velocity and viscosity, which are both used to calculate the Darcy friction factor. Pressure drop is proportional to the shear force within the system meaning an increased flow rate will cause a higher pressure drop.

Reynolds Number

The Reynolds number is the ratio between the inertial forces and viscous forces within a fluid and can be used to determine the difference between laminar and turbulent flow.[267] The Reynolds number (Re) is calculated as shown in Equation 46 where ρ = density (kgm^{-3}), u = velocity of the fluid (ms^{-1}), L = linear length (m), μ = dynamic viscosity of the fluid (Pa·s, N·s m^{-2}, kg·m^{-1}s^{-1}), ν = kinematic viscosity of the fluid (m^{2}s^{-1}).

$$Re = \frac{inertial\ forces}{viscous\ forces} = \frac{\rho u L}{\mu} = \frac{uL}{\nu} \tag{46}$$

A fluid flowing with a small Reynolds number (Re < 2100) means that viscous forces dominate and are the main mechanism of energy dissipation, this is described as Laminar flow. A high Reynolds (Re > 4000) number means the viscous forces are negligible and the flow is described as turbulent.[265]

Friction factor

The measure of the interaction between the fluid and pipe surface, which is used to calculate the friction losses with pipe flow, is known as the friction factor. There are two widely known friction factors; Darcy friction factor (f_D) or Fanning friction factor (f_F). The Darcy friction factor is derived from 'Moody charts', which plot experimental values for pipes, whereas the Fanning friction factor is a direct ratio between the local shear stress and the local kinetic energy density.[268] The Fanning friction factor (f_F) is calculated as shown in Equation 47 where τ = local shear stress (kg·s·m^{-2}), ρ is the density (kg·m^{-3}) and u is the bulk flow velocity (ms^{-1}). It should be noted that the Fanning friction factor is 1/4th of the Darcy friction factor so care should be taken with use.

$$f_F = \frac{\tau}{\rho \frac{u^2}{2}} = \frac{2\tau}{\rho u^2} \tag{47}$$

Friction factor with laminar flow in a circular pipe

For laminar flow where there is no mixing perpendicular to the direction of flow the Darcy friction factor is a very simple relationship between itself and the Reynolds number as shown in Equation 48.[269]

$$f_D = \frac{64}{Re} \tag{48}$$

Friction factor from Colebrook Equation

The frictional factor can be calculated from experimental data and the corresponding tables formulated for them. Before Colebrook there were separate approximations for different regions of Reynolds number that corresponded well to the experimental data. For example, the limiting Prandtl equation for fully smooth pipes is defined in Equation 49. [52]

$$\frac{1}{\sqrt{f_D}} = 2\log\left(\frac{Re\sqrt{f_D}}{2.51}\right) \tag{49}$$

Another valid limiting relationship was the von Karman relationship for a fully rough surface, defined in Equation 50.[270]

$$\frac{1}{\sqrt{f_D}} = 2\log\left(\frac{3.7\ D_H}{\varepsilon}\right) \tag{50}$$

Colebrook neatly combined those expressions for Re = 4000 to 10^8 to form the Colebrook-White Equation as defined previously in Equation 51.[271]

$$\frac{1}{\sqrt{f_D}} = -2\log\left[\frac{\epsilon}{3.7\ D_h} + \frac{2.51}{Re\sqrt{f_D}}\right] \tag{51}$$

The Colebrook equation shows the relationship between the Darcy friction factor (f_D), the roughness of the pipe wall (ϵ) and hydraulic diameter D_H.

Friction factor from Haaland Equation

As the Colebrook equation is implicit for f_D, the solution can only be found graphically or iteratively which is computationally expensive. There were a number of approximations added that reduce the computational time, which is especially useful for large scale systems. Haaland used Colebrook's approximation of the Prandtl formula and the von Karman relationship to form an equation explicit in f_D, known as the Haaland Equation, defined previously in Equation 6.[90]

$$\frac{1}{\sqrt{f_D}} = -1.8\log\left[\left(\frac{1}{3.7}\frac{\epsilon}{D_H}\right)^{1.11} + \frac{6.9}{Re}\right] \tag{6}$$

Although Haaland used an approximation for the smooth pipe limiting factor, the error of this approximation is within the error of the data used to calculate the Colebrook equation and is therefore comparable.[272]

Velocity profiles in different systems

The velocity profiles are calculated by solving the momentum conservation equations through balancing the pressure and viscous forces (assuming no potential forces such as gravity).

Velocity profile in a pipe

For laminar flow, the velocity profile as a function of radial position, $u(r)$, of a fluid is defined in Equation 52, where R is the radius of the pipe, μ is the dynamic viscosity and $\frac{dP}{dz}$ is the pressure drop of the fluid.[88,265]

$$u(r) = \frac{R^2}{4\mu}\frac{dP}{dz}\left(1 - \frac{r^2}{R^2}\right) \tag{52}$$

Velocity profile in an annular reactor

For an annular gap, the velocity profile as a function of radial position, is defined in Equation 53, where R is the outer diameter and R_{inner} is the internal diameter.[262]

$$u(r) = \frac{1}{4\mu}\frac{dP}{dz}\left((R^2 - r^2) - (R^2 - r^2)\frac{\ln\left({}^{R}/_{r}\right)}{\ln\left({}^{R}/_{R_{inner}}\right)}\right) \tag{53}$$

3.6.4. Dynamic vs steady state

Steady state modelling of chemical processes performs mass and energy balances across stationary processes that are not time dependent. Dynamic simulations are more computationally expensive as they perform mass and energy balances at each time point.[231] The advent of dynamic simulation has allowed for processes to be modelled online as well as investigating how effects such as a drop in temperature or pressure can affect the outputs.[273,274]

3.7. Solving differential equations numerically

The equations defined to model the behaviour of a system need to be solved computationally. The equations are often solved numerically as there are often complex derivatives that are also coupled to each other. For differential equations that cannot be solved analytically, a numerical solution can be used to approximate the functions through discretisation and subsequent calculations. A number of different methods can be used to solve differential equations, with two of the most well-known presented here to give understanding.[228]

3.7.1. Approaches for solving for differential equations

There are generally three different methods for calculating the derivative: forward facing, backward facing and central difference, these are illustrated in **Error! Reference source not found.**.[228] **Error! Reference source not found.** shows the method chosen for the estimation can produce different results.

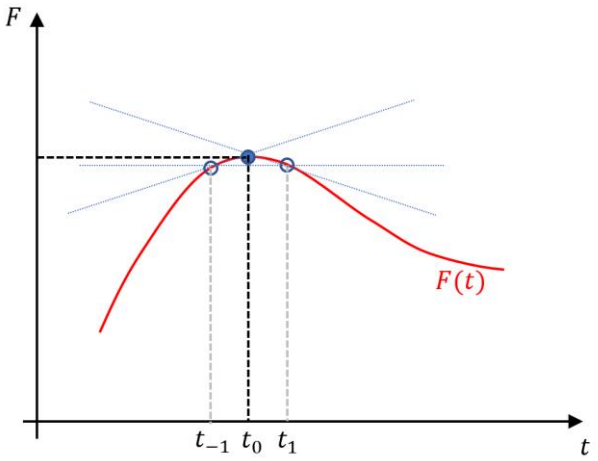


Figure 50 - A schematic to illustrate how differential equations can be solved numerically, where the gradient a function F(t) at a point is calculated by perturbing the function either backwards or forwards, as described below.

Forward facing

Forward facing methods solve differential equations using the current value (F_0, t_0) and future data value (F_1, t_1).and are often used in single-step predictor-corrector methods, as defined in Equation 54.

$$\frac{dF_0}{dt} \approx \frac{F_1 - F_0}{t_1 - t_0} \tag{54}$$

Backwards facing

The backwards facing methods solve differential equation by using the current value (F_0, t_0) and previous data value (F_{-1}, t_{-1}), as defined in Equation 55. Backwards-facing methods are common as often future data are not yet available and need to be predicted.

$$\frac{dF_0}{dt} \approx \frac{F_0 - F_{-1}}{t_0 - t_{-1}} \tag{55}$$

Central difference

For the central-difference method, the differential equation is calculated between the future value (F_1, t_1) and previous data value (F_{-1}, t_{-1}), as defined in Equation 56. The central difference method gives a more accurate approximation of the derivative compared to the forward and backward differences, but again relies on future values which is not always feasible.

$$\frac{dF_0}{dt} \approx \frac{F_1 - F_{-1}}{t_1 - t_{-1}} \tag{56}$$

3.7.2. Truncation errors

Truncation errors in a numerical method are the error caused from using simple approximations to represent exact mathematical formulas.[275] There are no truncation errors when exact solutions are used. However, with numerical methods the truncation error can reduced by either reducing the step size or using a better approximation. Using these two approaches to reduce the truncation error can, however, lead to an increased computational expense. The truncation error of different methods can be estimated and is usually split into either a local or global truncation error.

The local truncation error is the difference between the estimated value and the exact value at a certain point, whereas the global truncation error is the sum of all the local truncation errors over all iterations.[232]

3.7.3. Runge-Kutta methods

The Runge-Kutta methods are a group of both implicit and explicit iterative methods for the approximation of ordinary differential equations.[276,277] The theory behind the Runge-Kutta methods is that a differential function can be solved by examining the local gradient of a point and using that information to estimate either a previous or subsequent point. Euler's method is considered the simplest algorithm of the Runge-Kutta class and is outline below.[278] More complex algorithms such as

the ‘classic Runge-Kutta method’ use higher order approximations, where multiple points are used in the calculations.[279]

Euler’s forward method

Euler’s method solves first-order-first-degree differential equations that have initial conditions defined and is the simplest Runge-Kutta method.[278] The method is described in Equation 57 where Δt is the step size and F_n is a general function.

$$F'(t) = f\big(t, F(t)\big), F(t_0) = F_0 \tag{57}$$

Choosing a value for Δt where $t_n = t_0 + n\Delta t$, with one step of the Euler method from t_n to $t_{n+1} = t_n + \Delta t$ is:

$$F_{n+1} = F_n + \Delta t f(t_n, F_n)$$

Example of Euler’s forward method

An example of the results of Euler’s forward method are shown for Equation 58, where different step sizes have been used to estimate the solution and compared to the exact solution. The solutions for different step sizes and the exact solution are shown in **Error! Reference source not found.**, with the decreasing step size leading to a much closer solution.

$$\frac{dy}{dt} = y, y = e^t \tag{58}$$

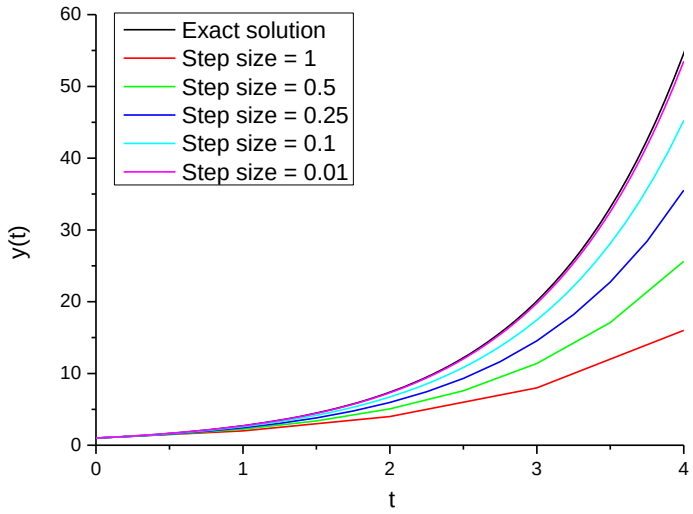


Figure 51 - Illustration of the accuracy of Euler's method using different step sizes to estimate the function $\frac{dy}{dt} = y$, showing the difference between the exact solution and Euler's estimated values using different step sizes.

In **Error! Reference source not found.**, the true error has been calculated for each of the estimations by comparing the value to the analytical solution, $y = 54.598$. The error is approximately halved when the step size is halved. The local truncation error is therefore assumed to be proportional to the step size.

Table 17 – A comparison of the values for the estimation of $\frac{dy}{dt} = y$ when t = 4, with the true error calculated by subtract ting the estimated value from the analytical solution, showing a decrease in error with decreasing step size.

Step size	$y(4)$	True error
1	16	38.60
0.5	25.63	28.97
0.25	35.53	19.07
0.1	45.26	9.338
0.01	53.52	1.078

Euler's backwards method

The derivation of Euler's backwards method is similar to the forward method but uses the previous point to estimate the next value instead, as shown in Equation 59.

$$F'(t) = f\big(t, F(t)\big), F(t_0) = F_0 \tag{59}$$

$$F_{n+1} = F_n + \Delta t f(t_{n+1}, F_{n+1})$$

The solution is implicit as the new approximation F_{n+1} appears on both sides of the equation. As the equation is implicit, solving the equation is more complex than the forward Euler method. Implicit equations can be solved using a number of different methods, such as fixed-point iteration or Newton's method.[231]

3.7.4. Newton's method

Newton's method is an algorithm that finds the roots of algebraic equations. In its simplest form the function can be a single variable function, but more complex functions can be solved using the same principles.[275] The principle of Newton's method is explained below through the use of an example.

Example of Newton's method

To find a root of a simple one-variable function, $F(x)$, the tangent of the function is calculated at an initial starting point, x_0, using calculus, and illustrated in **Error! Reference source not found.**. The assumption is that the approximation can be improved using Equation 60.

$$x_1 = x_0 - \frac{F(x_0)}{F'(x_0)} \tag{60}$$

This process is then be repeated, until an acceptable accuracy tolerance limit is reached, and is represented by a more general formula shown in Equation 61.

$$x_{n+1} = x_n - \frac{F(x_n)}{F'(x_n)} \tag{61}$$

This process can also be shown geometrically, as shown in **Error! Reference source not found.**. The tangent at the initial point, x_0, is calculated with the x-intercept of this initial tangent, x_1, calculated. The tangent of the function at x_1 is calculated, with the process of finding the x-intercept repeated until a minimal difference is observed between the x-intercept and the function's x value. This method of calculation can be used for more complex functions with multiple variables and system of equations.

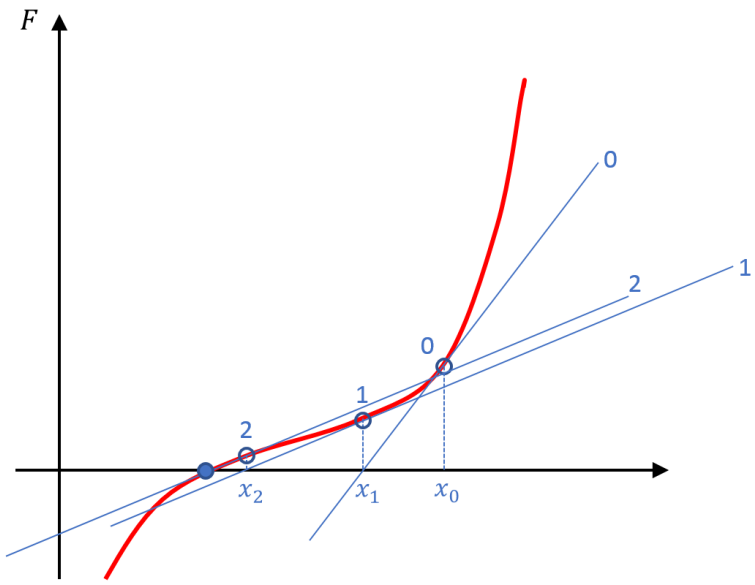


Figure 52 – An illustration of Newton's method for finding the root of a function. An initial point is taken, where the gradient is estimated, this gradient is then extrapolated to the axis before the function is calculated at this axis intercept. This process is repeated until the difference between consecutive estimated axis intercepts is considered to be negligible.

3.8. Parameter estimation

Parameter estimation is the process of using observations of a dynamic system to develop more accurate mathematical models that describe the system characteristics.[280] An initial model, with a set number of parameters, is developed to mimic the system in question. A number of different techniques are able to estimate the parameters of the model. Fundamentally, the approach is based on least-squares minimisation between the model response and the system response.

The different algorithms follow a similar path for estimating the parameters; an initial parameter value is guessed, and the model output calculated and compared to experimental values. After this, a new parameter value is calculated, and the model output is calculated and compared to experimental values. This process is calculated until the difference between the model output and measurements are minimal. A simplified diagram describing the parameter estimation process is shown in **Error! Reference source not found.**.[280]

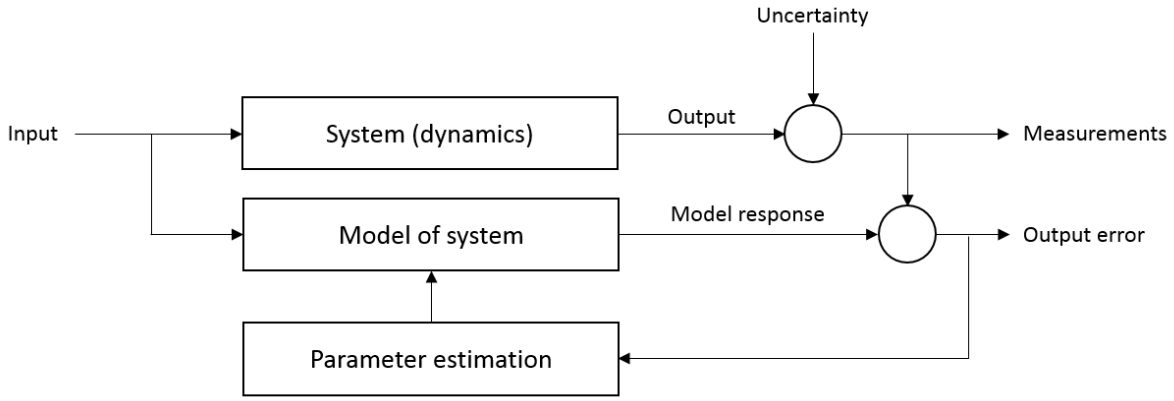


Figure 53 – A schematic explaining the process of parameter estimation, where experiments are inputted into the model before the output is analysed and the parameter estimate adjusted to improve the model. This process is repeated until the error reaches an acceptable difference.[280]

Parameter estimation is an empirical approach and hence the validity of the estimated parameters should always be checked by the operator. For example, an estimated kinetic parameter could become negative to indicate the reversal of a reaction to fit the data but is not a physically valid value. The estimation of unrealistic values can be avoided through setting parameter value boundaries.

3.8.1. Parameter estimation methods

Measurements used in parameter estimation contain uncertainty due to measurement noise and environmental noise. Before parameter estimation is carried out there are a number of processes that can be carried out to aid with the estimation:

- Understanding the uncertainty in the measuring instrument;
- A prior understanding of the statistics associated with the observation matrix;
- Knowing the range of the sensor's measurement signal and typical range of parameter values;
- Pre-processing of measurements; and
- Removing outliers from the measurements.[280]

Maximum likelihood estimation

Maximum likelihood estimation (MLE) is a method used to estimate the value of parameters for a model, such that the parameter values maximise the likelihood that the process described by the model produces the data that is observed. The likelihood that the model describes the observations is plotted as a function of parameter values, known as the likelihood function, which is then maximised. The approach of using prior 'beliefs' that are updated with observations derives from Bayesian statistics.[281–283]

Bayesian Statistics

Bayesian statistics is a statistical approach that aims to explain observed events with degrees of belief behind said event. This contrasts from Frequentist statistics that approaches the probability of an event occurring from the frequency of an event occurring.[284] The Bayesian probability approach assumes an event happens and then looks at the likelihood that a certain function explains this. Bayesian statistics allows for the use of measurement errors as Bayes Rule, defined in Equation 62, allows you to calculate the actual probability of an event given the measured test probability, as shown below, where $P(A \mid B)$ is a conditional probability of the likelihood A has occurred given that B is true.

$$P(A|B) = \frac{P(B \mid A)P(A)}{P(B)} \tag{62}$$

MLE method

The estimated parameter values obtained by MLE are those values which maximise the likelihood function (Equation 63) with the probability density equal to the likelihood function at the parameter values. This approach is taken as it is less computationally expensive compared to calculating the full probability density. The different stages of MLE are explained below: [285]

$$P(\Theta \mid y, I) = \frac{P(y \mid I, \Theta)P(\Theta \mid I)}{P(y \mid I)}$$

- Prior probability function tells us what is known about the parameters *before* any data $P(\Theta|I)$

- Likelihood probability density function tells us how well the data *fits* the model $P(y|\, I, \Theta)$
- Posterior probability density function tells us the probability density function *after* the data is analysed. $P(\Theta|y, I)$
- Evidence is the trust in the data: $P(y|I)$ usually marginalised through using:

$$P(y|I) \;=\; \int P(y|I,\Theta)\; P(\Theta|I)\; d\Theta$$

By solving the maximum likelihood parameter estimation, MLE determines values for the model parameters (Θ) that maximise the probability that the mathematical model will predict the measured values. The algorithm assumes independent, normally distributed measurement errors (ε_{ijk}), with zero means and standard deviations (σ_{ijk}), with a maximum likelihood objective function (J) as follows, where the equation parameters are defined in **Error! Reference source not found.**:

$$J = \frac{N}{2}\ln(2\pi) + \frac{1}{2}\; min_{\Theta}\left\{\sum_{i=1}^{NE}\sum_{j=1}^{NV_i}\sum_{k=1}^{NM_{ij}}\left[\ln\left(\sigma_{ijk}^2\right) + \frac{\left(\check{z}_{ijk} - z_{ijk}\right)^2}{\sigma_{ijk}^2}\right]\right\} \tag{63}$$

Table 18 - The definition of the parameters used within the Maximum Likelihood Estimation method.

Term	Definition
$\boldsymbol{N}$	Total number of measurements taken during all the experiments
$\boldsymbol{\Theta}$	Set of model parameters to be estimated
$\boldsymbol{NE}$	Number of experiments performed
$\boldsymbol{NV_i}$	Number of variables measured in the ith experiment
$\boldsymbol{NM_{ij}}$	Number of measurements of the jth variable in the ith experiment
$\boldsymbol{\sigma_{ijk}^2}$	Variance of the kth measurement of variable j in experiment i – determined by the variables defined variance model
$\boldsymbol{\check{z}_{ijk}}$	k^{th} measured value of variable j in experiment i
$\boldsymbol{z_{ijk}}$	k^{th} (model-)predicted value of variable j in experiment i

Once the initial estimation is computed, the measured response and estimated response are compared with the response error used to compute the objective function, J. The first and second derivatives are then calculated using Equation 64, where Θ is the estimated parameters at iteration i where $\nabla_{\Theta}^2 J(\Theta)$ and $\nabla_{\Theta} J(\Theta)$ are the first and second gradients of the objective function.

$$\Theta_{i+1} = \Theta_i + [\nabla_{\Theta}^2 J(\Theta)]^{-1}[\nabla_{\Theta} J(\Theta)] \tag{64}$$

The second derivative of the objective function, $\nabla^2_\theta J(\Theta)$ is estimated, using a Gauss-Newton method, and is known as the Fisher information matrix. The Fisher information matrix provides a measure of the relative accuracy of the estimated parameters. The inverse of the Fisher information matrix gives the variance and covariances between parameters.[280] A schematic of the MLE algorithm is shown in **Error! Reference source not found.**, where the algorithm continues until pre-defined convergence limits are matched.

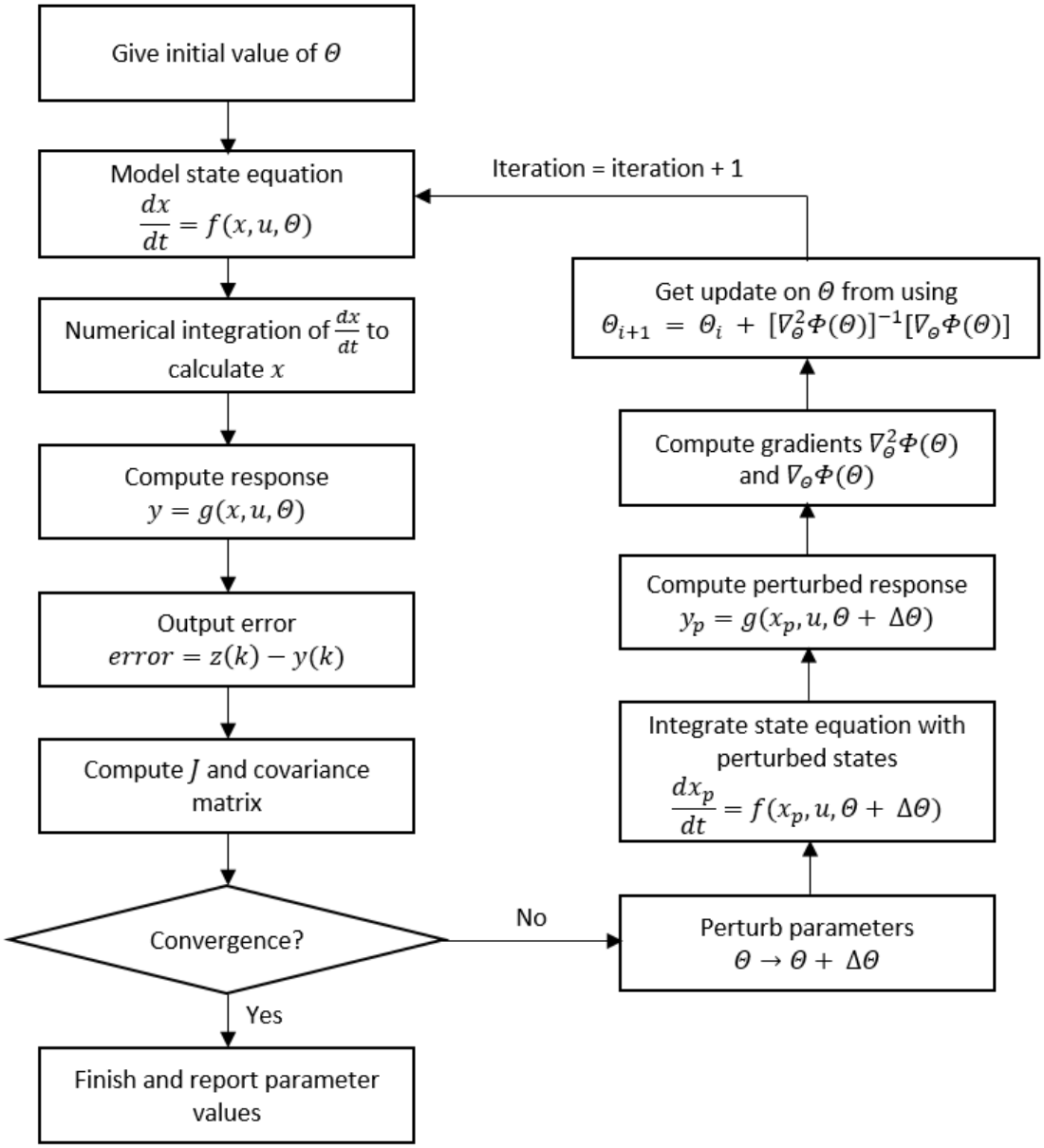


Figure 54 – A detailed schematic of the iterative process for finding accurate estimated parameters using MLE. Initial parameter values are used to calculate the model output, with the error compared and the likelihood function, J, calculated. The likelihood function is then checked for convergence and if its not deemed to have converged, the

parameters are perturbed, so the gradient and divergence of the parameters can be calculated, which is used to estimate the next parameter iteration.[280]

3.8.2. Parameter correlation

Parameters in models can often be correlated to each other such that a change in one will lead to a change in others. For parameter estimations this can be a challenge as, during the estimation, changing the guesses of a parameter to improve the accuracy can have *knock on effects*, such as reducing the accuracy of a different parameter.[231]

Covariance-variance matrix

The correlation between parameters is a normalised measure of the covariances between the different parameters and the individual variances of the parameters. The formula for calculating the correlation, ω_{ij}, between two parameters i and j, is shown in Equation 65, where v_{ij} is the variance between the two parameters and v_{ii} and v_{jj} are the individual variances of i and j, respectively.[286]

$$\omega_{ij} = \frac{v_{ij}}{\sqrt{v_{ii}v_{jj}}} \tag{65}$$

Reducing correlation between parameters

Often with kinetic parameter estimations there are high correlations between parameters as the pre-exponential factors and activation energies can both be changed to match a result. Also, there is often correlation between parameters for different reactions as they often run in series. One method of reducing the correlation is the reparameterization of the Arrhenius equation using a reference temperature, T_{ref}.[287–289] The original Arrhenius equation is defined in Equation 44, followed by two reparameterised Arrhenius equations, defined in Equations 67, 68, 69 and 70 as the Ã-E_A and Ã-B reparameterised Arrhenius equations, respectively.[231,290,291]

$$k = A_0 exp\left(\frac{-E_A}{RT}\right) \tag{66}$$

$$k = \tilde{A}exp\left(\frac{-E_A}{RT}\right), \tilde{A} = A_0 exp\left(\frac{-E_A}{RT_{ref}}\right) \tag{67,68}$$

$$k = exp\left(\tilde{A} + B\left(\frac{T - T_{ref}}{T}\right)\right), B = \frac{E_A}{RT_{ref}} \quad (69, 70)$$

Choice of reference temperature to reduce correlation

Using reference temperatures within reparameterised Arrhenius equations is common for kinetic estimations.[288] However, the choice of the reference temperature is less studied, with a commonly used definition the inverse average of the temperatures used in the estimation, as defined in Equation 71. [289]

$$\frac{1}{T_{ref}} = \frac{1}{N_E}\sum_{i=1}^{N_E}\frac{1}{T_i} \quad (71)$$

Optimising T_{ref} for the reparameterised Arrhenius equation

Although the T_{ref} defined above often reduces the correlations significantly, the reference temperatures can be changed to reduce the correlation between parameters further.[289] The A-B reparameterised Arrhenius equation, defined in Equations 69 and 70, can be used to calculate the parameters at a new T_{ref}, using the previously estimated parameters, indicated by a *, as shown in Equation 72.

$$A = A^* - B + B^*, \qquad B = \frac{B^* T^*_{ref}}{T_{ref}} \quad (72)$$

The new parameter estimations, Θ, can then be written as a function of the initial parameter estimations, Θ^*, as shown in Equation 73.[292]

$$\Theta = g(\Theta^*) \quad (73)$$

The covariance matrix, $\mathbf{V}$, of the estimated parameters at the new reference temperature can then be calculated from the covariance matrix of the initial estimation, $\mathbf{V}^*$, where $\boldsymbol{G}$ is a N_Θ x N_Θ matrix of the first derivatives of $g(\Theta^*)$ with respect to each parameter, as defined in Equation 74 where N_Θ is the number of parameters.[292]

$$\boldsymbol{V} = \boldsymbol{G^T V^* G} \quad (74)$$

$$\mathbf{G} = \begin{bmatrix} \frac{\partial g_1}{\partial \Theta_1^*} & \cdots & \frac{\partial g_{N_P}}{\partial \Theta_1^*} \\ \vdots & \ddots & \vdots \\ \frac{\partial g_1}{\partial \Theta_{N_P}^*} & \cdots & \frac{\partial g_{N_P}}{\partial \Theta_{N_P}^*} \end{bmatrix}$$

A minimum search algorithm can then be used with a norm of the correlation matrix, calculated from $\boldsymbol{V}$, such that the reference temperatures minimise the norm of the correlation matrix. A number of different norms can be used, with the Euclidean norm the most commonly used.[293]

3.8.3. Uncertainty of sensors

With MLE, the experimental data used is expected to have a certain degree of uncertainty associated with it. In this case, the experimental data is assumed to be normally distributed, with the uncertainty of the experimental data either provided to the estimation algorithm or also estimated using the experimental data.[283] The experimental data used in this work were typically the yields of the reactions. The yields in this work were calculated using a number of different methods, with a varying degree of accuracies. The assumed accuracies were then used within the parameter estimations. For example, typical NMR yield methods with internal standards have an assumed accuracy of *ca* ± 5-10%.[294] The uncertainty in quantitative NMR and GC methods is assumed to be smaller, around *ca.* ± 1%.[295,296]

A novel spectroscopic method for calculating the yield of a reaction was also developed using Raman spectroscopy, to explore the potential of online measurements. The uncertainty for this method was unknown and was estimated within the parameter estimation process, as discussed in Chapter 5.

3.9. Model validation

Once the parameters have been estimated, the model needs to be validated using experimental data to ensure the future predictive capabilities. The simplest method for this is using a graphical comparison between the experimental values and the predicted values, as shown in **Error! Reference source not found.**.

Further to visual analysis, there are a number of more detailed statistical analyses that can be carried out to get a quantitative measure of the validity of the models. A number of these techniques for validation are discussed below.[297] For model validation, both the estimated parameters and the predicted output values of the model need to be validated.

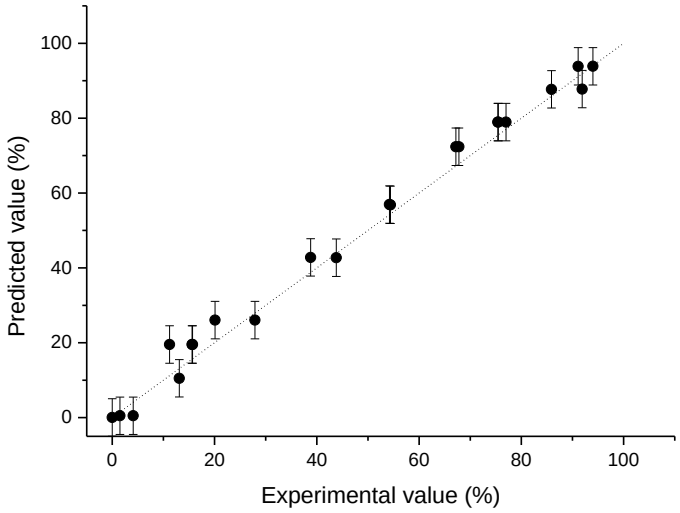


Figure 55 – A comparison of experimental and predicted values of a model, which can be used as an initial check for the validity of a model. More quantitative measures of model validity are discussed below.

3.9.1. Estimated parameter validation

The validation of the estimated parameter values can be validated by understanding the error in the value relative to the degrees of freedom of the estimation.

95% t-value

The t-test can be used to test significance of a parameter to a confidence level, α, of usually 90% or 95%. The t-value for the estimated parameters, $\hat{\theta}$, is calculated as shown in Equation 75 where σ_i is the standard deviation of the parameter. The degrees of freedom, n_{df}, in the estimation is equal to the number of experimental values, N_E, minus the number of parameters, N_Θ, that were estimated.[298]

$$t = \frac{\hat{\theta}}{Y_i(0.95)}, \qquad Y_i(\alpha) = t\left(\frac{1+\alpha}{2}, n_{df}\right)\sigma_i \tag{75}$$

$$n_{df} = N_E - N_\Theta$$

The calculated t-value is then compared with the reference t-value for the statistics, $Y_r(\alpha) = t\left(\frac{1+\alpha}{2}, n_{df}\right)$, showing whether the standard deviation and confidence interval are small compared to the value of the parameter.

Confidence ellipsoids

Confidence ellipsoids show the region of parameter values where the equality defined in Equation 76 is valid; where Θ is parameter i and j, with the $\hat{\theta}$ indicating the estimated parameter, V is the variance or covariance between the parameters, N_Θ is the number of parameters, s^2 is the unbiased estimator of the sample variance (defined in Equation 77), α is the confidence parameter and F is the F-distribution.

$$\begin{pmatrix}\Theta_i - \hat{\theta}_i \\ \Theta_j - \hat{\theta}_j\end{pmatrix}^T \begin{pmatrix}V_{ii} & V_{ij} \\ V_{ji} & V_{jj}\end{pmatrix} \begin{pmatrix}\Theta_i - \hat{\theta}_i \\ \Theta_j - \hat{\theta}_j\end{pmatrix} \leq N_\Theta s^2 F(\alpha, N_\Theta, N - N_\Theta) \tag{76}$$

$$s^2 = \frac{1}{N - N_\Theta} \sum_{i=1}^{NE} \sum_{j=1}^{NV_i} \sum_{k=1}^{NM_{ij}} \frac{\left(\check{z}_{ijk} - z_{ijk}\right)^2}{\sigma_{ijk}^2} \tag{77}$$

The α % confidence region means that if the experiments were repeated with slightly different values observed, α % would fall within the defined region.[297]

3.9.2. Model output validation

As well as validating the parameter values, the output of the model has to be validated against experimental results, especially those not used within the parameter estimation method.

Absolute average difference

The absolute average difference (AAD) is a measure is the average of the absolute deviations of a set of values, x_i, from a certain central value usually the mean of the set, $\bar{x}$. The equation for the AAD is defined in Equation 78. [298]

$$AAD = \frac{1}{n}\sum_{i=1}^{n}|x_i - \bar{x}| \tag{78}$$

Root mean square error

The Root Mean Square Error (RMSE) is the standard deviation of the residuals and is a measure of how widely distributed the residuals are, and is defined in Equation 79.[298]

$$RMSE = \sqrt{\sum_{i=1}^{N}\frac{\left(x_{i,pred} - x_{i,exp}\right)^2}{N}} \tag{79}$$

The RMSE and AAD are similar measures, with RMSE amplifying any outliers due to the use of the squared term in the equation.

Goodness of fit test

The goodness of fit test, also known as the χ^2-test, estimates how likely it is that an observed difference between the predicted values and measured values arose by chance and determine whether the model adequately fitted the measured data.[299,300] Pearson's χ^2-test examines whether the predicted values follow a specified distribution. The χ^2 value is calculated as shown in Equation 80, where O_i is the observation values of type i and E_i is the expected values of type i, and p_i is the fraction of the population of type i asserted by the null hypothesis. The value chosen for p_i is 0.01, 0.05 or 0.1 in typical engineering problems.[298]

$$\chi^2 = \sum_{i=1}^{n}\frac{(O_i - E_i)^2}{E_i} \tag{80}$$

The calculated χ^2 value can then be checked against critical values, χ^2_{crit}, which are well defined in literature. The degrees of freedom, n_{df}, for the comparison with critical χ^2 values is calculated, as shown below, where N_E is the number of experimental measurements and N_Θ is the number of estimated parameters.

$$n_{df} = N_E - N_\Theta$$

$$\chi^2_{crit} = \chi^2(p_i, n_{df})$$

Lack of fit test

The lack of fit test uses a similar approach to the goodness of fit test, however instead compares the error in the model with the error of the measurement. The F-value is calculated as shown in Equation 81, where σ_c is the variation in the model values and σ_m is the variance of the measured values.[298] The F value is then compared with critical value, F_{crit}, with the selected significance level, α, using F-value tables.[298]

$$F = \frac{\sigma_c}{\sigma_m} \tag{81}$$

$$F_{crit} = F(\alpha, n_{df})$$

The t-test

The Bias test, also known as the t-test is used to identify subsets of observations from either variables or experiments where model bias may be present. It is used to identify whether the mean of the residuals is zero for each subset of experiments.[298] There are two well-known t-tests: the student t-test or Welch's t-test.[301,302]

Welch's t-test

Welch's t-value is calculated for two different sets as shown in Equation 82, where $\bar{X}$ is the sample mean, s is the sample standard deviation, n is the sample size and s_i^2 is the unbiased estimator of the variance.[302] The degrees of freedom, $n_{df,Welch}$, for the Welch t-test is defined in Equation 83. The

t-value is then compared with known t-values with a chosen significance level to judge whether the null-hypothesis can be rejected.

$$t = \frac{\bar{X}_1 - X_2}{\sqrt{\frac{s_1^2}{n_1} + \frac{s_2^2}{n_2}}} \tag{82}$$

$$n_{df,Welch} = \frac{\left(\frac{s_1^2}{n_1} + \frac{s_2^2}{n_2}\right)}{\frac{\left(s_1^2/n_1\right)^2}{n_1 - 1} + \frac{\left(s_2^2/n_2\right)^2}{n_2 - 1}} \tag{83}$$

Student t-test

The student t-test is a statistical hypothesis test where the test statistic follows a Student's t-distribution under the null hypothesis. The one-sample t-test is used to test the null hypothesis that the population mean, $\bar{X}$, is equal to a specified value, μ_0. The t-value is calculated as shown in Equation 84, where s is the standard error of the mean and n is the sample size. [301]

$$t = \frac{\bar{X} - \mu_0}{s/\sqrt{n}} \tag{84}$$

3.10. Process optimisation

Optimisation in chemistry laboratories is often carried out by changing single variables at a time until the optimal conditions are found. One benefit of modelling is that once the model has been made and validated the optimal conditions can be found computationally. This optimisation can be carried out manually by changing values and observing the model output, in a way similar to typical laboratory optimisations. An alternative way to optimise the process is mathematical optimisation of the model for a desired outcome, such as yield, known as the objective function.[303]

A benefit of the mathematical optimisation method is that the conditions found are optimal conditions. Also, different outcomes can be optimised for, such as yield, space-time yield or productivity, by defining different objective functions. A disadvantage of the mathematical method is

that the model needs to be defined and validated which requires a certain number of experiments. As the scale increases, the testing of multiple parameters is expected to be more efficient using a computational model compared to traditional optimisation methods.[303]

3.11. Sensitivity analysis

Sensitivity analysis allows the model to be understood better by understanding the way uncertainty in values can affect the outcome of the models. This allows the operators to understand the model better and then decide how much effort should be spent on reducing uncertainty in variables. [298] With both sensitivity and uncertainty analysis there are two definitions that are required:

- Factor – the variables inputted into the model that are changed within the model, with the distribution of the variables defined by the user to see how the output variables are changed, for example, the activation energy.
- Response – variables that are measured during the sensitivity analysis to understand how it is changed by the factors, for example the reaction yield.

3.11.1. Sensitivity analysis

The sensitivity measures used here are sensitivity indices as the parameters are uncertain or there is non-linearity in the model. The sensitivity indices therefore measure averages over the entire space of interest; two of the most well-known techniques are variance-based or elementary effects sensitivity analysis.[304,305]

The choice between each method is largely down to the differences in complexity of the model in question. Variance-based sensitivity analysis is considered more detailed but is more computationally expensive, whereas elementary effects sensitivity analysis can be used for highly complex models as it is less computationally expensive.[305]

Variance based sensitivity analysis

Variance-based sensitivity analysis is the study of how the variance of the model output depends on the input factors that are affected by uncertainty.[304] Variance-based sensitivity indices measure the influence of individual factors on the model output. There are two types of variance-based sensitivity indices:

- first-order effect index: S_i; and
- total effect index: S_{Ti}.

The first-order effect indices measure the individual effect contribution of each input to the variance of the output. Generally, the larger the value of S_i, the greater the influence on the output of a defined factor. The equation for calculating S_i is shown in Equation 85 where $\sigma^2_{i,y}$ is the variance attributed to factor i on response y and σ^2_y is the variance observed for response y.

$$S_i = \frac{\sigma^2_{i,y}}{\sigma^2_y} \tag{85}$$

The total effect index S_{Ti} indices measure the contribution of both the first-order effects and higher-order effects from the interactions with other factors. Again, the larger value of S_{Ti} indicates a greater contributing effect. The equation for calculating $S_{T,i}$ is shown in Equation 86 where $\sigma^2_{i,y}$ is the total variance attributed to factor i on response y and σ^2_y is the variance observed for response y.

$$S_{T,i} = \frac{\sigma^2_{T,i,y}}{\sigma^2_y} \tag{86}$$

For simplicity, the sensitivity indices defined above indicate what part of the variance in the response to which factor. For example, variance-based sensitivity analysis can be applied to Equation 87, with factors x_1 and x_2 and response y, with x_i belonging to different sets, as shown in **Error! Reference source not found.**.[84]

$$y = x_1^2 + 3x_2 \tag{87}$$

Table 19 – A table showing the variance-based sensitivity indices for the above equation, with the higher number indicating a greater sensitivity to that factor. It shows that when x is between 0 and 10 the outcome is most sensitive to x_1, whereas when x is between 0 and 1 the output of the equation is most sensitive to x_2.

	$x \in [0, 10]$		$x \in [0, 1]$	
	S_i	$S_{T,i}$	S_i	$S_{T,i}$
x_1	0.92	1.02	0.03	0.12
x_2	-0.01	0.08	0.88	0.97

The sensitivity analysis indices calculated for the above equation do not have a defined meaning, however the most influential factors can be identified.

Variance-based sensitivity analysis can then be used in different settings, such as factor prioritisation or factor fixing.

Factor prioritisation can be used to identify which factors account for most of the output variance. Understanding the effect each factor has on the output allows the factors to be ranked in terms of their effect on the output and which factors may need more accurate measurements. The first-order effect index is considered to provide the ranking of the factors.[304]

Factor fixing can be used to identify factors in the model which make no significant impact to the variance of the output. The identified factors can then be fixed anywhere in their range of variation without changing the output; this can help simplify models. The total effect index can be used to judge the effect of a factor, with S_{Ti} = 0 indicating the factor does not influence the output.[304]

The main disadvantage with variance-based sensitivity analysis is its high computational cost, which can become prohibitive for complex models. This computational expense can be reduced through screening important factors.

Elementary effects

The elementary effects (EE) method screens a number of important factors from a large number of input factors in a complex model. This method is used when the number of uncertain factors is high and/or the model is expensive to compute. EE uses an approach where factors are iterated one at a

time.[305] The effect of different factors is calculated, with different indices from the method discussed above:

- The mean of elementary effects, μ_{EE}, assess the overall influence of the factor on output. The mean of absolute values of elementary elements, μ_{EE}^{*}, can also be used in place of S_{Ti} when the computational cost of the model is large.[306]
- The standard deviation of elementary effects, σ_{EE}, estimates the higher-order effect due to non-linearity and interactions between parameters.

For EE, the sensitivities are calculate based on the approximation shown in Equation 88, where $EE_{i,j}$ is the elementary effect for factor i for sample j, u_i is factor i, y is the response and Δ is the difference in factors changed one at a time between steps.

$$EE_{i,j} = \frac{y(u_1, \ldots, u_i + \Delta, \ldots, u_n) - y(u_1, \ldots, u_i, \ldots, u_n)}{\Delta} \forall i \in 1, \ldots, n \tag{88}$$

The different elementary effects are estimated by randomly sampling different trajectories and the averaging the effect. The mean of the elementary effects for factor i, $\mu_{EE,i}$, and standard deviation of the elementary effects for factor i, $\sigma_{EE,i}$, can be calculated as shown in Equations 89 and 90, where n is the number of samples

$$\mu_{EE,i} = \frac{1}{n}\sum_{j=1}^{n} EE_{i,j} \tag{89}$$

$$\sigma_{EE,i} = \sqrt{\frac{1}{n-1}\sum_{j=1}^{n}\left(EE_{i,j} - \mu_i\right)^2} \tag{90}$$

Applying EE sensitivity analysis to Equation 91 is shown below, with factors x_1 and x_2 and response y, with x_i belonging to different sets, as shown in **Error! Reference source not found.**.[84]

$$y = x_1^2 + 3x_2 \tag{91}$$

Table 20 - A table showing the elementary effects indices for the above equation, with the higher number indicating a greater sensitivity to that factor. It shows that when x is between 0 and 10 the outcome is most sensitive to x_1, whereas when x is between 0 and 1 the output of the equation is most sensitive to x_2.

	$x \in [0, 10]$		$x \in [0, 1]$	
	μ_{EE}	σ_{EE}	μ_{EE}	σ_{EE}
x_1	111	60.5	1.11	0.65
x_2	30	13.4	3.0	1.34

Similarly to variance-based sensitivity analysis, the most influential factors can be identified by looking for the largest indices measure for each factor.

3.12. Numerical methods used in this work

The numerical solvers used in this work were those developed by PSE and included within the gPROMS developer environment. An in-depth description of the way they work is currently unavailable as the solvers are proprietary and considered world-leading within the Process modelling sector.[84] A brief description of each solver is therefore described below.

3.12.1. Solvers used within gPROMS ProcessBuilder

The solvers for each different class of problems are described below, with the choice of solver and associated parameters able to be customised by the user.

Linear algebraic equations

For linear algebraic equations there were two solvers available, shown in **Error! Reference source not found.**, with the MA48 solver and updated version of the well-known MA28 solver.[307]

Table 21 - The name and description of the solvers used within gPROMS to solve linear algebraic equations.

Solver name	Description
MA28	For sparse unsymmetric system of m linear equations and n unknowns using Gaussian elimination.
MA48	An updated version of the MA28 solver.

Non-linear algebraic equations

For non-linear algebraic equations there were two solvers available, shown in **Error! Reference source not found.**, with both derived from Newton type methods, with BDNLSOL a proprietary solver.[84,308]

Table 22 - The name and description of the solvers used within gPROMS to solve non-linear algebraic equations.

Solver name	Description
BDNLSOL	Newton type with block decomposition to handle sparsity.
SPARSE	A sparse (Quasi-)Newton solver without block decomposition.

Differential-algebraic equations

There were three solvers available for differential-algebraic equations within gPROMS, as described in **Error! Reference source not found.**, with a variable time step used with a check taken between each step for a minimal error check. [84,308]

Table 23 - The name and description of the solvers used within gPROMS to solve differential-algebraic equations.

Solver name	Description
DAEBDF	Proprietary solver based on a variable-time-step and -order backwards differentiation formula.
DASOLV	Predictor-corrector backwards differentiation formula method with variable-time-step and -order.[309]
SRADAU	Implements a variable time step and is a fully implicit Runge-Kutta method.

4. Modelling photochemical reactions and reactors

4.1. Chapter Overview

This chapter describes the development of models for the various photochemical reactors used within the group, which enabled reaction output to be predicted. Initially an idealised reaction scheme was used with a number of assumptions, using a Beer-Lambert analogous law to model the absorption of photons. This model was then developed further using the two-flux approximation to model the absorption of light as well as introducing modelling the flow of material through the reactors.

A model of the excimer reactor was then used to estimate the quantum yield of multiple reactions, assuming the manufacturer's quoted lamp power was accurate, using the Maximum Likelihood Estimation (MLE) technique. The quantum yields estimated were then used to accurately predict the performance of reactions under different wavelengths and conditions. Furthermore, the quantum yield predicted in the Excimer flow reactor was also able to predict the performance of Excimer batch reactor experiments. The reverse was also shown to be true, showing the robustness of the method, considering the limitations and assumptions made.

Also presented is the development of photo-kinetic schemes to consider photosensitisers using a Bodenstein-like assumption to simplify the scheme. The assumption was shown to be valid on different reaction schemes and was validated with experimental results.

The quantum yields estimated with the excimer reactor model and experimental results were then used to understand the performance of the more complex reactors within the group, such as the fluorinated ethylene propylene (FEP) tubular reactor and Vortex reactor. Complex models for both of these reactors were developed, using an additional dimension, but proved to be too computationally expensive. This went against the benefits of using the fast-process model to quickly understand processes. Further assumptions were made for the models of both the Vortex and FEP tubular reactors, with experimental results used to validate the models.

4.2. Introduction to photochemical chapter

The modelling of photochemical reactions and reactors has limited literature precedent, especially for the synthesis of chemical compounds. This has been seen as a limitation for the development of photochemistry as a commonly-used chemical method, with Oelgemöller et al. highlighting the need for chemical engineering principles within photochemistry.[126] To the author's knowledge, Aillet et al. developed the first, and only, model to calculate the quantum yield of a chemical reaction with regards to chemical synthesis.[156]

Process models are widely used within the chemical industry to predict, monitor and optimise chemical reactions.[310] Traditionally, these process models have been focussed on thermal chemical reactions with the reactor design being the most distinct differences between each process. For photochemistry to be used on an industrial scale, an accurate process model would be needed. Aillet's method, introduced above, is not considered a process model as the calculations are used to calculate the product of the quantum yield and lamp irradiance.

The need for an accurate photochemical process model was therefore identified as a key stage in the development of photochemistry as an industrial technique. For this, a number of steps were taken for the development from an idealised batch reactor to an accurate model for multiple reactors. Another benefit of creating a process model was that parameter estimation could be used to estimate the quantum yield of a reaction.

As there have been multiple different reactor designs and lamps used by colleagues in Nottingham, the model developed was needed to be robust and flexible enough to be used between designs. For the more complex designs, Computational Fluid Dynamics (CFD) was expected to be needed to compare, as the mixing behaviours were expected to be complex. A comparison between the CFD model and gPROMS' process model was expected throughout to ensure congruency and, therefore, accuracy for the more complex reactor predictions.

As a large part of this Chapter involved the development of a process model for a photochemical reactor the relevant points are introduced and discussed in turn, rather than discussed within this introduction section.

4.3. Aims of photochemical research section

The aims for the photochemical research section, defined in Section 2.8, are repeated here to give further context. The aims set for the modelling of the photochemical reactions were:

Aim 4.1 - Develop a process model of a photochemical reactor

Aim 4.2 - Use photochemical process model to understand photochemical reaction kinetics and compare outputs with experimental results

Aim 4.3 - Use kinetics to predict reactor performance of reactions for; unimolecular reactions, multi-component reactions with competing absorbances, photosensitised reactions and consecutive reactions

Aim 4.4 - Develop models of more complex photochemical reactors

Aim 4.5 - Use photochemical model in conjunction with the high-temperature water process model to predict performance of a daisy-chained process

4.4. Initial model development

Photochemical reaction rate is largely governed by the absorption of light by the reactive molecules. This meant that the modelling of the absorption of light was crucial for the modelling of photoreactors. The initial model development will be explained using an idealised reaction, before experimental results are modelled.

4.4.1. Modelling the absorption of light

The light entering used within the initial models was assumed to be linear and parallel. This assumption allowed the absorption of light to be based on a relationship analogous to the Beer-Lambert law, defined previously in Equation 14.

$$A = -\log_{10}\left(\frac{I}{I_0}\right) = \varepsilon LC \tag{14}$$

The Beer-Lambert law was used to derive an equation for the amount of light absorbed within a small volume (dV = A x dz), as shown in Figure 56. Using this relationship for a small volume, the volumetric rate of photon absorption (LVRPA) per volume was derived, as shown in Equation 92, where α is the Napierian molar absorption coefficient and i represents the species that reacts and j represents another species that absorbs light. The Napierian molar absorption coefficient is defined in Equation 93, where ε is the decadic molar absorption coefficient.

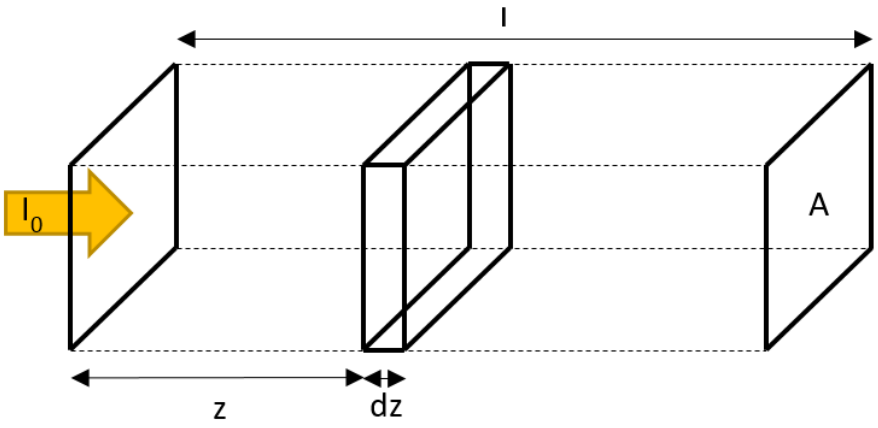


Figure 56 - Schematic for the derivation of the light intensity where I_0 - initial light intensity (mol $s^{-1}cm^{-1}$), L - reactor length (cm), z - distance into reactor (cm) and A - cross sectional area of light (cm^2), where LVRPA stands for the local volumetric rate of photon absorption.

$$LVRPA = \frac{I_{abs,A}}{V_z} = I_0 \alpha_i \, C_i e^{-\int_0^z \sum \alpha_{i,j} \, C_{i,j} \, dz} \tag{92}$$

$$\alpha_i = \varepsilon_i ln(10) \tag{93}$$

4.4.2. Rate of photoreaction

The absorption of light by a starting material is the driving force of a photochemical reaction. Within the model, this is considered using the LVRPA, as calculated above. The rate of reaction also relies on

a value known as the quantum yield, Φ, which is a measure of how much product is formed per amount of light absorbed. The rate of a photochemical reaction was defined as shown in Equation 94 with an idealised reaction where A converts to B upon the absorption of light.

$$A + hv \rightarrow B$$

$$Rate_{A \rightarrow B} = \Phi \, LVRPA_A \tag{94}$$

4.4.3. Quantum Yield

The quantum yield of a reaction is a measure of the efficiency the reaction has compared to the number of photons it has absorbed. Within this work, the true differential quantum yield was used as it is relevant to the molecule that absorbs light and goes onto react, as this aided with the model development. Within this Chapter this definition of quantum yield will be defined using ϕ. See Appendix II for further details regarding alternative definitions to the quantum yield.

4.4.4. Reactor model design and assumptions

Initially, a simplified reactor model was proposed, with the design based on a photoreactor within the group. The reactor was a simple cylindrical batch reactor illuminated from one end by parallel fully collimated light. As the light was fully collimated it allowed for the absorption of the light to be modelled using equations analogous to the Beer-Lambert law, as derived above. A schematic of the simplified reactor model is shown in Figure 57.

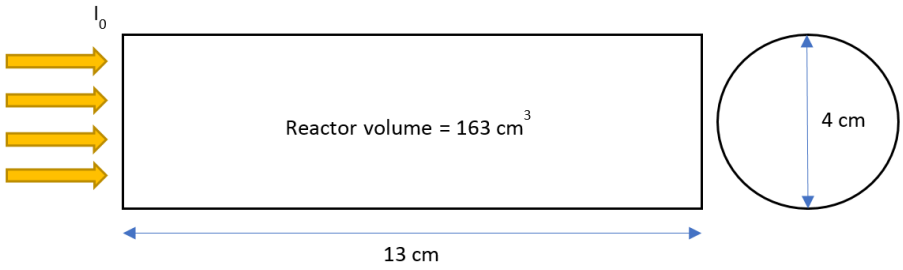


Figure 57 - A schematic of the simplified initial model of the photochemical reactor, which was based on a reactor previously used within the group. The light was assumed to be monochromatic and fully collimated.

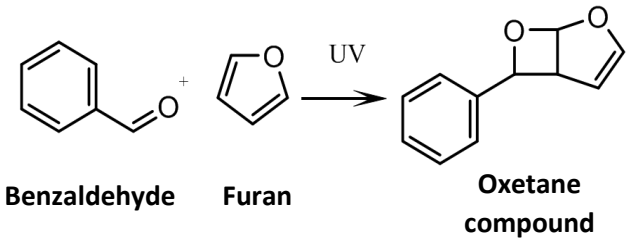
For the development of a model, there were a number of assumptions made for the development of the photochemical reactor model. These are outlined below:

- the photoreactions take place in a cell with planar and parallel windows of area A;
- there is no mixing or diffusion of the fluid;
- incident light is monochromatic;
- the incidence of the light is perpendicular to the front window;
- initial intensity of the light is constant ($mol \cdot s^{-1} \cdot cm^{-2}$);
- the reaction fluid is not opaque, it can absorb light but not scatter light; and
- the exit window does not reflect light.

4.4.5. Example reaction – Paternó-Büchi

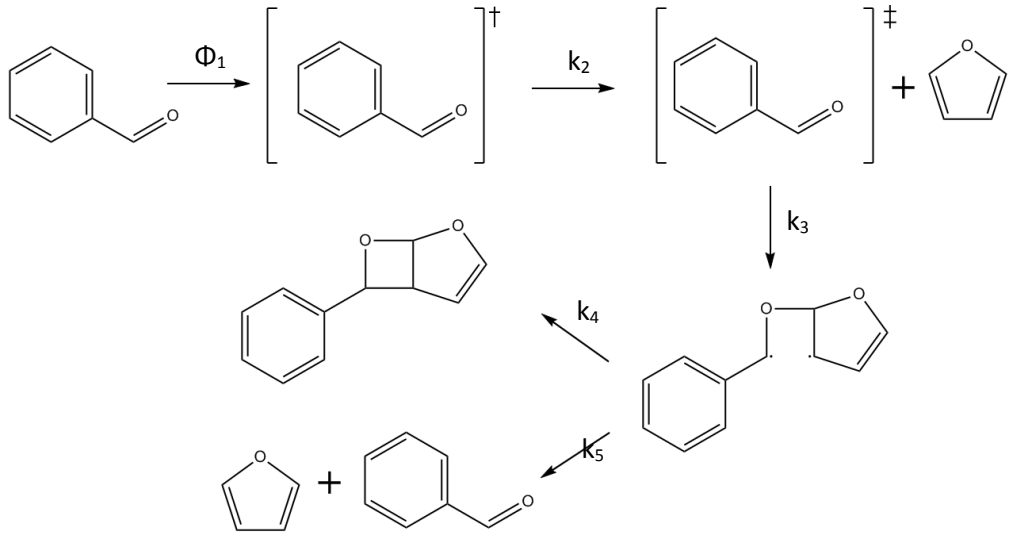
To test the development of the reactor model, an example reaction was needed. The Paternó-Büchi reaction was chosen as it was a relatively well-studied reaction that had been previously used within the group, and hence offered the possibility of comparing with experimental results in future.[311–313] The reaction is a photochemical reaction between a carbonyl and an alkene to form four membered rings. Scheme 1 shows the reaction between benzaldehyde and furan to form the oxetane compound.

Scheme 1 - Overall mechanism for the Paternó-Büchi reaction showing the reaction between benzaldehyde and furan to form an oxetane. This reaction was used as a test case for the development of the photochemical reactor models.



The reaction was broken down into multiple steps involving the absorption of light and excitation of benzaldehyde, before reacting with furan to form reactive intermediates. The multiple steps of the proposed reaction are shown in Scheme 2.

Scheme 2 - The proposed mechanism for the Paternò–Büchi photochemical reaction scheme of benzaldehyde (1) with furan (4) to form the oxetane (6).



The reaction mechanism shown in Scheme 2 is also summarised below, with a separation between photochemical and thermal steps of the mechanism:

Photochemical Reactions

Reaction 1: benzaldehyde + hν(365 nm) → ^{1}[benzaldehyde]*

Thermal Reactions

Reaction 2: ^{1}[benzaldehyde]* → ^{3}[benzaldehyde]*

Reaction 3: ^{3}[benzaldehyde]* + furan → ^{1}[biradical]$^{\neq}$

Reaction 4: ^{1}[biradical]$^{\neq}$ → oxetane

Reaction 5: ^{1}[biradical]$^{\neq}$ → benzaldehyde + furan

Reaction parameters

The quantum yields and kinetic parameters of the subsequent steps, shown in Table 24, were collated from a range of literature sources as there was not a single source for all values.[312,314] The quantum yield was assumed to be 0.5 as a literature value could not be found for these conditions.

Table 24 - The quantum yield and kinetic parameters for the idealised Paternò–Büchi reaction scheme, adapted from literature sources, with the quantum yield assumed as 0.5 as there was limited literature values for this.[312,314]

Photo reactions	Quantum yield
1	0.5
Thermal reactions	**Rate constant (variable units)**
2	2.4×10^{10} s^{-1}
3	1.2×10^{9} $dm^3 \cdot mol^{-1} \cdot s^{-1}$
4	0.27×10^{9} s^{-1}
5	0.24×10^{9} s^{-1}

Effect of discretisation on results

For process models that solve differential equations, the separation of the discretisation points can have a large effect on results.[315] It was therefore important to check that the output values were not affected by the number of discretisation points used in the calculations; this is also often called the 'mesh size' in fluid dynamics engineering.[279]

A variety of discretisation points (DPs), ranging from 13 to 1300, for the reactor model described above were tested. Figure 58 shows the attenuation of light at the beginning of the reaction along the reactor length, with the intensity of light approaching the Beer-Lambert law as the number of discretisation points increases.

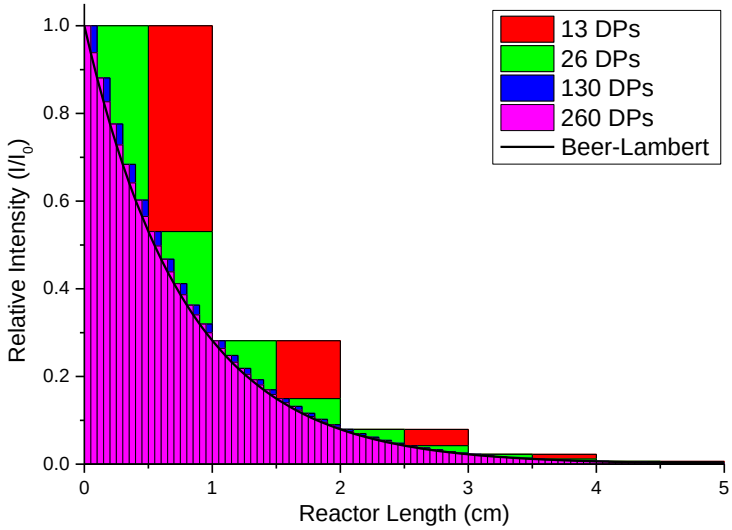


Figure 58 – Intensity of light with varying number of discretisation points (DP) at t = 0 along with the Beer-Lambert relationship (–). Please note after 5 cm nearly all the light has been absorbed and the intensity is insignificant.

For 1300 DPs there was minimal difference between the Beer-Lambert law values and the model's calculated values. However, there are practical reasons not to choose a large numbers of DPs as it can become computationally expensive, especially with multiple dimensions.[315] The use of higher number of DPs may also not offer significant changes in the calculated values. For example, the difference in calculated yields between 260 and 1300 DPs was minimal, as can be seen in Figure 59.

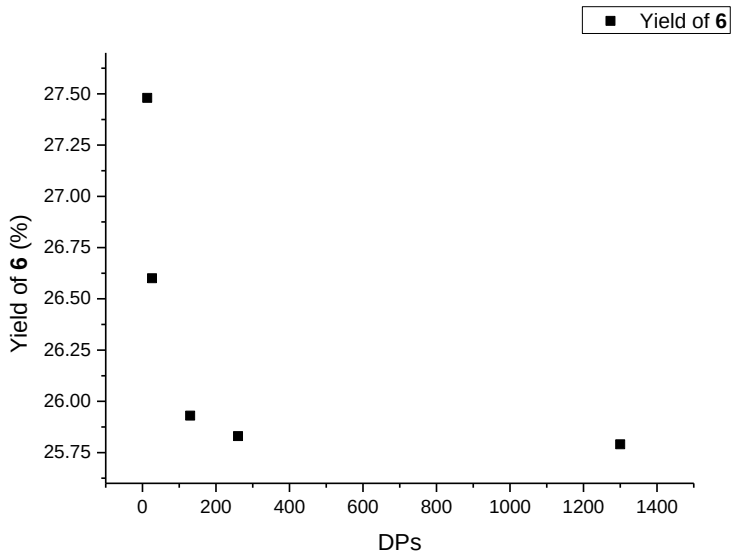


Figure 59 - The calculated yield of oxetane product after 5 hours of illumination with an increasing number of discretisation points, showing the sensitivity to the value.

Variable mesh sizes

It should also be noted that the mesh sizes do not have to be regularly spaced; the DPs can have a higher density in a region of expected rapid change.[316] This is often found with fluid flow as the velocity profile is the steepest closest to the walls. For the absorption of light, a greater gradient will be expected nearest the irradiated wall.

Initial model development – no mixing case

The concentration of the oxetane product relative to the initial concentration of the limiting reagent (benzaldehyde), is shown in Figure 60(a). The increase in the concentration of the oxetane product along the reactor with time shows the reaction development, and as there was no mixing in this case a 'front' of the product develops and moves along the reactor. This effect of a front moving along the

reactor was also shown with the relative light intensity shown in Figure 60(b), as the product was formed the solution near the light becomes transparent and the light intensity moved along the reactor.

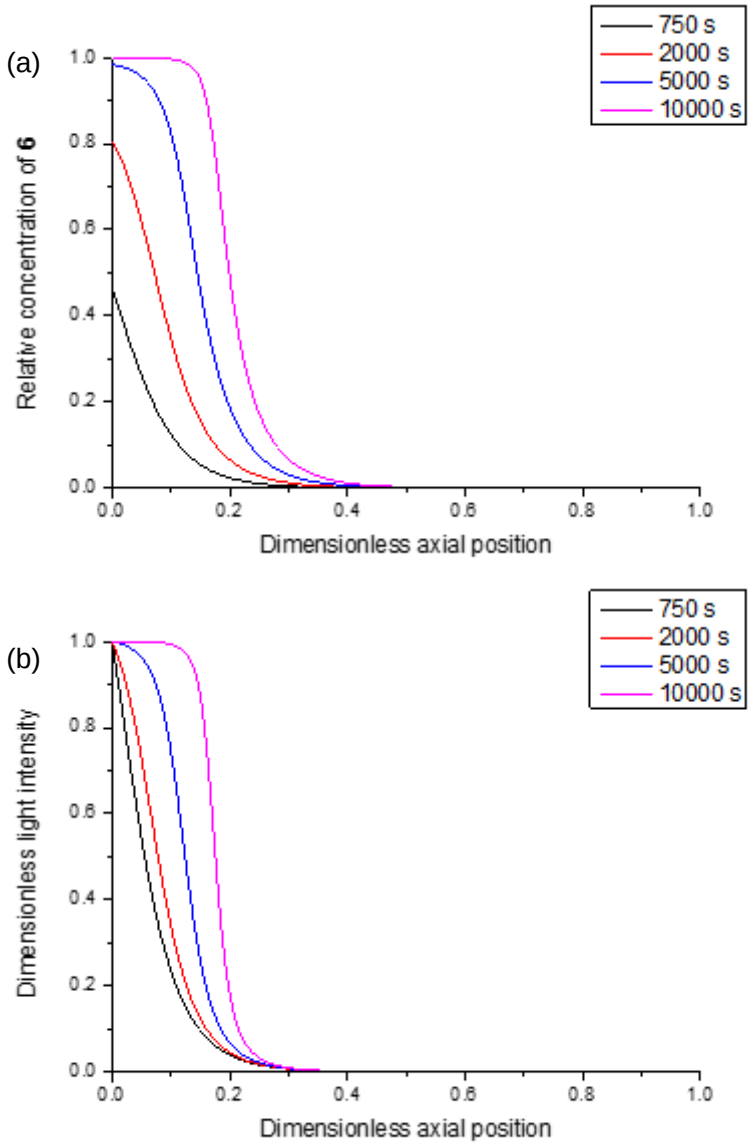


Figure 60 – The initial model results for the no mixing case where (a) is the concentration of the oxetane product relative to the starting concentration along the reactor length and (b) is the dimensionless light intensity along the reactor showing a 'front' develop with time.

Initial model development – fully mixed case

These conditions were repeated for the larger reactor with a fully mixed reactor vessel, where there were no concentration gradients. As it was fully mixed, the concentration was constant along the whole reactor, with the total concentration of the product increasing with time, as shown in Figure

61(a). The light intensity does not form a 'front' that moves along the reactor and rather shows decreasing attenuation as the concentration of the absorbing species react to form the product, which does not absorb, as can be seen in Figure 61(b).

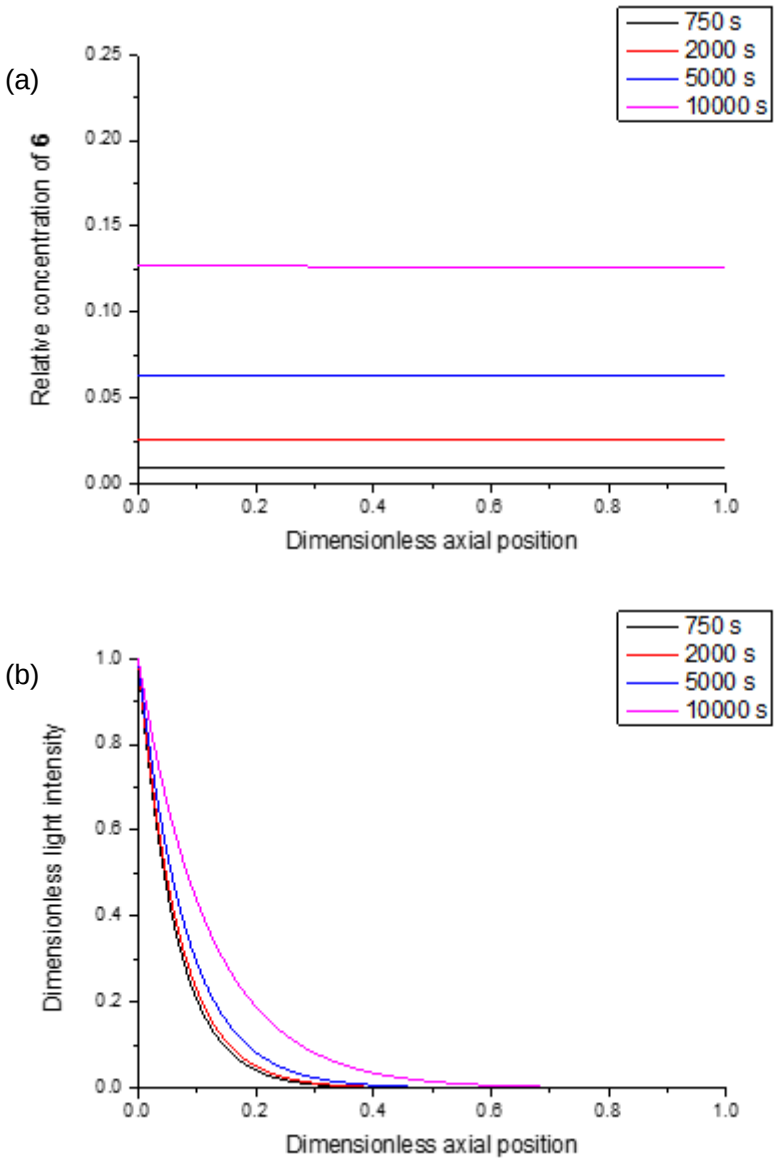


Figure 61 - The initial model results for the fully mixed case where (a) is the concentration of the oxetane product (6) relative to the starting concentration along the reactor length and (b) is the dimensionless light intensity along the reactor showing a decrease in light attenuation with time as the absorbing species are reacted.

4.5. Comparison with CFD

All CFD calculations were carried out by colleague Dr. Medhat Sharabi.

The idealised model results predicted by the gPROMS process model were compared with the CFD calculations to ensure congruency. All of the results were calculated using commercial CFD software Ansys Fluent with the calculations performed on a high-performance computer (HPC).[317] For the idealised batch case, with no mixing, the results were compared and showed negligible difference between the two models, as shown in Figure 62.

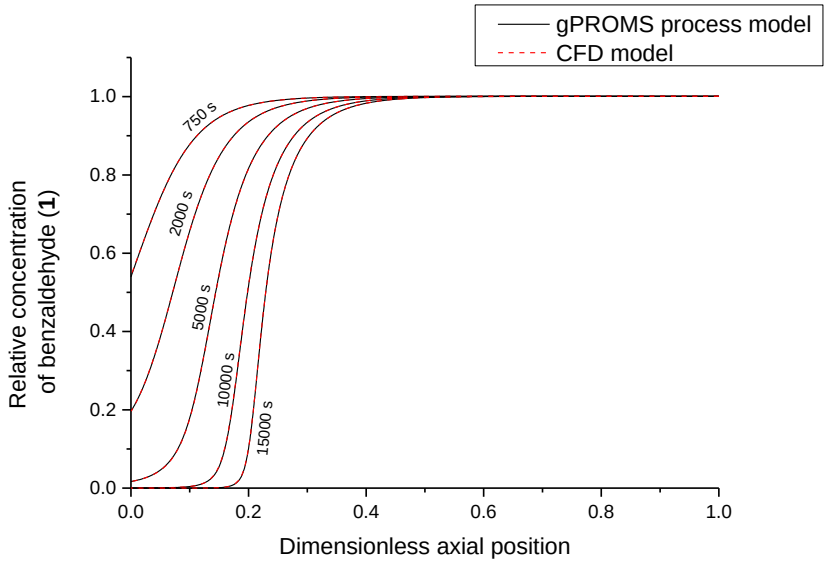


Figure 62 - The relative concentration of benzaldehyde (1) along the reactor with the no mixing case, again showing a 'front' develop along the reactor. The differences between the gPROMS model and CFD model was negligible.

A fully mixed case was not achievable with the CFD model for the original reactor size. As CFD models physical effects, a fully mixed case needed a physical effect that could mimic the reactor to appear fully mixed. Multiple different options for the physical effect were attempted with limited success for the original reactor size, including: stirrers, paddles and velocity sources.[257]

To overcome this issue for the fully mixed case, a shorter reactor of 5 cm was modelled as it was hoped this would allow for a physical effect to ensure the reactor was fully mixed. The shorter reactor was able to produce a fully mixed case using negligibly thin paddles such that the volume of the reactors

was not affected. The dimensionless concentration of the oxetane product for the shorter reactor is shown in Figure 63, where the difference between the two values is negligible. This equivalence showed that it was possible to use the diffusion coefficient as a proxy for mixing of the reactor.

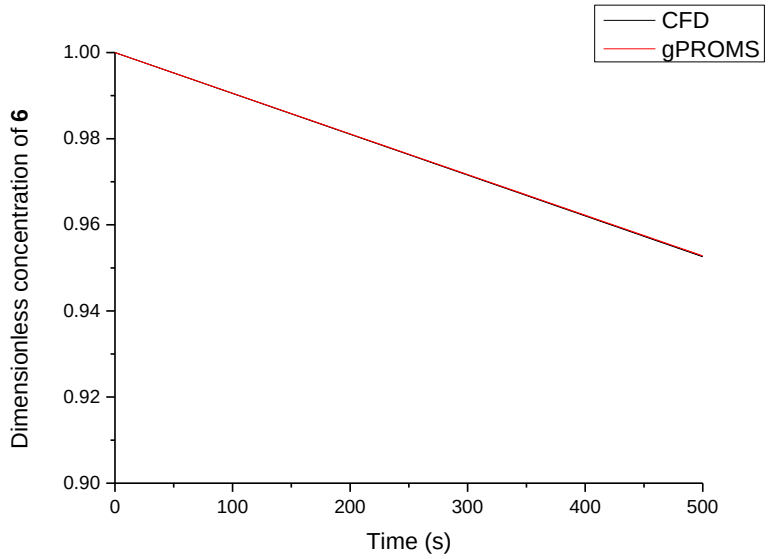


Figure 63 - The dimensionless concentration of the oxetane product with time for the fully mixed case in the shorter reactor, showing neglible difference between the gPROMS and CFD models.

4.6. Introduction to excimer reactor models

The initial model development described above showed that the modelling of a photochemical reactor and reactions was possible. However, the reactor used was an idealised version of a cylindrical batch reactor used in the laboratory and was not wholly applicable to the reactors used experimentally. The reactors used experimentally were often either annular or cylindrical reactors with either batch or flow set-ups, such as the excimer flow and batch reactors.

The orientation of the light for both the excimer batch and flow reactors was different compared to the initial model, as they were illuminated on the curved surface rather than from the end. To incorporate this change into the model, cylindrical coordinates were used. For the excimer flow reactor model, a term was introduced for the movement of material through an annular channel within the mass balance equation, as shown in Section 4.6.4. A schematic of the annular flow reactor

is shown in Figure 64, with the blue arrows indicating movement of the fluid and the yellow arrows indicating the direction of the light entering the excimer reactor model.

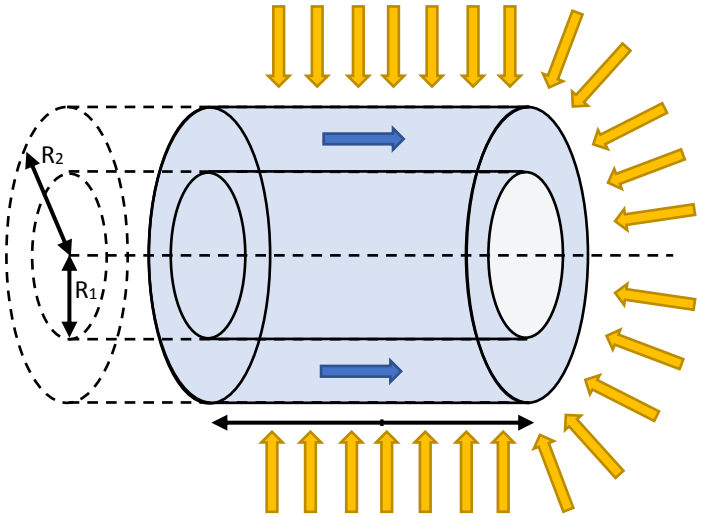


Figure 64 - A schematic of an annular flow photochemical reactor with the illuminated reactor wall from the outside. The yellow arrows indicate the illumination of light, the blue arrows indicate flow of material and R_1 and R_2 are the internal radius and external radius of the reactors, respectively.

It was possible to model the light emitting from the centre, similarly to the immersion well reactors described in the introduction, by changing the boundary conditions for the equation for the light's 'radiative transfer equation' (RTE).

4.6.1. Radiative transfer equation for annular reactors

Previously the Beer-Lambert equation was considered sufficient for a linear reactor as the lamp was assumed to emit parallel light. However, with a cylindrical reactor, this assumption was not valid as the circular shape can either increase or decrease power as the light diverges or converges, respectively, as shown in Figure 65. However, this effect was expected to be minimal with the excimer flow reactors, as the gap size is 120 µm, for larger gap sizes such as with the excimer batch reactors this effect could become considerable.

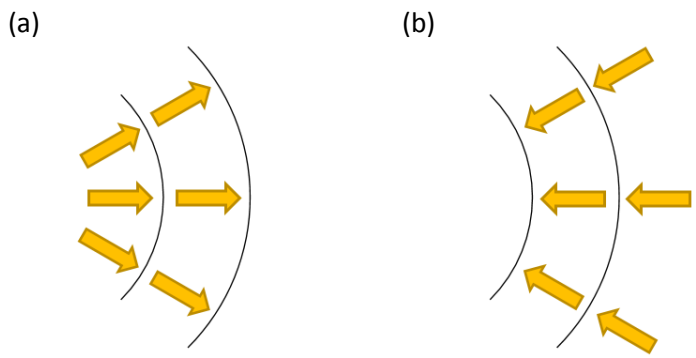


Figure 65 - A schematic of (a) the divergence of light and (b) the convergence of light in an annular set-up, which leads to a decrease and increase in light intensity per unit area, respectively.

To model the light aggregation effect in three dimensions there were two possible options; a discrete ordinate method which integrates over the angular space or the two-flux approximation, with both described in Section 2.4.8.[172]

Choice of RTE for this work

The two-flux approximation was chosen for subsequent calculations as it allowed for the irradiance to be calculated using gPROMS PDE solvers without having to introduce an extra dimension. The extra dimension would increase calculation time and therefore would not be useful for the intended goal of the fast process modelling of the reactors, which can be used for reactor output prediction.

4.6.2. Comparison of two-flux method with previous Beer-Lambert law

The excimer reactor model was used to compare between the two absorption models as the annular gap (120 µm) was much smaller than the reactor radius (0.68 cm); and hence the increase in light intensity from the convergence of irradiation was assumed to be negligible. The results for fully collimated light are shown in Figure 66, negligible difference can be seen, as was expected. A difference was observed when the collimation factor was changed such that the light entering the reactor was fully isotropic at the reactor surface. The irradiance of the isotropic light was attenuated at double the rate in the radial dimension compared to the fully collimated case. The difference was expected as the collimation factors (k_H) are 2 and 1 for the isotropic and fully collimated cases,

respectively. This was expected as the light intensity leaves the surface in all directions rather than just perpendicular to the surface.

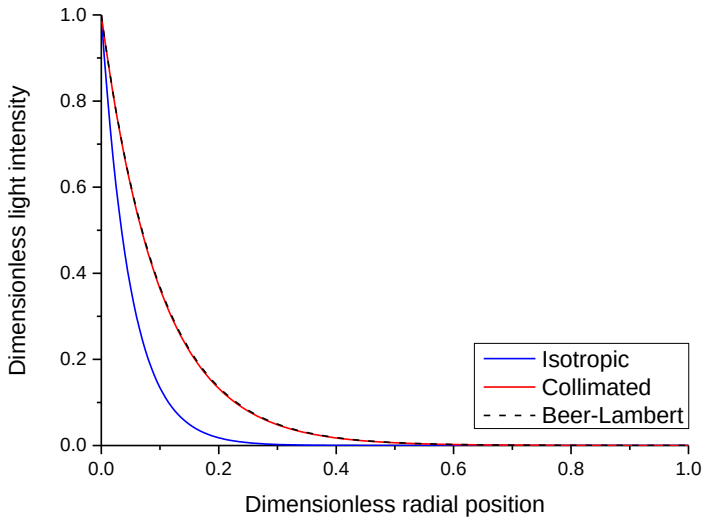


Figure 66 - A comparison of the isotropic and collimated cases used in the two-flux approximation with the Beer-Lambert law used for the excimer flow reactor, with an annular gap of 120 µm, showing the good agreement between the two methods when fully collimated light is used.

Effect of collimation

The effect of collimation was investigated further using an idealised system of annular flow at 1 ml·min^{-1} with a 1 mm gap. The equivalent lamp power as the 308 nm excimer lamp flow, with 0.01 mol·dm^{-3} and total absorption of the medium as 8688 dm^{3}·mol^{-1}·cm^{-1} and molecular diffusion was also assumed. This absorption coefficient value was chosen to match literature values, which carried out an investigation into the effect of mass transfer on reaction rates.[126] The reaction was a simple A → B photoreaction with a quantum yield of 1, with either just A being the only absorbing species (β = 1) or both A and B being equally absorbing (β = 0.5). The normalised light intensity is plotted in Figure 67 with the concentration of A at equilibrium shown in Figure 68, for both isotropic and collimated cases.

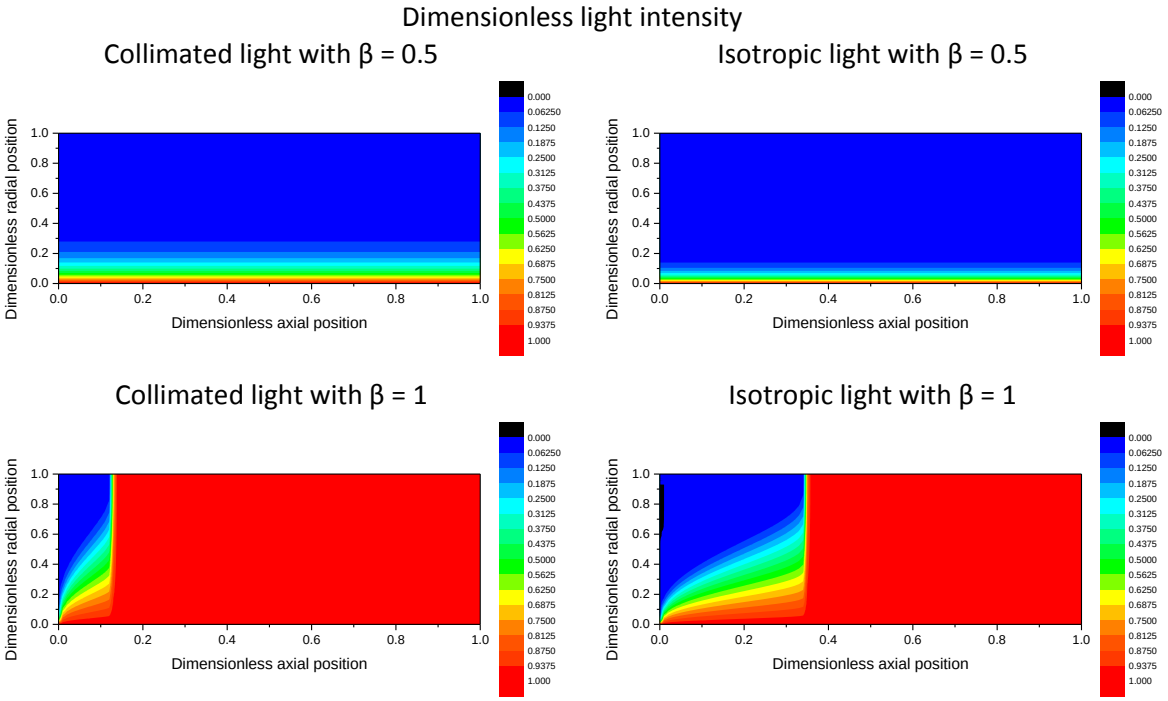


Figure 67 - The dimensionless light intensity when either collimated light is used with a singular absorbing species or a competing absorption is occurring. The effect of isotropic light compared to the collimated light was the greater attenuation of light, while the competing absorption factor means that light is attenuated all along the reactor whereas with a singularly absorbing species the reactor becomes irradiated throughout as the absorbing reactant is consumed.

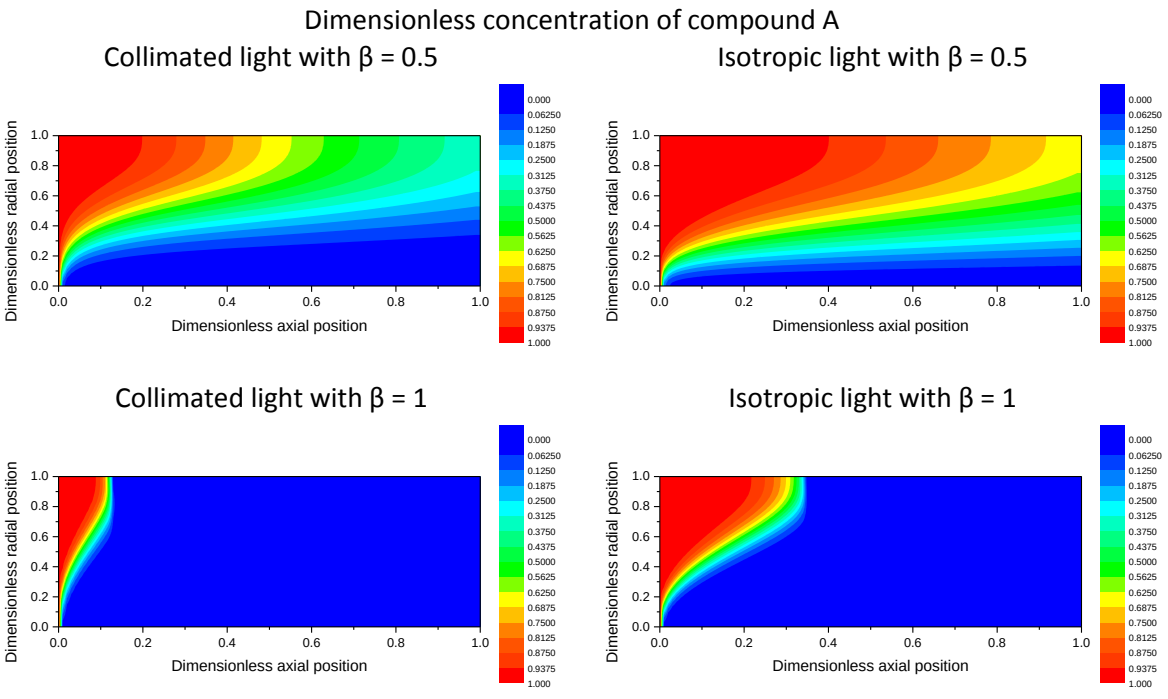


Figure 68 - The dimensionless concentration of compound A when either collimated light is used with a singular absorbing species or a competing absorption is occurring. The effects of collimation were similar to the attenuation of light and with the singularly absorbing species meant the absorbing reagent was consumed.

The major differences shown between the models in Figure 67 were the distance which the light passed into the reactor with either isotropic or collimated light. This distance was shown to affect the outcome of the reaction in this case, as shown with the concentration of A in Figure 68. The yield for the collimated model with β = 0.5 was 84 %, while the isotropic model produced a yield of 58 %. As the collimation factor for the different excimer lamps was unknown, the fully collimated case was chosen for future calculations for consistency with literature.[156,174]

4.6.3. Lamp power and actinometry

The irradiance power for the lamp was provided by the manufacturer's specifications when installed. For the modelling of the reactors, there were two options for the choice of the lamp power to be used in the calculations; using the manufacturer's specification or using actinometry to measure the amount of light absorbed.

Actinometry has previously been attempted within the group, with the lamp power for the excimer flow lamp at 308 nm, using azobenzene, being estimated at 2.46 x 10^{-8} eins·s^{-1}·cm^{-1} which is 20 % of the manufacturer's specification.[318] For the 222 and 282 nm flow lamps actinometry was attempted using uridine, however results were inconclusive as the flowrates required to produce reliable calculations produced a backpressure above the safety limit of the reactors. Considering this, for further calculations, the manufacturer's specification was used.[318]

4.6.4. Excimer flow reactor

The excimer flow reactor has a small irradiated volume (1.37 cm^3) with an annular gap of 120 µm. This small gap allowed higher concentrations to be used than with comparable batch reactors as a high proportion of the fluid is irradiated. As mentioned previously, the small gap also has some disadvantages as large flowrates cannot be used due to safety concerns with the build-up of back pressure.

Flow regime

The introduction of a flow regime to the reactor meant an equation was needed to govern the movement of the fluid throughout the reactor. The equation for the velocity profile, $u(r)$, with the radial position, r, is shown in Equation 28, where μ is the kinematic viscosity. The pressure drop, $\frac{dP}{dL}$, was calculated using the Darcy-Weisbach equations, as previously defined in Equation 5, where f_D is the Darcy friction factor, ρ is the density, v is the fluid velocity and D_H is the hydrodynamic diameter.[88]

$$u(r) = \frac{1}{4\mu}\frac{dP}{dL}\left[(R_2^2 - r^2) - (R_2^2 - R_1^2)\left(\frac{ln\left({R_2}/{r}\right)}{ln\left({R_2}/{R_1}\right)}\right)\right] \tag{53}$$

$$\frac{dp}{dz} = f_D\frac{\rho}{2}\frac{\langle v\rangle^2}{D_H} \tag{5}$$

The f_D was equal to $\frac{64 \times 1.49}{Re}$ as expected for laminar flow in an annular pipe, where Re is the Reynolds number calculated as shown in Equation 95, where v is the linear velocity of the fluid and L is the length of the reactor.[77]

$$Re = \frac{\rho v L}{\mu} \tag{95}$$

Due to the small annular gap the shape of the profile was very similar to that for infinite parallel plates where u_{max} is 1.5 times u_{avg}, as can be seen with the velocity profile shown in Figure 69.[265]

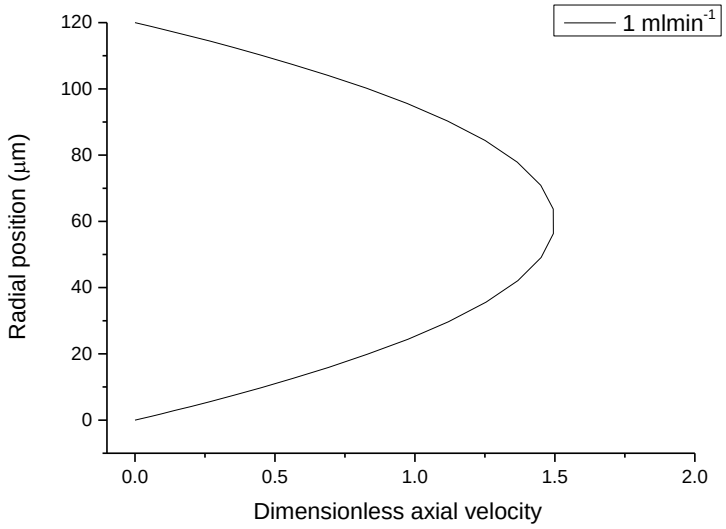


Figure 69 - The dimensionless velocity profile of the annular excimer reactor, where the maximum velocity is 1.5 times the average velocity, similar to the theoretical maximum for flow between two parallel plates.[265]

For consistency the residence time distribution (RTD), or $\mathbf{E_\theta}$ curve, of the Excimer reactor governed by this flow equation was checked against the CFD model to show both models were consistent. A molecular diffusion coefficient of 1 x 10^{-5} $cm^2 \cdot s^{-1}$ was used as this a typical value for these conditions.[319] A pulse of material was injected into the reactors and the output of the reactors was observed over time. The result of this RTD is shown in Figure 70, where $\mathbf{E_\theta} = \bar{t}\mathbf{E}$ and $\bar{t}$ is the average residence time expected as per the flow rate and reactor volume.[229] The legend shows the number of discretisation points used for each dimension, with 3000 axial and 50 radial discretisation points, which showed good agreement with the CFD model. These findings showed that the models were in agreement as the difference was due to numerical diffusion in the PDE solvers, rather than the underlying equations.[279,320] The 3000 axial and 50 radial discretisation points took 48 hours to compute within gPROMS, compared to less than 5 minutes for the 200 axial and 20 radial discretisation points case. This smaller number of discretisation points was considered to be sufficiently accurate because the gradients of concentration were not expected to be as high as the injected pulse used in these experiments.

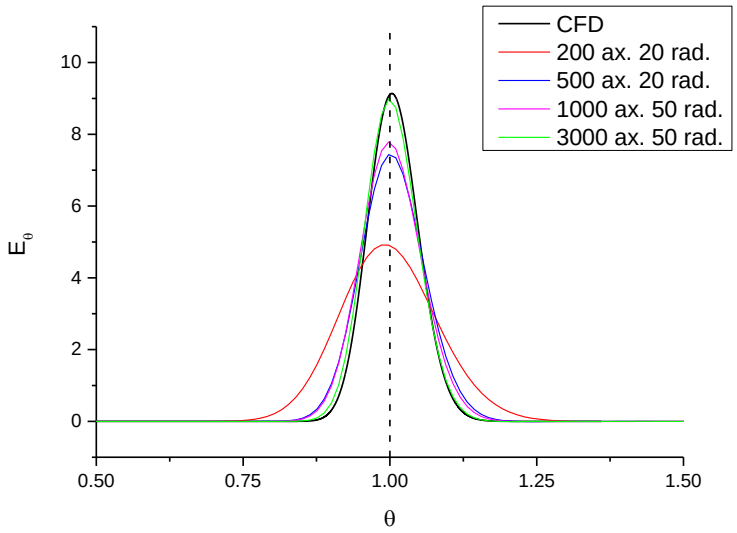


Figure 70 - The E_θ curve for the Excimer reactor using a number of different mesh sizes compared with the CFD model of the excimer reactor.[229] The increasing accuracy with discretisation points showed the difference was due to numerical diffusion, rather than a difference in the models.

4.6.5. Excimer batch reactor

The excimer batch reactor is a cylindrical reactor that is placed inside of the wide-bore excimer lamps and irradiated from the outside. However, it had a much greater irradiated volume (*ca.* 120 cm^3) than the excimer flow reactors. The excimer batch models used the two-flux approximation as described above, with a higher number of discretisation points due to the larger radius (1.27 cm). The excimer batch reactors also have a small stirrer in the centre to ensure mixing; the effectiveness of this stirrer is discussed later.

4.7. Excimer flow results

The excimer flow model described above was then used with experimental data to investigate the robustness and predictive capabilities of the model. Firstly, the isomerisation of 2-pyridone is presented as the quantum yield has been reported in the literature; it was used as a test case for model validity.[321] The gPROMS model is also compared to a literature method for calculating the quantum yield from experimental values.[156] This literature method was then used alongside the gPROMS process model to calculate the quantum yields of a decarboxylative cyclisation reaction. The

gPROMS model was used to predict quantum yields when the literature method becomes invalidated. The modelling of a third reaction in the excimer flow reactor, the formation of Cookson's dione, is subsequently presented.

After experimental results were validated with the excimer flow, similar principles were applied to the excimer batch reactor to predict both quantum yields and reaction performance for two photosensitised reactions.

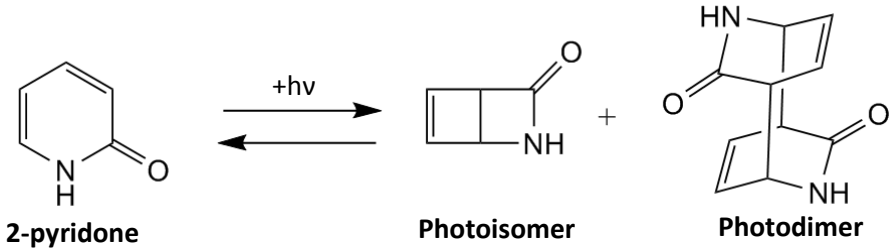
4.7.1. 2-Pyridone Isomerisation

The experiments and measurements for the isomerisation of 2-pyridone were carried out by my colleague and PhD student Toby Waldron-Clarke.

The absorption of a photon by 2-pyridone can cause two separate photoreactions, forming either the photoisomer or photodimer. The quantum yield of both reactions has been reported in the literature as 2.60 % in aqueous solution. [321]

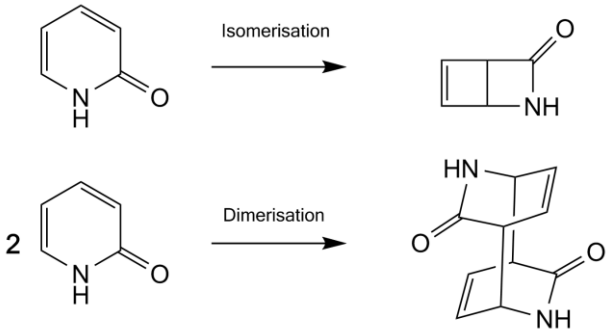
The overall reaction is shown in Scheme 3, where a photochemical reaction step formed the products, which can then thermally relax back into the 2-pyridone species. For this reaction, it was assumed that the backwards step was minimal in the reaction time taken and hence could be ignored.[321]

Scheme 3 - The overall reaction for the photoisomerisation of 2-pyridone. The reverse reaction is a thermal process, which was assumed to be negligible with the timescale of the reaction considered in this work.[321]



The process model used was the previously described excimer model at 308 and 282 nm. For the process model, the reaction was separated into two distinct reactions that could be inputted into the model. The two reactions were called the 'isomerisation' and 'dimerisation', as described in Scheme 4.

Scheme 4 - The separated reactions that can occur with the absorption of a photon by 2-pyridone, with an isomerisation and a dimerization the possible reactions.



The UV/Vis absorption spectrum for 2-pyridone, shown in Figure 71, at 1 x 10^{-4} mol·dm^{-3} in water, with the molar absorption coefficient at the relevant wavelengths is shown in Table 25. The UV/Vis absorption spectrum for both the isomer and dimer products showed no absorption in the relevant region, which was expected due to the loss of aromaticity.[322]

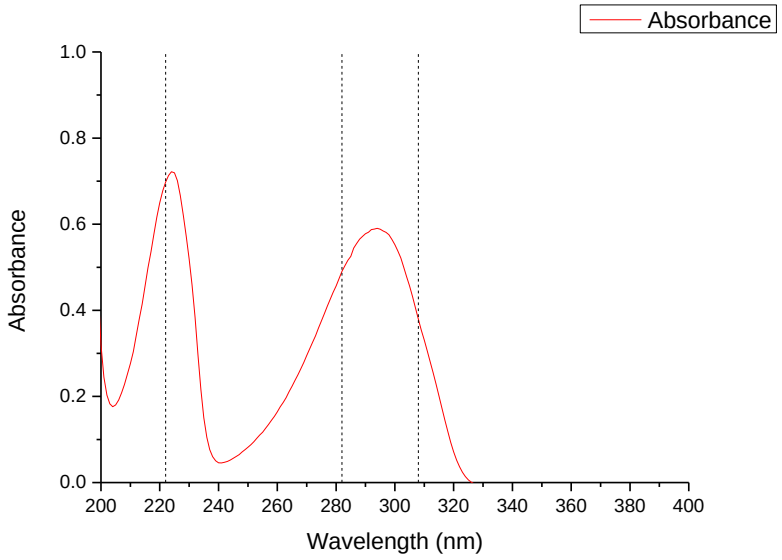


Figure 71 - The UV/Vis spectrum of 2-pyridone at 1 x 10^{-4} mol·dm^{-3} in acetonitrile, with 222, 282 and 308 nm wavelengths highlighted as they are relevant to the excimer lamps used for this work.

Table 25 - The decadic molar absorption coefficients for 2-pyridone at 222, 282 and 308 nm, with these values used within the reactor model to understand the absorption of light.

Wavelength (nm)	**222**	**282**	**308**
Molar Absorption Coefficient of 2-pyridone (mol dm^{-3} cm^{-1})	7109	4700	4093

Experimental results

The photoreaction of 2-pyridone to form the photoisomer and photodimer was carried out at three different concentrations within the Excimer flow reactors. At each concentration, 5 different flowrates were used for the different wavelengths. The yields of the isomer, dimer and recovery of the starting material were calculated using ^{1}H Nuclear Magnetic Resonance (NMR) with external standard, with the results and conditions shown in Table 26. The experiments used for the estimation are shown in black, with the experiments used for the internal validation shown in **red**. The experiments chosen for the validation were outside of the experimental space of those used in the estimation, to highlight the model's robustness and predictive capabilities.

Table 26 - The experimental results for the 2-pyridone experiments for the Excimer flow reactors at 308 and 282 nm at a range of flowrates and concentrations. The yields were calculated by ^{1}H NMR using an internal standard.

Concentration ($mol \cdot dm^{-3}$)	Flow Rate ($cm^3 min^{-1}$)	Photoproduct yield (%)	Dimer Yield (%)	SM recovered (%)	Mass balance (%)
		308 nm			
0.01	0.2	61	11	17	89
	0.67	28	7	52	87
	0.8	26	7	58	90
	1	22	5	63	90
	1.5	16	4	70	91
	2	13	3	74	91
0.02	0.2	44	9	29	82
	0.67	18	8	62	88
	0.8	16	7	65	88
	1	14	6	69	89
	1.5	10	5	75	90
	2	8	4	79	91
0.03	0.2	32	15	36	84
	0.67	13	11	64	87
	0.8	12	10	67	88
	1	10	6	71	87
	1.5	8	5	81	93
	2	6	4	83	93
		282 nm			
0.01	0.2	65	10	12	87
	0.67	35	8	48	91
	0.8	30	7	54	91
	1	26	6	59	91
	1.5	20	5	67	92
	2	16	4	72	92
0.02	0.2	54	19	20	93
	0.67	23	10	57	90
	0.8	21	9	61	91
	1	15	7	68	90
	1.5	11	5	73	89
	2	9	4	77	90
0.03	0.2	39	19	28	90
	0.67	16	11	60	87
	0.8	14	10	62	86
	1	12	8	67	87
	1.5	9	6	74	89
	2	7	5	77	89

Aillet method for quantum yield estimation of 2-pyridone

The calculated 'Aillet value', shown in red in the previously defined Equation 23, was plotted against the residence time, with the gradient of this graph is equal to $\Phi \frac{I^{W,photon}}{\Delta c}$. The gradient can be used to calculate the quantum yield as the photon irradiance, $I^{W,photon}$ is known.

$$C_{A0}\left(X + \frac{1}{B_0} ln\left[\frac{1 - e^{-B_0}}{1 - e^{-B_0(1-X)}}\right]\right) = \Phi \frac{I^{W,photon}}{\Delta c} t \qquad (23)$$

For both wavelengths the results from the 0.2 ml·min^{-1} experiments were ignored as the residence time (410 s) were much greater than the others and skewed the data as the conversion reached a limit.

Aillet method at 308 nm

The graph of the calculated 'Aillet value' for the experiments at 308 nm plotted against residence time is shown in Figure 72. The slope of the graph for 308 nm, $\Phi \frac{I^{W,photon}}{\Delta c}$, is equal to 5.59 x 10^{-5} mol·dm^{-3}·s$^{-1,}$ which, with the lamp manufacturer's specification, gave a quantum yield of 0.54 %. If the literature value of the quantum yield of 2.60 % is fixed, the lamp power was equal to 21 % of the lamp manufacturer's specification.[321] It should be noted that the 21 % was also the value calculated with the initial actinometry tests at 308 nm completed in the group previously.[318]

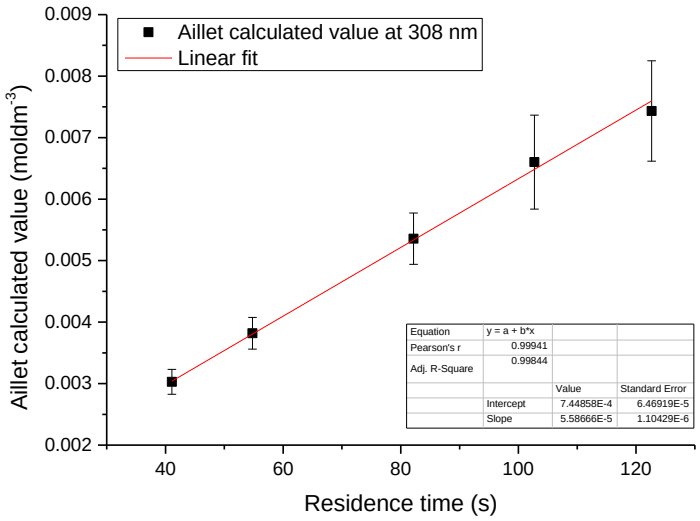


Figure 72 - The calculated Aillet value plotted against residence time for 2-pyridone at 308 nm. The gradient and intercept used in the calculation of the Aillet value were 5.59 x10^{-5} mol·dm^{-3}·s^{-1} and 7.45 x 10^{-4} mol·dm^{-3}, respectively.

Aillet method at 282 nm

The graph of the calculated 'Aillet value' for the experiments at 282 nm plotted against residence time is shown in Figure 73. The slope of the graph for 282 nm, $\Phi \frac{I^{W,photon}}{\Delta c}$, is equal to 6.15 x 10^{-5} mol·dm^{-3}·s^{-1} which, with the lamp manufacturer's specification, gave a quantum yield of 0.88 %. If the literature value of the quantum yield of 2.60 % is fixed, the lamp power was equal to 36 % of the lamp manufacturer's specification.[321]

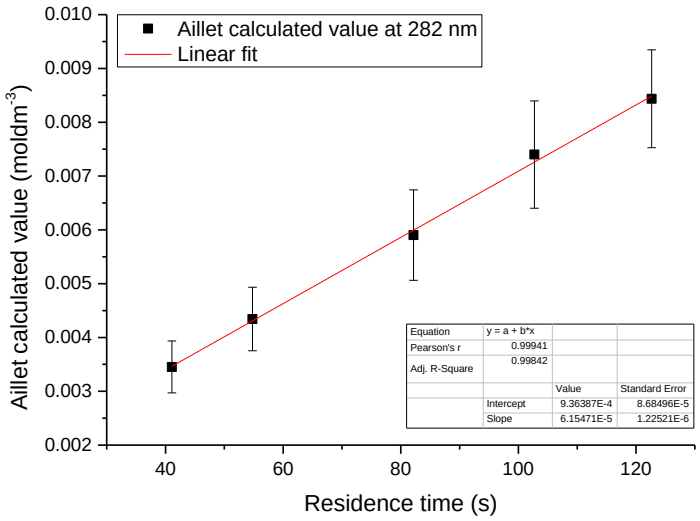


Figure 73 - The calculated Aillet value plotted against residence time for 2-pyridone at 282 nm. The gradient and intercept used in the calculation of the Aillet value were 6.15 x10^{-5} mol·dm^{-3}s^{-1} and 9.36 x 10^{-4} mol·dm^{-3}, respectively.

For the Aillet method the value of the quantum yield was largely dependent on the lamp power used in the calculation, which was to be expected. A comparison with the parameter estimation method of the quantum yield for the photoreaction of 2-pyridone is shown below using both the lamp manufacturers specified lamp power and the lamp power calculated using the Aillet method to match the literature quantum yield.[321]

Parameter estimation strategy

The estimation of the quantum yield of the photoreaction of 2-pyridone used the experimental results shown in black in Table 26. Initially the quantum yields were estimated using the experimental yields for the product yields and starting material recovery, at both the manufacturer's quoted lamp power and the lamp power predicted by Aillet's method to match the literature value.[321] After the initial estimation is estimated using the original experimental data, further estimations were carried out where the inputted data were processed in order to improve the accuracy of the prediction.

For the estimations outlined below, just the results predicted in the validation of the model are shown, as the results used in the estimation are expected to be close to the experimental values. A more in-

depth comparison of the values used for the estimation and validation is shown later, to highlight the similarities in results between the two lamp powers.

gPROMS Parameter estimation at 308 nm

Using initial experimental data (308 nm)

The original experimental data was used in the initial estimation of the quantum yields. The standard deviation of the sensors for each component was initially assumed to be 5 %, as per expectations for ^{1}H NMR yields with internal standards. However, the initial estimations failed to converge and hence the uncertainty of the sensor was unknown and had to be estimated. The predicted experimental values for each lamp power are shown in Figure 74, while the respective estimated quantum yields are shown in Table 27 with the standard deviation (SD) shown in brackets.

Table 27 - The estimated quantum yields for both the isomerisation and dimerisation of 2-pyridone at 308 nm using all of the experimental data with the manufacturers lamp power specification and the power predicted as per Aillet's method.

Lamp Power	ϕ_{isom} (% ±SD)	ϕ_{dim} (% ±SD)	Correlation	RMSE of value (%)
100%	0.339 (±0.024)	0.040 (±0.005)	0.219	8.69
21%	1.615 (±0.116)	0.189 (±0.026)	0.219	8.69

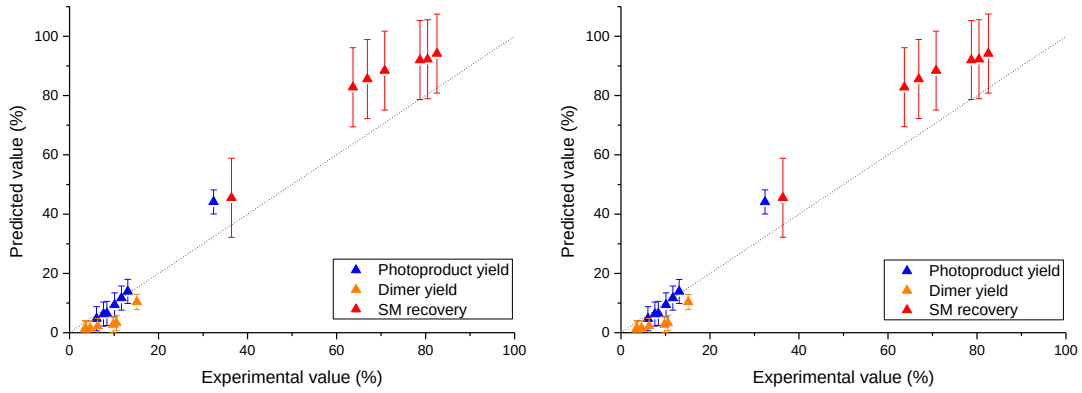


Figure 74 - The predicted model results using the estimated parameters using the raw experimental data for the isomerisation of 2-pyridone at 308 nm. With (a) the manufacturers specification and (b) 21% of the manufacturers specification as estimated by Aillet's calculations.

The most obvious issue with this prediction was the lack of fit for the starting material recovery in the estimations using the original experimental data, shown in Figure 74, which meant that the predictions

made by the model were not validated. This was not unexpected as the experimental mass balance showed a consistent loss of *ca.* 10 %, which was not considered in the kinetic model for this estimation.

It was observed that if the recovery of the starting material is ignored in the calculation of the Root Mean Squared Error (RMSE), the value is reduced 3.28 %, suggesting the model could better predict the experimental results of the photoproduct and dimer.

Experimental data without the recovery of starting material (308 nm)

As the previous estimation suggested the model could predict the experimental results of the photoproduct and dimer well, the recovery of the starting material was ignored in the next estimation. A fixed standard deviation of 5 % was used for both sensors in this estimation as the previous estimations had suggested values around *ca.* 3.5 % for the estimation, which meant some of the validated results were outside of this range. A standard deviation of 5 % is also widely accepted for experimental values calculated by ^{1}H NMR with an internal standard. The predicted experimental values for each lamp power are shown in Figure 75, while the respective estimated quantum yields are shown in Table 28.

Table 28 - The estimated quantum yields for both the isomerisation and dimerisation of 2-pyridone at 308 nm using the experimental data for the photoproduct and dimer, without the starting material recover, for the manufacturers lamp power specification and the power predicted as per Aillet's method.

Lamp Power	ϕ_{isom} (% ±SD)	ϕ_{dim} (% ±SD)	Correlation	RMSE of value (%)
100 %	0.321 (±0.023)	0.038 (±0.009)	0.299	3.81
21 %	1.527 (±0.110)	0.181 (±0.043)	0.300	3.81

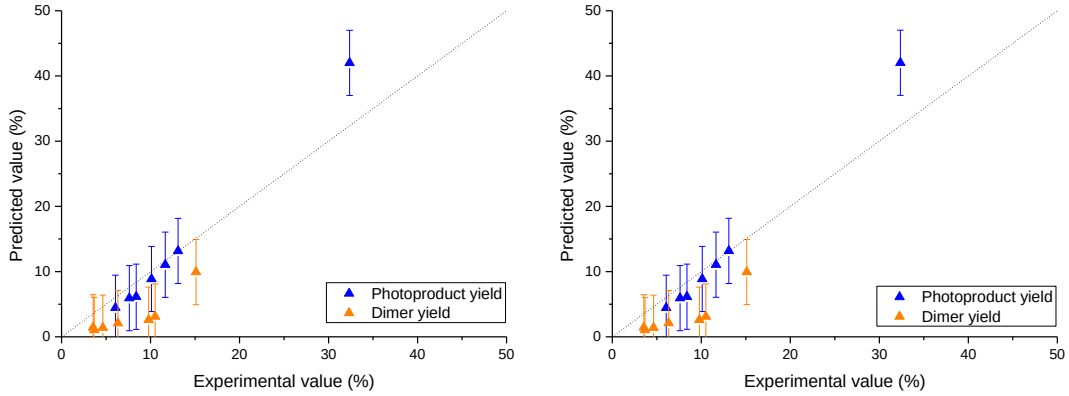


Figure 75 - The predicted model results using the estimated parameters from the experimental data for the photoproduct and dimer for the isomerisation of 2-pyridone at 308 nm without the starting material recovery. With (a) the manufacturers specification and (b) 21 % of the manufacturer's specification

The results for this estimation did not show an obvious error and improved the RMSE compared to the previous estimation. This inconsistent result was for the slowest flowrate, 0.2 ml·min^{-1}, and can be seen *ca.* 32 % in Figure 75.

Normalised experimental data (308 nm)

As mentioned with the initial estimation, the loss in mass balance was not previously considered. The experimental data used for the estimation were normalised using the mass balance of each reaction, as shown in Equation 96, with the quantum yield then estimated using the normalised data.

$$Yield^{A}_{norm} = \frac{Yield^{A}}{Mass\ balance} \tag{96}$$

The experimental values were predicted for the experiments used in the validation. As these predicted values were normalised, the data was 'un-normalised' using the average mass balance of the experiments used in the estimation. The results for this normalisation process are shown in Figure 76 (a) and (b) for 100 % and 30 % lamp power, respectively. Again, a standard deviation for the normalised sensors was 5 %, which was slightly reduced when *un-normalised*.

Table 29 - The estimated quantum yields for both the isomerisation and dimerisation of 2-pyridone at 308 nm using the normalised experimental data with the manufacturers lamp power specification and the power predicted as per Aillet's method.

Lamp Power	ϕ_{isom} (% ±SD)	ϕ_{dim} (% ±SD)	Correlation	RMSE of value (%)
100 %	0.399 (±0.019)	0.047 (±0.008)	-0.147	3.76
21 %	1.902 (±0.091)	0.226 (±0.037)	-0.146	3.76

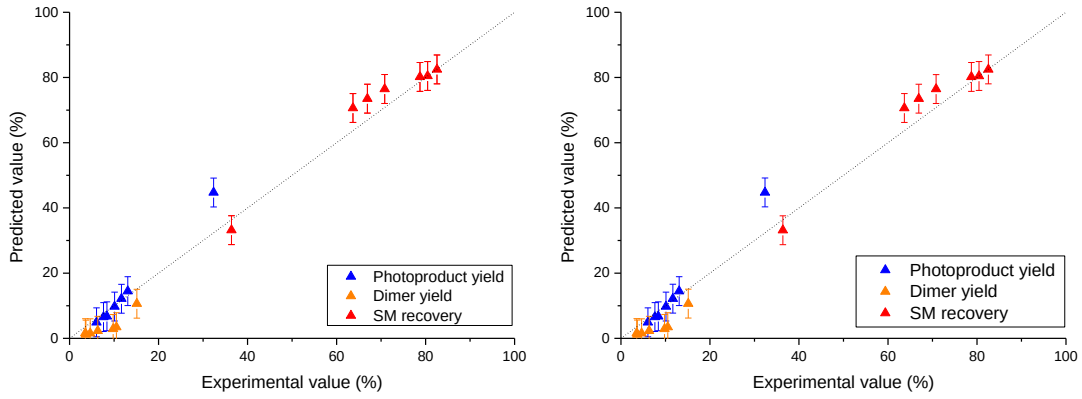


Figure 76 - The predicted model results using the estimated parameters from the normalised experimental data for the photoproduct and dimer for the isomerisation of 2-pyridone at 308 nm. With (a) the manufacturers specification and (b) 21 % of the manufacturer's specification.

The normalisation process produced the best prediction for all of the experimental data used, but also involved the most data processing outside of the parameter estimation, which shows the balance that needs to be made between data processing and experimental values.

Parameter estimation at 282 nm

For the estimations carried out at 282 nm, the same estimations were carried out as those with 308 nm. The reduced lamp power was 36 % of the manufacturer's specification as calculated using Aillet's method. For consistency, the same process was followed for the results at 282 nm, with a more simplified description of each result given as the results were similar to the results at 308 nm.

Using initial experimental data (282 nm)

Similarly to the estimation using the original experimental results at 308 nm, the predicted values at 282 nm also showed a large uncertainty for the recovery of the starting material. A comparison

between the experimental results and predicted results for the original experimental results at 282 nm is shown in Figure 77, with the respective estimated quantum yields shown in Table 30.

Table 30 - The estimated quantum yields for both the isomerisation and dimerisation of 2-pyridone at 282 nm using the raw experimental data with the manufacturers lamp power specification and the power predicted as per Aillet's method.

Lamp Power	ϕ_{isom} (% ±SD)	ϕ_{dim} (% ±SD)	Correlation	RMSE of value (%)
100 %	0.624 (±0.039)	0.097 (±0.031)	-0.0127	7.46
36 %	1.732 (±0.109)	0.269 (±0.087)	-0.00867	7.46

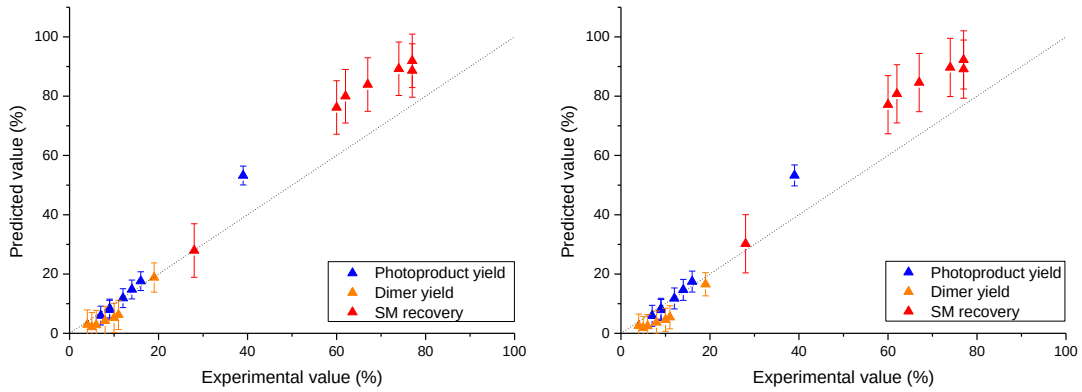


Figure 77 - The predicted model results using the estimated parameters from the raw experimental data for the isomerisation of 2-pyridone at 282 nm. With (a) the manufacturers specification and (b) 36 % of the manufacturer's specification

Experimental data without the starting material (282 nm)

Similarly to the results at 308 nm the results were predicted well, with an outlier for the slower flowrate of 0.2 ml·min^{-1}. A comparison between the experimental results and predicted results for the estimation ignoring the starting material recovery at 282 nm is shown in Figure 78, with the respective estimated quantum yields shown in Table 31.

Table 31 - The estimated quantum yields for both the isomerisation and dimerisation of 2-pyridone at 308 nm using the experimental data for the photoproduct and dimer without the starting material recovery, for the manufacturers lamp power specification and the power predicted as per Aillet's method.

Lamp Power	ϕ_{isom} (% ±SD)	ϕ_{dim} (% ±SD)	Correlation	RMSE of value (%)
100 %	0.585 (±0.040)	0.082 (±0.014)	0.382	4.04
36 %	1.624 (±0.080)	0.227 (±0.040)	0.381	4.04

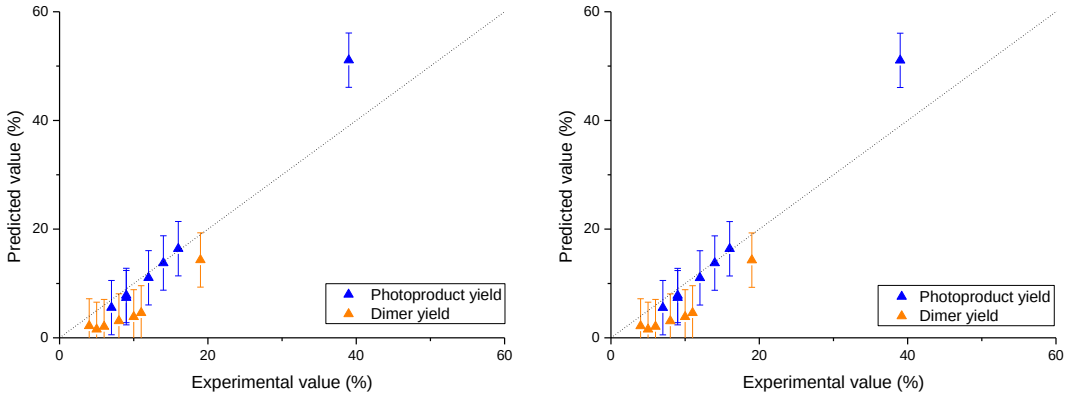


Figure 78 - The predicted model results using the estimated parameters from the experimental data for the photoproduct and dimer for the isomerisation of 2-pyridone at 282 nm without the starting material recovery. With (a) using the manufacturers specification and (b) 21 % of the manufacturer's specification

Normalised experimental data (282 nm)

The estimation for the normalised results at 282 nm showed the best predictive performance, which matches those observed with the results at 308 nm. The predicted results are shown in Figure 79, with the estimated parameters shown in Table 32. Again, there was an outlier at 0.2 ml·min^{-1} which overestimated the yield of the photoproduct.

Table 32 - The estimated quantum yields for both the isomerisation and dimerisation of 2-pyridone at 282 nm using the normalised experimental data with the manufacturers lamp power specification and the power predicted as per Aillet's method.

Lamp Power	ϕ_{isom} (% ±SD)	ϕ_{dim} (% ±SD)	Correlation	RMSE of value (%)
100 %	0.696 (±0.032)	0.095 (±0.012)	-0.073	4.34
36%	1.375 (±0.063)	0.187 (±0.024)	-0.073	4.34

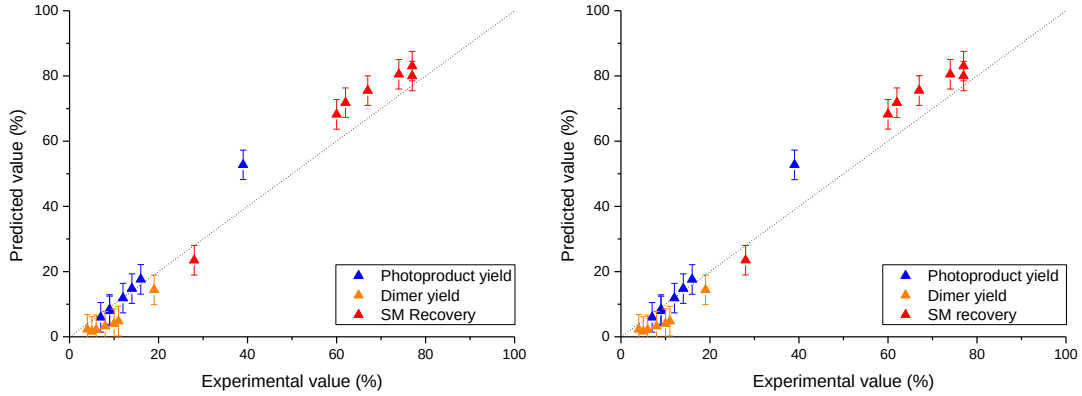


Figure 79 - The predicted model results using the estimated parameters from the experimental data for the photoproduct and dimer for the isomerisation of 2-pyridone at 282 nm. With (a) the manufacturers specification and (b) 36 % of the manufacturer's specification.

Summary of parameter estimations for photoreaction of 2-pyridone

The similarities between the predictions at different lamp powers showed that the predicted quantum yield values largely relied on the lamp power used in the calculations. The value of the quantum yield for the reduced power estimation was almost identical to the equivalent percentage of the quantum yield of the full power estimation, which can be seen in Table 33. The combined quantum yield of 2.13 % for the normalised reaction at 308 nm is similar to the 2.60 % quoted in literature.[321]

Table 33 - A comparison of the estimated quantum yields at both 308 and 282 nm for the different techniques used to treat the data, with the manufacturer's lamp power specification and the value predicted by Aillet's method.

Wavelength (nm)	Data set	Lamp Power	ϕ_{isom} (% ±SD)	ϕ_{dim} (% ±SD)	RMSE of value (%)
308	Original data	100	0.339 (±0.024)	0.040 (±0.005)	8.69
		21	1.615 (±0.116)	0.189 (±0.026)	8.69
	No SM sensor	100	0.321 (±0.023)	0.038 (±0.009)	3.81
		21	1.527 (±0.110)	0.181 (±0.043)	3.81
	Normalised	100	0.399 (±0.019)	0.047 (±0.008)	3.76
		21	1.902 (±0.091)	0.226 (±0.037)	3.76
282	Original data	100	0.624 (±0.039)	0.097 (±0.031)	7.46
		36	1.732 (±0.109)	0.269 (±0.087)	7.46
	No SM sensor	100	0.585 (±0.040)	0.082 (±0.014)	4.04
		36	1.624 (±0.080)	0.227 (±0.040)	4.04
	Normalised	100	0.696 (±0.032)	0.095 (±0.012)	4.34
		36	1.375 (±0.063)	0.187 (±0.024)	4.34

For a comparison between both methods a combination of the quantum yields estimated using MLE is required because Aillet's method uses the total conversion to calculate the quantum yield. A simple addition of the two quantum yields for the isomerisation and dimerization reactions was carried out. For both wavelengths the best match between the quantum yields estimated using MLE and Aillet's method were with the normalised method, a comparison at both wavelengths is shown in Table 34. Although the results were not identical, they were considered sufficiently similar, considering the different assumptions made within the two models.

Table 34 - A comparison between both the Aillet and MLE method for estimating quantum yields. The red entries show that these values were fixed so that the lamp power could be estimated.

		Estimated combined quantum yield (% ±SD)	
Wavelength	Lamp power	Aillet method	MLE method
308	100 %	0.54 (±0.01)	0.45 (±0.02)
	21 %	2.60 (±0.05)	2.13 (±0.10)
282	100 %	0.88 (±0.02)	0.79 (±0.03)
	36 %	2.60 (±0.05)	2.19 (±0.09)

The formation of the dimer product also had a concentration effect which was not considered within the model and would have added uncertainty to the estimated values. This concentration effect of the formation of the dimer can be seen in Figure 80, where the ratio of the product formation to the dimer formation shows a significant step effect with each concentration.

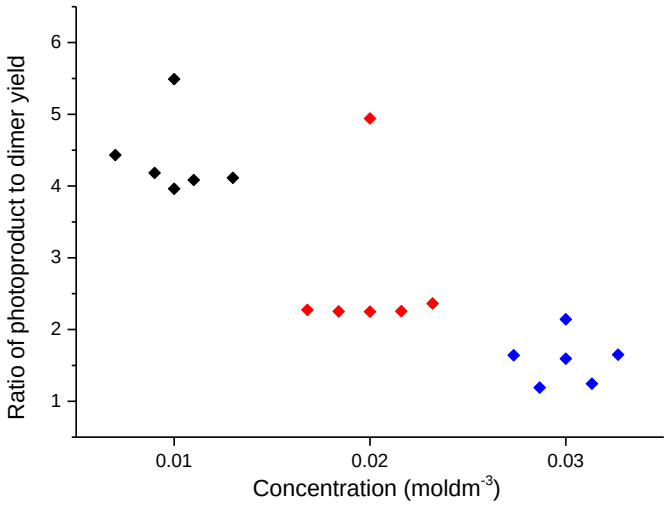


Figure 80 - The ratio of the photoproduct to the dimer at three different starting concentrations, showing the dependence of the dimer formation on concentration.

The above results demonstrated the possibility of using the gPROMS model for both predicting reaction performance and, assuming an accurate lamp power can be used, quantum yield estimation. In subsequent calculations the manufacturer's specification was used as the aim of the process model development was to be used for performance prediction, rather than quantum yield estimation. Also, as there are a number of Excimer lamps available within the laboratory and quantum yields vary with both wavelength and reaction, there was not a consistent way to compare relative efficiencies. Previous attempts at actinometry had also shown high uncertainty and a potential safety issue due to high flowrates, and hence back-pressure, associated with the glass excimer reactors.[318]

4.7.2. Photodecarboxylative cyclisation of potassium *N*-phthalimidobutanoate

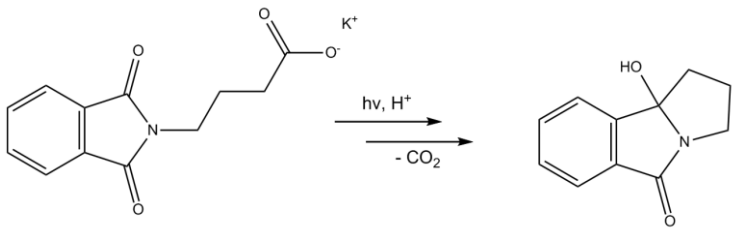
The experiments and measurements for the photodecarboxylative cyclisation of potassium *N-phthalimidobutanoate were carried out by colleague Dr. Erica DeLaney and have been published.*[186]

The photodecarboxylative cyclisation of pthalimides has been widely studied due to its importance in synthetic organic chemistry.[323–328] These reactions can be either inter or intra-molecular reactions to efficiently form products with benign CO_2 being the only waste product. Another benefit of these

reactions is that they can be carried out in aqueous mixtures with organic solvents such as acetone or acetonitrile.

For intramolecular versions of this reaction the decarboxylation only occurs at the α-position when carboxylic acids are used. However, by producing the potassium salts of the carboxylic acids the carboxylic groups can be 'activated' such that they will react to form intramolecular ring systems, as shown in Scheme 5.[329–331]

Scheme 5 - The overall reaction scheme of the photodecarboxylative cyclisation of potassium *N*-phthalimidobutanoate to form the tricyclic compound.



Potassium *N*-phthalimidobutanoate **Tricyclic compound**

The photodecarboxylative cyclisation of the potassium salt of potassium *N*-phthalimidobutanoate to form the tricyclic compound, as shown in Scheme 5, was carried out in the Excimer flow reactors. The lamps used for this flow reaction were 222, 282 and 308 nm; at each wavelength eight different experiments were carried out with two different concentrations and four different flowrates.

Experimental results

The experimental results for the photodecarboxylative cyclisation for the are shown in Table 35, with the values used in the estimation shown in black and those used in the model validation shown in red.

Table 35 - The experimental values for the photodecarboxylative cyclisation, with the values shown in red indicating those used in the estimation and those in black indicating those used in the validation.

Wavelength (nm)	Concentration of potassium *N*-phthalimidobutanoate ($mol \cdot dm^{-3}$)	Flow rate ($ml \cdot min^{-1}$)	Yield of product (%)
308	0.1	0.2	89
	0.1	0.5	78
	0.1	1	50
	0.1	1.5	26
	0.2	0.2	96
	0.2	0.5	53
	0.2	1	32
	0.2	1.5	22
282	0.1	0.2	82
	0.1	0.5	74
	0.1	1	61
	0.1	1.5	35
	0.2	0.2	77
	0.2	0.5	63
	0.2	1	39
	0.2	1.5	26
222	0.1	0.2	83
	0.1	0.5	54
	0.1	1	34
	0.1	1.5	22
	0.2	0.2	22
	0.2	0.5	19
	0.2	1	17
	0.2	1.5	11

Model input

The photoreaction was assumed to be a single step for this model, with potassium *N*-phthalimidobutanoate transformed into the tricylcic product, with the rate depending on the absorption of light and quantum yield. The density and viscosity of the solvent were assumed to be the same as standard conditions as the reactor was not heated or under significant pressure.

The UV/Vis spectrum for the potassium *N*-phthalimidobutanoate starting material and tricylic product is shown in Figure 81 (a) and (b), with the corresponding decadic absorption coefficients shown in Table 36; for this reaction, the product was also found to absorb light.

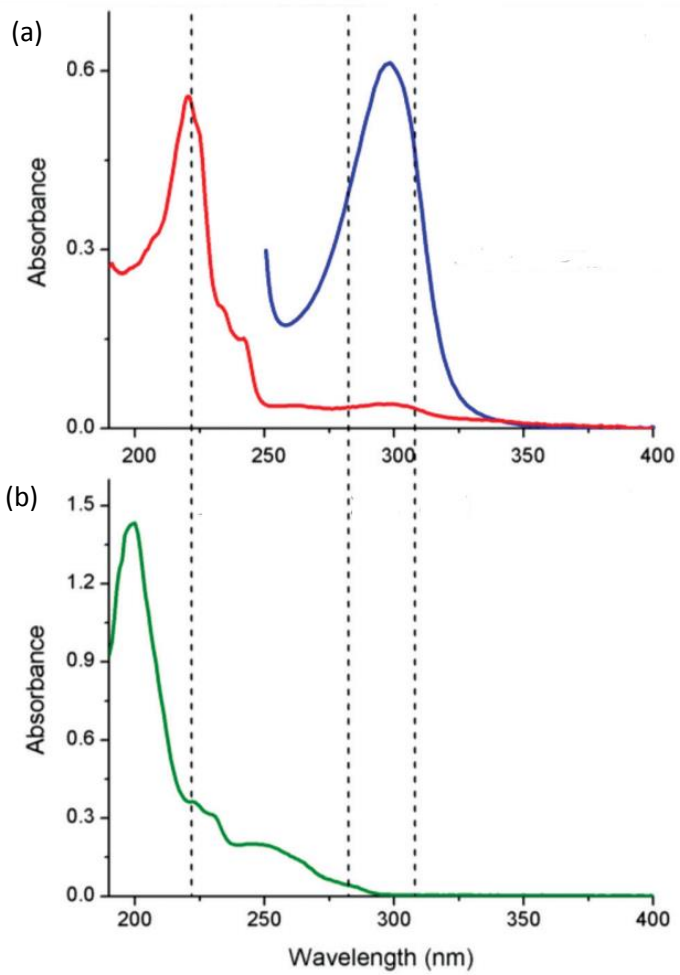


Figure 81 – The UV/Vis absorption spectra for (a) potassium *N*-phthalimidobutanoate starting material in 1:1 acetonitrile:water mixture, with a concentration of 1 x 10^{-5} mol·dm^{-3} shown in red and 2.9 x 10^{-4} mol·dm^{-3} shown in blue and (b) the cyclised product also absorbed light at some wavelengths, with the spectra taken at 5 x 10^{-5} mol·dm^{-3} shown in green. All spectra taken by Dr. Erica Delaney with a 1 cm pathlength and reported in literature.[186]

Table 36 - The molar decadic extinction coefficients for the pthalimide starting material and tricyclic product.

	Molar decadic extinction coefficient (dm^{3}mol^{-1}cm^{-1})		
Compound	**308 nm**	**282 nm**	**222 nm**
Potassium *N*-phthalimidobutanoate	1370	1180	53000
Tricyclic product	100	1000	7400

Photodecarboxylative cyclisation at 308 nm

At 308 nm, potassium *N*-phthalimidobutanoate was the only species found to absorb light and hence the reaction could be considered similar to the isomerisation of 2-pyridone. Both the predicted values used in the estimation and the validation of the model are shown in Figure 82. The estimated quantum yield for the reaction for the reaction at 308 nm was **5.65 ± 0.6 %**, with an RMSE for the predicted values of **6.26 %.** As shown in Figure 82, both the experiments used for the estimation and validation showed good agreement across a wide range of experimental values. The quantum yield, as calculated using Aillet's method was 5.24 ±0.76 %, showing good agreement with the MLE method (See Appendix II for the calculations).

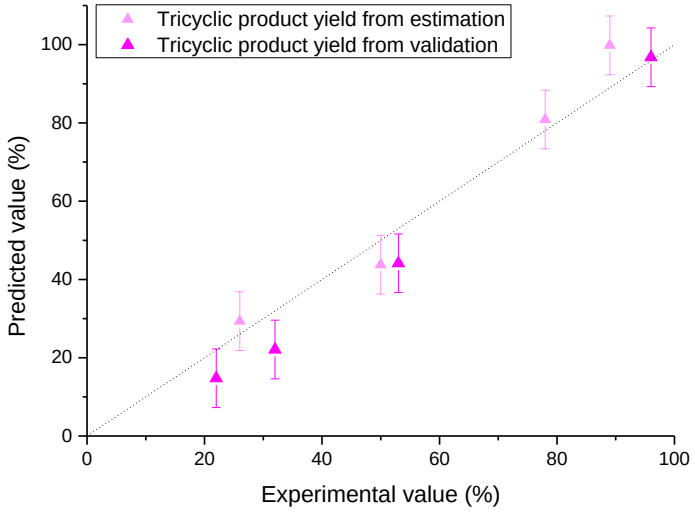


Figure 82 - The predicted values for the photodecarboxylative cyclisation at 308 nm, with the values used in the estimation shown with an increased transparency with the values used in the validation shown in full colour. The error bars are one standard deviation (7.5 %) each way.

Photodecarboxylative cyclisation at 282 nm

At 282 nm the tricyclic product was also found to absorb light and hence there was a competitive feature between the two products for the light. Both the predicted values used in the estimation and the validation of the model are shown in Figure 83. The estimated quantum yield for the reaction at 282 nm was **13.3 ± 1.7 %**, with an RMSE for the predicted values of **8.11 %**.

The quantum yield, as calculated using Aillet's method was 9.30 ±3.69 %, showing a considerable divergence with the MLE method (See Appendix II for the calculations). This divergence between the methods was expected as the assumptions of Aillet's method were no longer valid due to the competing absorption between species.

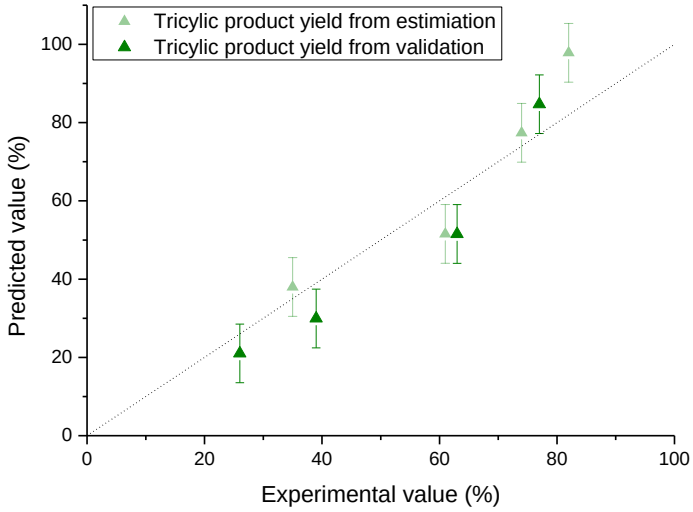


Figure 83 - The predicted values for the photodecarboxylative cyclisation at 282 nm, with the values used in the estimation shown with an increased transparency with the values used in the validation shown in full colour. The error bars are one standard deviation (7.5 %) each way.

Photodecarboxylative cyclisation at 222 nm

Similarly to the reaction at 282 nm, there is a competitive feature for the absorption of light between the two compounds at 222 nm. However, at 222 nm, both the starting material and products are more strongly absorbing than at 282 and 308 nm. For the Aillet method, the highly absorbing species meant the calculated values tend towards $C_{A,0}(1-X)$ and hence little information can be gleaned from the method. However, with the computational model the highly absorbing medium along with the competing absorption can be considered. Both the predicted values used in the estimation and the validation of the model are shown in Figure 84. The estimated quantum yield for the reaction at 222 nm was **13.6 ± 1.6 %**, which is congruent with the value estimated at 282 nm. Although the quantum yield was similar to that at 282 nm, the RMSE for the predicted values was **9.72 %**, which

was greater than the uncertainty of the sensor. This increased RMSE was largely due to the experiment carried out with 0.2 mol·dm^{-3} of the starting material at 0.2 ml·min^{-1}, which the model predicted to give a yield *ca.* 60% yield.

The quantum yield, as calculated using Aillet's method was 6.28 ±1.81 %, showing a considerable divergence with the MLE method (See Appendix II for the calculations). Again, this divergence between methods was expected as the competing absorption between species, and considerably high absorption of a species, meant Aillet's assumptions were no longer valid due.

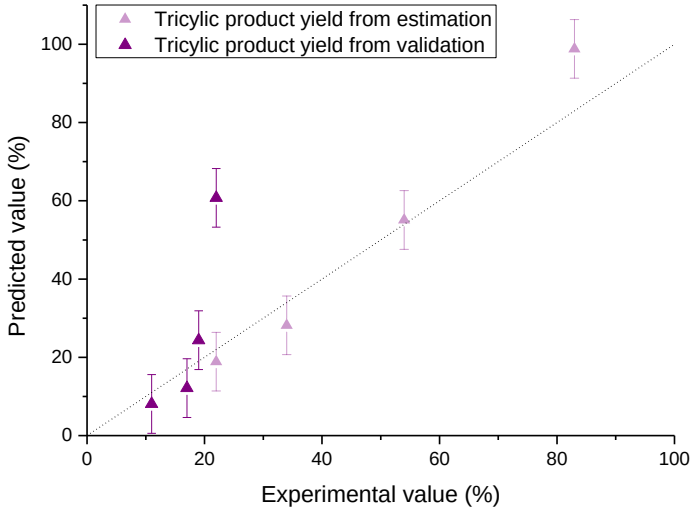


Figure 84 - The predicted values for the photodecarboxylative cyclisation at 222 nm, with the values used in the estimation shown with an increased transparency with the values used in the validation shown in full colour. The error bars are one standard deviation (7.5%) each way. There seemed to be an anomalous data point *ca.* 20 % for the experimental value which is discussed below.

Comparison of all wavelengths

When the Aillet method is valid, with a single absorbing species, both methods showed good agreement. However, as can be seen in Table 37, when the Aillet method becomes invalid the estimated quantum yields diverge, the Aillet calculations can be found in Appendix II. The gPROMS method was considered more valid as the competing absorption of species was accounted for along with the highly absorbing values at 222 nm, whereas the Aillet method becomes invalidated with multiple absorbing species.[156] The standard error of Aillet's method was calculated from the error of

the gradient calculation and the gPROMS MLE method calculated the standard deviation. For 308 nm both show similar values when the Aillet method is valid but diverge when Aillet's method is invalid.

Table 37 - A comparison of the estimated quantum yields at 222, 282 and 308 nm, where the manufacturer's lamp power specification was used, showing good agreement when Aillet's method was valid and a difference when Aillet's method becomes invalidated as per the assumptions used.

	Quantum yield (%)		
Wavelength (nm)	**gPROMS method (±SD)**	**Aillet method (±std. er.)**	**Aillet method valid**
308	5.65 (±0.6)	5.24 (±0.76)	Yes
282	13.3 (±1.7)	9.30 (±3.69)	No
222	13.6 (±1.6)	6.28 (±1.81)	No

When all the predicted results are plotted together, as shown in **Error! Reference source not found.**, it shows that the method is generally robust across all of the wavelengths. However, there were two issues with the initial model; an overestimation of products at high yields and the anomalous result of 0.2 mol·dm^{-3} at 0.2 ml·min^{-1} for the 222 nm Excimer flow lamp.

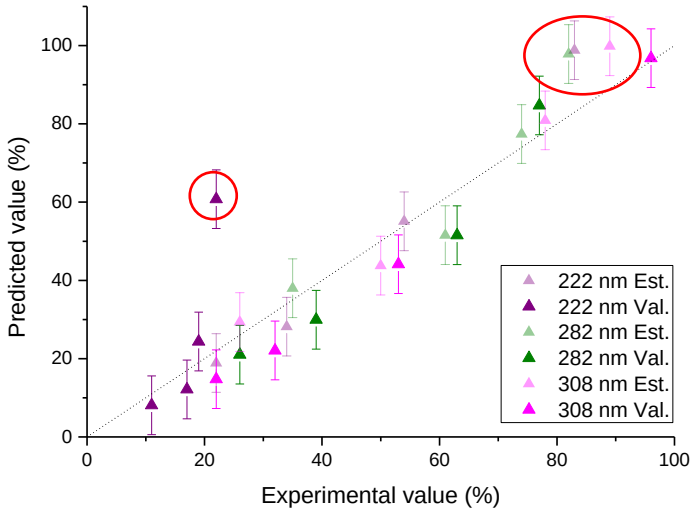


Figure 85 - A comparison of the predicted values for the product yield and the experimental values at 222, 282 and 308 nm. The error bars are one standard deviation (5%) each way, while the red circle highlight possible anomalous results.

Two possibilities were considered for the overestimation of higher yields; the accuracy of the analysis and the breakdown of the product, which the model did not consider or the deposition of a breakdown

product. Firstly, the model and sensors were accurate for the values < 90 % so this was considered unlikely. The breakdown of the product was thought to be possible as initial experiments in a batch system displayed a reduction in yield for long exposure times. To consider this, an alteration was made to the model, so the product could absorb light and react to form an unknown breakdown product. The results for this alteration to the model are shown in Figure 86, where for the higher yields the predicted values are closer to the experimental values. An improved RMSE for the yield, ignoring the anomalous result, of 5.11 % compared to 7.86 % for the single reaction highlights the improvement.

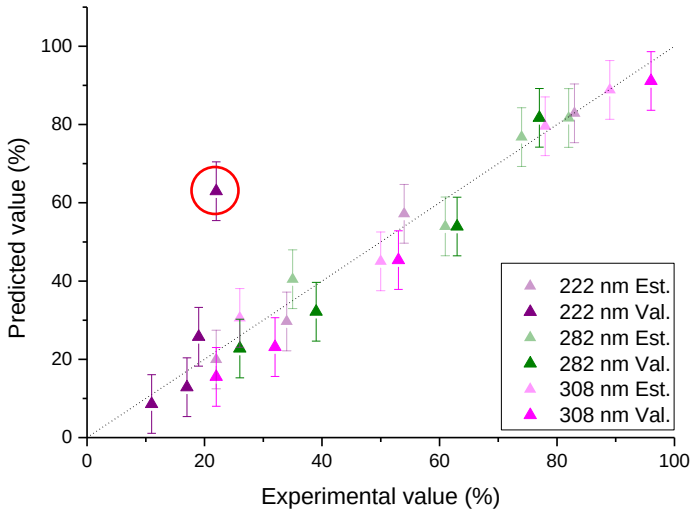


Figure 86 - A comparison of the predicted values for the product yield and the experimental values at 222, 282 and 308 nm, with the inclusion of a subsequent photodegradation step in the model, showing better agreement for at high yields. The error bars are one standard deviation (5%) each way, while the red circle shows an anomalous result.

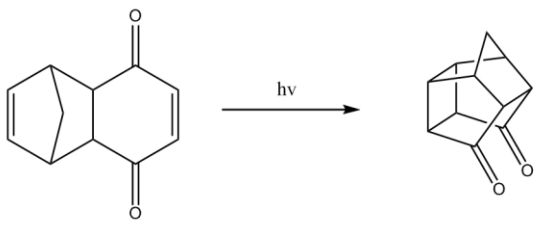
Unfortunately, the anomalous result for 0.2 mol·dm^{-3} at 0.2 ml·min^{-1} for the 222 nm Excimer flow lamp was still present. This result was initially thought to be due to a deposit of an unknown compound, likely to be the breakdown product, on the inside of the reactor which would have reduced the yield.

4.7.3. Reaction of Cookson's dione

The experiments and measurements for Cookson's dione in the Excimer reactors were carried out by colleague Adam Lee.

The formation of a cage compound from Cookson's dione is a simple unimolecular reaction, where the cage-like compound is formed from the [2+2] cycloaddition of Cookson's dione, as shown in Scheme 6.[332] The reaction has been shown to perform efficiently at a range of different UV wavelengths, while not forming other products. It has also been used in a number of examples as a test case for reactor optimisation, both within the group at Nottingham and elsewhere.[136,156,333]

Scheme 6 - The formation of the 'cage-like' compound from the [2+2] cycloaddition of Cookson's dione.



Cookson's dione **Cage-like compound**

Cookson's dione in excimer flow reactor

The Excimer flow lamp wavelength selected for the validation experiments was 282 nm as it showed the best overlap with the absorption of Cookson's dione for the available Excimer lamps, shown in Figure 87. The UV/Vis absorption spectrum of Cookson's dione is shown in Figure 87 highlighting the wide absorption profile of the compound in the UV range.

The dashed lines at 254, 282 and 308 nm indicate the major emission lines of three relevant lamps discussed in this section; the absorption coefficients at these wavelengths are shown in Table 38.

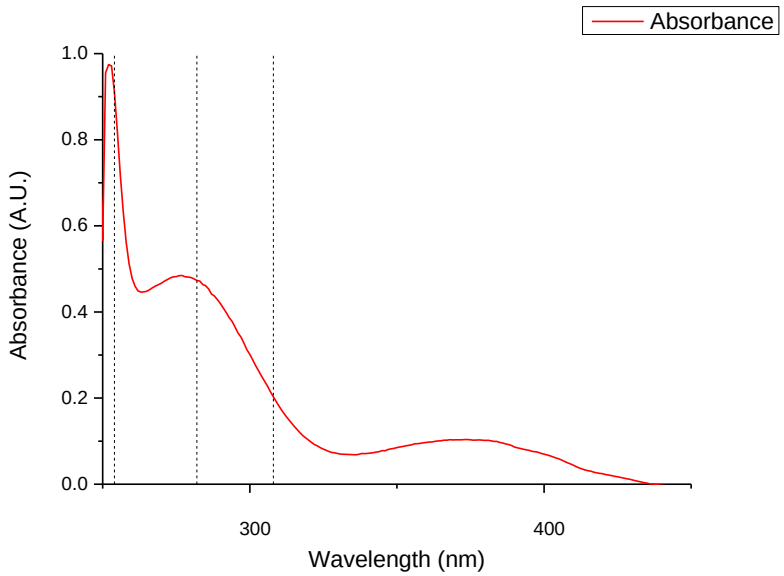


Figure 87 - The UV/vis spectrum of Cookson's dione reaction at 0.002 mol·dm^{-3} in acetonitrile. The wavelengths of 254, 282 and 308 nm are highlighted as these are relevant for this work.

Table 38 - The absorption coefficients of Cookson's dione in acetonitrile at the major emission lines of three relevant lamps. The * indicates the lamps are for the Excimer flow reactor.

Wavelength (nm)	Absorption coefficient (dm^{3}mol^{-1}cm^{-1})
254	472
282*	246
308*	110

Experimental results for Cookson's dione in Excimer flow reactor

The concentration of the starting material was chosen as 0.25 M using five different flowrates, ranging from 0.1 ml·min^{-1} to 1 ml·min^{-1}. The experiments' yields and starting material recovery for the 282 nm Excimer flow reactor measured by GC analysis are shown in Table 39. Those experiments shown in **red** were used in the estimation of the quantum yield.

The yields of the 0.25 ml·min^{-1} experiments were originally around 70 %, much lower than the 96 % shown below. However, once the results were analysed it was clear they were anomalous and were repeated. The 0.25 ml·min^{-1} experiments were last in the run and after inspection of the reactor, a thin discoloured layer could be seen on the inside of the reactor, as seen in Figure 88. This thin layer would have reduced the amount of light transmitted into the reactor and reduced the productivity.[186]

Table 39 - A summary of the experimental results for Cookson's dione at 282 nm used in the parameter estimation, shown in red, and those used for the validation in black. Those marked with * indicate those that were repeated after examination of the results and reactor.

Flowrate (ml·min^{-1})	Cage-like product Yield (%)	Starting material recovery (%)	Mass balance (%)
1	**45%**	**54%**	**99%**
1	**44%**	**54%**	**98%**
1	45%	54%	99%
0.75	58%	42%	100%
0.75	57%	41%	98%
0.75	58%	41%	99%
0.5	**70%**	**27%**	**98%**
0.5	**72%**	**28%**	**100%**
0.5	71%	28%	99%
0.25	96% (69%*)	3.2%	99%
0.25	96% (71%*)	1.7%	98%
0.25	96% (69%*)	1.7%	98%
0.1	**96%**	**1.3%**	**97%**
0.1	**96%**	**0.8%**	**97%**
0.1	98%	0.7%	99%



Figure 88 - (a) A picture of the clean reactor and (b) a picture of the reactor after the final experiment showing discolouration - a sign of fouling.

These experiments were repeated, with the final values shown in Table 39, and validated using modelling, as shown below.

Modelling Cookson's dione in the Excimer flow reactor

The model developed for the Excimer reactor consisted of a single reaction, with Cookson's dione converting into the cage-like compound after the absorption of a photon. The rate of absorption of photons by Cookson's dione was calculated using the manufacturer's specification of lamp intensity

at 282 nm, along with the absorption coefficient of Cookson's dione at 282 nm. The quantum yield of the reaction at 282 nm is unknown, therefore it was estimated using experimental results. Assuming the manufacturer's light intensity specification was accurate, the MLE-estimated quantum yield for this reaction was $\mathbf{\Phi_{282nm} = 24.9 \pm 0.5\ \%}$.

For this case, Aillet's assumptions were valid, with the Quantum yield predicted using Aillet's method being $\mathbf{\Phi_{282nm} = 22.7 \pm 2.59\ \%,}$ which agreed well with the MLE method (Please see Appendix II for more details).

A comparison of the experimental and computational values for product yield and starting material yield is shown in Figure 89 (a,b), showing good agreement, with an RMSE of 2.02 % for the cage product and 1.55 % for the starting material recovery.

The quantum yield, as estimated using this method, was not as high as expected for Cookson's dione.[156] The most likely reason for a lower quantum yield was that the current lamp output is below the manufacturer's specifications.

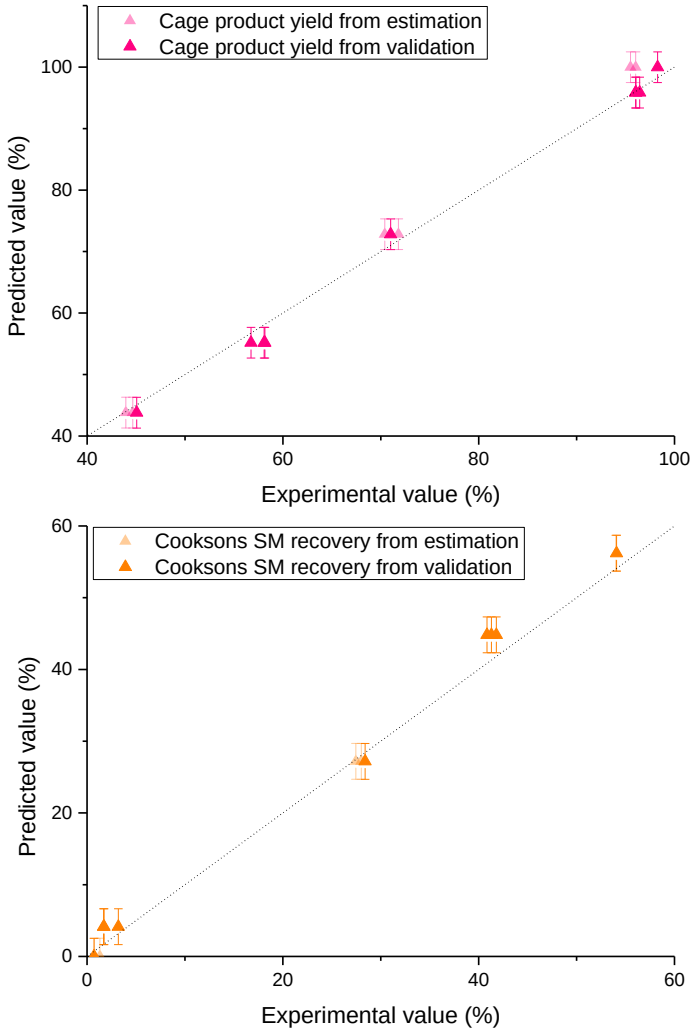


Figure 89 - A comparison between the predicted and experimental values for (a) the cage product yield used in the estimation (▲) and validation (▲) and (b) starting material recovery used in the estimation (▲) and validation (▲). The error bars shown are one standard deviation (2.5 %) each way. The experiments used in the validation show good agreement with predicted values.

Excimer Reactor CFD and Process Model Comparison

As the eventual aim was to compare the results of the Process model and CFD model of the Vortex reactor with experimental values, a comparison of the models for the excimer flow reactors is presented for consistency. These values are taken at equilibrium (3000 s), with the yield of the cage-like compound along the axial dimension shown in Figure 90, with minimal differences between the two models.

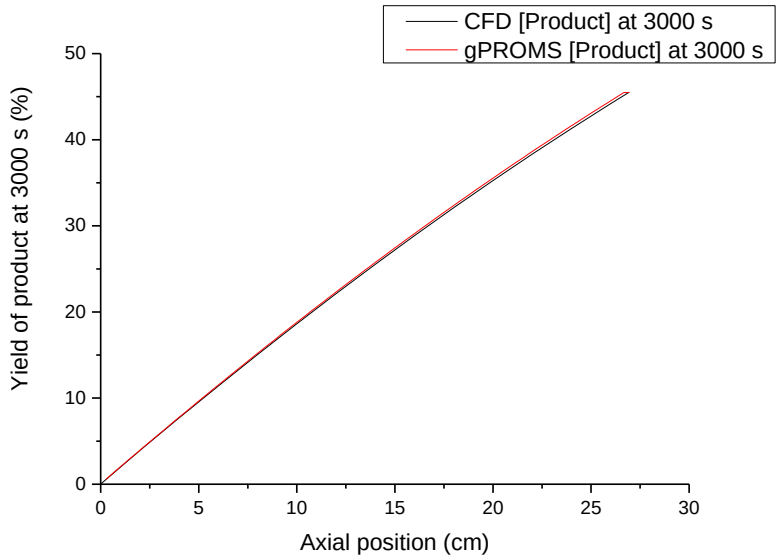


Figure 90 - Comparison of the predicted yield of 8 along the axial dimension of the Excimer flow reactor, showing minimal difference between the two computational methods.

To investigate other possible differences between the two models, the light intensity and concentration of the cage-like compound, across the radial direction, is shown in Figure 91 (a) and (b). The light intensity shows minimal difference between the two methods. The concentration of the cage-like compound across the radial dimension shows a small deviation between the two methods. However, the difference between the two concentrations is less than 1% across all values.

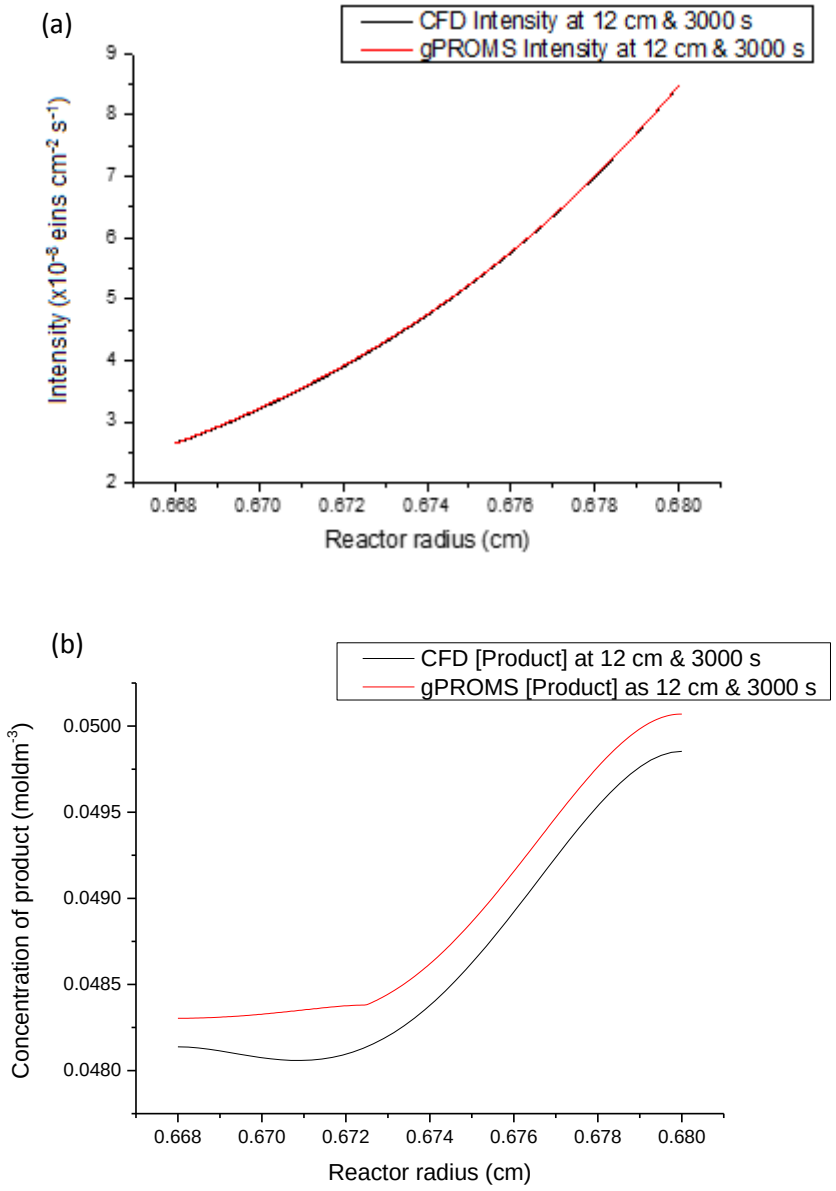


Figure 91 - (a) The intensity (x10^{-8}) of light across the radial direction and (b) the concentration of the cage-like compound across the radial dimension at 12 cm. The intensity shows negligible difference between the two, while the concentration of the product shows a small difference between the two models which is <1% of the value, which was also considered negligible.

The comparisons between the gPROMS process model and the CFD models show good agreement with experimental results, this will be used to assist the development of the Vortex reactor.

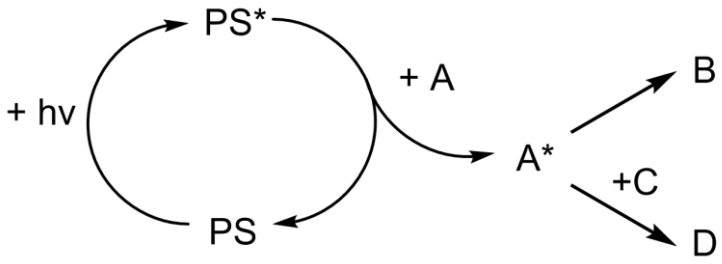
4.8. Use of photosensitisers

Photosensitisers are generally used in photochemical reactions for two reasons: to increase the number of photons absorbed or for transferring energy to a species that does not absorb photons at the relevant wavelengths. For example, photosensitisers have been used to produce triplet oxygen, which has been used within the group as a step to produce the anti-malarial drug artemisinin. [130,131,135]

4.8.1. Photosensitisers in kinetic schemes

The introduction of a photosensitiser into a kinetic scheme adds an initial step such that the absorption of light by the photosensitiser starts a reaction. This additional step is shown in Scheme 7, where PS denotes the photosensitiser and A, B, C, and D are typical reagents with * denoting excited states.

Scheme 7 - An idealised reaction scheme of typical reagents A, B, C and D using a photosensitiser (PS) where * indicates an excited state.



The estimations discussed below showed highly correlated factors likely due to the relative difference in timescales of photoreactions compared to the solvers. Considering this difference in timescales, a Bodenstein-like assumption was used for the photosensitiser's excited state.[151,334] The concentration of the photosensitiser excited state was assumed to be constant, relative to the amount of light it absorbs. This separated the reaction scheme into steps of combined reactions, where Scheme 7 would be simplified into Scheme 8 using ϕ'. This is defined as the 'quantum kinetic parameter' within this work, as described below.

Scheme 8 - Simplified scheme of the use of photosensitisers with combined reactions of Scheme 7, with the Bodenstein-like assumption used to simplify the reaction scheme.

$$A \xrightarrow[\Phi_1']{+\ hv,\ PS} B \qquad A + C \xrightarrow[\Phi_2']{+\ hv,\ PS} D$$

The first stage of the reaction was therefore combined such that the overall rate of the initial reaction was dependent on the absorption of light by the photosensitiser ($LVRPA_{PS}$) and the limiting starting material. The limiting starting material, denoted by A in Scheme 7, is excited by the quasi-steady state photosensitiser. The rate of two reactions in Scheme 8 is therefore calculated as shown in Equation 97.

$$Rate_1 = \Phi_1' LVRPA_{PS}[A] \ ; \quad Rate_2 = \Phi_2' LVRPA_{PS}[A][C] \tag{97}$$

The quantum kinetic parameters for the reactions are different to the quantum yields used previously as the combination of the reactions combined kinetic effects from multiple reactions into a single parameter. Due to this difference, the quantum yields were named 'quantum kinetic parameters' and denoted with a '. For example, the units of the quantum kinetic parameters Φ_1' and Φ_2', shown in Scheme 8, are $dm^3 \cdot mol^{-1}$ and $dm^6 \cdot mol^{-2}$, respectively. This assumption is explored in the following section using an example, as well as being further discussed in Appendix II.

As the photosensitiser was not consumed with the reaction, the attenuation of light into the reactor was constant and hence mixing became essential. For the excimer flow model, this was not a large issue due to the microchannel, however became more obvious with larger gaps such as with the excimer batch reactors.

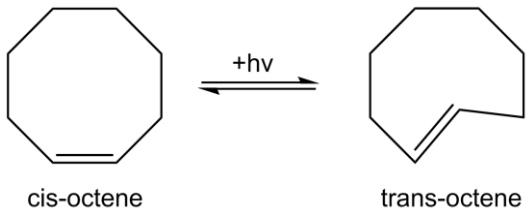
4.8.2. Cis-/trans-cyclooctene with photosensitiser

The experiments and measurements for the isomerisation of cis-/trans-cyclooctene were carried out by colleague Adam Lee.

Cyclo-octene is the first shortest cyclic alkene that is able to isomerise to form the trans- isomer of itself, as shown in Scheme 9. Trans-octene have become an interesting target for synthetic chemists

due to its inherent high reactivity.[335,336] A number of methods have been investigated to produce trans-octene; including both thermal and photochemical steps.[337–339]

Scheme 9 - A scheme to show the photoisomerisation of cis-octene to form trans-octene, without a photosensitiser. It should be noted that a photosensitiser can also be used to promote this reaction.



The photoreaction of the cis- isomer can be initiated by either direct absorption or via a photosensitised mechanism. The photosensitised mechanism is known to form an equilibrium, this limits the yield of trans-octene to *ca.* 20 %.[340,341] The direct isomerisation method has been shown to produce a yield of *ca.* 50 % however has only been carried out on a small batch scale.[342–344] The direct photoisomerization method is also limited by the possible lamps used as the absorption band of cis-octene is observed < 210 nm. [47]

The isomerisation of cis-octene was carried out using both the excimer flow reactors and the excimer batch reactors with the use of methyl benzoate as a photosensitiser. The absorption spectrum of methyl benzoate is shown in Figure 92, with the decadic molar absorption coefficients shown in

Table 40.

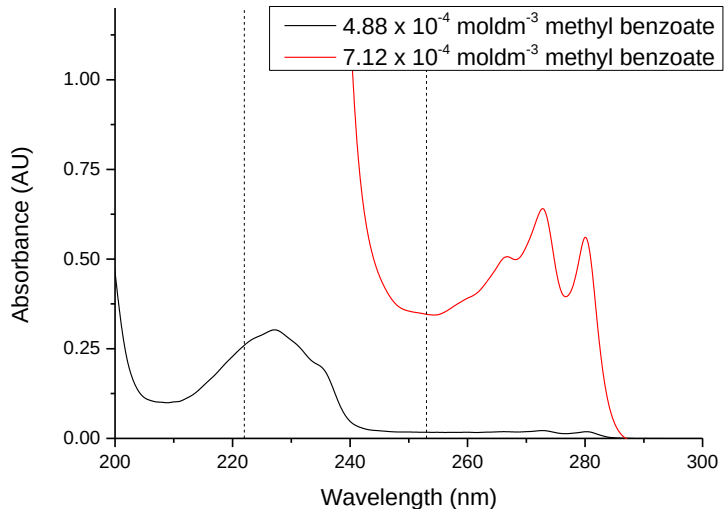


Figure 92 - The UV/Vis absorption spectrum of methyl benzoate photosensitiser at two different concentrations in acetonitrile, with the spectra at 4.88 x 10^{-4} mol·dm^{-3} shown in red and 7.12 x 10^{-4} mol·dm^{-3} shown in black.

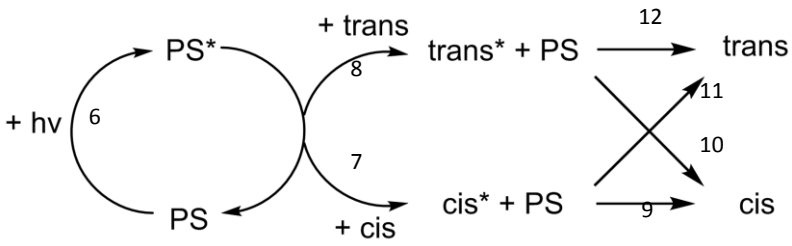
Table 40 - The decadic molar absorption coefficient of the photosensitiser, methyl benzoate, at 222 and 253 nm

Wavelength (nm)	Methyl benzoate decadic absorption coefficient (±std. er., $dm^3 \cdot mol^{-1} \cdot cm^{-1}$)
222	550
253	510

Initial tests

As the photosensitised mechanism was known to create an equilibrium between the two isomers, limited at *ca.* 20 %, the mechanism in Scheme 10 was proposed. This reaction scheme allows both isomers to interconvert via reaction with the excited state of the photosensitiser (PS*).

Scheme 10 - The initially proposed mechanism for the photosensitised isomerisation of cis-octene, where PS represents the photosensitiser and * indicates an excited state. The numbers represent the different reaction steps.



The initial reaction was assumed to be a photochemical reaction, with all subsequent reactions considered to be thermal reactions. As the temperature in the model was assumed to be constant, just the kinetic parameters for the reaction were estimated rather than the pre-exponential factor

and activation energy. The estimated values from this initial estimation are shown in Table 41. As mentioned in the introduction, the standard deviations and the correlation of each factor were unable to be calculated as it was assumed the variance-covariance matrix was singular due to the highly correlated factors.

Table 41 - The estimated kinetic parameters for the initially proposed mechanism for the photosensitised isomerisation of cis-octene. The standard deviations could not be calculated as the covariance-variance matrix was singular as the parameters were highly correlated.

Photoreaction	Quantum yield
6	1
Thermal reaction	**Kinetic parameter (units indicated)**
7	263000 $dm^3 \cdot mol^{-1} \cdot s^{-1}$
8	177000 $dm^3 \cdot mol^{-1} \cdot s^{-1}$
9	2240 s^{-1}
10	381 s^{-1}
11	6120 s^{-1}
12	230 s^{-1}

The highly correlated parameters for this reaction meant that no reliable conclusions could be drawn from the estimated values. In light of the issue regarding highly correlated parameters, the new model was proposed to overcome this issue.

Updated model

As the timescales of the photoreactions and excited states were considered much shorter than the process model's typical timescale, the multiple steps shown in Scheme 10 were combined into the proposed model shown in Scheme 11. The combined reactions were hoped to reduce the correlations between parameters without losing the predictive capabilities.

Scheme 11 - The simplified model for the photosensitised isomerisation of cis-octene, with the combined step of the photosensitiser absorbing a photon and reacting



Previous models and estimations had used the excimer flow models for both the estimation and validation of models. The experiments used for quantum kinetic parameter estimation of the photosensitised isomerisation of cis-octene were carried out in the batch excimer reactor. The yields

were calculated at different time points by taking small volumes for analysis. The excimer lamp chosen was the 253 nm Batch Excimer lamp with an output power of 17.3 $W \cdot m^{-2}$, as per manufacturers specifications. The mixing of the batch reactor needed to be investigated as the efficiency of the mixer was unknown.

Mixing effect in batch excimer reactor

The excimer batch reactor had a considerably larger irradiated volume, *ca.* 120 cm^3, compared to the excimer flow reactor. This larger volume and path length meant the mixing will have a much more pronounced effect compared to the excimer flow where minimal mixing occurs. The excimer batch reactor is designed such that a stirrer can ensure mixing of the reagents. For the model, this offered a challenge as the amount of mixing would be hard to quantify without considerable further research. Instead of further work investigating the extent of mixing, the overall effect of mixing was investigated in the model.

As has been suggested within the model development section, the effect of mixing can be mimicked through the use of a dispersion coefficient. Initial tests showed that changing the dispersion value affected the yields of both products. As the quantum kinetic parameters were being estimated from experimental data, the estimated values were expected to be affected by the dispersion value chosen. To address this issue, two different mixing conditions were chosen for investigation; molecular diffusion and a fully mixed reactor.

Molecular diffusion case

A dispersion coefficient of 1 x 10^{-5} $cm^2 \cdot s^{-1}$, typical for the conditions, was chosen in both the axial and radial directions.[345] The standard deviation of both yield sensors was chosen as 2.5 % as the results were analysed by quantitative ^1H NMR and showed good repeatability when ran in triplicate. The estimation was carried out, giving the quantum kinetic parameters at 253 nm for each reaction shown in Table 42, with the estimated yields shown in Figure 93.

Table 42 - The estimated quantum kinetic parameters for the photosensitised isomerisation of cis-octene, with just molecular diffusion at 253 nm.

Photoreaction	Quantum kinetic parameter (±SD, dm^3mol^{-1})
cis-octene → trans-octene	7.78 (±13.31)
trans-octene → cis-octene	16.65 (±31.76)

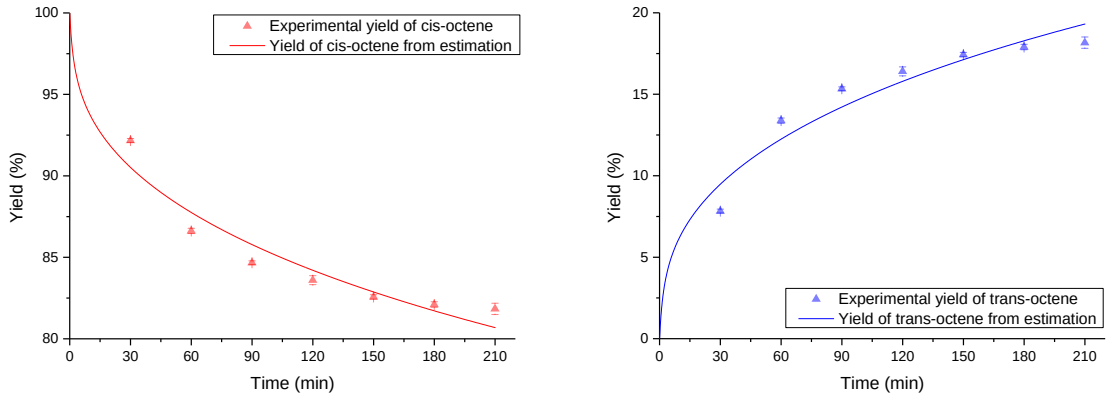


Figure 93 – The predicted results for the yield of (a) cis-octene and (b) trans-octene shown by the line compared to the experimental values for the photosensitised isomerisation of cis-octene, with just molecular diffusion. The predicted values show the right trends, but do not fit the experimental values well.

Although the predicted yields showed the correct trends, they did not give a close fit to the experimental values. This difference is further exemplified by the uncertainty of the estimated quantum kinetic parameters.

Fully mixed case

A fully mixed case was then investigated, where the concentration is constant over the whole reactor volume. As above, the yield sensors' standard deviation was set as 2.5 %, with the estimated quantum kinetic parameters for 253 nm shown in Table 43, with the estimated yields for both cis- and trans-octene shown in Figure 94.

Table 43 - The estimated quantum kinetic parameters for the photosensitised isomerisation of cis-octene, with a fully mixed reactor vessel at 253 nm.

Photoreaction	Quantum kinetic parameter (±SD, $dm^3 \cdot mol^{-1}$)
cis-octene → trans-octene	5.05 (±1.33)
trans-octene → cis-octene	1.13 (±0.22)

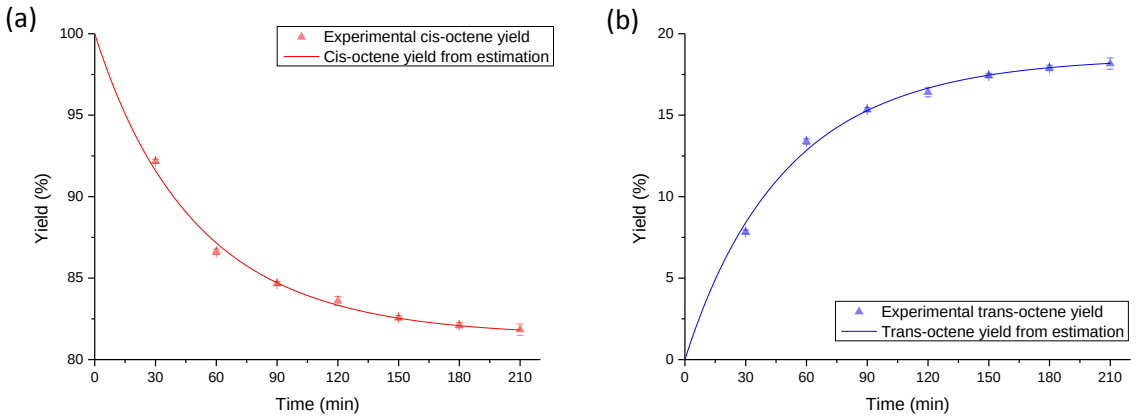


Figure 94 - The predicted results for the yield of (a) cis-octene and (b) trans-octene shown by the line compared to the experimental values for the photosensitised isomerisation of cis-octene, with a fully mixed reactor vessel. The predicted values agree much better with experimental values when compared with the molecular diffusion case.

As Figure 94 shows, both the predicted yields for the fully mixed case fit more closely than the molecular diffusion case presented above. The uncertainty in the estimated quantum kinetic parameters is also reduced in comparison to the molecular diffusion case.

For both cases, the estimated parameters exhibited a high correlation between each other, with the molecular diffusion case showing a correlation of 0.999 and the fully mixed case showing a correlation of 0.967. Unfortunately, a method to reduce this correlation was unlikely to succeed due to the nature of the reaction scheme, where the concentration of each product depends upon the other reaction.

Validation of other cases for cis-/trans-octene isomerisation

Previously, the use of flow reactors has allowed for a number of experiments to be used for the estimation of parameters while the remaining experiments have been used to validate the model. Using batch reactions does not allow for the facile and fast alteration of conditions and hence the parameters were estimated at a single condition, with data points collected over time. Once the parameters were estimated from the batch reactor with the 253 nm excimer lamp, the model was then validated by predicting experimental results for both batch and flow results at 222 nm.

Validation of 222 nm batch

The results of the yield for both cis- and trans-octene were predicted in time, assuming the same quantum kinetic parameter as estimated with 253 nm experiments. The experimental values and validated model predictions at 222 nm are shown in Figure 95. Both of these show good agreement between predicted and experimental values.

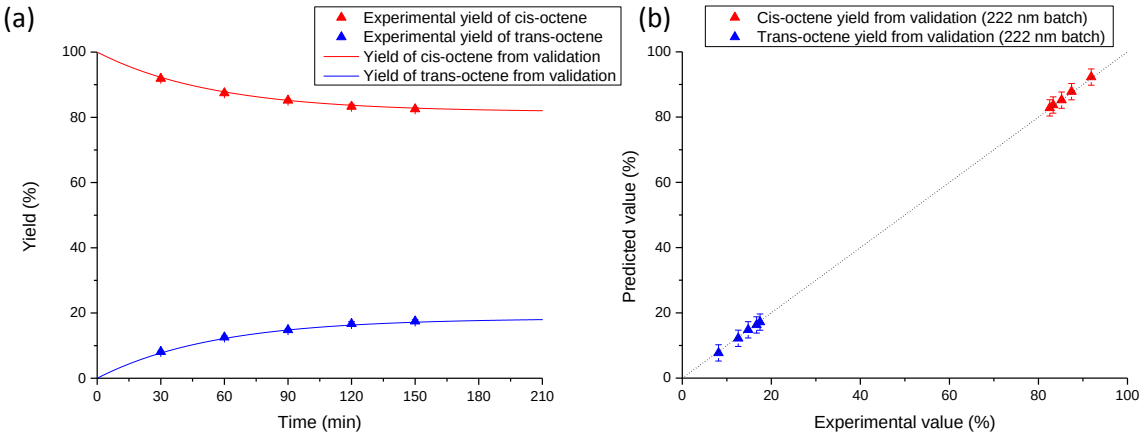


Figure 95 - A comparison of the predicted yields from the validation of the photosensitised reaction at 222 nm, with the results shown in time in (a) and as a comparison in (b). For this, the same data points are presented using two different methods.

Validation of 222 nm flow

The predicted yields for both cis- and trans-octene at the excimer flow reactor outlet, at equilibrium, are shown in Figure 96. Again, the model predicts the results well, with an RMSE of 3.8%, which is larger than the 2.5 % sensor yield standard deviation used in the estimation.

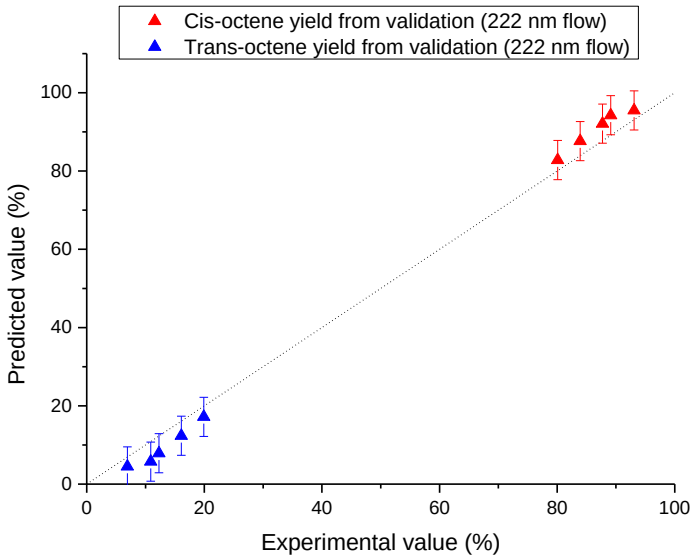


Figure 96 - A comparison of the predicted results for the photosensitised isomerisation of cis-octene in the excimer flow reactors at 222 nm showing good agreement using the quantum kinetic parameter estimated with the 253 nm Batch Excimer lamp and reactor.

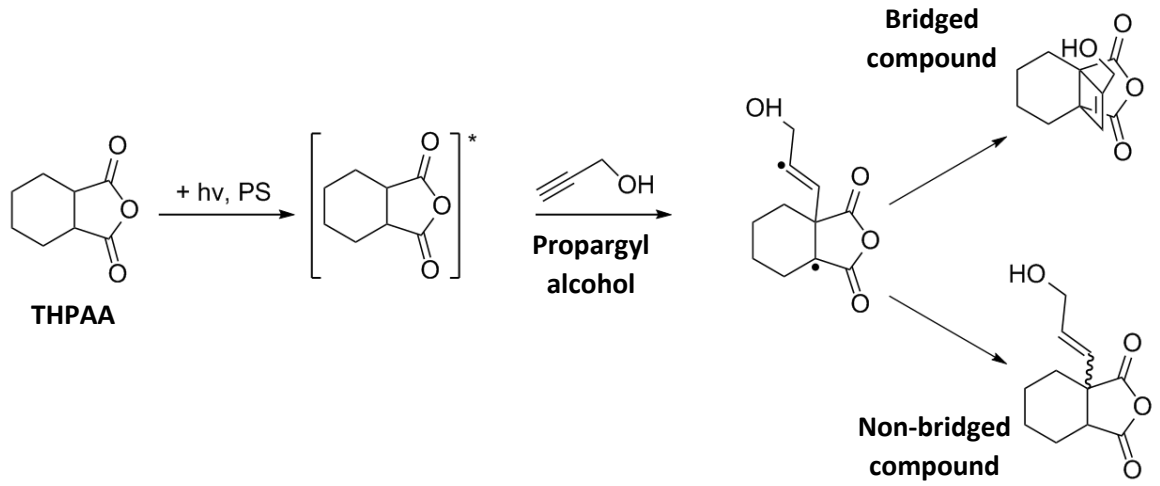
The slight difference could be due to a number of different factors, such as the lamp power being below the manufacturers specifications as for all of these models this had been assumed. Another possible reason was the uncertainty introduced from the additional factors needing to be considered in the mass balance from the flow of material.

4.8.3. Photocyclisation of THPAA and propargyl alcohol

The experiments and measurements for the reaction of THPAA with propargyl alcohol were carried out by colleague Jonny Hunter and Dr. Rowena Howie.

The photoreaction of tetrahydrophthalic acid anhydride (THPAA) with propargyl alcohol, shown in Scheme 12, is a reaction currently being studied with colleagues in Nottingham and Bristol. The reaction is hoped to be the first step in a daisy-chained process, with a thermal reactor connected subsequently in series, where the bridged compound undergoes an electrocyclic ring opening to form an 8-membered ring.

Scheme 12 - The overall reaction mechanism of the photosensitised reaction of THPAA with propargyl alcohol



The reaction mechanism shown in Scheme 12 was used for estimating the kinetics of each reaction, including both a photosensitised and non-photosensitised photoreaction as THPAA also absorbed light. A breakdown pathway for the bridged product was also included as a decrease in the yield of this product had been observed for long exposure times. A reduction in mass balance had also been observed for the flow reactions, which was thought to be due to the production of breakdown products.

Table 44 - The decadic absorption coefficients of the reagents used in the photoreaction of THPAA with propargyl alcohol. The UV/Vis spectra measurements for this reaction was carried out by Adam Lee.

	Decadic absorption coefficient ($dm^3 \cdot mol^{-1} \cdot cm^{-1}$)	
Compound	**282 nm**	**308 nm**
THPAA	125	63
TXO	5620	2530
Bridged product	85	71
Non-bridged product	28	25

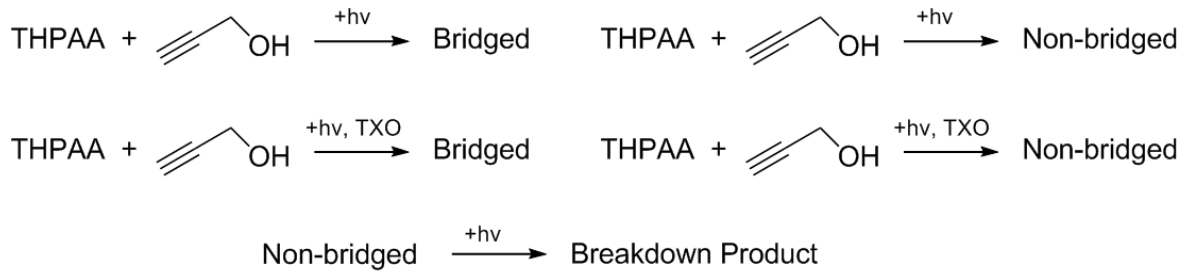
As with the cis-trans octene reaction, the initial parameter estimations had led to parameter values that were highly correlated and containing large uncertainties of the order 10^6 $dm^3 \cdot mol^{-1} \cdot cm^{-1}$.

Combining reactions

As proposed above, the combining of reactions that are considered fast in comparison to the process model was a possible method to address the highly correlated estimated values. The reactions of

THPAA to form either the bridged or non-bridged products were combined such that both a photosensitised and non-photosensitised reaction can proceed. The multiple reactions steps shown in Scheme 13 have been changed into multiple single step reactions that proceed simultaneously to form both of the products. The estimation was carried out using the excimer flow reactor model with five experiments with the photosensitiser, thioxanthone (TXO), and five experiments without the photosensitiser. The table of experimental results is shown in Appendix II, with the values shown in the results comparisons below.

Scheme 13 - The multiple reactions proposed for the photoreaction of THPAA with propargyl alcohol with the use of a photosensitiser



Without photosensitiser in batch reactor

As the reaction was being optimised in the laboratory, initial tests used a non-photosensitised reaction in the batch excimer reactor. The sensors used for the experimental results were the bridged and non-bridged products. Although further data was gathered, such as the recovery of starting material as the mass balance showed significant errors, this was ignored as the breakdown products were not identified. As the experimental results were variable the standard deviations for the yield sensors were set at 10 % yield. For the batch excimer experiments, the 282 nm lamp was used for the estimation, with the 308 nm lamp used as an external validation. The estimated quantum kinetic parameters are shown in Table 45, with the experimental results and model predictions shown in Figure 97.

Table 45 - The estimated quantum kinetic parameters for the photoreaction of THPAA and propargyl alcohol without a photosensitiser

Photoreaction	Quantum kinetic parameter (±SD, units indicated)
Bridged product formation (no TXO)	2.635 (±0.692) dm^3mol^{-1}
Non-bridged product formation (no TXO)	1.333 (±0.543) dm^3mol^{-1}
Photodegradation	0.644 (±0.306)

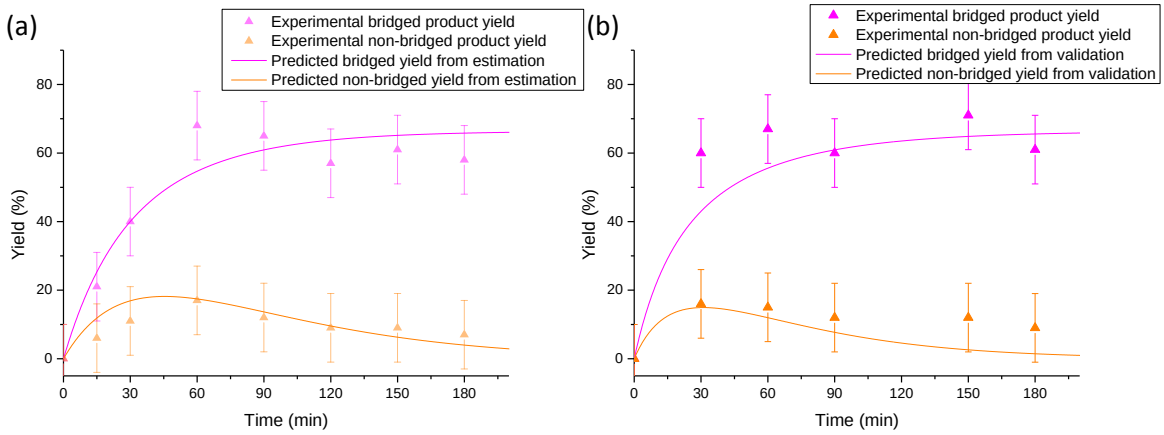


Figure 97 - A comparison of the experimental results for the reaction of THPAA and propargyl alcohol without a photosensitiser, with the results used in the estimation shown in (a) and the predicted results shown in (b). The experimental results are shown as the points, with error bars show one standard deviation (10%) each way, while the lines is the model-predicted values.

The predicted output values for 308 nm, displayed in Figure 97, show good agreement with the initial formation of both major products before the degradation of the non-bridged product.

With photosensitiser in batch excimer reactor

For the inclusion of the reactions with the photosensitiser, TXO, the quantum kinetic parameters for the non-photosensitised reactions were fixed. The estimated quantum kinetic parameters for the photosensitised reactions were estimated, with the values shown in Table 46, with the italicised reactions indicating that they were fixed from the previous estimation. The experimental yields and model estimation and validation over time are shown in Figure 98 (a) and (b), respectively.

Table 46 - The estimated quantum kinetic parameters for the photoreaction of THPAA and propargyl alcohol with a photosensitiser. The *italicised* values were fixed from the previous estimation.

Photoreaction	Quantum kinetic parameter (±SD, units indicated)
Bridged product formation (no TXO)	*2.635 (±0.692) dm^3mol^{-1}*
Non-bridged product formation (no TXO)	*1.333 (±0.543) dm^3mol^{-1}*
Bridged product formation (with TXO)	30.64 (±23.4) dm^6mol^{-2}
Non-bridged product formation (with TXO)	13.51 (±17.0) dm^6mol^{-2}
Photodegradation	*0.644 (±0.306)*

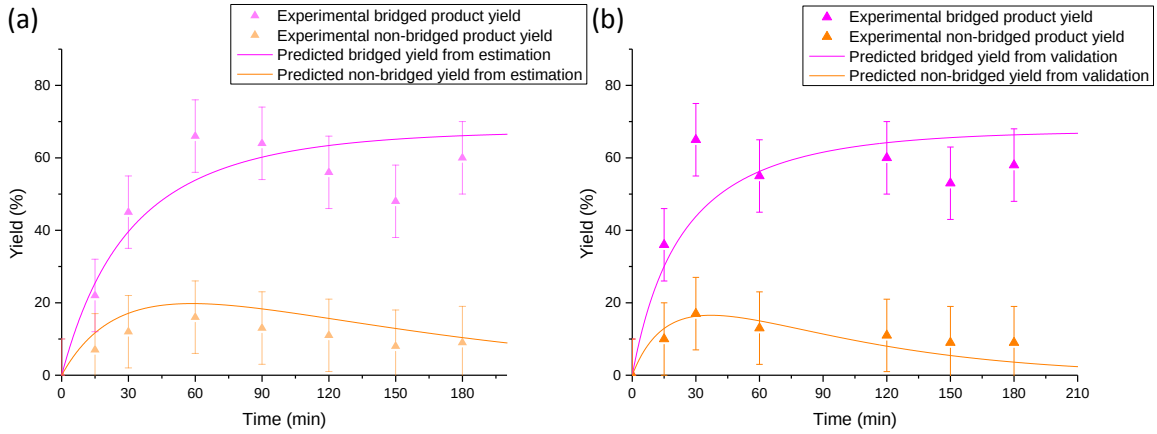


Figure 98 - A comparison of the experimental results for the reaction of THPAA and propargyl alcohol with a photosensitiser, with the results used in the estimation shown in (a) and the predicted results shown in(b). The experimental results are shown as the points, with error bars show one standard deviation (10%) each way, while the lines is the model-predicted values. The results shown here are similar to those displayed in the previous figure, with an apparent limit met *ca.* 65%.

With photosensitiser in flow excimer reactor

The quantum kinetic parameters estimated using the batch reactor performances outlined above were then used within the excimer flow reactor model at 308 nm. A comparison of the experimental and predicted results, with and without TXO, are shown in Figure 99 (a) and (b), respectively.

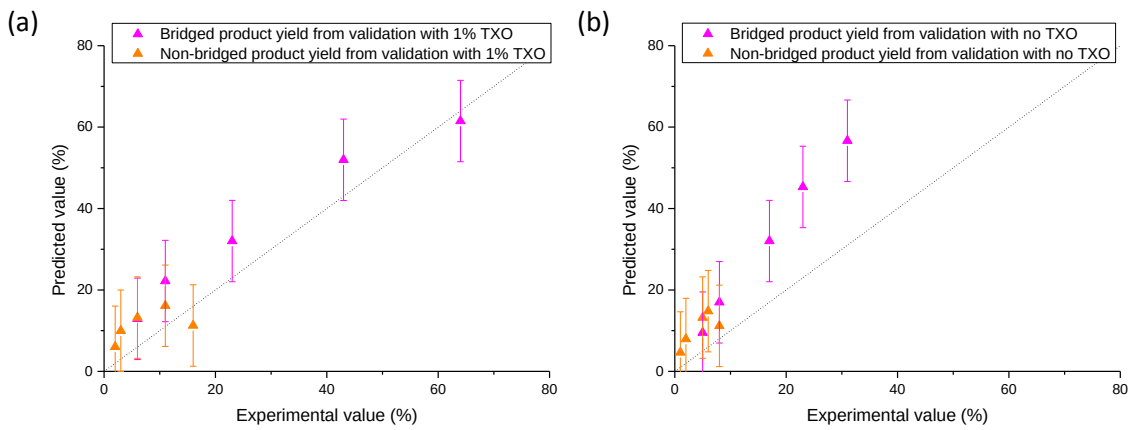


Figure 99 – (a) A comparison of experimental results for the reaction of THPAA and propargyl alcohol with a photosensitiser and the predicted values in the 308 nm excimer flow reactor and (b) A comparison of experimental results for the reaction of THPAA and propargyl alcohol without a photosensitiser and the predicted values in the 308 nm excimer flow reactor. The predicted values with a photosensitiser are within the error, whereas without the photosensitiser the predicted values are greater than experimental values, possibly due to the uncertainty in lamp power.

As can be seen in Figure 99(b), the model overestimated the yield of the bridged product for the results without TXO. The model also overestimated the performance for many of the experiments with TXO, with a number of other factors possibly affecting these results. The most likely error is the manufacturers power specification throughout all of these experiments being not comparable between reactor lamps. This theory is also supported by the fact that the 253 nm Excimer flow lamp used for the estimation is brand new and hence has not had time to reduce in efficiency like the other lamps used in these experiments.

4.9. Vortex Model Development

Reactors with Taylor Vortices were first developed to aid with mixing in predominantly thermal chemical reactions. More recently, vortex reactors have been adapted for photochemical transformations.[135,346,347] The Taylor vortices are particularly useful for photochemistry as they refresh the reaction mixture close to the irradiated surface, which helps address the inherent issue of light attenuation in photochemical reactors, as shown in Figure 100.[126]

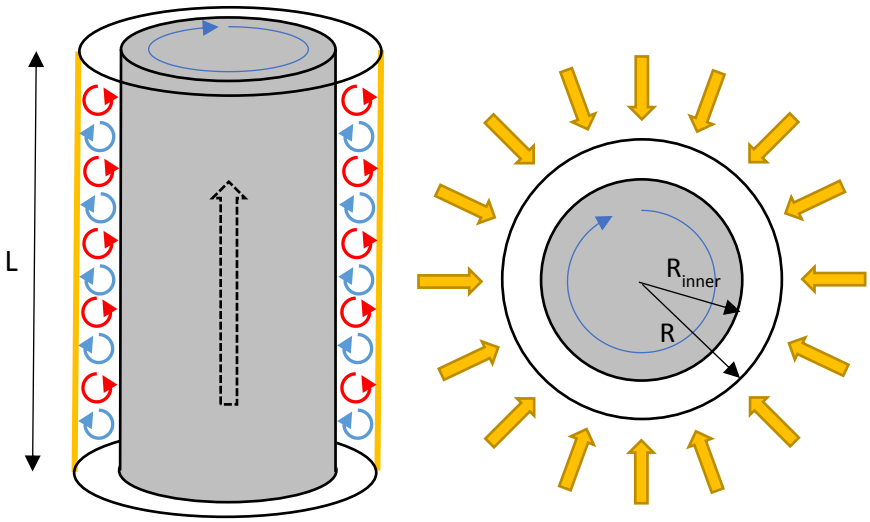


Figure 100 - A schematic of the Vortex reactor with the blue and red alternating arrows representing the Taylor vortices. L represents the length of the reactor and R and R_{inner} is the reactor radius and the radius of the rotating pipe, respectively. The dashed arrow represents the direction of flow.

Within the laboratory at Nottingham, the Vortex reactor is one of the largest reactors and reaction optimisations can use large quantities of material. The capability to predict the performance of the Vortex reactor computationally from smaller scale experiments was an attractive prospect. In order to achieve this goal a computational model was needed to predict performance.

One possible route to predict performance is to use highly detailed models of Taylor vortices developed using Computational Fluid Dynamic (CFD) techniques. However, these are computationally expensive, with calculations often taking several days.[135,258] Developing an accurate process model that could predict experimental results would be preferable for reaction optimisation and scale up as

typical process model calculations are much less computationally expensive, often taking in the order of minutes.[348]

To develop an accurate model, an idealised system was chosen to model in both CFD and gPROMS; the Paternó-Büchi reaction was chosen as with the initial model development. Parameters could then be easily changed within the process model to match the CFD result. Once the CFD model matched the gPROMS to an acceptable accuracy, the Process model was used with experimental results to predict the intensity of the lamp used with the Vortex reactor.

4.9.1. Model proposal

For the initial development of the Vortex reactor models, there was not any experimental results as the reactor was being built within the workshop, hence the model was developed through consultation with literature and CFD calculations.

Simplified model

Process models for Vortex reactors have previously been proposed in the literature, often with each Taylor vortex as a small Continuous Stirred Tank Reactor (CSTR) with material flowing from each Vortex CSTR to the next.[188,349,350] For thermal reactions each 'CSTR vortex' would have an average temperature and concentration of species. However, for photochemistry it was decided that this approach would be unsuitable as the spatial position is critical for the reaction due to the attenuation of light in the radial direction.

The initial model was developed for the Vortex reactor set up as an annular reactor with external radiation, similar to the Excimer reactor, as shown in Figure 100. The length of the reactor was 15 cm, the reactor radius was 1.1 cm and internal radius, R_{inner}, equal to 1 cm. This set up led to an annular gap of 1 mm, which was the first set up built with the Vortex reactor. It should also be noted that the rotating cylinder in the centre can be replaced with different cylinders such that the annular gap becomes 2, 3 or 4 mm.

Although the lamp used was one block of LEDs, the light entering the reactor was assumed to be fully collimated, perpendicular to the surface of the reactor and uniform across the whole surface.[126] This meant that the process model would be axisymmetric and would considerably reduce the calculation time needed and is discussed further below.

As the CSTR approach for photochemistry was decided to be unsuitable, a new model was proposed after inspection of the CFD models of the Vortex reactor, as shown in Figure 101. The use of the dispersion coefficient as a proxy for mixing had been shown with both the excimer batch reactor and initial model development.[351] For the vortex model different zones of dispersion along the reactor was proposed. The size of these zones and dispersion coefficients are discussed below, as these were altered to match CFD results.

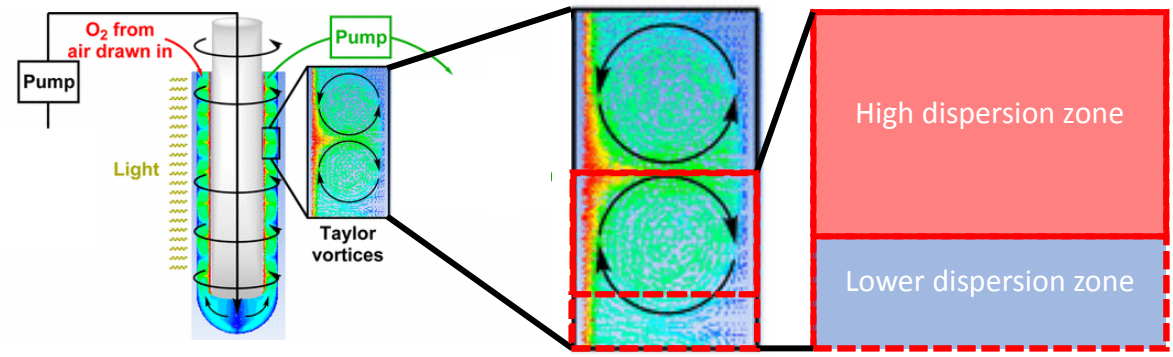


Figure 101 - A schematic of the different dispersion zones used in the development of a process model suitable for the Vortex reactor. A higher and lower dispersion zone was used within the model to mimic the complex mixing of the Taylor vortices.

4.9.2. Idealised model based on Paternò–Büchi reaction

To test this proposed model, a model reaction was needed that could be compared with the CFD model and experimental results. While the Vortex reactor was built, a photochemical reaction scheme was proposed, such that comparisons between the Process model and CFD model could be completed. An idealised version of the Paternò–Büchi reaction was selected for comparison as it is a well-known photochemical reaction and could be performed in the laboratory.[311] The proposed reaction scheme

and corresponding kinetic values were collated and adapted from literature sources, as shown in Scheme 1 and Table 24.[312,314] The absorption coefficients of the benzaldehyde species at 365 nm was 11 $dm^3mol^{-1}cm^{-1}$, as per literature studies.[352] The light was assumed to be monochromatic at 365 nm with an output power of 400 $W \cdot m^{-2}$.

Scheme 14 - The proposed Paternò–Büchi photochemical reaction scheme of benzaldehyde with furan to form the oxetane.

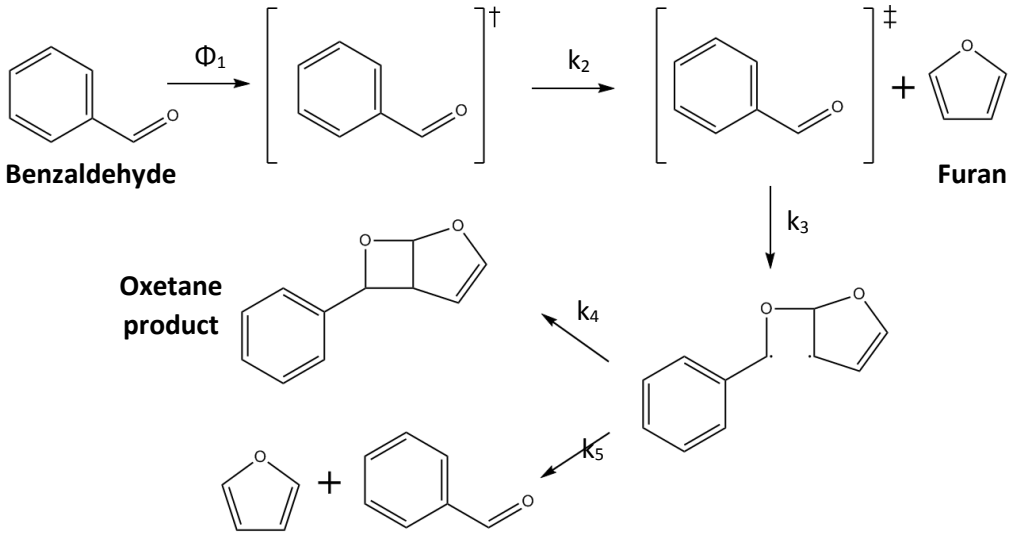


Table 47 - The quantum yield and kinetic parameters for the idealised Paternò–Büchi reaction scheme, adapted from literature sources.[312,314]

Photo reactions	Quantum yield
1	0.5
Thermal reactions	**Rate constant (variable units)**
2	2.4×10^{10} s^{-1}
3	1.2×10^{9} $dm^3 \cdot mol^{-1} \cdot s^{-1}$
4	0.27×10^{9} s^{-1}
5	0.24×10^{9} s^{-1}

Initial calculations, using typical experimental concentrations of **1**, were encouraging for the proposed model. However, due to the low absorption coefficient, much of the light was in excess and the effect of mixing was minimised. To further investigate the viability of the model, an abnormally high concentration of benzaldehyde (4.63 $mol \cdot dm^{-3}$ - equivalent of 0.5 mass fraction) was chosen for the model such that most of the light was absorbed within a small distance of the reactor wall, as shown

in Figure 102. The role of mixing would then be accentuated as reactions would only take place within a small region, close to the reactor wall.

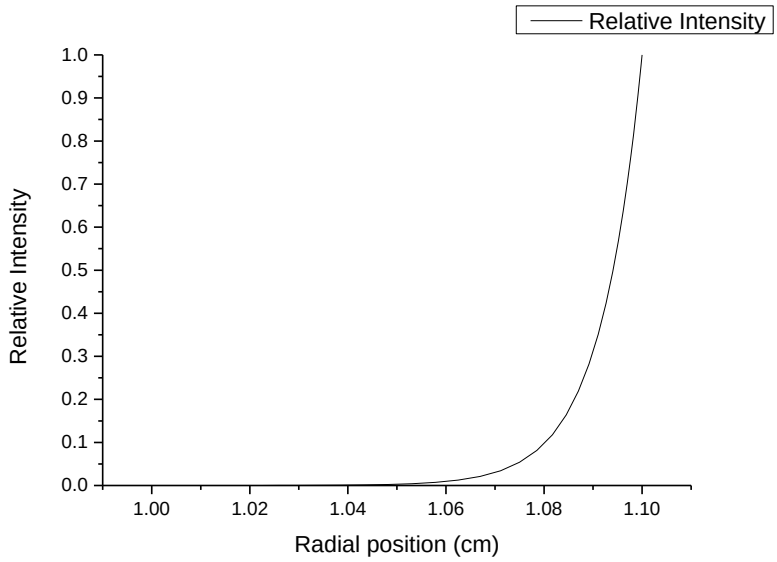


Figure 102 - The relative light intensity across the radial dimension for the Paternò–Büchi reaction, with a 4.26 mol·dm^{-3} concentration of benzaldehyde to accentuate the role of mixing.

Model descriptions with differing dispersion values

As mentioned above, the dispersion coefficients for the Vortex reactor were used as a proxy for mixing as dispersion ensures unreacted species will diffuse towards the irradiated zone. During model development several different dispersion values were tried whilst trying to match the Process model to the more complex CFD model. A selection of these results are shown in Figure 103, with the best match shown in red. The models displayed are described below along with the dispersion coefficient values shown in Table 48.

Models A and B were split into 50 sections, as this was the number of Taylor vortices found during the CFD modelling of a 1 mm gap. Model A was then split such that $^1/_3{}^{rd}$ was of lower dispersion and $^2/_3{}^{rds}$ at higher dispersion. Model B was split into sixths such that $^1/_6{}^{th}$ had lower dispersion values and $^5/_6{}^{ths}$ had higher dispersion values. Model C used the parameter estimation to match dispersion

coefficients for the whole reactor to the CFD results. Model D was also split into 50 zones with a layer of $^1/_7{}^{th}$ of the section width of molecular diffusion and the rest being of high dispersion.

Table 48 - The dispersion values and zone fractions for the different proposed Vortex process models, as shown in Figure 103.

		High dispersion zone dispersion coefficient ($cm^2 \cdot s^{-1}$)		Lower dispersion zone dispersion coefficient ($cm^2 \cdot s^{-1}$)	
Model	**High dispersion fraction**	**Axial direction**	**Radial direction**	**Axial direction**	**Radial direction**
A	2/3	0.2	0.1	0.02	0.1
B	5/6	0.2	0.1	0.02	0.1
C	All	0.0728	0.4144	0.0728	0.4144
D	1/7	0.2	0.1	1×10^{-5}	1×10^{-5}

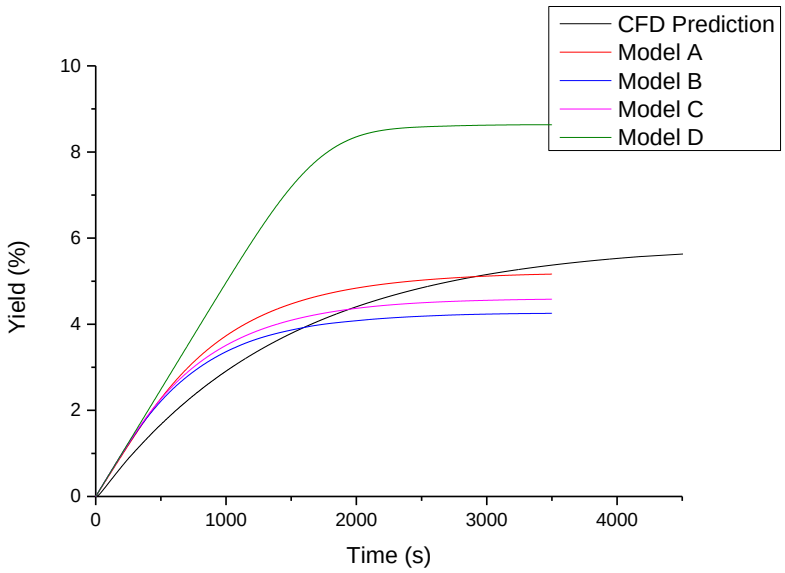


Figure 103 - Comparison of the different dispersion models against the CFD results, shown in black. A summary of the different models can be found in Table 48. Model A shows the greatest similarity where the vortex is split into 2/3rds higher dispersion and 1/3rds lower dispersion.

CFD and Process Model comparison

The biggest difference between the two models was the rate of production of the oxetane product over time, with the CFD model showing a more gradual rate of production. A wide range of parameters within the Process model were changed to match this initial rate, however no significant improvements could be made.

As Process Model A was able to accurately predict the yields (<1 % difference) compared to the CFD model at equilibrium, it was decided to proceed with further model development using experimental results.

4.9.3. Vortex reactor experimental results for Cookson's dione

The experiments and measurements for Cookson's dione in the Vortex reactors were carried out by colleague Dr. Darren Lee.

As both the Process model and CFD model showed good agreement for an idealised model of the Vortex reactor, Cookson's dione was chosen as a test case as the quantum yield had been estimated using the Excimer model. A considerable difference was seen between the experimental set up and the model setup, mostly related to how the light was treated.

Vortex Lamp set up

Firstly, a difference between the experimental set up and computational models should be highlighted. A schematic of the experimental set up of the lamp is shown in Figure 104(a), where the lamp shines light towards one side of the reactor from a distance of *ca.* 5 cm. This is unlike the computational model of the Vortex reactor, as shown in Figure 104(b), which assumed uniform irradiation around the reactor. Modelling the experimental set up would require a radial dimension for the light, which led to much longer computational times and outweighed the benefits of the Process model; to be used to quickly predict scale-up performance. By assuming uniform irradiance, the light entering the reactor was hoped to be 'averaged out' around the reactor, which it was hoped the high rotation speeds of the fluid would encourage.

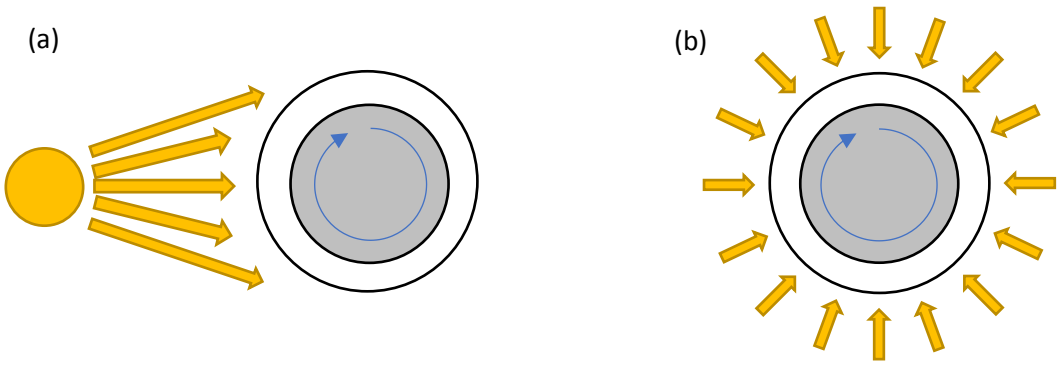


Figure 104 - Schematic of the different lamp set ups possible with the vortex reactor where (a) shows the experimental set up with a lamp that irradiates a certain section of the reactor and (b) an idealised version where the irradiance is averaged out over the surface of the reactor.

The experiments with Cookson's dione reaction in the Vortex reactor used a single high-pressure 1400 W Jenton mercury arc lamp. The lamp was assumed to emit light at 254 nm as this was the dominant absorbance band within the region that the starting material, Cookson's dione, absorbs as can be seen in Figure 105. Conveniently, the 254 nm emission also overlapped well with the absorbance maxima of Cookson's dione, 253 nm.

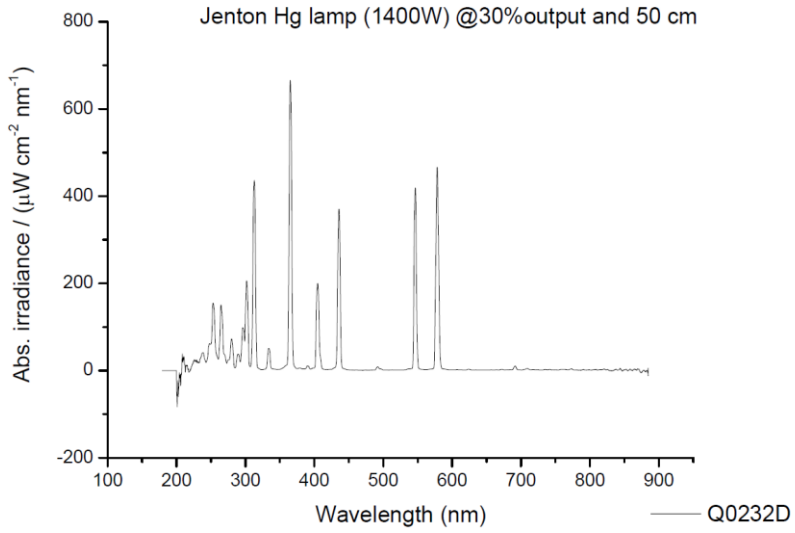


Figure 105 - Optical power spectra of the 1400 W Jenton Hg arc lamp measured 50 cm away from the lamp at 30% of the output. This spectrum was taken by Dr. Darren Lee.

The lamp spectra, in Figure 105, were measured 50 cm away from the lamp at 30 % of the power output so that the optical power meter was able to detect safely, this also highlighted another difference between models and experiment. The models assumed a single wavelength of light and

corresponding absorption by species at said wavelength. Furthermore, the optical power output values were wavelength dependent and hence complex to model.

Considering these assumptions, the estimation of a lamp power for the high-power mercury arc lamp was carried out using experimental values below.

Experimental results for Cookson's dione in the Vortex reactor

During the construction of the Vortex reactor, both quartz and Pyrex were used as the external reactor wall. Quartz was expected to perform better than Pyrex as it has a higher transmission for the relevant UV wavelengths.[353] The experimental results using both quartz and Pyrex are shown in Table 49.

Table 49 - A table of experimental results for the reaction of Cookson's dione in the Vortex reactor at 0.5 mol·dm^{-3}. Yields were calculated using ^{1}H NMR and a biphenyl internal standard.

Pyrex			Quartz		
Flow Rate (mL min^{-1})	**Conv. (%)**	**Yield (%)**	**Flow Rate (mL min^{-1})**	**Conv. (%)**	**Yield (%)**
1	100	<99	1	-	-
2	100	<99	2	-	-
3	100	<99	3	-	-
4	100	<99	4	-	-
5	94	94	5	99	94
8	-	-	8	90	89
10	63	59	10	74	74
			10 (no argon flow)	73	71

Vortex lamp power estimation

The estimated quantum yield, at 282 nm, for the Cookson's dione Excimer flow results was then used to estimate the average lamp power received into the Vortex reactor. As Cookson's dione is known to be an efficient reaction over a wide range of wavelengths, the quantum yield at 254 nm was assumed equal to the quantum yield at 282 nm. An average lamp irradiance around the whole surface was then estimated. The results for the estimation of the lamp irradiance for both Pyrex and quartz, are shown in Table 50.

Table 50 - Estimated values for the averaged light intensity entering the Vortex reactor, for both Quartz and Pyrex outer walls.

Reactor Material	Averaged estimated initial intensity ±SD (Wm^{-2})
Quartz	11100 ± 472
Pyrex	9120 ± 380

For these results, all the experiments were used in the estimation of the lamp power as there was a limited number of results. The difference between quartz and Pyrex was significant, with quartz light irradiance *ca.* 21 % greater than that of Pyrex. This increase can also be seen in the result at 10 $ml \cdot min^{-1}$ where quartz is *ca.* 25 % more productive than the Pyrex equivalent. Although the difference was expected, calculating the relative difference from first principles would be highly complex and hence using a semi-empirical model, with parameter estimation, is better suited.[354]

Vortex Reactor Model Comparison with CFD

The Vortex models, in both gPROMS and CFD were then compared using the estimated light power shown previously. The model predictions for the original 1 mm gap sized reactor, at different flowrates is shown in Figure 106. This comparison showed good agreement across both models and supports the use of gPROMS as a simplified version. The gPROMS model took in the order of minutes to finish, whereas the CFD models took in the order of days to finish. The major difference between the two models was the time taken to reach equilibrium, with gPROMS model reaching equilibrium faster. This difference was observed in the initial model development and was thought to be due to the use of an axial dispersion coefficient which would *push* reagents to the end of the reactor as they form, whereas CFD would model better mixing.

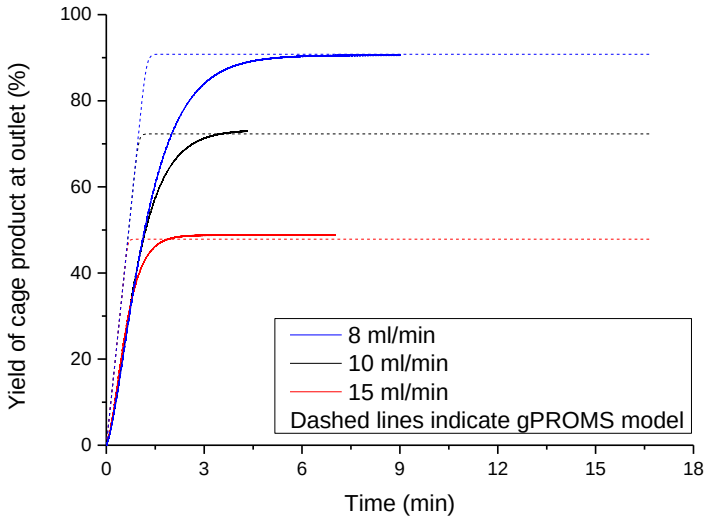


Figure 106 - A comparison of the CFD and gPROMS model for the Vortex model at 8, 10 and 15 ml·min^{-1} showing good agreement between the CFD and gPROMS' models, as well as consistent differences between the flowrates as shown in the experimental results.

The effect of the spin speed was also compared with both models. Unfortunately, a parameter for spin speed was not used in the gPROMS model and hence was compared with the base case. However, as can be seen in Figure 107, changing the revolutions per minute (rpm) did not cause a large difference for the 1 mm gap.

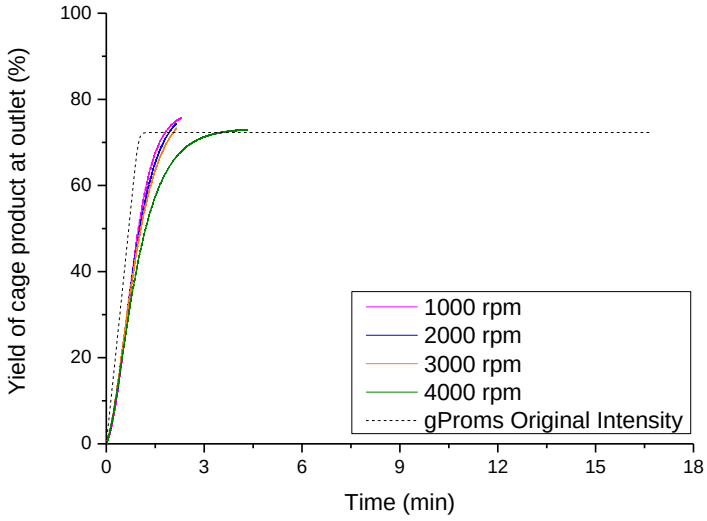


Figure 107 - A comparison of the gPROMS vortex model with the CFD model at 4 different rotation speeds showing the CFD results converging on a similar value to that predicted by the gPROMS process model. It should be noted that the CFD models were stopped after conclusions were drawn due to computational expense.

To investigate the models further, the flowrate was fixed at 10 ml·min^{-1} while the gap size of the reactor was altered, with the predicted results shown in Figure 108. Again, both of the models showed good agreement. The increase in gap size showed no effect on the overall yield for both the models and experimentally.

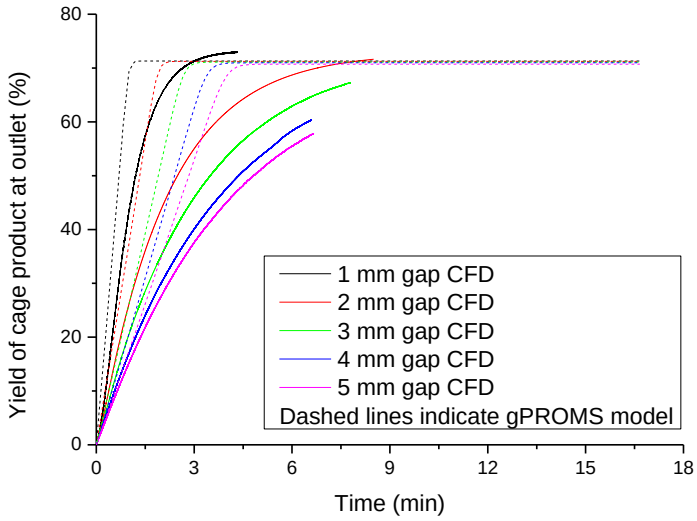


Figure 108 - A comparison of both the CFD and gPROMS model of the vortex reactor with different gap sizes showing the CFD models all converging on a similar value as predicted by the gPROMS process model. It should be noted that the CFD models were stopped after conclusions were drawn due to computational expense.

4.10. FEP tubular reactor model development

The experiments and measurements for the reaction of THPAA with propargyl alcohol were carried out by colleague Jonny Hunter and Dr. Rowena Howie.

To increase the production of chemicals in flow, so that the process can be daisy-chained with a thermal reactor an FEP tubular reactor was used with a mercury arc lamp. The FEP tubular reactor had a much greater hydrodynamic diameter compared to the excimer flow reactor and hence much greater flowrates could be used. The elevated flowrates allowed for a much greater production of the desired compounds; which was needed for demonstrating the ability of producing 1 kg/day. The internal FEP tube diameter was 0.5 cm and the coil diameter was 6.5 cm.

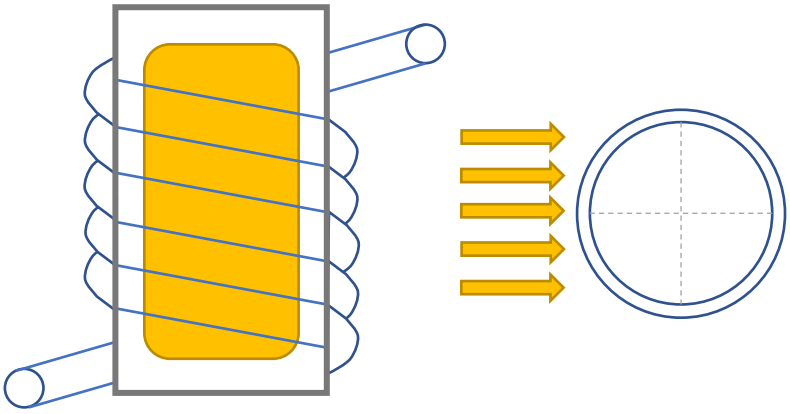


Figure 109 - An idealised drawing of the proposed model for the FEP tubular reactor. The FEP tube had an internal diameter of 0.5 cm and the internal diameter of the coiled tubing was 6.5 cm.

Initially the FEP tubular reactor was modelled as an extended tubular reactor, with a constant wall source from one direction, as shown in Figure 109. This model allowed for the attenuation of light across the direction perpendicular to the flow, rather than in a cylindrical orientation as shown previously. For this different orientation a new RTE was proposed where the pathlength was calculated using cylindrical coordinates, including an azimuthal (θ) angular dependence, as shown in

Figure 110. The model used an angular dependence to calculate the pathlength, with the pathlength of the light entering the reactor shown in Equation 97.

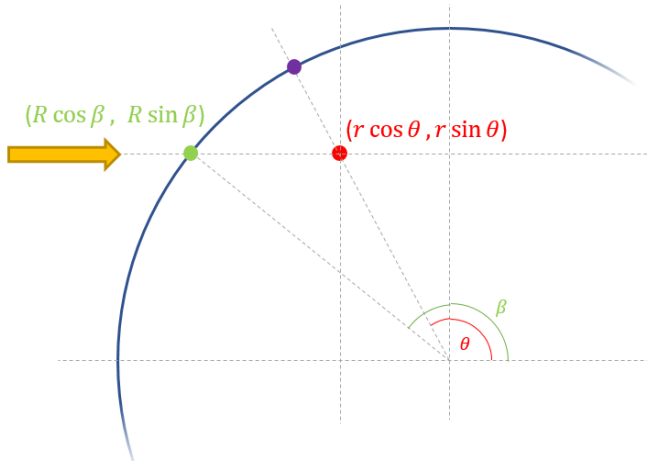


Figure 110 - A schematic of the FEP tubular reactor and the calculations used to measure the pathlength of light entering the reactor

$$Pathlength = r\cos\theta + R\cos\left(arcsin\left(\frac{r\sin\theta}{R}\right)\right) \tag{97}$$

This model initially assumed a lamp power at 254 nm, with the angular dependence of the light shown in Figure 111. One interesting feature, shown in Figure 111, is the difference between the light at the front of the reactor at the start of the reaction compared to the end of the reactor at the end of the reaction. Without a photosensitiser a front of light develops as the absorbing species react, compared to with a photosensitiser the light distribution stays near constant as the photosensitiser is not used up.

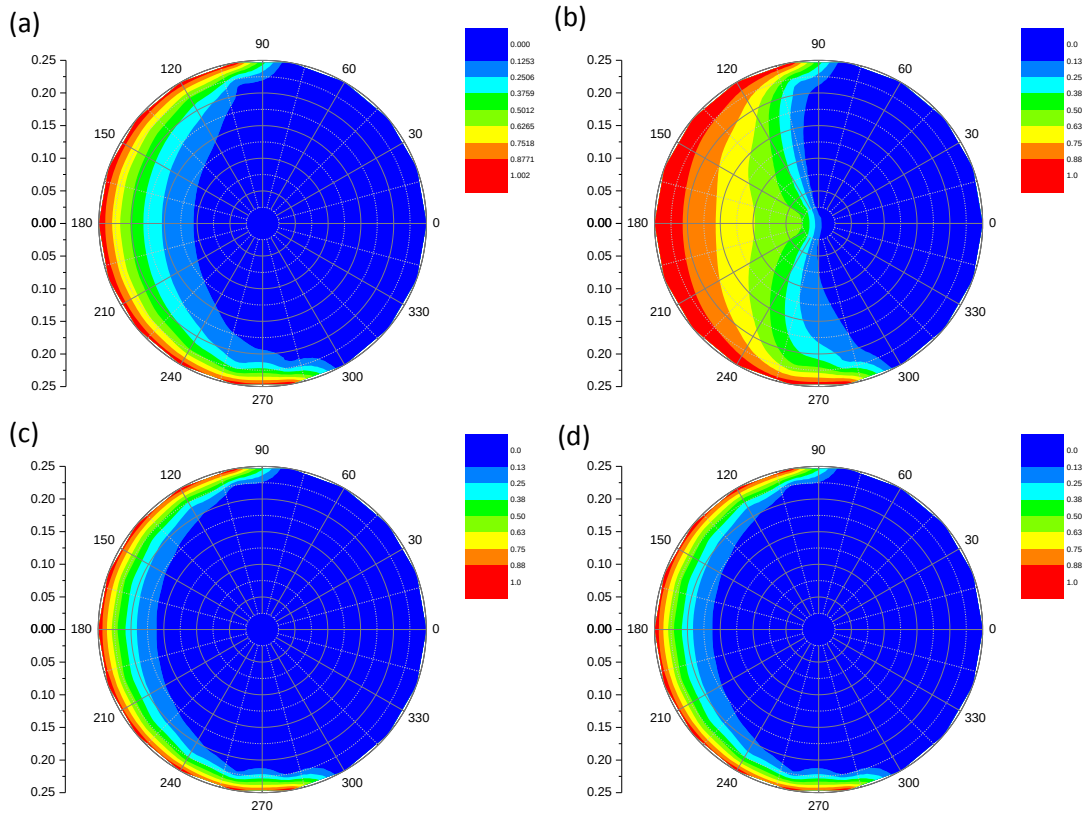


Figure 111 - The dimensionless light intensity across the FEP tubular reactor, with (a) and (b) showing the start and end of the reactor and reaction, respectively, without a photosensitiser; and (c) and (d) show the start and end of the reactor and reaction, respectively, with a photosensitiser.

The initial plan was to use this model to estimate the light intensity of the mercury arc lamp used in the reactions. However, due to the angular dependence of the light the computational time taken to complete each calculation shown above was *ca.* 30 minutes compared to 1 minute for the excimer flow reactors. To overcome this a simplified FEP tubular reactor was proposed with annular flow.[156]

4.10.1. Simplified FEP tubular reactor

The simplified FEP tubular reactor was similar to the annular flow reactors used with the excimer flow reactor models, with the lamp on the inside of the annulus rather than outside, as shown in Figure 112.[156] The dimensions used were matched as best as possible to the total volume, length and width. The dimensions of the simplified annular-like FEP reactor were a length of 71 cm, with an internal radius of 3 cm and an external radius of 3.271 cm. The specific light power was unknown, however, as the experiments were carried out before the modelling commenced all of the experiments contained little information, with all giving *ca.* 70 % yield.

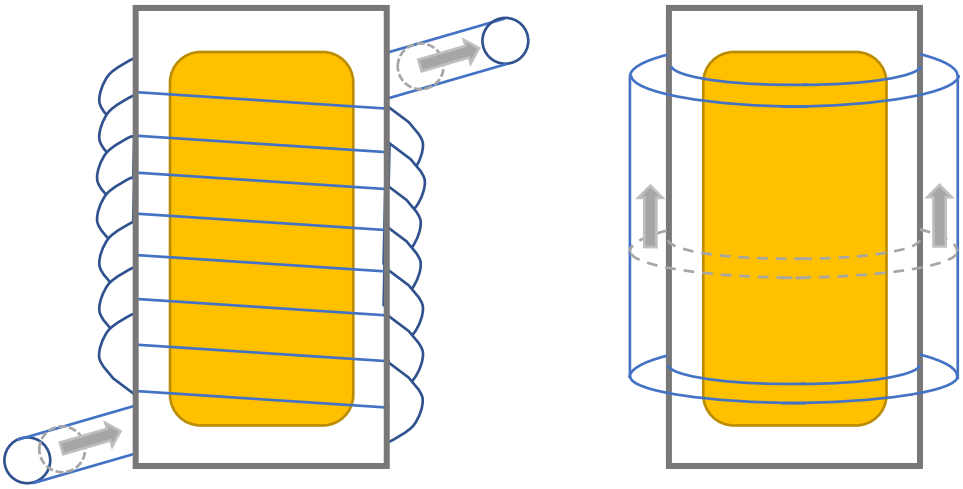


Figure 112 - A schematic of the FEP tubular reactor and the simplified annular reactor that is designed to mimic the FEP reactor

As there was little information for the lamp power estimation, a sensitivity analysis was carried out as an alternative. A range of lamp powers and flowrates were used in the model, showing little effect, with a consistent yield for the bridged yield of 68 % across a wide range of factor values. The lamp used was a mercury arc lamp that emits across a wide range of wavelengths, which the photosensitiser absorbs, giving a full-conversion value for the bridged product yield of *ca.* 68 %. This yield for the bridged product was also observed by colleagues using the Firefly reactor in Bristol.

As seen in Figure 113, any value for the irradiance over 500 $W \cdot m^{-2}$, which would be expected for a mercury arc lamp, does not change the value away from the *ca.* 68 % yield. The production of the non-

bridged compound is still affected but as this is not the desired product, and goes on to breakdown with long exposure, it was not concerning.

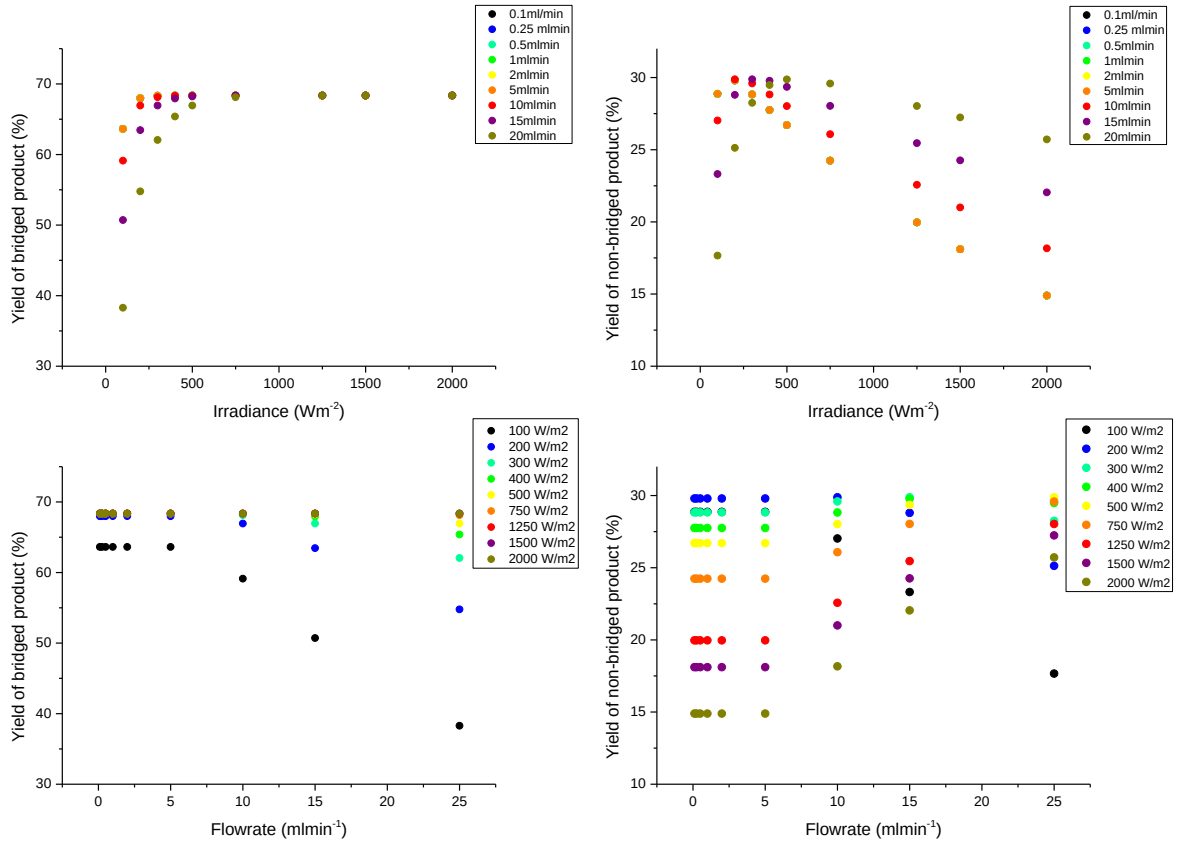


Figure 113 - Sensitivity analysis of the effects of flowrate and irradiance on the FEP tubular reactor, showing for any irradiance value above *ca.* 500 W·m^{-2} the yield of the bridged product is *ca.* 68 %, while the yield of the non-bridged product shows much greater variation

The modelling of this reaction was then able to be used in the next chapter, where the bridged product undergoes a hydrolysis and electrocyclic ring-opening reaction.

4.11. Chapter summary

A photochemical reactor batch model was developed from first principles to satisfy an idealised photochemical reaction scheme. The model was then developed further to incorporate an annular geometry as well as the flow of materials. These models were used to model the excimer reactors as this offered singular wavelengths, which helped simplify calculations. The models were then used to estimate quantum yields and compared well with literature methods and values. Actinometry was not attempted as previous attempts in the group had shown that for accurate results a flowrate was required that created a backpressure above the safety rating of the reactors.

The manufacturer's lamp power was used for further calculations as the aim of the project was for prediction of reactor performance. The capabilities of predicting reactor performance was shown across both batch and flow systems at multiple different wavelengths.

The use of photosensitisers was also investigated, where a number of further assumptions were needed to reduce correlations between parameters. The reproducibility of the estimations with photosensitisers was shown between batch and flow reactors for two different reaction schemes.

Two more complex reactor models were developed; the FEP tubular reactor and the Vortex model reactor. The FEP tubular reactor initially involved complex radial dependence of light pathlength, which was found to be too computationally expensive and hence a simplified annular reactor assumption was used.

With the Vortex reactor, initially, a complex model involving angular dependence of flow was attempted however this was also too computationally expensive. A simplified model was then used with different zones of diffusion to *mimic* the mixing of the vortexes.

Throughout the development of the models a comparison with CFD calculations was carried out to ensure both approaches were congruent. This allowed for more understanding with the comparison of the complex Vortex reactor as the assumptions regarding the absorption of light were the same.

Both models showed good agreement for the output yield at equilibrium across most conditions. The major difference between the gPROMS process model and the CFD model was the initial rate of reaction, with the gPROMS model approaching equilibrium much quicker. The speed of the gPROMS model compared to the CFD model was thought to be the greatest advantage.

For a more complex photosensitised reaction, where the reaction proceeded with and without photosensitiser, the predictive capabilities were shown, however these were more uncertain. For scale-up of this reaction with the FEP tubular reactor, this uncertainty did not affect the final yield of the desired product of *ca*. 68% which was also observed independently by colleagues using the Firefly reactor in Bristol. The validated model of this step of the reaction will be used in the next chapter where the subsequent thermal step will be modelled in the thermal reactor.

4.12. Future work

As mentioned in the introduction to the photochemical modelling, the amount of light is a crucial parameter used within the models. As the aim of this work was to predict the performance of the reactor under different conditions, the accuracy of the lamp power was not considered to be a highly important issue. This was because the method of estimation considered the lamp power and estimated a quantum yield relative to this value. Actinometry had been previously considered for measuring this, although the systems chosen showed a high degree of uncertainty along with safety concerns for the glass reactors. To use the technique to accurately estimate quantum yields, the light power would need to be measured more accurately and hence in future, different actinometry systems could be investigated.

For the quantum kinetic parameter defined using a Bodenstein-like assumption, it would be interesting to see how far the quantum kinetic parameter had an inverse concentration dependence as assumed. This could be investigated by carrying out further reactions at difference concentrations of starting materials and photosensitisers.

The models developed have been shown to be robust across a range of reactions, reactors and conditions. However, with the Vortex reactor, the lamp power was estimated using the experimental results of Cookson's dione reaction. It would therefore be interesting to follow a different reaction through estimating the quantum yield in the excimer flow reactor and then predicting the performance of the reactor using the estimated lamp power.

5. Modelling reactions in a high-temperature water reactor

5.1. Chapter Overview

This chapter lays out development of a computational model for two high-temperature water (HTW) reactors, (Internal volumes of 43 cm^3 and 0.77 cm^3) which were used to estimate the kinetic parameters for two consecutive reactions. Initially a ring-opening step was investigated with experimental results from the larger reactor. A process of reparameterization of the Arrhenius equation was also used to reduce uncertainty and correlation between parameters, with an optimal reference temperature identified to reduce the correlations.

A similar process was then used for a multi-step reaction within the larger reactor. However, due to the high yielding experimental results there was limited information contained within the experiments. The separate reactions were combined into a single step within the model which reduced uncertainty in the values at the expense of understanding the mechanism and relative rates. Using this assumption highlighted the limitations of this method, that uncertainty in the values could be reduced by making further assumptions.

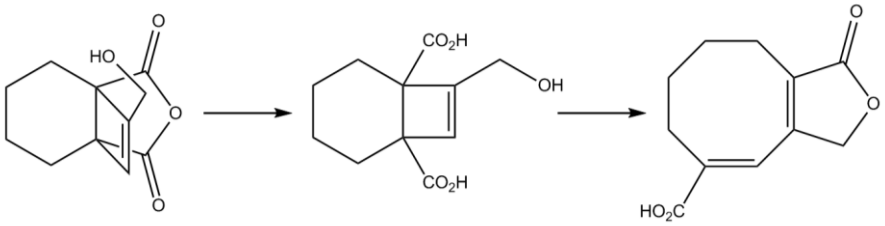
To understand the reactions further, a smaller reactor was developed so more experiments could be carried out while reducing the material usage. The experimental results for the multistep reaction were used in the parameter estimation, again using the reparameterization and reference temperature optimisation to reduce parameter uncertainty and correlations.

The estimated kinetic parameters were used to accurately predict the performance of the previously presented experiments in the larger reactor. The performance of the reaction was also predicted at 60 $ml \cdot min^{-1}$, which was the expected output of the production of the starting material from colleagues at the University of Bristol. A new reactor design was then proposed by using the model to define the dimensions that would increase yield and reduce reactor footprint.

5.2. Thermal chapter introduction

The production of medium and large cyclic ring systems is of great importance in organic synthesis, as they are often found within biologically relevant compounds.[355] The synthesis of ring systems through direct cyclisation is often challenging due to the strain of the ring molecules and unfavourable entropic factors. [356] The reluctance to directly cyclise is most acutely observed for 8-, 9- and 10- membered rings. To form these ring systems alternative approaches are required, such as through ring-expansion and rearrangement or fragmentation reactions; for example, strategies involving the expansion of 4-membered rings have proved useful within synthesis.[357] An example of this electrocyclic ring opening used in this work is shown in Scheme 15.

Scheme 15 - The hydrolysis of the bridged compound to form the diacid before an electrocyclic ring-opening step to for the ring-opened product. It should be noted that the bridged compound is formed in a photochemical step discussed in the previous chapter.



Bridged compound **Diacid** **Ring-opened product**

Colleagues from the University of Bristol have previously investigated the thermolysis of the 'bridged product', a 6:4 multi-ring system, formed from the photochemical reaction of THPAA with propargyl alcohol (discussed in the previous chapter) which produces an 8:5 ring-opened product. Another interesting outcome of this reaction is that the process is formally forbidden due to the disrotatory mode of action.[355]

The reaction was optimised by colleagues using the equipment available in Bristol, eventually finding optimal conditions of being kept at in xylene at 140 °C for 48 hours, achieving a yield of 95%. This process was therefore seen as an opportunity to greatly improve the processes' efficiency and sustainability credentials, using the specialised equipment and abilities at Nottingham.

It was hoped that the high-temperature reactors would lead to an increased reaction rate, as well as helping to overcome the entropic limitations. The replacement of xylene as the solvent was also considered a key task as it is considered a health hazard and is often sourced from non-renewable sources.[358,359]

Modelling of the newly developed process in tandem with experiments was considered to be crucial for optimising the process, especially for the eventual multi-reactor process. The initial experiments were carried out before the model was developed, with the final experiments being guided by the model to understand the model better.

5.3. Aims of HTW research section

The aims for the high-temperature water research section of this Thesis, defined in Section 2.8, were:

Aim 5.1 - Develop a process model for a high-temperature water reactor

Aim 5.2 - Use a high-temperature water process model to understand reaction kinetics and compare reactor performance prediction with experimental results

Aim 5.3 - Use kinetics to predict reactor performance for a variety of reactions

Aim 5.4 - Use a high-temperature water model in conjunction with the photochemical process model to predict performance of a daisy-chained process

Aim 5.5 - Optimise multi-step reaction process

5.4. High temperature water reactor model development

The different aspects of the high temperature water reactor are discussed below, alongside the assumptions taken.

5.4.1. Model description

A schematic of the reactor model is shown in Figure 114, showing a coiled tube that is placed inside a heating block, depicted by the red dashed line. The model of the high temperature thermal coil reactor was developed within Process Systems Enterprise's *gPROMS© ProcessBuilder 1.3.1*. The inner diameter of the reactor tube is 0.305 cm, with a coil diameter, D_c, of 7 cm and length of 600 cm. The temperature of the heating block, as measured by a K-type thermocouple inside the heating block, was assumed to be the fixed temperature of the reactor wall. The initial concentration was calculated at standard temperature and pressure, before being introduced into the reactor where it changed depending on conditions.

The mathematical relationships of the model have been developed from engineering principles so that, with parameter estimation, a hybrid model can be developed to predict behaviour outside of the experimental space.

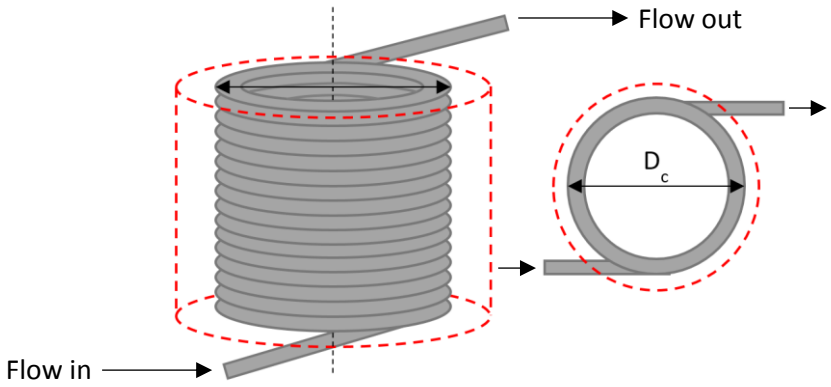


Figure 114 - A schematic of the model, showing the coiled tubular reactor inside a heating block depicted by the red dashed line. D_c is the coil diameter and is used in the calculations of effective dispersion coefficients discussed below.

The kinetics used in the model used either the standard Arrhenius equation or a reparameterised version of the Arrhenius equation to reduce uncertainty and correlations, discussed below. The kinetic

scheme did not consider the possible non-linear effect of HTW with changing temperature, such as the increased acidity/basicity which could increase the rate of the hydrolysis or the possible transition state stabilisation of HTW.

Physical properties

The physical properties, such as density, viscosity or thermal conductivity, of the reaction mixture were calculated using the Peng-Robinson Advanced 1978 (PR-78A) equation of state (EoS).[72] Due to the low concentration of reagents, the physical properties calculated for this system were assumed to be equal to that of the solvent. Initial tests were carried out using the SAFT-γ Mie EoS as PR-78A was unable to predict fluid behaviour without previous physical property data. With SAFT-γ Mie and a concentration of starting material of 0.275 mol·dm^{-3}, the maximum used experimentally, the change in properties shown in Table 51. Unfortunately, SAFT-γ Mie is unable to calculate viscosity and thermal conductivity, so the change could not be considered for these parameters. The difference was assumed to be minimal compared to the predicted model values, as shown with density and heat capacity, especially regarding the error associated with the error in the EoS.

Table 51 – A table to show the change in predicted physical properties using SAFT-γ Mie for the reaction mixture with and without the reagents. A small change is observed on the physical properties with the inclusion of the starting material and hence the assumption of using the solvent properties to predict physical behaviour was valid.

	Value predicted by SAFT-γ Mie at 230 °C and 15 MPa		
Property	**50:50 vol. H_2O:CH_3CN solvent**	**0.275 mol·dm^{-3} in 50:50 vol. H_2O:CH_3CN solvent**	**% Change from including reagent**
Density (kgm^{-3})	644	623	-3.2%
Heat Capacity (kJkg^{-1}K^{-1})	4.60	4.70	+2.2%

5.4.2. Mass balance

The mass balance of the reactor is described using a typical model for flow reactors, as shown in Equation 98, where t is time and $C_{i,z,r}$ is concentration of compound i at radial position r and axial

position z.[219] D_{ax} and D_{rad} are the axial and radial dispersion coefficients, respectively, while the rate of reaction for compound i, is summed over all reactions, j.

$$\frac{dC_{i,z,r}}{dt} = -u(r)\frac{\partial C_{i,z,r}}{\partial z} + D_{ax}\frac{\partial^2 C_{i,z,r}}{\partial z^2} + D_{rad}\frac{1}{r}\frac{\partial}{\partial r}\left(r\frac{\partial C_{i,z,r}}{\partial r}\right) + \sum rate_{i,j} \tag{98}$$

The fluid was assumed to be incompressible as the fluid was a liquid and the velocity was relatively small compared to the speed of sound.[77,265] The velocity of the fluid across the radial direction, $u(r,z)$, was calculated using Equation 52, where u is the linear velocity, R is the reactor internal radius, μ is the kinematic viscosity and P is the pressure.[219]

$$u(r,z) = \frac{R^2}{4\mu}\left(\frac{dP}{dz}\right)\left(1 - \frac{r^2}{R^2}\right) \tag{35}$$

$$\frac{dp}{dz} = f_D\frac{\rho}{2}\frac{\langle v\rangle^2}{D_H} \tag{5}$$

$$f_D = \frac{64}{Re} \tag{99}$$

The pressure drop per length, $\frac{\mathrm{dP}}{\mathrm{dz}}$, was calculated as per the Darcy-Weisbach equation previously defined in Equation 5, where f_D is the Darcy friction factor, ρ is the density of the fluid and u_{avg} is the average linear velocity of the fluid. As laminar flow was expected, and the pressure drop was not expected to be a key factor, the Darcy friction factor was calculated from Equation 99, where Re is the Reynolds number.[265] The coiled shape was expected to affect the dispersion within the reactor and is discussed below.[267,360]

5.4.3. Energy balance

The energy balance of the reactor is governed by Equation 100, where T is the temperature and δ is the thermal diffusivity of the fluid.[219] The thermal diffusivity, δ, of the fluid was calculated as per Equation 101, where k_T is the thermal conductivity, ρ is the density of the fluid and c_p is the heat capacity. The boundary condition of the heated reactor is shown in Equation 102, with the reactor

assumed to have a constant temperature at the wall of the reactor, where k_{HT} is the heat transfer coefficient.[262]

$$\frac{\partial T}{\partial t} = \frac{\delta}{R - r}\frac{\partial}{\partial r}(R - r)\frac{\partial T}{\partial r} + \delta\frac{\partial^2 T}{\partial z^2} - u(z,r)\frac{\partial T}{\partial z} \quad (100)$$

$$\delta = \frac{k_T}{\rho c_p} \quad (101)$$

$$k_T\frac{\partial T}{\partial r} = k_{HT}(T_{wall} - T_{heater}) \quad (102)$$

The change in temperature of the reaction due to the enthalpy of reaction was ignored as it was estimated using the gSAFT γ-Mie equation of state and was shown to be negligible compared to the heating of the reactor (See Appendx III). Also, as mentioned previously, water's high heat capacity means that it often acts as a heat buffer for reactions.[236] A heat transfer coefficient, k_{HT} = 0.1 $Wcm^{-2}K^{-1}$, was used as per expected values for heat transfer for the forced convection of hot water over stainless steel. The thermal conductivity of the fluid was calculated using the PR-78A EoS.[72]

The final yields were calculated by ^{1}H NMR when the solution had been cooled down to room temperature after the BPR, and hence the equivalent concentration at the outlet was calculated within the model.

5.4.4. Effect of Dispersion

Dispersion within flow reactors can have a considerable effect on the conversion and yields of chemical reactions.[219] Coiled reactors is known to have a considerable effect on dispersion due to the formation of Dean vortices, which greatly increase dispersion perpendicular to flow, as shown in Figure 115.[361] The dispersion coefficient is therefore expected to be higher than molecular diffusion for coiled reactors, and is known as the effective dispersion coefficient.

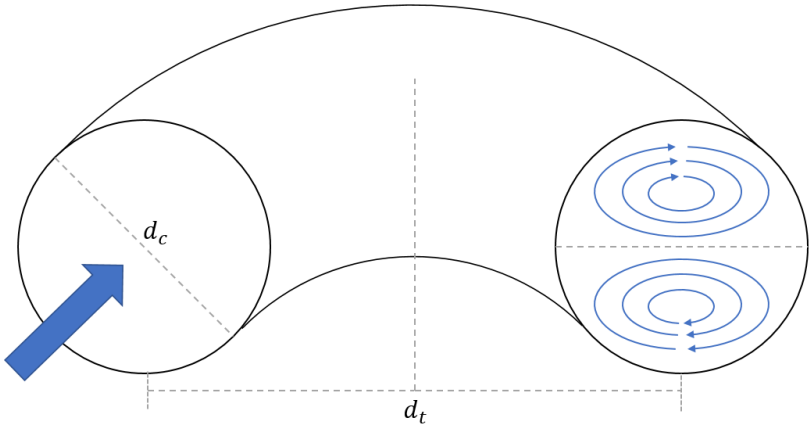


Figure 115 – A diagram depicting the formation of Dean vortices perpendicular to the fluid flow when a fluid flows through a curved pipe. The direction of flow is indicated by the blue arrows, with d_t indicating the diameter of the tube and d_c indicating the diameter of the coil.[361]

The effective Dispersion coefficient can be calculated using Equation 103, as proposed by Aris, where D_m is the molecular diffusion coefficient, κ is the dispersion ratio dependent on fluid flow and geometry, d_t is the tube diameter and u is the mean axial velocity.[362]

$$D_s = D_m + \kappa \frac{d_t^2 u^2}{192 D_m} \tag{103}$$

The dispersion ratio in coiled tubes depends on both the Dean number (De) and the Schmidt number (Sc), as defined in Equations 104 and 105, respectively. d_t is the diameter of the tube and d_c is the diameter of the coil, Re is the Reynolds number for the flow and D_m is the molecular diffusion coefficient for the fluid.[361,363]

$$De = Re \sqrt{\frac{d_t}{d_c}} \tag{104}$$

$$Sc = \frac{\mu}{\rho D_m} \tag{105}$$

The effect of Dean vortices can be calculated using a number of different mathematical relationships that have been published. [364–366] There are various graphical methods for calculating the effective dispersion ratio, with different sources reporting different values depending on the conditions.

However, in the region of interest (*ca.* $DeSc$ = 1000) the models were consistent. The dispersion ratio was therefore calculated using the relationship reported by R.N. Iyer at. al, shown in Equation 106.[365]

$$\kappa = 1.65 - 0.863\log\left(\mathrm{De}\sqrt{\mathrm{Sc}}\right) + \left[0.113\left(\log\sqrt{\mathrm{Sc}}\right)\right]^2 \qquad (106)$$

To investigate the range of values of κ relevant to the thermal reactor, the parameters values estimated by the PR-A EoS were inputted into Equation 106. The expected dispersion coefficient values ranged from 0.59 $cm^2 \cdot s^{-1}$ to 5.42 $cm^2 \cdot s^{-1}$ within the experimental space used for the larger reactor. See Appendix III for more details.

The lowest expected dispersion coefficient value for the larger reactor, 0.590 $cm^2 \cdot s^{-1}$, was relatively large for this system. The reaction was modelled using this dispersion coefficient value at a flowrate of 34 $ml \cdot min^{-1}$, with the concentration profile across the radial direction plotted in Figure 116. The radial variation in concentration is negligible (*ca.* 0.5 %) for D = 0.590 $cm^2 \cdot s^{-1}$. Greater dispersion coefficient values would reduce the variation in concentration across the radial dimension even further. It can therefore be assumed that the radial dispersion of this system was large enough such that the fluid exhibits plug-flow-like behaviour.

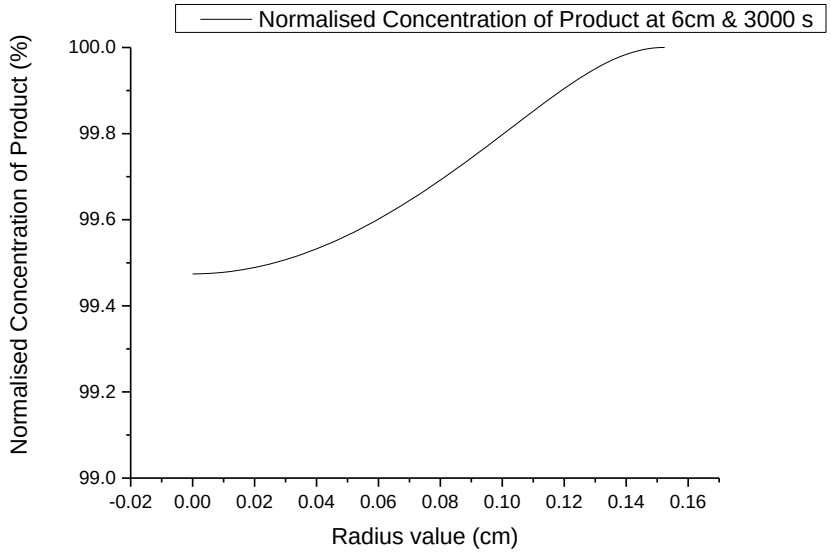


Figure 116 - The normalised concentration of 3 across the radial dimension at equilibrium with D = 0.590 $cm^2 \cdot s^{-1}$ at a flowrate of 34 $ml \cdot min^{-1}$, showing negligible variation across the radial dimension.

5.5. Ring opening step in larger reactor

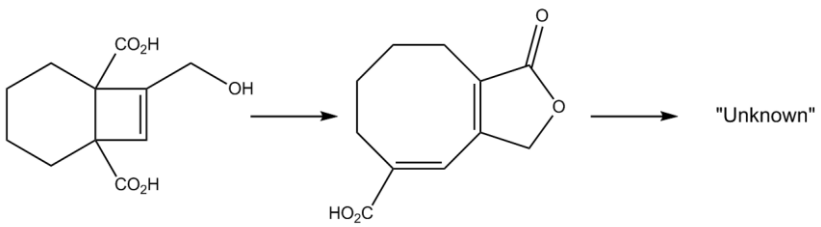
The experimental results for this section were kindly collected by PhD Student Bryan Tambosco and Dr. Rowena Howie.

The electrocyclic ring opening of the diacid to form the 8-membered ring opened product was first carried out experimentally in the custom-built reactor with an internal volume of 43.9 cm^3. The ring-opening step was thought to be the rate limiting step in the overall scheme as it is a symmetry forbidden step, with the formation of the ring-opened product only being observed at elevated temperatures.[355] The variables that were changed to explore the reaction spaces were: flowrate, temperature, pressure and initial concentration of the diacid starting material.

5.5.1. Model input for larger reactor

The reaction scheme used in the thermal reactor model is shown in Scheme 16; a breakdown of the product was included as a reduction in mass balance and was observed at certain conditions. As the yields had been calculated by ^1H NMR, the yield sensor's standard deviation was fixed at 5% of the yield. The breakdown step was included to consider the reduction in mass balance, but the amount of "unknown" was not used in the estimation. For the hydrolysis step, the introduction of a water molecule was not considered within the model as the reaction solvent was 50% water by volume and hence concentration effects were assumed to be negligble.

Scheme 16 - The initial estimations were carried out on the electrocyclic ring opening of the diacid to form the 8 membered ring-opened product, followed by the possible breakdown of the product.



5.5.2. Experimental results

In total, 33 different experiments were carried out at a range of flow rates, temperatures, pressures, and concentrations. The experimental conditions and corresponding yields, starting material recovery and mass balance are shown in Table 52. The 11 experiments shown in **red** were used for the estimation of parameters with the remaining experiments used to validate the model. These experiments for the parameter estimation were chosen as a spread across the reaction space.

Table 52 - The experimental results collected by Bryan Tambosco and Dr. Rowena Howie for the electrocyclic ring-opening of the diacid followed by the breakdown of the product in the larger reactor. The experiments shown in red were used for the parameter estimation while the experiments in **black** were used in the model validation.

Temperature (°C)	Pressure (bar)	Flow rate ($ml \cdot min^{-1}$)	Initial Concentration diacid ($mol \cdot dm^{-3}$)	Recovery of diacid starting material (%)	Yield of ring-opened product (%)	Mass balance (%)
230	**150**	**19**	**0.0624**	**15.6**	**75.4**	**91.0**
230	150	19	0.0613	17.6	73.4	91.0
245	125	26.5	0.0915	13.0	81.1	94.1
245	175	26.5	0.038	11.8	77.1	88.9
215	**175**	**11.5**	**0.0908**	**20.1**	**67.8**	**87.9**
215	**175**	**26.5**	**0.0373**	**54.4**	**38.8**	**93.2**
215	125	11.5	0.0882	24.0	67.3	91.3
215	**125**	**26.5**	**0.0893**	**54.2**	**43.8**	**98.0**
215	125	11.5	0.0371	23.8	68.6	92.4
245	125	26.5	0.0375	11.8	78.1	89.9
245	**175**	**11.5**	**0.0879**	**4.10**	**91.1**	**95.2**
215	175	26.5	0.088	50.3	40.3	90.6
245	**175**	**26.5**	**0.0867**	**13.1**	**85.9**	**99.0**
230	150	19	0.0678	15.4	72.5	87.9
215	**175**	**11.5**	**0.0407**	**27.9**	**67.2**	**95.1**
245	**125**	**11.5**	**0.0941**	**1.5**	**94.0**	**95.5**
200	150	19	0.0665	67.0	25.6	92.6
230	200	19	0.0683	8.80	76.8	85.6
230	**150**	**19**	**0.0673**	**15.7**	**75.5**	**91.2**
230	150	19	0.0645	17.0	78.5	95.5
230	150	19	0.0638	16.1	78.7	94.8
230	150	34	0.0666	25.6	68.2	93.8
260	150	19	0.063	1.40	93.4	94.8
230	100	19	0.0654	16.9	70.1	87.0
230	**150**	**4**	**0.0634**	**0**	**91.9**	**91.9**
230	**150**	**19**	**0.1258**	**11.2**	**77.0**	**88.2**
230	150	19	0.0676	17.6	78.1	95.7
230	150	19	0.0652	16.0	78.0	94.0
230	150	19	0.0667	17.1	78.3	95.4
230	150	19	0.0649	15.7	76.8	92.5
230	150	19	0.0632	17.7	75.4	93.1
215	175	11.5	0.039	27.9	67.2	95.1
215	125	26.5	0.0394	50.7	38.2	88.9

5.5.3. Kinetic parameter estimations for the ring-opening step in larger reactor

The kinetic parameter estimation shown below goes through a number of mathematical steps in order to reduce the uncertainty in the values and reduce correlations between parameters. The standard Arrhenius equation was used initially before subsequent reparameterised versions were used to reduce uncertainty and parameter correlation.

Initial estimation with standard Arrhenius

The initial estimation used the standard Arrhenius equation, defined in Equation 66, and took over nine hours for completion. The length of calculation was likely due to the high correlation between parameters and large standard deviations which can be seen in Table 53, so that any small change in one value would lead to changes in others.

$$k = A_0 exp\left(\frac{-E_A}{RT}\right) \tag{66}$$

Table 53 - The estimated kinetic parameters for the standard Arrhenius equation for the ring-opening and breakdown steps in the larger reactor. The standard deviations of the estimated parameters were considerably larger compared to the values, which was thought to be due to the high correlation between parameters.

Reaction	A_0 (±SD) (s^{-1})	E_A (±SD) ($kJ \cdot mol^{-1}$)
Ring-opening	1.757 (±3.91) x 10^8	97.69 (±9.16)
Breakdown	29.22 (±724)	49.12 (±105)

The high correlation between parameters is shown in the correlation matrix in Table 54, where the parameters for each reaction are completely correlated, as shown by the value of 1.

Table 54 - The correlation matrix of the estimated parameters for the ring-opening and breakdown steps using the standard Arrhenius equation, showing the high correlation between the activation energy and pre-exponential factor for each reaction.

Parameter	No.	1	2	3	4
$E_{A,1}$	**1**	1			
$E_{A,2}$	**2**	0.227	1		
A_1	**3**	1	0.224	1	
A_2	**4**	0.228	1	0.225	1

The predicted performance of the experiments used during the estimation and validation are shown in Figure 117 (a) and (b), respectively. The predicted values show that even though the estimated parameters contain large errors and are highly correlated, the model still accurately predicted the performance of the experiments.

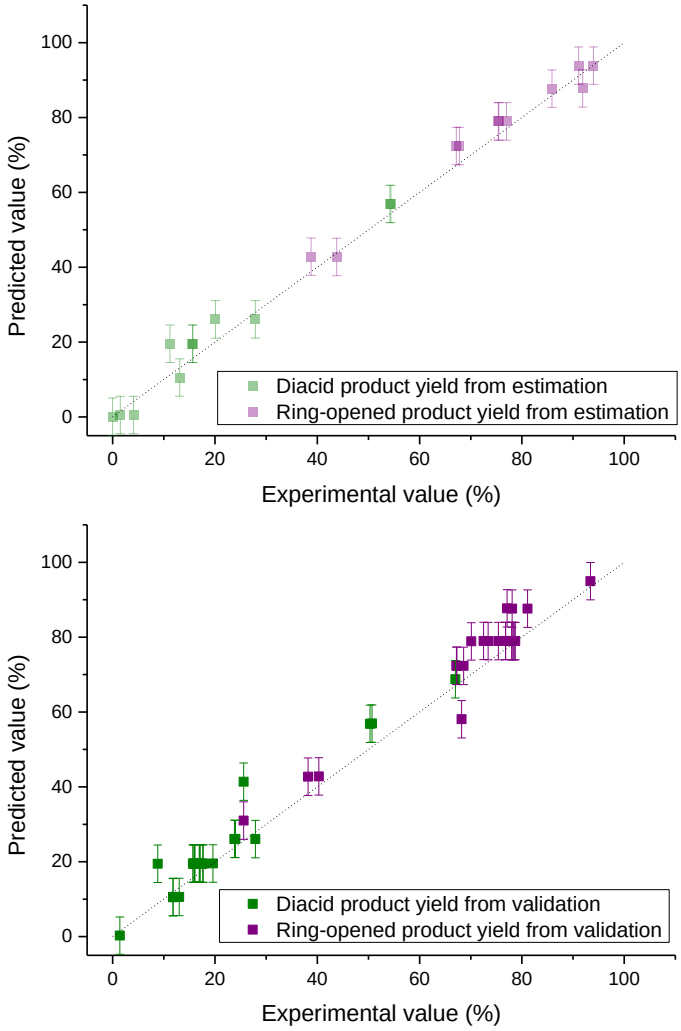


Figure 117 - (a) The predicted values of the experiments used in the initial Arrhenius estimation, showing good agreement which was expected and (b) the prediction of experimental values for experiments not used in the estimation, showing that the estimated parameters accurately predict values outside of the experimental space used in the estimation. The yield of the diacid product is shown with ■ and the yield of the ring-opened product shown by ■, with the error bars a standard deviation each way. The dashed line indicates a perfect fit between prediction and experiment.

Further estimations were carried out using reparameterised Arrhenius equations to reduce the standard deviations and correlation of parameters. The initial estimated parameters were used to help

guide initial parameter guesses and value boundaries for further estimations, which helped to reduce computational time.

Estimation with reference temperature (ÃE$_A$ - T$_{ref}$ = 230.65 °C)

As the initially estimated parameters were highly correlated, the Arrhenius equation was reparameterised to include a reference temperature which was hoped to reduce the correlations between estimated parameters. The first reparameterised Arrhenius equation used is defined in Equation 67 and 68.

$$k = exp\left(\tilde{A} - \frac{E_A}{R}\left(\frac{1}{T} - \frac{1}{T_{ref}}\right)\right) \tag{67}$$

$$\tilde{A} = ln\, A_0 - \frac{E_A}{RT_{ref}} \tag{68}$$

The reference temperature used was calculated from the inverse average of the experimental temperatures, as defined in Equation 71.[289]

$$\frac{1}{T_{ref}} = \frac{1}{n}\sum_{i=1}^{n}\frac{1}{T_i} \tag{71}$$

The estimated kinetic parameters are shown in Table 55. The standard deviation of the activation energies were unchanged, as expected with this reparameterization method.[289] The correlation matrix for the estimated parameters is shown in Table 56, which shows the reduced correlations between parameters compared to the standard Arrhenius.

Table 55 - The estimated kinetic parameters using the A-E$_A$ reparameterised Arrhenius equation and T$_{ref}$ value = 230.65 °C for the ring-opening and breakdown steps in the larger reactor.

Reaction	Ã$_1$ (±SD)	E$_A$ (±SD) (kJ·mol^{-1})
Ring-opening	-4.336 (±0.055)	97.68 (±9.16)
Breakdown	-8.353 (±0.396)	49.08 (±105)

Table 56 - The correlation matrix of the estimated parameters for the ring-opening and breakdown steps using the A-E_A reparameterised Arrhenius equation and T_{ref} value = 230.65 °C. The correlation between parameters has been reduced using the reparameterised equation.

Parameter	No.	1	2	3	4
$E_{A,R}$	1	1			
$E_{A,B}$	2	0.151	1		
A_R	3	0.665	-0.0369	1	
A_B	4	0.0132	-0.44	0.227	1

The correlation between reaction parameters was reduced further using a second reparameterised Arrhenius equation.

Estimation with reference temperature (ÃB - T_{ref} = 230.65 °C)

A different reparameterised Arrhenius equation, defined in Equations 48 and 49, was also used to reduce the correlation between parameters. The benefit of using this equation was that an optimisation algorithm could be subsequently used to choose T_{ref} to further reduce the correlation.

$$k = exp\left(\tilde{A} + B\left(\frac{T - T_{ref}}{T}\right)\right) \tag{69}$$

$$B = \frac{E}{R\,T_{ref}} \tag{70}$$

The estimated parameters using this method are shown in Table 57. The values for Ã show a small amount of uncertainty along with B for the ring-opening step, however, with B for the breakdown step there was significant uncertainty in the value.

The correlation matrix for the estimated parameters is shown in Table 58, which shows identical correlations to the previous estimation. This equivalency was expected as the difference between the two estimations was an identical mathematical operation on all values.

Table 57 - The estimated kinetic parameters using the A-B reparameterised Arrhenius equation and T_{ref} = 230.65 °C value for the ring-opening and breakdown steps in the larger reactor.

Reaction	Ã (±SD)	B (±SD)
Ring-opening	-4.336 (±0.055)	23.32 (±2.19)
Breakdown	-8.353 (±0.396)	11.72 (±24.95)

Table 58 - The correlation matrix of the estimated parameters for the ring-opening and breakdown steps using the A-B reparameterised Arrhenius equation and average T_{ref} value. The correlation between parameters is identical to the A-E_A correlation matrices showing the mathematical similarity.

Parameter	No.	1	2	3	4
$\tilde{A}_R$	**1**	1			
$\tilde{A}_B$	**2**	0.151	1		
B_R	**3**	0.665	-0.0369	1	
B_B	**4**	0.0132	0.44	0.227	1

Reference temperature optimisation

As described in Section 3.8.2, an optimal value of T_{ref} can be found using an algorithm to minimise the norm of the correlation matrix, defined in Equation 107. The Eulerian norm of the covariance matrix is plotted in Figure 118, with T' defined below for each reaction, where a * indicates the initial estimation and 1 and 2 represent the ring-opening and breakdown step, respectively.

A minimisation algorithm in Matlab was then used to find the function minima, with the T' values being 1.0149 and 0.993 for reaction 1 and 2, respectively. The T' values correspond to new reference temperatures for each reaction of 223.26 °C and 234.21 °C for the ring-opening and breakdown step, respectively.

$$\boldsymbol{G} = \begin{bmatrix} 1 & 0 & 0 & 0 \\ 0 & 1 & 0 & 0 \\ 1 - \frac{T^*_{ref,1}}{T_{ref,1}} & 0 & \frac{T^*_{ref,1}}{T_{ref,1}} & 0 \\ 0 & 1 - \frac{T^*_{ref,2}}{T_{ref,2}} & 0 & \frac{T^*_{ref,2}}{T_{ref,2}} \end{bmatrix} T' = \frac{T^*_{ref}}{T_{ref}} \qquad (107)$$

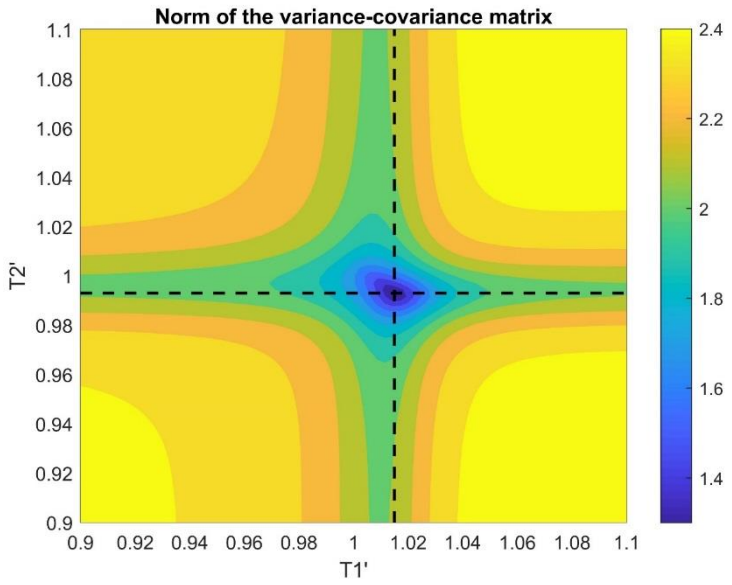


Figure 118 - A plot of the norm of the covariance matrix for varying T' values for each reaction. The values for T' were 1.0149 and 0.993 for the ring-opening and breakdown step, respectively. These T' values corresponded to 496.41 K and 507.36 K for the ring-opening and breakdown step, respectively.

The benefit of the Matlab method is the reduced computational expense of calculating the parameters without using the MLE method.[289] The new parameters were calculated using the relationships defined in Equation 108 where * indicates the initially estimated parameters. These calculations were incorporated into the same Matlab script used for the minimisation algorithm. The parameters calculated using the Matlab method are shown in Table 59.

$$A = A^* - B + B^* \quad , \quad B = \frac{B^* T_{ref}^*}{T_{ref}} \tag{108}$$

Table 59 - The estimated kinetic parameters predicted with the Matlab script using the A-B reparameterised Arrhenius equation and the optimised T_{ref} value for the ring-opening and breakdown steps in the larger reactor.

Reaction	Ã (±SD)	B (±SD)
Ring-opening	-4.683 (±0.041)	23.67 (±2.22)
Breakdown	-8.271 (±0.355)	11.64 (±24.77)

Estimation using optimised reference temperature (ÃB)

To show the validity of the Matlab method, the optimised reference temperatures of 223.26 °C and 234.21 °C were used to estimate the kinetic parameters using the MLE method. The parameters

estimated temperatures using gPROMS' MLE method with the optimal reference temperatures are shown in Table 60.

The correlation matrix for the estimated parameters from gPROMS is shown in Table 61, which shows the reduced correlations between parameters; the correlation table calculated using the Matlab showed negligible difference, as expected.

Table 60 - The estimated kinetic parameters predicted by gPROMS using the A-B reparameterised Arrhenius equation and the optimised T_{ref} value for the ring-opening and breakdown steps in the larger reactor. The values are identical to the values predicted by Matlab which shows the validity of both methods once the initial estimation has been made.

Reaction	Ã (±SD)	B (±SD)
Ring-opening	-4.683 (±0.041)	23.67 (±2.22)
Breakdown	-8.271 (±0.355)	11.64 (±24.77)

Table 61 - The correlation matrix of the estimated parameters for the ring-opening and breakdown steps using the A-B reparameterised Arrhenius equation and optimised T_{ref} value. The correlation between parameters has been reduced using the reparameterised equation.

Parameter	No.	1	2	3	4
$\tilde{A}_R$	**1**	1			
$\tilde{A}_B$	**2**	0.177	1		
$E_{A,R}$	**3**	0.0993	-0.0704	1	
$E_{A,B}$	**4**	-0.161	0.000343	0.227	1

The benefit of using the mathematical relationships is that the new parameters and their covariances can be calculated using the Matlab script developed taking *ca.* 5 seconds, compared to another estimation in gPROMS taking *ca*. 1 hour. However, it should be noted that the Matlab method is only valid when the sensors' standard deviations are fixed between estimations.

Estimation with optimised reference temperature ($\tilde{A}E_A$)

The optimal reference temperatures, defined above, for each reaction were then used in the first reparameterised Arrhenius equation so the standard deviations of the activation energy can be calculated and easily compared. The estimated values are shown in Table 62, showing a small change in value compared to those shown for the estimation using the averaged T_{ref} value in Table 55. The

correlation matrix for the estimated parameters is shown in Table 63, which show much-reduced correlations between parameters compared to the initial estimation shown in Table 54.

Table 62 - The estimated kinetic parameters using the A-E_A reparameterised Arrhenius equation and the optimised T_{ref} value for the ring-opening and breakdown steps in the larger reactor.

Reaction	Ã (SD) (s^{-1})	E_A (±SD) ($kJ \cdot mol^{-1}$)
Ring-opening	-4.683 (±0.042)	97.64 (±9.16)
Breakdown	-8.271 (±0.396)	47.36 (±105)

Table 63 - The correlation matrix of the estimated parameters for the ring-opening and breakdown steps using the A-E_A reparameterised Arrhenius equation and optimised T_{ref} value. The correlation between parameters has been reduced using the optimal T_{ref} and reparameterised equation.

Parameter	No.	1	2	3	4
$Ã_R$	**1**	1			
$Ã_B$	**2**	0.176	1		
$E_{A,R}$	**3**	0.0978	0.0718	1	
$E_{A,2}$	**4**	-0.162	0.012	0.230	1

The method of reducing correlations between parameters was successful, as shown by the correlation matrix shown in Table 56. Unfortunately, the standard deviation of the activation energy for the breakdown step was still considerably high, which was expected as the method is known to not reduce the uncertainty in the activation energy.[289] The activation energy of the breakdown step parameter's t-value of 0.215 was below the 95% reference t-value for the parameter of 1.73, which suggested the data used was not sufficient for an accurate estimation. The 95% confidence ellipsoids for the activation energy against Ã, for both reaction steps are plotted in Figure 119 (a) and (b), respectively. If more data was used for the estimation the confidence ellipsoids could be made smaller. However, the values were considered accurate enough, especially for the ring-opening step, which was considered the most important step.

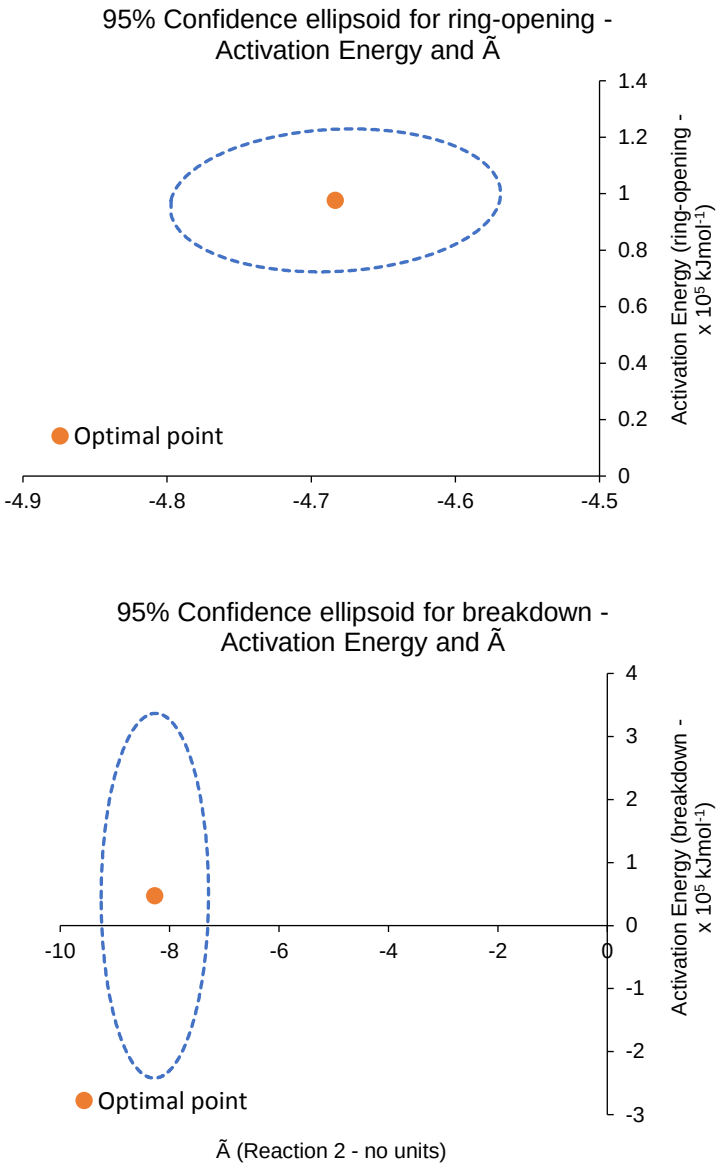


Figure 119 - The 95% confidence ellipsoids for the estimated parameters, with the activation energy plotted against Ã for the ring-opening step in (a) and the breakdown step in (b). The confidence ellipsoids for the ring-opening step were considered reasonably accurate, while for the breakdown step, there was a large uncertainty in the values which was not unexpected as significant enough breakdown of the product was only observed in a small number of samples.

As the breakdown step assumed the formation of an unknown breakdown product, further experiments were not carried out as this was not considered to be significant for the overall aim of the model. The predictive capabilities of the model were also considered accurate enough, which can be seen in Figure 120. The RMSE for the yields of the ring-opened product and the diacid were 4.82% and 4.70%, respectively.

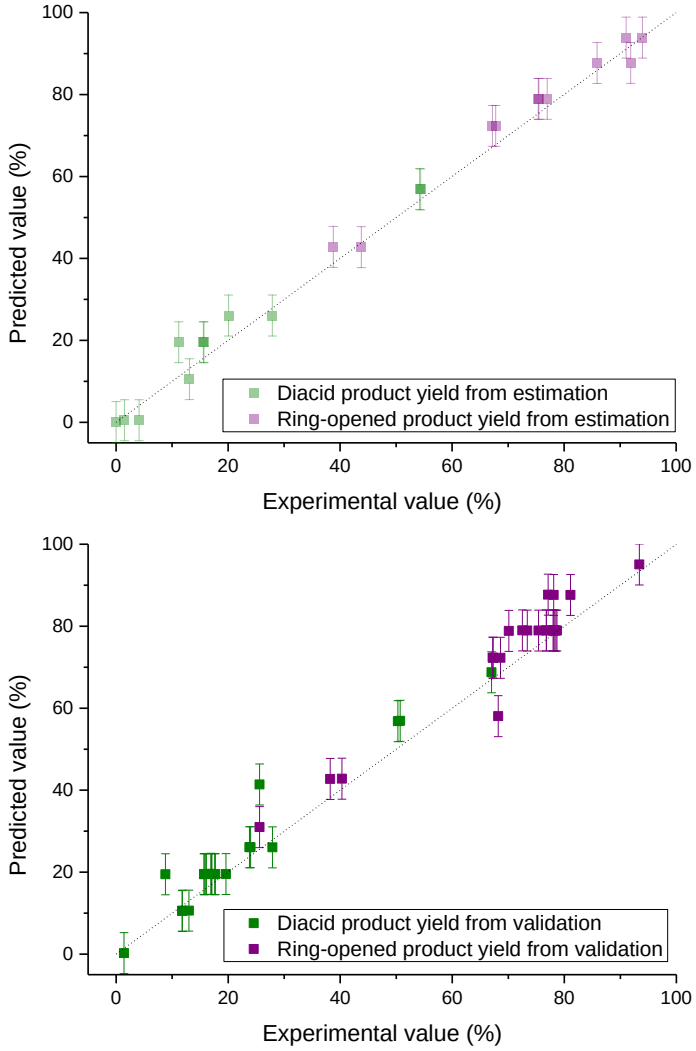


Figure 120 - (a) The predicted values of the experiments used in the optimised reference temperature reparameterised Arrhenius equation, showing good agreement which was expected and (b) the prediction of experimental values for experiments not used in the estimation, showing the estimated parameters accurately predicted values outside of the experimental space. The yield of the diacid product is shown with ■ and the yield of the ring-opened product shown by ■, with the error bars a standard deviation each way. The predictive capability is the same as the initial Arrhenius estimation. The dashed line indicates a perfect fit between prediction and experiment.

Effect of reparameterization on the predictive capabilities of the model

The reparameterization of the Arrhenius equation using reference temperatures for the reaction did not affect the overall estimation performance, as can be seen in Figure 121, where the initial Arrhenius model predictions matches the optimised reference temperature with Ã and E_A prediction.

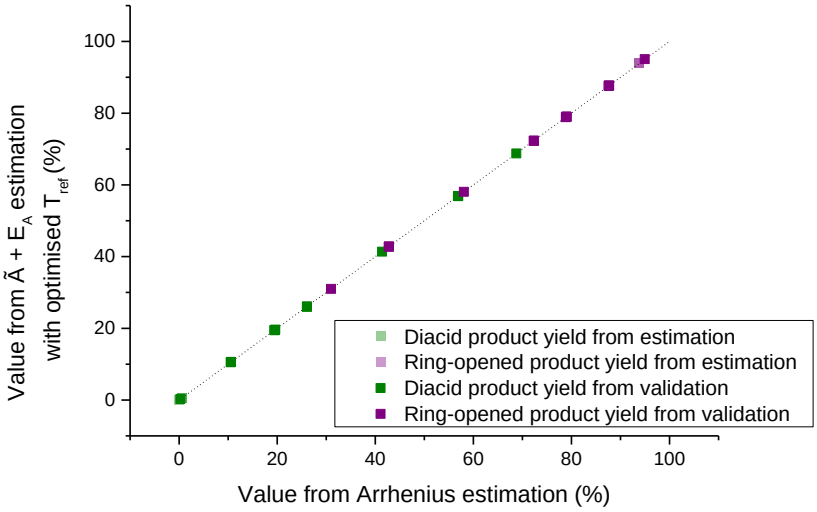


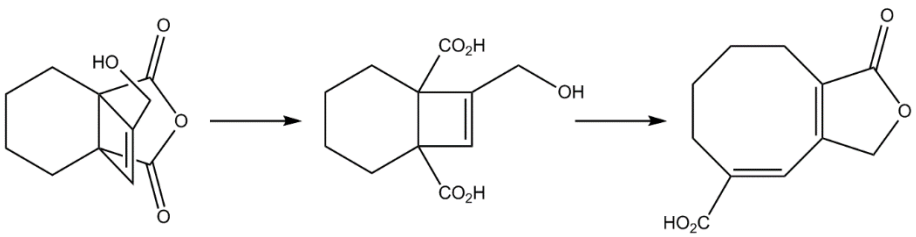
Figure 121 - A comparison of the predicted values using the initial Arrhenius and the reparameterised Arrhenius with optimised T_{ref}, showing the reparameterisation did not affect the predictive capabilities. The yield of the diacid product is shown with ■ and the yield of the ring-opened product shown by ■. The dashed line indicates a perfect fit between predictions.

5.6. Hydrolysis followed by ring-opening step in larger reactor

The experimental results for this section were kindly collected by Dr. Rowena Howie.

In the overall reaction process, the bridged compound produced from the photochemical reaction discussed in the previous chapter, is hydrolysed into the diacid which goes under the ring opening to form the ring-opened product. This multi-reaction step, shown in Scheme 17, was the main reaction of interest that needed to be understood for a daisy-chained process. The experimental results came from the laboratory optimisation of the process.

Scheme 17 - The multistep reaction scheme that involves the bridged product from the photoreaction undergoing a hydrolysis to form the diacid which undergoes an electrocyclic ring opening to form the 8 membered ring-opened product.



5.6.1. Model input

The reactor model used was the same as used in the previous section, with the only change coming from the reaction scheme and different starting materials. As the yields were calculated with ^{1}H NMR, the standard deviations of both yield sensors were 5% of the yield. For the hydrolysis step, the introduction of a water molecule was not considered within the model, as the reaction solvent was 50% water by volume and hence concentration effects were assumed to be negligible.

5.6.2. Experimental results

The experimental results for the reaction in series are shown in Table 64, where a high conversion of the bridged product starting material, and a high yield of the ring-opened product is observed. As before, the experiments shown in **red** were used for the estimation and the experiment shown in

black used for the validation. The experiment chosen for the validation was outside of the experimental space used for the estimation to try and show the predictive capabilities.

Table 64 - Experimental results for the multi-step reaction process of the hydrolysis followed by the ring-opening steps. The experiments shown in red were used in the estimation and the experiment shown in black was used in the validation of the model The experiment chosen to validate the model was chosen as it was outside of the experimental space used in the estimation and hence would show the predictive capabilities.

Temp (°C)	Flowrate ($ml \cdot min^{-1}$)	Concentration of bridged compound ($mol \cdot dm^{-3}$)	Recovery of bridged compound (%)	Yield of diacid (%)	Yield of ring-opened product (%)
260	34	0.0268	0	6	94
260	34	0.069	0	3	97
260	34	0.063	0	5	95
240	20	0.03264	0	8	92
250	20	0.03264	0	3	97
260	20	0.03264	0	0	99
250	25	0.153	0	2	98

5.6.3. Kinetic parameter estimation for multi-step reactions

For this multi-step reaction, a number of estimations were carried out in attempt to gain a further understanding of the reaction mechanism and reaction rates. Rather than showing the multiple estimations, as above, different approaches were taken to improve understanding as the high conversion of the reaction meant the data contained limited information.

Initial estimation with reference temperature ($\tilde{A}E_A$ - T_{ref} = 254.07 °C)

The initial estimation was carried out using a reference temperature of 254.07 °C, calculated using the inverse average defined previously. The estimated values for the activation energy and Ã are shown in Table 65.

Table 65 - The estimated parameters for the hydrolysis and ring-opening steps using experimental results from the larger reactor. All of the kinetic parameters show large uncertainty in the predicted values.

Reaction	E_A (±SD) ($kJ \cdot mol^{-1}$)	Ã (±SD) (no units)
Hydrolysis	15 (±4400)	-2.705 (±1.43)
Ring-opening	93 (±1400)	-2.843 (±7.91)

The standard deviation of all the estimated values are relatively large, along with correlation values above 0.9 for all parameters. This highlighted the lack of information within the experimental results, which was expected to be an issue as the yields for the ring-opened products were all >90%. The use of different rate equations was attempted but showed little difference in reducing the uncertainty. To overcome this some other approaches were attempted; the inclusion of further data from previous experiments, fixing the parameters from previous estimations and the combination of steps into a single reaction.

Inclusion of further data

To overcome the large uncertainty in the parameters, additional experiments were included for this estimation where the intermediate diacid was used as the starting material, as shown in Table 66. It was hoped that this would include more information about the separate reaction stages. The inclusion of these extra experimental results helped improve the estimations for the ring-opening step, as can be seen in Table 67, but showed little difference for the hydrolysis step.

Table 66 - The additional experiments that were used in the estimation to reduce errors in the estimation.

Temp (°C)	Flowrate ($ml \cdot min^{-1}$)	Concentration of bridged compound ($mol \cdot dm^{-3}$)	Recovery of bridged compound (%)	Yield of ring-opened product (%)
215	26.5	0.089	54	44
245	11.5	0.088	4	91
245	26.5	0.087	13	86
215	19	0.034	59	40

Table 67 - The estimated kinetic values the hydrolysis and ring-opening steps, using additional experiments of just the conversion diacid to the ring-opened product in the larger reactor. The uncertainty in the ring-opening step was reduce while the uncertainty in the hydrolysis step remained high.

Reaction	E_A (±SD) ($kJ \cdot mol^{-1}$)	Ã (±SD) (no units)
Hydrolysis	58 (±3.9 x 10^5)	7.57 (±4.2 x 10^5)
Ring-opening	102 (±16)	-3.24 (±0.27)

One noticeable observation was that although the kinetic parameters for the hydrolysis step had a large error, the rate of hydrolysis far exceeded that of the ring-opening step at the expected

conditions. This faster reaction for the hydrolysis was not unexpected as the reaction was carried out in a water:acetonitrile (50:50) mixture, with HTW known to increase acid/base catalysed reactions.[198]

Fixing of parameters

In Section 5.5.3 the kinetic parameters for the ring-opening step were estimated, as shown in Table 62. The kinetic parameter values for the ring-opening step were then fixed, leaving just the kinetic parameters of the hydrolysis step to be estimated, with the values shown in Table 68.

Table 68 - The estimated kinetic values the hydrolysis and ring-opening steps, with the values of the ring-opening step fixed from the initial estimation discussed in the previous section shown in *italics*.

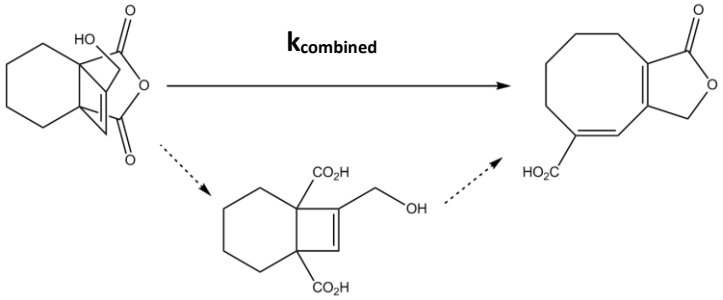
Reaction	E_A (±SD) (kJ·mol^{-1})	A (±SD) (no units)
Hydrolysis	149.6 (±1.07 x 10^6)	7.25 (±2.74 x 10^6)
Ring-opening	*97.6*	*-4.68*

As shown in Table 68, the standard deviations of the estimated parameters were significantly larger than the estimated values, hence why fixing the values did not improve the uncertainty in the estimation.

5.6.4. Combination of reactions

Both the inclusion of further data and fixing the parameters from a previous estimation did not reduce the uncertainty in the estimated parameters. A different model was then proposed, where both reactions are combined into a single step, as there was a large relative difference in rates between the two reactions in the initial estimation. As mentioned previously, the hydrolysis step being carried out in HTW was considered to proceed at a much greater rate than the formally forbidden ring-opening step.[198,355] The combined step is shown in Scheme 18, showing a single reaction where the bridged product converts into the ring-opened product directly.

Scheme 18 - A scheme showing the combination of the hydrolysis and ring-opening step into a single step, where the bridged product reacts to form the 8-membered ring product. As water was 50% of the solvent by volume the hydrolysis reaction was assumed to be much faster than the formally forbidden ring-opening step and hence the reactions could be combined.



Combining the two into a single reaction produced more consistent values with reduced uncertainty, as can be seen in Table 69.

Table 69 - The estimated values for kinetic parameters of the combined reaction using experimental data from the larger reactor, showing less uncertainty than the separate reactions discussed above. This highlights the limitations of the hybrid method as uncertainty in the values has been reduced by introducing assumptions.

Reaction	E_A (±SD) (kJ·mol^{-1})	Ã (±SD) (no units)
Combined Reaction	87.85 (±11.2)	-3.33 (±0.048)

The correlation between the two parameters was 0.324, and hence the values could be considered to represent the parameters well, as shown in the 95% confidence ellipsoid in Figure 122. To show the predictive capabilities of the model, the outlet concentration, instead of yield, are shown in Figure 123 as the yields were all mostly >90%.

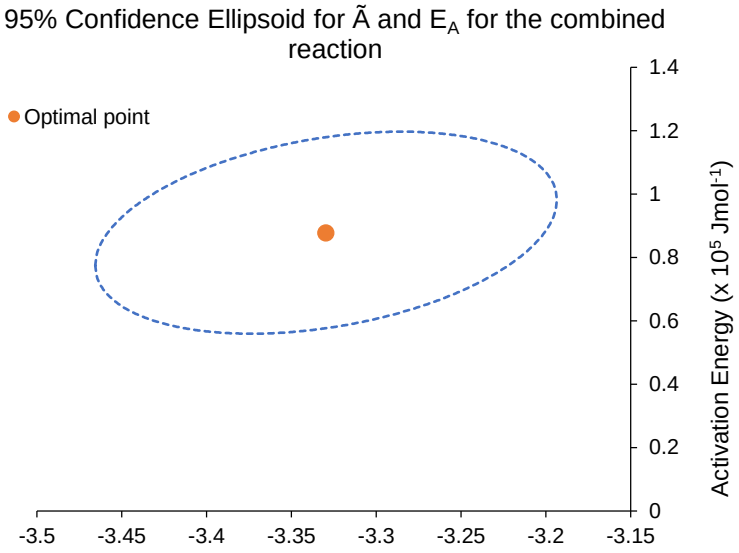


Figure 122 - The 95% confidence ellipsoid for the estimated values of E_a and A, for the combined reaction shown in Scheme 18.

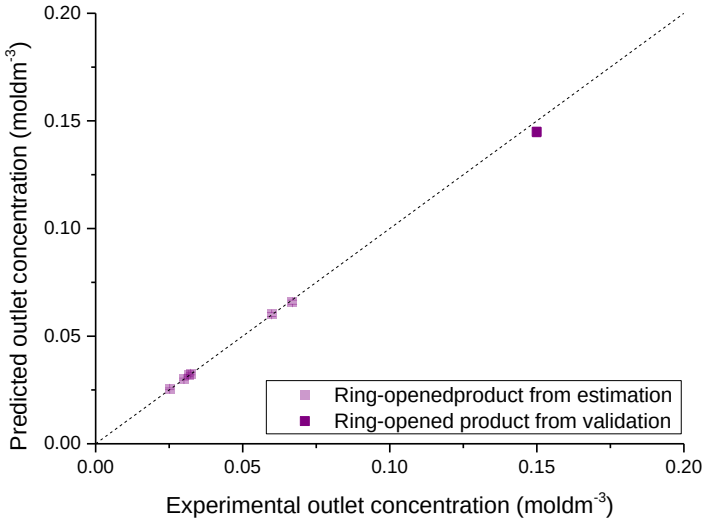


Figure 123 - A comparison of the outlet concentration of the ring-opened product for the experiments used in the estimation (■) and the predicted results (■). The outlet concentration was used in this case as the experimental yields were all > 90 %. The dashed line indicates a perfect fit between prediction and experiment.

5.7. Summary of the larger reactor experiments

Both the ring-opening step and multiple reactions have been accurately modelled using experiments carried out in the larger reactor. The uncertainty in the estimated kinetic parameters was reduced using a reparamaterisation of the Arrhenius equation using a reference temperature. The choice of the reference temperature was then optimised using a Matlab script developed within this work.

For the multi-step reaction, the data used contained limited information and hence the kinetic parameter estimations were limited in value. The additional experiments used did not reduce the uncertainty which was unexpected. The uncertainty in kinetic parameters was improved by combining the two reaction steps into a single step, which highlights the limitations of kinetic parameter estimations – mathematical uncertainty can be reduced by increasing the number of assumptions.

Modelling the multiple reactions was challenging due to the experimental values for the yield being >90% and therefore contained limited information for the modelling of the process. To address this issue, while reducing material and energy use, a smaller reactor was developed such that the reaction

kinetics could be understood further. It was hoped that shorter residence times could be achieved, which would have been challenging using the larger reactor with current laboratory capabilities.

5.8. Hydrolysis followed by ring-opening step in smaller reactor

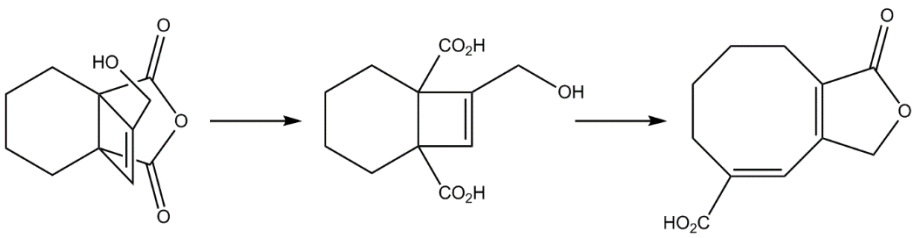
The experimental results for this section were kindly collected by Dr. Rowena Howie, Jonny Hunter and the spectroscopic measurements made by Dr. Ashley Love.

The previous experiments were been carried out in a reactor with an internal volume of 43.9 cm^3 at high flow rates. These high flow rates meant that a large amount of material was used for experimental optimisation. To overcome this, a smaller throughput reactor was designed and built that could be used for optimisation and understanding reaction mechanisms, while reducing material usage. The reactor built had an internal diameter of 0.0285 cm and a length of 3 m, giving a total volume of *ca.* 0.77 cm^3. The benefit of the smaller reactor was thought to be that higher flow rates would reduce the residence time, so intermediate steps of the reaction scheme could be studied.

5.8.1. Model input

The new dimensions of the reactor were entered into the model, with the underlying equations remaining the same. The kinetic model used was also the same as previously introduced for the hydrolysis followed by ring-opening steps as shown in Scheme 19. The effective dispersion coefficients were calculated and shown to also exhibit plug-flow-like behaviour – more details can be found in Appendix III.

Scheme 19 - The combined reaction of the hydrolysis of the bridged compound followed by the electrocyclic ring opening of the diacid to form the 8 membered ring-opened product.



5.8.2. Experimental results

The experiments were carried out at a range of flowrates, such that for some experiments the residence time was sufficiently short, so that the production of the diacid was expected to be considerable. For previous experiments, in the larger reactor, this was more difficult to carry out as the larger volume meant that a high flowrate would be needed that exceeded the current laboratory equipment capabilities. For the smaller reactor, this was less of an issue with a wide range of yields for the diacid found, as shown in Table 70.

The yields of each product were calculated using ^{1}H NMR and compared with a novel Raman method developed by Dr. Ashley Love where an aliquot was taken at equilibrium after the back-pressure regulator (See Appendix III for more details). As this method was developed for these experiments, the uncertainty in the sensors was unknown and hence the sensor's standard deviation was estimated as a parameter.

Table 70 - The experimental results for the hydrolysis of the bridged product followed by the electrocyclic ring-opening of the diacid to form the 8-membered ring-opened product in the smaller reactor.

Temperature (°C)	Pressure (bar)	Flow rate (ml·min^{-1})	Inlet concentration of bridged compound (mol·dm^{-3})	Yield of ring opened product (%)	Yield of diacid (%)	Recovery of bridged compound (%)
225	150	0.1	0.3	95	-	-
225	150	0.2	0.3	97	-	-
225	150	0.266	0.3	97	3	-
225	150	0.4	0.3	92	8	-
225	150	0.53	0.3	84	15	-
225	150	0.8	0.3	67	28	-
225	150	1.06	0.3	56	44	-
225	150	1.6	0.3	40	58	1
225	150	3.2	0.3	13	70	1
250	150	0.52	0.35	97	1	-
250	150	0.8	0.35	94	3	-
250	150	1.6	0.35	82	18	1
250	150	3.2	0.35	52	44	1

5.8.3. Kinetic parameter estimations

A similar approach to that described above for the estimation and optimisation of the reaction in the smaller reactor. Rather than repeating all of the steps again, as with the first reaction, just the key steps are presented below.

Initial estimation with standard Arrhenius equation

An initial estimation was carried out using the standard Arrhenius equation so parameter limits could be understood. The estimated kinetic parameters for the Arrhenius estimation for the hydrolysis and ring-opening step are shown in Table 71. The standard deviations for the recovery of the starting material and the yield of the product sensors were 1.96 % and 2.80 %, respectively. The covariance-variance matrix was assumed to be singular hence the standard deviations were not able to be calculated.

Table 71 - The estimated kinetic parameters for the standard Arrhenius equation for the hydrolysis followed by the ring-opening in the smaller reactor. The standard deviations of the estimated parameters were unable to be calculated as the parameters were highly correlated, with the covariance-variance matrix assumed to be singular.

Reaction	A (±SD) (s^{-1})	E_A (±SD) (kJ·mol^{-1})
Hydrolysis	8.07 x 10^9 (n/a)	98.9 (n/a)
Ring-opening	5.73 x 10^{11} (n/a)	123.9. (n/a)

Estimation with Ã and B reparameterised Arrhenius

The reparameterised Arrhenius equation with parameters Ã and B was used initially so the optimal reference temperatures can be calculated and optimised. The kinetic parameters estimated for this are shown in Table 72, with the correlation matrix in Table 73, showing relatively high correlations between parameters. The averaged inverse reference temperature of 233.81 °C was used for this estimation. The standard deviation for the sensors related to the recovery of the starting material and the yield of the product were estimated as 1.94% and 2.81%, respectively.

Table 72 - The estimated kinetic parameters for the A-B reparameterised Arrhenius equation, with a T_{ref} of 223.81 °C, for the hydrolysis followed by the ring-opening in the smaller reactor.

Reaction	$\tilde{A}_1$: (±SD)	B_1 (SD)
Hydrolysis	-0.732 (±0.133)	18.44 (±7.29)
Ring-opening	-2.309 (±0.037)	30.55 (±1.87)

Table 73 - The correlation matrix of the estimated parameters using the A-B reparameterised Arrhenius equation with a T_{ref} of 223.81 °C for the hydrolysis ($_H$) followed by the ring-opening ($_R$) in the smaller reactor. The correlation between parameters has been reduced using the average T_{ref} and reparameterised equation.

Parameter	No.	1	2	3	4	5	6
$\tilde{A}_H$	**1**	1					
$\tilde{A}_R$	**2**	-0.642	1				
B_H	**3**	0.738	-0.614	1			
B_R	**4**	-0.673	0.618	-0.787	1		
σ_{diacid}	**5**	0.0367	0.282	-0.172	0.0686	1	
$\sigma_{product}$	**6**	-0.0369	-0.281	0.172	-0.0686	-0.173	1

For the optimisation of the reference temperatures, the covariance-variance matrix used was the matrix between the 4 kinetic parameters. The standard deviation of the sensors was ignored as the standard deviation was expected to stay the same and would not affect the optimisation search of the

T_{ref} value. This similarity in σ for different estimations can be seen with the near-identical values for each sensor with this estimation, and the previous estimation with the standard Arrhenius.

The two-dimensional contour plot of T' for the two reactions is shown in Figure 124, giving T' values of 1.015 and 1.0137 for the hydrolysis and ring-opening reactions, respectively. These T' values were equivalent to reference temperatures of 226.32 °C and 226.96 °C for the ring-opening and hydrolysis step, respectively.

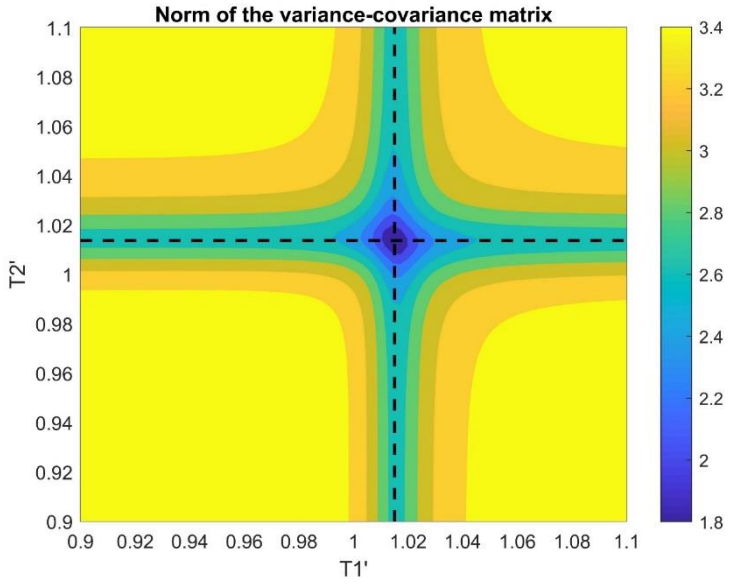


Figure 124 - A plot of the norm of the covariance matrix for varying T' values for each reaction. The values for T' were 1.0150 and 1.0137 for the hydrolysis and ring-opening step, respectively. These T' values corresponded to 226.32 °C and 226.96 °C K for the hydrolysis and ring-opening step, respectively. In this case 1 indicates the hydrolysis step and 2 indicates the ring-opening step.

Estimation with optimised reference temperature (ÃE$_A$)

The optimal reference temperatures of 226.32 °C and 226.96 °C calculated in the previous step were then used to estimate Ã and E_A for the reactions. The estimated kinetic parameters are shown in Table 74, with the correlation matrix shown in Table 74. The correlation matrix shows a reduction in the correlations between parameters when compared to the previous estimation, as shown in Table 75. The standard deviations for the recovery of the starting material and the yield of the product were 1.94 % and 2.81 %, respectively, which matched previous estimations.

Table 74 - The estimated kinetic parameters for the A-E_A reparameterised Arrhenius equation, with optimal T_{ref} values, for the hydrolysis followed by the ring-opening in the smaller reactor.

Reaction	$\tilde{A}$ (±SD)	E_A (±SD) (kJ·mol^{-1})
Hydrolysis	-0.985 (±0.093)	77.7 (±30.7)
Ring-opening	-2.767 (±0.030)	129 (±7.90)

Table 75 - The correlation matrix of the estimated parameters using the A- E_A reparameterised Arrhenius equation with optimal T_{ref} values for the hydrolysis followed by the ring-opening in the smaller reactor. The correlation between parameters has been greatly reduced using the optimal T_{ref} and reparameterised equation.

Parameter	No.	1	2	3	4	5	6
$\tilde{A}_H$	**1**	1					
$\tilde{A}_R$	**2**	-0.222	1				
$E_{A,H}$	**3**	0.023	-0.023	1			
$E_{A,R}$	**4**	-0.155	0.174	-0.787	1		
σ_{diacid}	**5**	0.239	0.287	-0.173	0.0685	1	
$\sigma_{product}$	**6**	-0.239	-0.287	0.173	-0.0686	-0.173	1

The confidence ellipsoids are shown in Figure 125, which show that there still remains some uncertainty within the estimated parameters, especially for the hydrolysis step of the reaction. This uncertainty around the hydrolysis reaction can also be seen in Table 76. The 95% t-value for the activation energy of the hydrolysis step, shown in **red**, lies below the reference t-value, shown in **bold**, which indicates the data used is not sufficient to accurately estimate this parameter. The effect of this lack of information is discussed below the comparison of the predicted and experimental results.

As mentioned previously, the model did not consider the possible non-linear effects of the increased acidity/basicity of HTW, which was expected to increase the reaction rate of the hydrolysis step, which could be a source of the lack of information regarding the hydrolysis step.

Table 76 – The estimated parameter and 95% t-values for the hydrolysis hydrolysis followed by the ring-opening in the smaller reactor. A reference t-value of 1.76 was used, with t-value for the activation energy of the hydrolysis step below this value indicating the data used was not sufficient for the estimation.

Parameter	Parameter value	Standard deviation	95% t-value
$\tilde{A}_H$	-0.985	0.093	4.92
$\tilde{A}_R$	-2.767	0.030	43.5
$E_{A,H}$ (kJ·mol^{-1})	77.7	30.7	1.18
$E_{A,R}$ (kJ·mol^{-1})	129	7.90	7.61
Reference t-value:			**1.76**

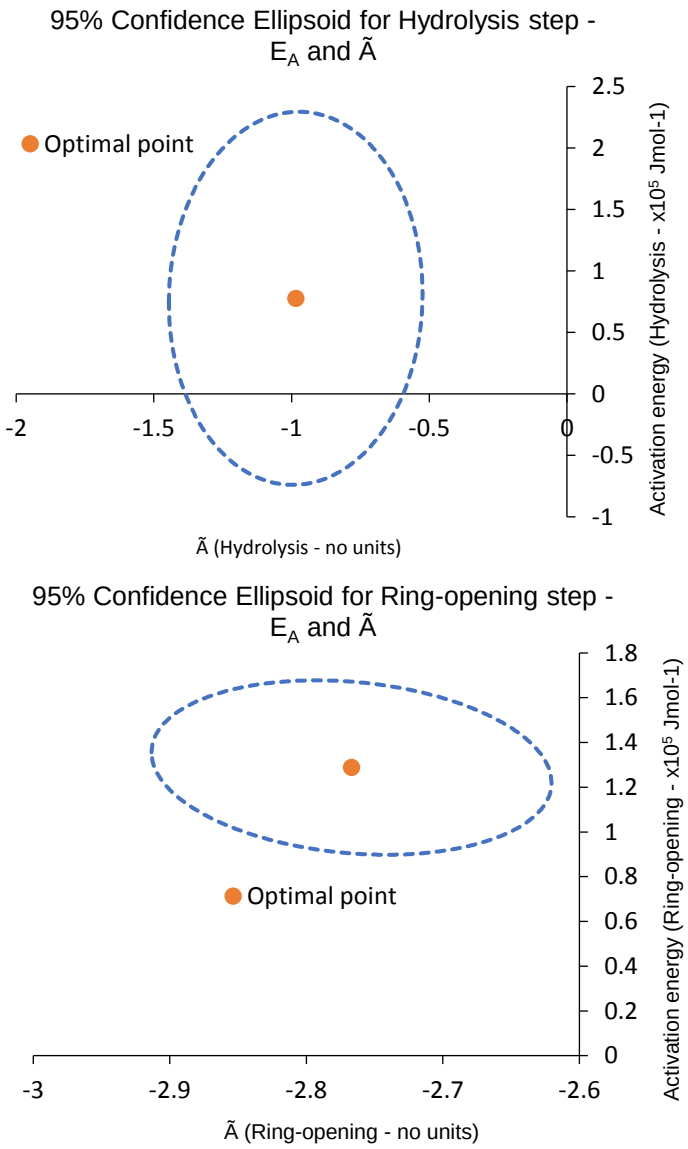


Figure 125 - The 95% confidence ellipsoids for the estimated parameters, with the activation energy plotted against Ã for the (a) the hydrolysis step and (b) the ring-opening step. The confidence ellipsoids for the ring-opening step were considered reasonably accurate, while for the hydrolysis step, there was greater uncertainty in the values which was not unexpected as there was only limited experiments with the diacid intermediate isolated.

Experimental results prediction and comparison

The reactor model and kinetic parameters were validated with three experiments within the experimental space of the estimation experiments. Both the estimation and validation predictions for the diacid and ring-opened product are shown in Figure 126 (a) and (b), respectively. The predicted values show good agreement and are within the estimated standard deviations of the sensors.

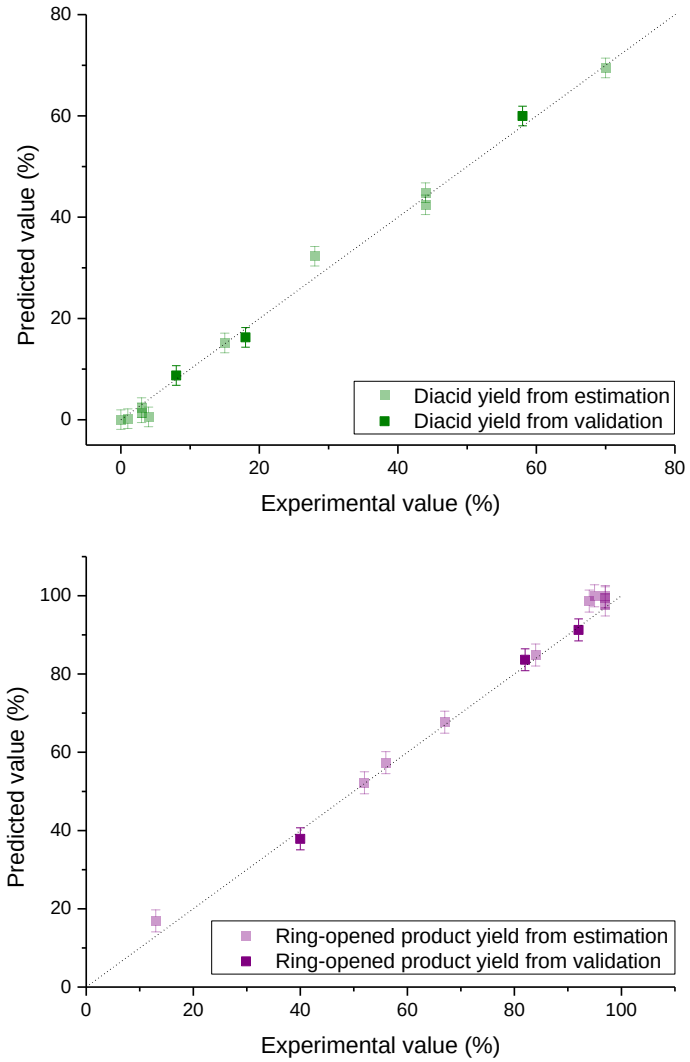


Figure 126 – (a) The predicted yield of the diacid in the smaller reactor with the experiments used for the estimation (■) and the validation (■), showing good agreement for both; (b) The predicted yield of the ring-opened product in the smaller reactor with the experiments used for the estimation (■) and the validation (■), showing good agreement for both. The difference between predicted and experimental results seemed to be lower than those with the larger reactor model. The error bars shown are a standard deviation each way, with the dashed line indicating a perfect fit.

5.9. Sensitivity analysis for the estimated parameters

Due to the lack of information regarding the activation energy of the hydrolysis step, a sensitivity analysis of the kinetic parameters estimated in the previous section was carried out to understand the kinetic parameter value's effects on the system outputs. The sensitivity analysis was also carried out as the estimation had suggested the data used in the estimation was not sufficient for the accurate

estimation of the activation energy of the hydrolysis step. By carrying out the sensitivity analysis the effect of this parameter on the overall system could be judged.

5.9.1. Variance based sensitivity analysis at set temperature

The sensitivity analysis was carried out at fixed conditions so that the effects of just the kinetic parameters could be more easily understood and presented. The kinetic parameters' values were set as the factors, with the estimated standard deviations used to set their uncertainty. The yields of the diacid and ring-opened products along with recovery of the bridged-product starting material were set as the responses.

A flow rate of 2 ml·min^{-1} and a temperature of 230 °C was used as these were towards the middle of the experimental range, and would predict yields where the effect of values could be observed. A four factor quasi-Sobol sampling method was used with 50 probability distribution samples, leading to 300 scenarios as per the $N_D(k_f + 2)$ sampling requirement of variance-based sensitivity analysis.[305] The first order and total effect of each factor is shown in Table 77 for each response, with the factors that have the largest effect on each response shown in **red**.

Table 77 – A table showing the sensitivity analysis results for both the first-order and total variance-based sensitivity effects, highlighting the importance of the Ã for both the hydrolysis and ring-opening steps for the model output. The largest value for each response is highlighted in red.

	Yield of diacid		Yield of ring-opened product		Recovery of bridged starting material	
Factor	**First order effect (S_i)**	**Total effect (S_{Ti})**	**First order effect (S_i)**	**Total effect (S_{Ti})**	**First order effect (S_i)**	**Total effect (S_{Ti})**
$\tilde{\mathbf{A}}_{\mathbf{hydrolysis}}$	0.1976	0.2042	0.5666	0.5032	0.9216	0.8382
$\tilde{\mathbf{A}}_{\mathbf{ring\ opening}}$	0.7882	0.7606	0.3981	0.3630	0.0694	$1.96\text{x}10^{-18}$
$\mathbf{E}_{\mathbf{A,\ hydrolysis}}$	0.0978	0.0041	0.0255	0.0770	0.1687	0.0747
$\mathbf{E}_{\mathbf{A,\ ring\ opening}}$	0.1029	0.0074	-0.0519	0.0035	0.0694	$3.15\text{x}10^{-18}$

The factor that affected the yield of the diacid was $\tilde{\mathbf{A}}$ for the ring opening step, with $\tilde{\mathbf{A}}$ for the hydrolysis step being the major affecting factor for both the yield of the ring-opened product and the recovery of the bridged starting material. The activation energies of both steps were not seen to be major factors in any of the responses. A graphical representation of the kinetic estimations is shown

in Figure 127, where the biggest correlations can be seen for the factors identified in the sensitivity analysis. It should be noted that graphical visualisations are not always the most useful in sensitivity analysis as multiple factors can have an effect on the responses.

The results from this sensitivity analysis show that although the t-value suggested the experimental data used did not contain enough information to define the activation energy of the hydrolysis step, the output of the reactor is not greatly affected by the value of this parameter.

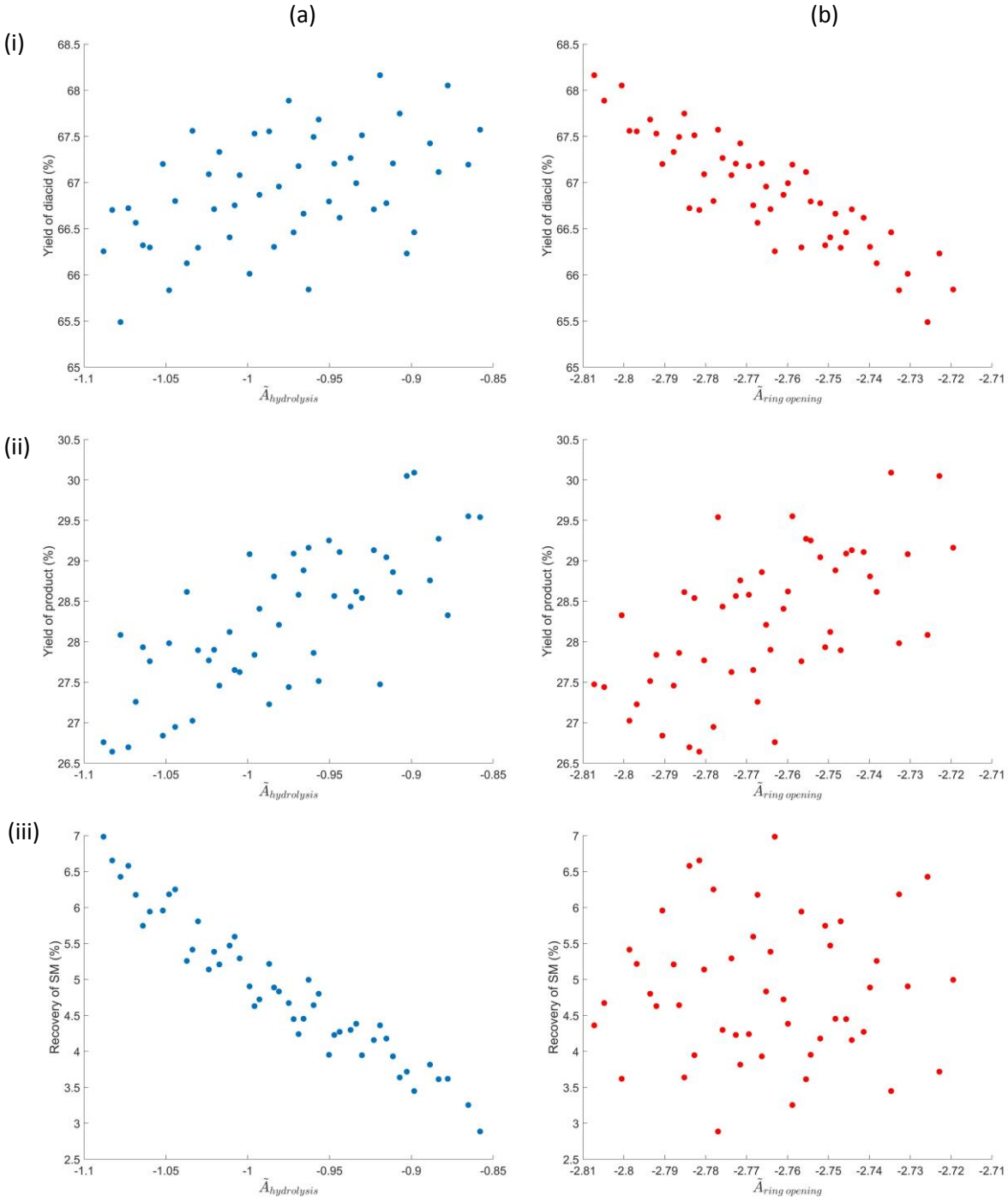


Figure 127 – A graphical representation of the sensitivity analysis at a set temperature of 230 °C with a flowrate of 2 mlmin^{-1}. (a), (b), (c) and (d) show the variation of the yields from changing $\tilde{A}_{hyd}$, $\tilde{A}_{ring\text{-}opening}$, $E_{A,hyd}$ and $E_{A,ring\text{-}opening}$, respectively. (i), (ii) and (iii) show the yield of diacid, the yield of the ring-opened product and the recovery of the starting material. Although the sensitivity analysis is not mathematically related to the correlation between the factors and responses, those that have the best correlations shown here are also have the greatest total effect, as shown in Table 69. This would be harder to pick out graphically for higher dimensions of factors, which is the reason a mathematical index is best.

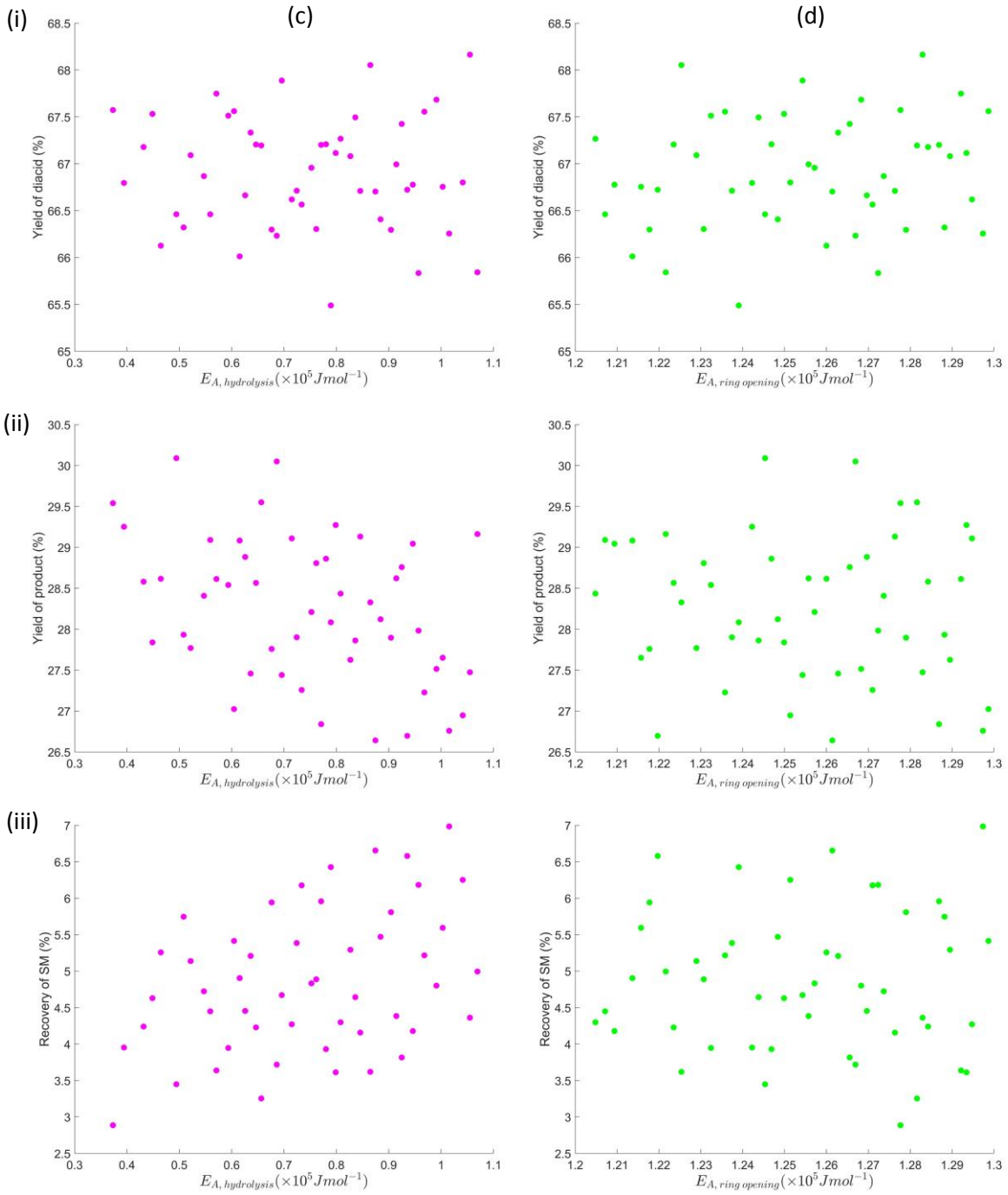


Figure 117 – A graphical representation of the sensitivity analysis at a set temperature of 230 °C with a flowrate of 2 mlmin^{-1}. (a), (b), (c) and (d) show the variation of the yields from changing $\tilde{A}_{hyd}$, $\tilde{A}_{ring\text{-}opening}$, $E_{A,hyd}$ and $E_{A,ring\text{-}opening}$, respectively. (i), (ii) and (iii) show the yield of diacid, the yield of the ring-opened product and the recovery of the starting material. Although the sensitivity analysis is not mathematically related to the correlation between the factors and responses, those that have the best correlations shown here are also have the greatest total effect, as shown in Table 69. This would be harder to pick out graphically for higher dimensions of factors, which is the reason a mathematical index is best.

5.10. Prediction of larger reactor from smaller reactor's estimated parameters

One of the benefits of the smaller reactor was that the material and energy use was greatly reduced during the optimisation process. However, for future reaction scale-up it also offered a route of understanding kinetic parameters at a small scale before being able to predict the performance of the larger reactor. The possibility of this prediction was investigated using the kinetics parameters estimated in the smaller reactor within the larger reactor models.

5.10.1. Prediction of the hydrolysis and ring-opening steps in the larger reactor

As the model was shown to be valid for the smaller reactor, the estimated kinetics were then used to predict the performance of the experiments carried out in the larger reactor. The T_{ref} used was 238.65 °C which is the inverse average of all the temperatures used in the estimation and the temperatures used in the larger reactor. The production of the diacid and ring-opened product was predicted for the reactions in series with a comparison shown in Figure 128, showing good agreement. The predicted outlet concentration of the two products are also shown in Figure 128, this shows the reproducibility of the model over different conditions, which the yields can mask when there is high conversion, as seen in the experimental values.

This performance prediction shows the possibility of estimating kinetic parameters in the smaller reactor, using small amounts of material, which could be used to accurately predict performance in the larger reactor.

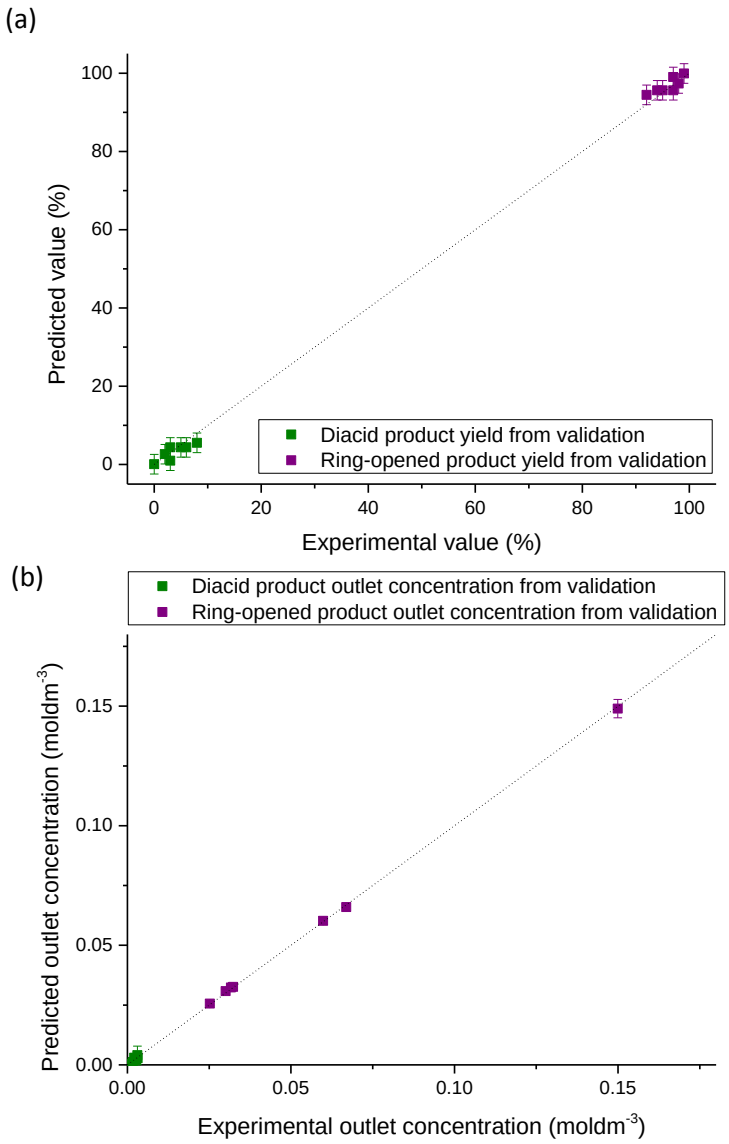


Figure 128 – A comparison of the predicted and experimental values for (a) the yield and (b) the concentration of the diacid (■) and the ring-opened product (■) in the larger reactor using the parameters estimated using experiments in the smaller reactor. The concentration is plotted here as the experiments were of high conversion which may have masked the accuracy of the model. The dashed line indicates a perfect fit between prediction and experiment.

5.10.2. Prediction of the ring-opening step in the larger reactor

The kinetic parameters for the ring-opening step estimated in the smaller reactor, with the reaction in series, were then used to predict the performance of the first experimental results presented above: the single-step conversion of the diacid to the ring-opened product. The predicted performance of these reactions can be seen in Figure 129, showing an accurate prediction of the conversion of the diacid and yield of the ring-opened product. The slight overestimation of the ring-opened product was

thought to be due to the kinetic scheme in the smaller reactor not considering the breakdown of the product, which had been observed for the larger scale reactor.

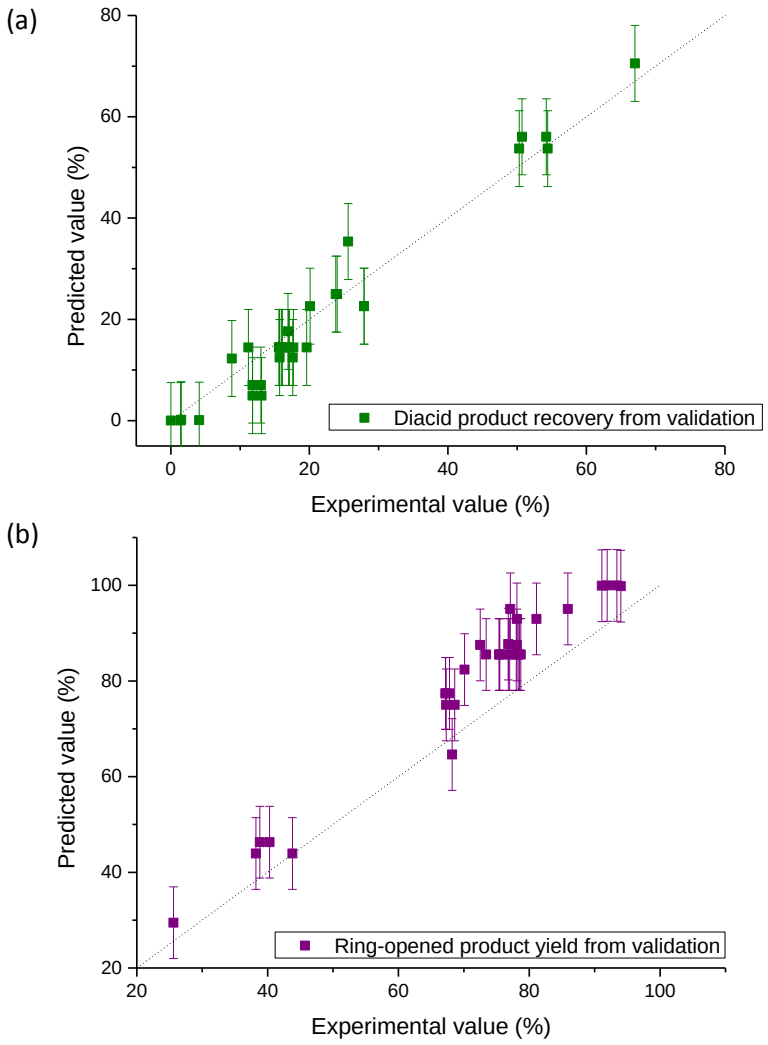


Figure 129 – A comparison of the predicted and experimental values for (a) the yield of the diacid (■) and (b) the yield of the ring-opened product (■) in the singular conversion of the diacid to the ring-opened product using kinetic parameters estimated with experiments in the smaller reactor. The diacid showed a good agreement between experimental and predicted values. However, the ring-opened product yield was overestimated which was thought to be due to the kinetic model in the smaller reactor not considering the breakdown of the product. The dashed line indicates a perfect fit between prediction and experiment.

This overestimation highlights some of the difficulties with scale up as some issues are not observed on a small scale, but can become significant at a larger scale. However, the RMSE was 3.94 % and 9.44 % for the diacid and ring-opened product, respectively, which was considered acceptable for the diacid as the yields had been calculated using ^{1}H NMR.

5.11. Daisy-chain with Photoreactor

As mentioned in Chapter 4 and in this Chapter's introduction (Section 5.2), a final goal of the modelling was to model a daisy-chained process up to *ca.* 1 kgday^{-1}. The bridged compound starting material for these reactions can be produced photochemically as outlined in the previous chapter. Colleagues in Bristol were able to produce the bridged compound at 30ml·min^{-1} with a *ca.* 70 % yield, with a starting concentration of THPAA of 0.5 mol·dm-3 in acetonitrile. This would then be diluted by 50 % water by volume in flow, giving an equivalent concentration for the bridged compound of 0.175 mol·dm^{-3} at 60ml·min^{-1}.

Prediction of performance with 60 ml·min^{-1}

The equipment in the laboratory in Nottingham was unable to reach flowrates of 60 ml·min^{-1}, so the reactor model was used to predict the performance.

Current reactor at 60 ml·min^{-1}

To understand what would have been feasible with the current equipment, the computational model was used to predict the performance at 60ml·min^{-1}. The yield of the final ring-opened product was 82 %, the equivalent of 2.6 kg per day, with the concentration profiles of the diacid and ring-opened product along the reactor shown at equilibrium in Figure 130.

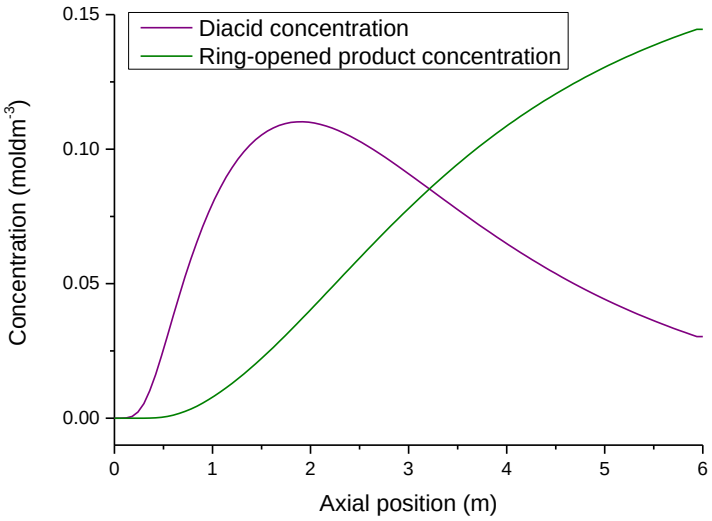


Figure 130 – The concentration profile for the diacid (—) and the ring-opened product (—) along the larger reactor at 260 °C and 60 ml·min^{-1}. This concentration profile was predicted using the parameters estimated from experiments in the smaller reactor. The outlet concentration of 0.145 mol·dm^{-3} of the ring-opened product is equivalent of 84 % yield.

Using the model to design an optimal reactor

The model was then used to predict a possible reactor size for a future reactor that would be able to produce a high yielding amount of the ring-opened product, assuming further pumps were also provided to reach 60 ml·min^{-1} flow rates. A reactor of 0.24" internal diameter and a length of 300 cm predicted a 96 % yield of the bridged product, as shown in Figure 131, which is the equivalent of *ca.* 3 kg per day. It should be noted that for this prediction no breakdown of the product was assumed as the kinetics did not consider this. In practise, it is likely that a proportion of the product would degrade and reduce the yield of the ring-opened product below 96 %.

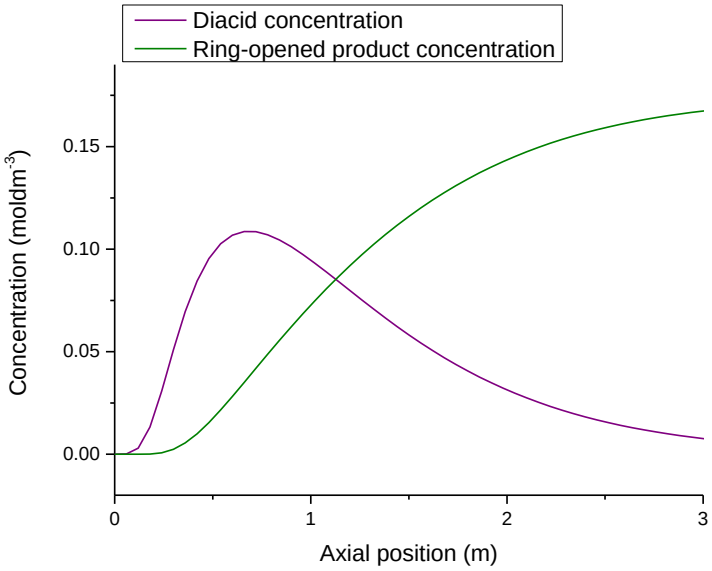


Figure 131 - The concentration profile for the diacid (—) and the ring-opened product (—) along a hypothetical reactor, with an internal diameter of 0.24" and 3 m length at 260 °C and 60 ml·min^{-1}. This reactor was designed using the parameters estimated from experiments in the smaller reactor. The outlet concentration of 0.168 mol·dm^{-3} of the ring-opened product is the equivalent of a 96 % yield.

5.12. Chapter Summary

A model was developed for the high-temperature reactor used within the group, with a number of assumptions used to allow for a numerically feasible model. Measuring the kinetics of the reaction, using typical techniques such as in-line spectroscopy, was unsuitable due to the extreme conditions used. To understand the kinetics of the reaction, parameter estimation was used for the kinetic parameters.

Initially the parameter estimation of the standard Arrhenius equation was used for just the ring-opening step in the larger reactor, followed by a possible breakdown of the product. The parameters had large uncertainties and high correlations between themselves, so a reparameterisation strategy was used to reduce the uncertainty and correlation. The estimated parameter values were then used to find the optimal reference temperature to reduce the correlations between parameters. The final parameter values for the ring-opening step, followed by a possible breakdown step showed a much-reduced correlation and uncertainty compared to the initial estimation using the standard Arrhenius equation.

Following from this, the hydrolysis of the bridged-compound produced in the photochemical step, discussed in the previous chapter, was carried out in the larger reactor, with the subsequent ring-opening step also carried out. This multi-step reaction was then modelled, with parameter estimation used to estimate the kinetics. The data used for this multi-step reaction system contained little information as the yield of each experiment was >90%. A number of techniques were used to produce reasonable results, with the combination of the reactions into a single step reducing the uncertainty to acceptable levels. The steps taken to reduce the uncertainty highlighted the limitations of the parameter estimation method used.

Due to the large use of material with the larger reactor, a smaller reactor was developed so less material could be used, while still understanding the reaction. Again, the parameter estimation method was used, followed by a number of subsequent steps to optimise the reference temperature of the reparameterised Arrhenius equation. The estimated kinetic parameters accurately predicted the experimental results, however, for the activation energy of the hydrolysis step, it was suggested that the data used lacked sufficient information to predict the parameter. The uncertainty in this parameter was investigated through sensitivity analysis and was showed to have little influence on the overall outcome of the process. This lack of difference was thought to be because the hydrolysis step occurred at a greater rate than the ring-opening step, and hence had little effect.

The kinetic values estimated in the smaller reactor were used to predict the performance of the results in the larger reactor, accurately predicting the results of the multi-step reaction process. The kinetic parameters were then used to predict the outcome of just the ring-opening step in the larger reactor. For just the ring-opening step, the kinetics predicted in the smaller reactor overestimated the experimental results, which was thought to be because a possible breakdown of the final product was observed in the larger reactor, which was not considered in the smaller reactor model.

The performance of the larger reactor at elevated flowrates, which Nottingham's laboratory equipment could not match, was then predicted. The model predicted a yield of 84% for the final

compound, equivalent of >2 kg per day, which was above the initial goal of 1 kg per day. The model was then used to design a possible new reactor to achieve yields of >95%, by doubling the internal diameter and halving the length. Looking to the future, this showed the possibility of understanding reaction kinetics in the smaller reactor, before predicting the performance of a larger scale process, as well as allowing new equipment to be designed to optimise processes further.

5.13. Future work

The modelling of the reactions in this chapter was often carried out retrospectively, after the experimental data had been collected. This retrospective approach led to some limitations in the capabilities, as the data had often been collected following typical chemical optimisation techniques, where parameters are changed to increase the yield of a single product. In future, it would be better if the modelling was to be used in a more proactive method, taking advantage of the Design of Experiments (DoE) to obtain information about the whole reaction process. By using DoE more proactively, it would be hoped to reduce material and energy use even further.

The possibility of predicting the performance of a reaction in the larger reactor, by estimating the kinetics in the smaller reactor was shown. However, this predictive capability has only been shown with one reaction, and hence increasing the library of reactions that have been modelled will hopefully further the validation of this method. It would also be interesting to see if the predicted yield of 84% for the larger reactor at a flow rate of 60 $ml \cdot min^{-1}$ was valid.

It may also be possible to have a number of different reactors built, such that when the kinetics of a reaction has been understood, a reactor can be chosen to optimally produce a certain result.

6. Thesis summary

As discussed in the introduction to this Thesis, the original aims were changed in light of the UK Government's CCS policy change, with the outcome being two separate parts: a part related to CCS and another part related to novel chemical reaction modelling. Both parts of the Thesis contain common themes of modelling and predictive capabilities which have been discussed throughout. This summary is therefore split into the subsequent chapters, with the aims defined in each chapter used as the basis of the summary.

Chapter 1 – CCS related work

Aim 1.1 - To carry out experimental work for determining the phase behaviour of tertiary systems of CO_2, H_2 and H_2O relevant to CCS pipeline operation

Experimental work was carried out using a previously developed spectroscopic method for measuring water solubility in a fluid mixture of 10 % H_2 + CO_2 at 40 °C and pressures above 8 MPa. The results showed a continuation of the trend of reducing water solubility with a decrease in density. Water solubility in 10 % H_2 + CO_2 followed the trend line defined with previously reported experimental work (Pure CO_2, 5 % N_2 + CO_2 and 10 % N_2 + CO_2), which the water solubility was shown to be dependent on density. The properties of N_2 and H_2 are significantly different such that the relationship between density and water solubility could be seen as a reliable indicator for predicting water solubility of varying CCS-relevant mixtures at the conditions chosen.

Aim 1.2 - To compare the experimental work on phase behaviour with the predictive capabilities of PSE's Equation of State

Both the experimental work carried out in this Thesis and previously reported values for the water solubility, density and viscosity of CCS-related mixture were compared with the predictive capabilities of two different EoSs. For water solubility, the EoSs underestimated the water solubility limits compared to the experimental values. This underprediction of the water solubility limits was seen as

being preferable than an overprediction if they were to be used within safety simulations. However, both the predicted and experimental limits were considerably above the previously suggested pipeline water limits, which suggested these safety limits could possibly be increased in future. Further work would also be needed at temperatures relevant to those found in countries such as the UK to confirm these findings.

For both density and viscosity, the predicted and experimental values were found to be within 5 % error of each other, in the region of interest, which was considered accurate compared to previously reported comparisons.

Aim 1.3 - To use PSE's software to understand the effect impurities with CO_2 has on the operation of pipelines, especially the pressure drop of a pipeline.

As the viscosity and density of the CCS-relevant mixtures had been shown to be accurate within the region of interest, the EoSs were used within a pipeline model to understand the effect impurities would have on pipeline behaviour. The pipeline model used was a proprietary model of PSE and was based on a single-phase plug flow model. An 0.5 m internal diameter pipeline with an equivalent flowrate of 5 million tonnes CO2 per year was used initially, with an inlet pressure of 10 MPa. The results showed little difference from the presence of impurities, when the CO2 was >90 %, with all predictions above the industry standard pressure drop. Subsequently, the effect of internal diameter and surrounding temperature was investigated, with both of these showing a greater effect than the role of impurities.

Aim 1.4 - Undertake a training exercise modelling existing experimental work on the pressure drop and phase behaviour of a CH_3CN mixture at elevated temperatures

A pipeline model was used to predict the pressure drop of a number of mixtures, with the results compared to experimental work previously carried out in the group. The model initially used pure isopropyl alcohol (IPA) to define the model, with a friction factor used to match the results. The model defined with pure IPA was then used to predict the pressure drop of an acetonitrile:water mixture,

which is typically reactive at elevated temperatures. Experimental results for this reactive mixture showed little formation of a reactive product, as per gas chromatography analysis. The measured pressure drop was predicted well by the model, which supported the validation of the method previously developed.

Future work

The method developed for measuring water solubility could be adapted for attenuated-total reflectance equipment, so a tool could be developed for online monitoring of pipelines. There would also be the possibility of integrating an ATR sensor into an Internet of Things (IoT) system. It would also be interesting to understand the economic impacts of impurities on future CCS pipeline networks.

Chapter 4 Photochemical reaction modelling

Aim 4.1 - Develop a process model of a photochemical reactor

Initially an idealised model of a photochemical batch reactor was developed using a Beer-Lambert derived equation to model the absorption of light by a reactive medium. This initial model used a number of simplifying assumptions, such as having parallel light with no movement of particles. The reaction kinetics of the Paternò-Büchi reaction were collated from a range of literature sources, with the quantum yield assumed so the calculations could be carried out. The results for this showed a front developing of reagents and light, as expected for the no mixed case. CFD was also used to model an identical set up, with results from both showing good agreement.

The two-flux approximation was then used with cylindrical coordinates to develop models for the excimer flow and batch reactors. For these reactor models, diffusion and flow of reagents was also considered. Initial calculations using the process model and CFD calculations were compared; again, both showed good agreement.

Aim 4.2 - **Use photochemical process model to understand photochemical reaction kinetics and compare outputs with experimental results**

Experimental results from the excimer flow models were modelled first, using MLE to estimate the quantum yields which was then used to predict reactor output. The estimated quantum yield for the photoisomerization of 2-pyridone was compared with the literature quantum yield. As the light power used in the model was the manufacturer's specified value, the estimated quantum yield was considerably lower than the literature value. For example, at 308 nm, the MLE estimated was 0.54 %, which was 21% of the literature value of 2.60%. It was noted that previous work in the group had carried out actinometry on the 308 nm lamp and calculated the number of photons entering the reactor to be 21% of the manufacturer's specification. The estimated quantum yields for the photoreaction of 2-pyridone were also compared with a literature method for calculating the quantum yield and showed good agreement when the assumptions in the literature method were valid.

Actinometry was then considered for all of the reactors that were to be used. However, as this work was focussed on model development, the manufacturer's specification was decided to be used as the estimated quantum yields would take the difference in lamp power into account. The estimated quantum yields were then used to validate the model with experimental results not used in the estimation; showing good agreement.

The excimer flow reactor models were then used with the estimation of quantum yields and reaction performance prediction of two further reactions; the photodecarboxylative cyclisation of potassium *N*-phthalimidobutanoate and the photoisomerization of Cookson's dione. The estimated quantum yields for both of these reactions were then also compared with the literature method for calculating the quantum yield. Both methods showed good agreement when the assumptions used in the literature method were valid. There was a difference in values when the literature method's assumptions were not valid, such as with competing absorbances, which the method developed in

this work considered. Again, for both of these reactions, the models were validated with experiments not used within the estimation.

Aim 4.3 - **Use kinetics to predict reactor performance of reactions for; unimolecular reactions, multi-component reactions with competing absorbances, photosensitised reactions and consecutive reactions**

The development of the photoreactor model discussed in the previous aim allowed the quantum yield of unimolecular reactions and reactions with competing absorbances. After this, the prediction of the performance of multi-component and photosensitised reactions was approached together because the photosensitiser was a separate component. Initially a similar approach was used as the unimolecular reaction, with a number of additional reactions included after the absorption of a photon by the photosensitiser. However, the estimated values for these reaction schemes had large uncertainties and high correlations between each other.

A novel Bodenstein-like assumption was made for the excited photosensitiser, which was assumed to have a concentration relative to the amount of light present in the reactor. For this, a 'quantum kinetic parameter' was used in place of a quantum yield. This assumption simplified the reaction schemes into fewer steps and reduced the uncertainty in the estimated parameters. This assumption was then used for the estimation of the 'quantum kinetic parameter' for the photosensitised isomerisation of cis-octene and the photocyclization of THPAA and propargyl alcohol. These models were also validated using experimental results not used within the parameter estimation.

Aim 4.4 - **Develop models of more complex photochemical reactors**

Two more complex reactors have been developed by colleagues at Nottingham; the vortex reactor and FEP tubular reactor.

The vortex reactor model produced highly complex mixing properties due to the formation of Taylor vortices. During the design and manufacture of the vortex reactor a CFD model had been developed which was used as a guide within this work. A major assumption was made for the development of

this work; the light entering the reactor being uniform and parallel to the surface which was unlike the experimental set up. This assumption was used as the process model was designed to be a rapid alternative to the CFD; including an angular dimension would have increased computational expense.

An idealised Paternò-Büchi reaction was used to compare results from the CFD model and process model. The dispersion coefficients varied along the reactor to mimic the mixing of the vortex, with the values chosen to ensure the CFD and process models showed good agreement. The vortex process model defined using the Paternò-Büchi was then used to understand the reaction of Cookson's dione in the vortex reactor.

As the quantum yield of the Cookson's dione reaction had previously been estimated in the excimer reactor, experimental results from the vortex reactor were used to estimate the lamp power of the vortex reactor. The assumptions of the light being uniform across the reactor surface and monochromatic meant the estimated lamp power value was likely to be inaccurate. However, the lamp power estimation meant that the performance of the vortex reactor could be predicted. A small number of experimental results were compared and showed good agreement. Further comparisons were made with both the process models and CFD models with all showing good agreement. An interesting conclusion of the vortex reactor modelling was how the rotation speed showed little effect on the output of the reaction, which could help reduce the temperature and energy use for the vortex reactor.

For the modelling of the FEP tubular reactor a model using trigonometry and the Beer-Lambert law was initially derived. As the trigonometric function required an angular dependence, the computational requirements increased considerably. This trigonometric function was used for the photosensitised reaction of THPAA with propargyl alcohol. After further consideration the angular dependence was removed and the FEP tubular reactor model was simplified to an annular reactor with dimensions relevant to the FEP tubular reactor. This simplification allowed for faster calculations alongside the prediction of the output of the reactor.

Aim 4.5 - Use photochemical model in conjunction with the high-temperature water process model to predict performance of a daisy-chained process

The FEP tubular reactor model was used to model the photosensitised reaction of THPAA with propargyl alcohol where the major product of this reaction was the starting material in a thermal reaction. The outcome of combining the photochemical and thermal steps is discussed further in Aim 4.4.

Future work

As mentioned in the introduction to Chapter 3, the lamp power for the excimer lamps was assumed to be equal to the manufacturer's specifications. This was deemed unlikely to be true, and although actinometry was not carried out, this would be an aim to pursue for reporting accurate quantum yield values. The Bodenstein-like assumption made as was a novel development and it would be interesting to understand this assumption further, using more experiments to further validate the method. Finally, further experiments need to be carried out to develop and understand the limitations of the vortex reactor model.

Chapter 4 HTW reaction modelling

Aim 5.1 - Develop a process model for a high-temperature water reactor

A reactor model of a coiled tubular reactor placed inside a heating block was modelled using engineering principles. The Advanced Peng-Robinson equation of state was used to calculate the physical properties of the reaction fluid. To simplify the model, the heat of the reaction was shown to be negligible compared to the heating profile caused by the high temperatures used experimentally (> 200 °C).

Aim 5.2 - **Use a high-temperature water process model to understand reaction kinetics and compare reactor performance prediction with experimental results**

The overall aim of the HTW reactor model was to model two reactions; the hydrolysis of the product formed in the photochemical step discussed above and a subsequent ring-opening step of the product from the hydrolysis step.

The electrocyclic ring-opening reaction step was modelled first, with the kinetic parameters estimated using the standard Arrhenius equation. Although the predicted yields were validated against experimental results, the estimated parameters contained large uncertainty and high correlations between parameters.

The Arrhenius equation was reparameterised with a reference temperature, before the kinetic parameters were estimated. Following this, an algorithm was used to optimise the reference temperature to reduce the correlation between parameters. The reparameterization method was shown to have no effect on the predicted reactor performance.

Following from this estimation, the hydrolysis step was introduced to the model before the ring-opening step. The experimental data for this were limited in information as all of the yields were over 90 %. The estimation of the kinetic parameters produced values with high uncertainties, which was not surprising due to the lack of information in the experimental data. A number of different methods were attempted to reduce this uncertainty, including the inclusion of extra experiments of just the ring-opening step. The method that was most successful in reducing the uncertainty was combining the hydrolysis step and ring-opening step together. As the reaction was carried out in a solvent mixture of water 50% vol. the hydrolysis step was expected to be rapid at the elevated temperatures, but also highlighted the limitations of the method; uncertainty is reduced by introducing assumptions.

A smaller reactor (internal volume 0.77 cm^3) was then manufactured as the previous experiments used large amounts of material (internal volume: of 43 cm^3). The smaller reactor was then hoped to be able to have shorter residence times so that the formation of the intermediate product could be further understood. The reactor model was then adjusted for the new dimensions and the kinetic parameters estimated. The reparameterization and reference temperature optimisation method was also used to reduce the correlations between parameters. The estimated kinetic parameters from the smaller reactor were then validated using experimental values for the smaller reactor.

The kinetic parameters estimated in the smaller reactor were then used to predict the performance of the experimental results of the larger reactor. The recovery of the starting material for this was found to be accurate, however, for the final product the model overestimated the production. This overestimation was thought to be due to the product breaking down, which had been observed in the larger reactor, but was not considered in the smaller reactor model.

Aim 5.3 - Use kinetics to predict reactor performance for a variety of reactions

The performance of two reactions that were part of the same scheme was carried out within this work. However, unfortunately this method was not carried out for any further reactions and would be a future aim of the project.

Aim 5.4 - Use a high-temperature water model in conjunction with the photochemical process model to predict performance of a daisy-chained process

Both models were used together, with the output of the prediction of the photo reactor equalling the input of the thermal reactor. As the models had been validated separately the daisy-chained model was used to predict the performance of the reactor at conditions that matched colleagues from the University of Bristol's flowrates but were unable to be reached in Nottingham due to equipment limitations.

It was hoped to develop a graphical user interface (GUI) so the daisy-chaining of processes could be made by defining an icon and using gPROMS 'drag and drop' process sheet builder. Some progress was made towards the development of icons that could be used within gPROMS but there was limited time due to writing. It is a future goal of the project to develop a GUI and easy-to-use method so that the method can be adopted more widely by members of the group.

Aim 5.5 - Optimise multi-step reaction process

The models developed within this work were used to predict the performance and operation of the reactors at a wide range of conditions. A mathematical optimisation was not carried out on the larger reactor for two reasons; the reaction was shown to be high yielding across a wide range of conditions and the breakdown of product was not considered in the smaller reactor model. If the breakdown was understood, the optimal conditions would be constrained and a mathematical optimisation would be more useful.

Future work

The high temperature water reactor model should be used more proactively in the future, possibly using design of experiments (DoE), as the majority of the work presented in this Thesis was carried out retrospectively. It would also be interesting to understand the accuracy of the predictions made at 60 ml·min^{-1} and for the hypothetical reactor design.

7. References

1. Intergovernmental Panel for Climate Change. *Carbon Dioxide Capture and Storage*. (2005).
2. Peletiri, S. P., Rahmanian, N. & Mujtaba, I. M. Effects of impurities on CO_2 pipeline performance. *Chem. Eng. Trans.* **57**, 355–360 (2017).
3. Fradet, A. et al. Technical and economic assessment of CO_2 transportation for CCS purposes. in *Global Pipeline Monthly* vol. 3 (2007).
4. de Visser, E. et al. Dynamis CO_2 quality recommendations. *Int. J. Greenh. Gas Control* **2**, 478–484 (2008).
5. Foltran, S. et al. Understanding the solubility of water in carbon capture and storage mixtures: An FTIR spectroscopic study of H_2O + CO_2 + N_2 ternary mixtures. *Int. J. Greenh. Gas Control* **35**, 131–137 (2015).
6. Intergovernmental Panel for Climate Change. *Climate Change*. https://www.ipcc.ch/pdf/assessment-report/ar4/wg2/ar4_wg2_full_report.pdf (2007).
7. Goldenberg, S. Exxon knew of climate change in 1981, email says – but it funded deniers for 27 more years. *The Guardian* (2015).
8. UK Government. *Climate Change Act*. (2008).
9. UK Government. UK becomes first major economy to pass net zero emissions law. https://www.gov.uk/government/news/uk-becomes-first-major-economy-to-pass-net-zero-emissions-law (2019).
10. Anable, J., Lane, B. & Kelay, T. *An evidence base review of public attitudes to climate change and transport behaviour*. (2006).
11. Department for Business Energy and Industrial Strategy. *2017 UK greenhouse gas emissions: final figures - statistical summary*. https://www.gov.uk/government/statistics/final-uk-greenhouse-gas-emissions-national-statistics-1990-2017 (2019).
12. Allam, R. et al. Demonstration of the Allam Cycle: An Update on the Development Status of a High Efficiency Supercritical Carbon Dioxide Power Process Employing Full Carbon Capture. in *Energy Procedia* vol. 114 5948–5966 (Elsevier Ltd, 2017).
13. Dyke, K. J., Schofield, N. & Barnes, M. The impact of transport electrification on electrical networks. *IEEE Trans. Ind. Electron.* **57**, 3917–3926 (2010).
14. Gasser, T., Guivarch, C., Tachiiri, K., Jones, C. D. & Ciais, P. Negative emissions physically needed to keep global warming below 2°C. *Nat. Commun.* **6**, (2015).
15. Intergovernmental Panel for Climate Change. *Mitigation Pathways Compatible with 1.5°C in the Context of Sustainable Development*. (2018).
16. Rhodes, J. S. & Keith, D. W. Biomass with capture: negative emissions within social and environmental constraints: an editorial comment. *Clim. Change* **87**, 321–328 (2008).
17. Bui, M. et al. Carbon capture and storage (CCS): The way forward. *Energy and Environmental Science* vol. 11 1062–1176 (2018).
18. Intergovernmental Panel for Climate Change. *Climate Change and Land*. (2019).
19. United Nations. Conference of the Parties Report of the Conference of the Parties on its

twenty-first session , held in Paris from 30 November to 13 December 2015 Paragraphs. **01192**, (2015).

20. British Geological Survey. How can CO_2 be stored? *Enhanced Oil Recovery (EOR)* http://www.bgs.ac.uk/discoveringGeology/climateChange/CCS/howcanCO2bestored.html (2005).

21. Olah, G. A., Prakash, G. K. S. & Goeppert, A. Anthropogenic chemical carbon cycle for a sustainable future. *J. Am. Chem. Soc.* **133**, 12881–12898 (2011).

22. UKCCSRC. What is CCS? https://ukccsrc.ac.uk/about/what-ccs (2019).

23. IEAGHG. *CO_2 Pipeline Infrastructure*. http://ieaghg.org/docs/General_Docs/Reports/2013-18.pdf (2014).

24. Hasan, M. M. F., First, E. L., Boukouvala, F. & Floudas, C. A. A multi-scale framework for CO_2 capture, utilization, and sequestration: CCUS and CCU. *Comput. Chem. Eng.* **81**, 2–21 (2015).

25. CCUS Cost Challenge Taskforce. *Delivering Clean Growth*. https://assets.publishing.service.gov.uk/government/uploads/system/uploads/attachment_data/file/727040/CCUS_Cost_Challenge_Taskforce_Report.pdf (2018).

26. Department for Business Energy and Industrial Strategy. *Contracts for Difference Allocation Round 3 Results*. https://assets.publishing.service.gov.uk/government/uploads/system/uploads/attachment_data/file/838914/cfd-ar3-results-corrected-111019.pdf (2019).

27. IEAGHG. *Deployment of CCS in the Cement Industry*. https://ieaghg.org/docs/General_Docs/Reports/2013-19.pdf (2013).

28. Martynov, S. B., Daud, N. K., Mahgerefteh, H., Brown, S. & Porter, R. T. J. Impact of stream impurities on compressor power requirements for CO_2 pipeline transportation. *Int. J. Greenh. Gas Control* **54**, 652–661 (2016).

29. Figueroa, J. D., Fout, T., Plasynski, S., McIlvried, H. & Srivastava, R. D. Advances in CO_2 capture technology—the US Department of Energy's Carbon Sequestration Program. *Int. J. Greenh. gas Control* **2**, 9–20 (2008).

30. Wang, M., Lawal, A., Stephenson, P., Sidders, J. & Ramshaw, C. Post-combustion CO2 capture with chemical absorption: A state-of-the-art review. *Chem. Eng. Res. Des.* **89**, 1609–1624 (2011).

31. IEAGHG. *Integrated Carbon Capture and Storage Project at Saskpower's Boundary Dam*. (2015).

32. Global CCS Institute. *CO_2 capture technologies: pre-combustion capture*. http://www.globalccsinstitute.com/publications/co2-capture-technologies-pre-combustion-capture (2012).

33. Massachusetts Institute of Technology. Kemper County IGCC Fact Sheet: Carbon Dioxide Capture and Storage Project. https://sequestration.mit.edu/tools/projects/kemper.html (2016).

34. Global CCS Institute. Oxy Combustion with CO_2 Capture. 6 (2012).

35. Sanchez-Vicente, Y., Drage, T. C., Poliakoff, M., Ke, J. & George, M. W. Densities of the carbon dioxide + hydrogen, a system of relevance to carbon capture and storage. *Int. J. Greenh. Gas Control* **13**, 78–86 (2013).

36. Kennedy, J. L. *Oil and gas pipeline fundamentals*. (Pennwell books, 1993).

37. Aspelund, A. & Jordal, K. Gas conditioning—The interface between CO_2 capture and transport. *Int. J. Greenh. Gas Control* **1**, 343–354 (2007).

38. Wetenhall, B. et al. Impact of CO_2 impurity on CO_2 compression, liquefaction and transportation. in *Energy Procedia* vol. 63 2764–2778 (Elsevier Ltd, 2014).

39. Choi, Y.-S., Nesic, S. & Young, D. Effect of impurities on the corrosion behavior of CO_2 transmission pipeline steel in supercritical CO_2− water environments. *Environ. Sci. Technol.* **44**, 9233–9238 (2010).

40. Carruthers, K. Environmental Impacts of CO2-EOR. *Scottish Carbon Capture & Storage* **44**, (2014).

41. International Energy Agency. Study of Potential Impacts of Leaks From Onshore CO_2 Storage Projects on Terrestrial Ecosystems. (2007).

42. Permentier, K., Vercammen, S., Soetaert, S. & Schellemans, C. Carbon dioxide poisoning: a literature review of an often forgotten cause of intoxication in the emergency department. *International Journal of Emergency Medicine* vol. 10 (2017).

43. Duncan, I. J., Nicot, J.-P. & Choi, J.-W. Risk Assessment for future CO_2 Sequestration Projects Based CO_2 Enhanced Oil Recovery in the U.S. *Energy Procedia* **1**, 2037–2042 (2009).

44. Wu, J. Y. et al. Full-scale experiments to study shock waves generated by the rupture of a high-pressure pipeline. *Process Saf. Prog.* **35**, 414–423 (2016).

45. Chmilar, J. F. NACE International standard practice SP0169: control of external corrosion on underground or submerged metallic piping systems. (2010).

46. Chevallier, J. Carbon futures and macroeconomic risk factors: A view from the EU ETS. *Energy Econ.* **31**, 614–625 (2009).

47. Lemmon, E. W., Huber, M. L. & McLinden, M. O. NIST reference fluid thermodynamic and transport properties–REFPROP. (2007).

48. Coan, C. R. & King Jnr., A. D. Solubility of Water in Compressed Carbon Dioxide, Nitrous Oxide, and Ethane. Evidence for Hydration of Carbon Dioxide and Nitrous Oxide in the Gas Phase1 1. *J. Am. Chem. Soc.* **7**, 0–5 (1971).

49. Deiters, U. K. & Schneider, G. M. High pressure phase equilibria: experimental methods. *Fluid Phase Equilib.* **29**, 145–160 (1986).

50. Wiebe, R. & Gaddy, V. L. The solubility of carbon dioxide in water at various temperatures from 12 to 40 and at pressures to 500 atmospheres. critical phenomena*. *J. Am. Chem. Soc.* **62**, 815–817 (1940).

51. Wiebe, R. & Gaddy, V. L. The solubility in water of carbon dioxide at 50, 75 and 100, at pressures to 700 atmospheres. *J. Am. Chem. Soc.* **61**, 315–318 (1939).

52. Sabirzyanov, A. N., Shagiakhmetov, R. A., Gabitov, F. R., Tarzimanov, A. A. & Gumerov, F. M. Water Solubility of Carbon Dioxide under Supercritical and Subcritical Conditions. *Theor. Found. Chem. Eng.* **37**, 51–53 (2003).

53. Dohrn, R., Fonseca, J. M. S. & Peper, S. Experimental methods for phase equilibria at high pressures. *Annu. Rev. Chem. Biomol. Eng.* **3**, 343–367 (2012).

54. Jacob Stang, H. G., Lovseth, S. W., Storset, S. O., Malvik, B. & Rekstad, H. Accurate

measurements of CO_2 rich mixture phase equilibria relevant for CCS transport and conditioning. in *Energy Procedia* vol. 37 2897–2903 (Elsevier B.V., 2013).

55. Hagoort, J. Phase behaviour. *Dev. Pet. Sci.* **23**, 49–67 (1988).

56. Zambiasi, G. The critical point, and the phenomenon of the disappearance of the meniscus when a liquid is heated under constant volume. *Philos. Mag. Ser. 5* **36**, 231–232 (1893).

57. Jachowicz, R. S. & Makulski, W. J. Optimal measurement procedures for a dew point hygrometer system. *IEEE Trans. Instrum. Meas.* **42**, 828–833 (1993).

58. Jachowicz, R. S. & Zalewski, D. Hygrometer with fibre optic dew point detector. *Sensors Actuators A. Phys.* **42**, 503–507 (1994).

59. Ke, J., Reid, K. E. & Poliakoff, M. The application of a shear mode piezoelectric sensor to monitoring the high-pressure phase behaviour of asymmetric binary systems. *J. Supercrit. Fluids* **40**, 27–39 (2007).

60. Wang, Z. et al. Near-infrared spectroscopic investigation of water in supercritical CO_2 and the effect of $CaCl_2$. *Fluid Phase Equilib.* **338**, 155–163 (2013).

61. Jackson, K., Bowman, L. E. & Fulton, J. L. Water solubility measurements in supercritical fluids and high-pressure liquids using near-infrared spectroscopy. *Anal. Chem.* **67**, 2368–2372 (1995).

62. Novitskiy, A. A., Ke, J., Comak, G., Poliakoff, M. & George, M. W. A modified golden gate attenuated total reflection (ATR) cell for monitoring phase transitions in multicomponent fluids at high temperatures. *Appl. Spectrosc.* **65**, 885–891 (2011).

63. Harrick, N. J. & Du Pre, F. K. Effective thickness of bulk materials and of thin films for internal reflection spectroscopy. *Appl. Opt.* **5**, 1739–1743 (1966).

64. King, M. B., Mubarak, A., Kim, J. D. & Bott, T. R. The mutual solubilities of water with supercritical and liquid carbon dioxides. *J. Supercrit. Fluids* **5**, 296–302 (1992).

65. Gillespie, P. C., Wilson, G. M. & Association, G. P. *Vapor-liquid and Liquid-liquid Equilibria: Water-methane, Water-carbon Dioxide, Water-hydrogen Sulfide, Water-npentane, Water-methane-npentane*. (Gas Processors Association, 1982).

66. Song, K. Y. & Kobayashi, R. Water content of CO_2 in equilibrium with liquid water and/or hydrates. *SPE Form. Eval.* **2**, 500–508 (1987).

67. Wiebe, R. & Gaddy, V. L. The Solubility of Hydrogen in Water at 0, 50, 75 and 100° from 25 to 1000 Atmospheres. *J. Am. Chem. Soc.* **56**, 76–79 (1934).

68. Poliakoff, M., Howdle, S. M. & Kazarian, S. G. Vibrational Spectroscopy in Supercritical Fluids: From Analysis and Hydrogen Bonding to Polymers and Synthesis. *Angew. Chemie Int. Ed. English* **34**, 1275–1295 (1995).

69. Ke, J. et al. New phase equilibrium analyzer for determination of the vapor-liquid equilibrium of carbon dioxide and permanent gas mixtures for carbon capture and storage. *Rev. Sci. Instrum.* **85**, 085110 (2014).

70. Lemmon, E. W., McLinden, M. O. & Friend, D. G. Thermophysical Properties of Fluid Systems. in *NIST Chemistry WebBook, NIST Standard Reference Database Number 69* (eds. Linstrom, E. D. & Mallard, W. G.) (National Institute of Standards and Technology, 2017). doi:10.18434/T4D303.

71. Adegboye, M. A., Fung, W.-K. & Karnik, A. Recent Advances in Pipeline Monitoring and Oil Leakage Detection Technologies: Principles and Approaches. *Sensors (Basel).* **19**, (2019).

72. Robinson, D. B. & Peng, D.-Y. *The characterization of the heptanes and heavier fractions for the GPA Peng–Robinson programs, Gas processors association*. (1978).

73. Lafitte, T. et al. Accurate statistical associating fluid theory for chain molecules formed from Mie segments. *J. Chem. Phys.* **139**, 154504 (2013).

74. Papaioannou, V. et al. Group contribution methodology based on the statistical associating fluid theory for heteronuclear molecules formed from Mie segments. *J. Chem. Phys.* **140**, 54107 (2014).

75. Mohitpour, M., Golshan, H. & Murray, A. *Pipeline Design and Construction: A Practical Approach*. (The American Society of Chemical Engineers, 2003).

76. Li, X. & Yang, D. Determination of mutual solubility between CO_2 and water by using the Peng-Robinson equation of state with modified alpha function and binary interaction parameter. *Ind. Eng. Chem. Res.* **52**, 13829–13838 (2013).

77. Levenspiel, O. *Engineering flow and heat exchange*. (Plenum Press, 1998).

78. IEAGHG. *Transmission of CO_2 and Energy*. *IEA* https://ieaghg.org/docs/General_Docs/Reports/PH4_6 TRANSMISSION REPORT.pdf (2002).

79. Chandel, M. K., Pratson, L. F. & Williams, E. Potential economies of scale in CO_2 transport through use of a trunk pipeline. *Energy Convers. Manag.* **51**, 2825–2834 (2010).

80. Diamantonis, N. I., Boulougouris, G. C., Mansoor, E., Tsangaris, D. M. & Economou, I. G. Evaluation of cubic, SAFT, and PC-SAFT equations of state for the vapor-liquid equilibrium modeling of CO 2 mixtures with other gases. *Ind. Eng. Chem. Res.* **52**, 3933–3942 (2013).

81. Mazzoccoli, M., De Guido, G., Bosio, B., Arato, E. & Pellegrini, L. A. CO2-mixture properties for pipeline transportation in the CCS process. in *Chemical Engineering Transactions* vol. 32 1861–1866 (2013).

82. Konovalov, A. N., Popov, V. K., Yusupov, V. I. & Yamaguchi, T. High-temperature vibrational densitometer for high-pressure aggressive media. *Russ. J. Phys. Chem. B* **3**, 1125–1130 (2009).

83. Wakeham, W. A., Huber, M. L., Hanley, H. J. M. & Wakeham, W. A. The Corresponding–States Principle: Dense Fluids. in *Transport Properties of Fluids: Their correlation, Prediction and Estimation* (Cambridge University Press, 1996).

84. PSE. gPROMS. (2015).

85. Nazeri, M., Chapoy, A., Burgass, R. & Tohidi, B. Viscosity of CO_2-rich mixtures from 243 K to 423 K at pressures up to 155 MPa: New experimental viscosity data and modelling. *J. Chem. Thermodyn.* **118**, 100–114 (2018).

86. Al-Siyabi, I. Effect of impurities on CO_2 stream properties. *PhD Thesis. Heriot-Watt University* (2013).

87. Pensado, A. S., Pádua, A. A. H., Comuñas, M. J. P. & Fernández, J. Viscosity and density measurements for carbon dioxide + pentaerythritol ester lubricant mixtures at low lubricant concentration. *J. Supercrit. Fluids* **44**, 172–185 (2008).

88. Brown, G. The History of the Darcy-Weisbach Equation for Pipe Flow Resistance. *Proc. Environ. Water Resour. Hist.* **38**, (2002).

89. Martynov, S., Mac Dowell, N., Brown, S. & Mahgerefteh, H. Assessment of Integral Thermo-Hydraulic Models for Pipeline Transportation of Dense-Phase and Supercritical CO $_2$. *Ind. Eng. Chem. Res.* **54**, 8587–8599 (2015).

90. Haaland, S. E. Simple and Explicit Formulas for the Friction Factor in Turbulent Pipe Flow. *J. Fluids Eng.* **105**, 89–90 (1983).

91. Perry, R. H. & Green, D. *Perry's Chemical Engineers Handbook*. (McGraw-Hill Book Co, 1984).

92. Comak, G. et al. Pressure-Drop Method for Detecting Bubble and Dew Points of Multicomponent Mixtures at Temperatures of up to 573 K. *J. Chem. Eng. Data* **63**, 935–942 (2018).

93. Poliakoff, M., Fitzpatrick, J. M., Farren, T. R. & Anastas, P. T. Green chemistry: science and politics of change. *Science (80-.).* **297**, 807–810 (2002).

94. Budde, F., Ezekoye, O., Hundertmark, T., Prieto, M. & Simons, T. J. Chemicals 2025: Will the industry be dancing to a very different tune? *McKinsey & Company* (2017).

95. Office for National Statistics. GDP(O) Low Level Aggregates National Accounts. (2017).

96. Office for National Statistics. Employee Jobs by Industry. (2017).

97. Matlin, S. A., Mehta, G., Hopf, H. & Krief, A. The role of chemistry in inventing a sustainable future. *Nat. Chem.* **7**, 941 (2015).

98. Welton, T. Editorial Overview: UN Sustainable Development Goals: How can sustainable/green chemistry contribute? There can be more than one approach. *Curr. Opin. Green Sustain. Chem.* **13**, A7–A9 (2018).

99. Sheldon, R. A. Organic synthesis-past, present and future. *Chem. Ind.* 903–906 (1992).

100. Böschen, S., Lenoir, D. & Scheringer, M. Sustainable chemistry: starting points and prospects. *Naturwissenschaften* **90**, 93–102 (2003).

101. Anastas, P. T. & Kirchhoff, M. M. Origins, current status, and future challenges of green chemistry. *Acc. Chem. Res.* **35**, 686–694 (2002).

102. Anastas, P. & Eghbali, N. Green Chemistry: Principles and Practice. *Chem. Soc. Rev.* **39**, 301–312 (2010).

103. Anastas, P. T. & Warner, J. 12 Principles of Green Chemistry. *American Chemical Society* https://www.acs.org/content/acs/en/greenchemistry/principles/12-principles-of-green-chemistry.html (2019).

104. Anastas, P. T. & Zimmerman, J. B. Peer Reviewed: Design Through the 12 Principles of Green Engineering. *Environ. Sci. Technol.* **37**, 94A-101A (2003).

105. Trost, B. M. Atom Economy—A Challenge for Organic Synthesis: Homogeneous Catalysis Leads the Way. *Angewandte Chemie International Edition in English* vol. 34 259–281 (1995).

106. Sheldon, R. A. The: E factor 25 years on: The rise of green chemistry and sustainability. *Green Chem.* **19**, 18–43 (2017).

107. Sheldon, R. A. The E Factor: fifteen years on. *Green Chem.* **9**, 1273 (2007).

108. Martinez, C. A. et al. Development of a chemoenzymatic manufacturing process for Pregabalin. *Org. Process Res. Dev.* **12**, 392–398 (2008).

109. Phan, T. V. T., Gallardo, C. & Mane, J. GREEN MOTION: A new and easy to use green

chemistry metric from laboratories to industry. *Green Chem.* **17**, 2846–2852 (2015).

110. Newman, S. G. & Jensen, K. F. The role of flow in green chemistry and engineering. *Green Chemistry* vol. 15 1456–1472 (2013).

111. Jiménez-González, C. et al. Key green engineering research areas for sustainable manufacturing: A perspective from pharmaceutical and fine chemicals manufacturers. *Org. Process Res. Dev.* **15**, 900–911 (2011).

112. Hook, B. D. A. et al. A practical flow reactor for continuous organic photochemistry. *J. Org. Chem.* **70**, 7558–7564 (2005).

113. Vapourtec. Introducing the UV-150 Photochemical Reactor. https://www.vapourtec.com/products/flow-reactors/photochemistry-uv-150-photochemical-reactor-features/ (2018).

114. Lester, E. et al. Reaction engineering: The supercritical water hydrothermal synthesis of nano-particles. *J. Supercrit. Fluids* **37**, 209–214 (2006).

115. Cambridge Reactor Design. Introducing the Ammonite Electrolysis Cells. https://www.cambridgereactordesign.com/ammonite/ammonite-specs.html (2018).

116. Wegner, J., Ceylan, S. & Kirschning, A. Flow chemistry - A key enabling technology for (multistep) organic synthesis. *Advanced Synthesis and Catalysis* vol. 354 17–57 (2012).

117. Fahim, M. A., Alsahhaf, T. A. & Elkilani, A. Thermal Cracking and Coking. in *Fundamentals of Petroleum Refining* 123–152 (Elsevier, 2010). doi:10.1016/b978-0-444-52785-1.00006-1.

118. Ley, S. V. On being green: Can flow chemistry help? *Chem. Rec.* **12**, 378–390 (2012).

119. Gutmann, B., Cantillo, D. & Kappe, C. O. Continuous-flow technology - A tool for the safe manufacturing of active pharmaceutical ingredients. *Angewandte Chemie - International Edition* vol. 54 6688–6728 (2015).

120. Poechlauer, P. et al. Pharmaceutical Roundtable Study Demonstrates the Value of Continuous Manufacturing in the Design of Greener Processes. *Org. Process Res. Dev.* **17**, 1472–1478 (2013).

121. Yoshida, J. I., Kim, H. & Nagaki, A. Green and sustainable chemical synthesis using flow microreactors. *ChemSusChem* **4**, 331–340 (2011).

122. Lee, S. L. et al. Modernizing Pharmaceutical Manufacturing: from Batch to Continuous Production. *Journal of Pharmaceutical Innovation* vol. 10 191–199 (2015).

123. Dallinger, D. & Kappe, C. O. Why flow means green – Evaluating the merits of continuous processing in the context of sustainability. *Current Opinion in Green and Sustainable Chemistry* vol. 7 6–12 (2017).

124. Su, Y., Straathof, N. J. W., Hessel, V. & Noël, T. Photochemical transformations accelerated in continuous-flow reactors: Basic concepts and applications. *Chem. - A Eur. J.* **20**, 10562–10589 (2014).

125. Tucker, J. L. Green Chemistry: Cresting a Summit toward Sustainability. *Org. Process Res. Dev.* **14**, 328–331 (2010).

126. Loubière, K., Oelgemöller, M., Aillet, T., Dechy-Cabaret, O. & Prat, L. Continuous-flow photochemistry: A need for chemical engineering. *Chem. Eng. Process. - Process Intensif.* **104**, 120–132 (2016).

127. Fischer, M. Industrial Applications of Photochemical Syntheses. *Angewandte Chemie International Edition in English* vol. 17 16–26 (1978).

128. DeRosa, M. C. & Crutchley, R. J. Photosensitized singlet oxygen and its applications. *Coordination Chemistry Reviews* vols 233–234 351–371 (2002).

129. Turconi, J. et al. Semisynthetic artemisinin, the chemical path to industrial production. *Org. Process Res. Dev.* **18**, 417–422 (2014).

130. Amara, Z. et al. Applying green chemistry to the photochemical route to artemisinin. *Nat. Chem.* **7**, 489–495 (2015).

131. Miller, S. J. Sustainable chemical synthesis using singlet oxygen. (University of Nottingham, 2018).

132. Sun, Z. C., She, Y. Bin, Zhou, Y., Song, X. F. & Li, K. Synthesis, characterization and spectral properties of substituted tetraphenylporphyrin iron chloride complexes. *Molecules* **16**, 2960–2970 (2011).

133. Oliveira, A., Saggioro, E. M., Pavesi, T., Moreira, J. C. & Ferreira, L. F. V. Solar photochemistry for environmental remediation-advanced oxidation processes for industrial wastewater treatment. in *Molecular Photochemistry-various Aspects* (InTech, 2012).

134. Méndez-Portillo, L. S., Heniche, M., Dubois, C. & Tanguy, P. A. Numerical investigation of the hydrodynamics of split-and-recombination and multilamination microreactors. *AIChE J.* **59**, 988–1001 (2013).

135. Lee, D. S. et al. Continuous Photo-Oxidation in a Vortex Reactor: Efficient Operations Using Air Drawn from the Laboratory. *Org. Process Res. Dev.* **21**, 1042–1050 (2017).

136. Elliott, L. D. et al. A small-footprint, high-capacity flow reactor for uv photochemical synthesis on the kilogram scale. *Org. Process Res. Dev.* **20**, 1806–1811 (2016).

137. Le, C. “Chip” et al. A General Small-Scale Reactor To Enable Standardization and Acceleration of Photocatalytic Reactions. *ACS Cent. Sci.* **3**, 647–653 (2017).

138. Jolliffe, H. G. & Gerogiorgis, D. I. Process modelling and simulation for continuous pharmaceutical manufacturing of artemisinin. *Chem. Eng. Res. Des.* **112**, 310–325 (2016).

139. Radmer, R. J. & Kok, B. Light Conversion Efficiency in Photosynthesis BT - Photosynthesis I: Photosynthetic Electron Transport and Photophosphorylation. in (eds. Trebst, A. & Avron, M.) 125–135 (Springer Berlin Heidelberg, 1977). doi:10.1007/978-3-642-66505-9_6.

140. Ciana, C.-L. & Bochet, C. G. Clean and Easy Photochemistry. *CHIMIA International Journal for Chemistry* vol. 61 650–654.

141. Hoffmann, N. Photochemical reactions as key steps in organic synthesis. *Chemical Reviews* vol. 108 1052–1103 (2008).

142. March, J. *Advanced organic chemistry: reactions, mechanisms, and structure*. (John Wiley & Sons, 1992).

143. Zimmerman, H. E. Mechanistic Organic Photochemistry. *Angew. Chemie Int. Ed. English* **8**, 1–11 (1969).

144. Turro, N. J. Geometric and Topological Thinking in Organic Chemistry. *Angewandte Chemie International Edition in English* vol. 25 882–901 (1986).

145. Olivucci, M. & Santoro, F. Chemical Selectivity through Control of Excited-State Dynamics.

Angew. Chemie Int. Ed. **47**, 6322–6325 (2008).

146. Schapiro, I., Melaccio, F., Laricheva, E. N. & Olivucci, M. Using the computer to understand the chemistry of conical intersections. *Photochemical and Photobiological Sciences* vol. 10 867–886 (2011).

147. Protti, S., Ravelli, D. & Fagnoni, M. Wavelength dependence and wavelength selectivity in photochemical reactions. *Photochem. Photobiol. Sci.* **18**, 2094–2101 (2019).

148. Josland, S., Mumtaz, S. & Oelgemöller, M. Photodecarboxylations in an Advanced Meso-Scale Continuous-Flow Photoreactor. *Chem. Eng. Technol.* **39**, 81–87 (2016).

149. Elgue, S. et al. Flow photochemistry: A meso-scale reactor for industrial applications. *Chim. Oggi/Chemistry Today* **33**, 58–61 (2015).

150. Oelgemoeller, M. Highlights of Photochemical Reactions in Microflow Reactors. *Chemical Engineering and Technology* vol. 35 1144–1152 (2012).

151. Mauser, H. & Gauglitz, G. *Photokinetics: theoretical fundamentals and applications*. vol. 36 (Elsevier, 1998).

152. Atkins, P. W. & De Paula, J. *Atkins' Physical chemistry*. (Oxford University Press, 2002).

153. Sidebottom, H. W., Badcock, C. C., Calvert, J. G., Rabe, B. R. & Damon, E. K. Lifetime studies of the biacetyl excited singlet and triplet states in the gas phase at 25.deg. *J. Am. Chem. Soc.* **94**, 13–19 (1972).

154. Palmisano, G., Augugliaro, V., Pagliaro, M. & Palmisano, L. Photocatalysis: a promising route for 21st century organic chemistry. *Chem. Commun.* 3425–3437 (2007) doi:10.1039/B700395C.

155. Skell, P. S. & Woodworth, R. C. Structure of Carbene. *J. Am. Chem. Soc.* **79**, 6577 (1957).

156. Aillet, T., Loubiere, K., Dechy-Cabaret, O. & Prat, L. Photochemical synthesis of a "cage" compound in a microreactor: Rigorous comparison with a batch photoreactor. *Chem. Eng. Process. Process Intensif.* **64**, 38–47 (2013).

157. Specht, A., Bolze, F., Nicoud, J. F. & Goeldner, M. Characterization of One- and Two-Photon Photochemical Uncaging Efficiency BT - Chemical Neurobiology: Methods and Protocols. in (ed. Banghart, M. R.) 79–87 (Humana Press, 2013). doi:10.1007/978-1-62703-345-9_6.

158. Hatchard, C. G. & Parker, C. A. A new sensitive chemical actinometer-II. Potassium ferrioxalate as a standard chemical actinometer. *Proc. R. Soc. London. Ser. A. Math. Phys. Sci.* **235**, 518–536 (1956).

159. Wolf, H. P., Bohning, J. J., Schnieper, P. A. & Weiss, K. Appararus for the measurement of Quantum Yields and Rates of Photochemical Reactions. *Photochem. Photobiol.* **6**, 321–329 (1967).

160. Corrie, J. E. T., Kaplan, J. H., Forbush, B., Ogden, D. C. & Trentham, D. R. Photolysis quantum yield measurements in the near-UV; A critical analysis of 1-(2-nitrophenyl)ethyl photochemistry. *Photochemical and Photobiological Sciences* vol. 15 604–608 (2016).

161. Halsted, C. P. Brightness, Luminance, and Confusion. *Soc. Inf. Disp.* **9**, 21–24 (1993).

162. OMEGA. What is light intensity? Shining a light on intensity measurement. https://www.omega.co.uk/technical-learning/shining-a-light-on-intensity-measurement.html (2018).

163. French, A. P. & Taylor, E. F. *An introduction to quantum physics*. (CRC Press, 1979).

164. Shevell, S. K. *The Science of Color: Second Edition*. *The Science of Color: Second Edition* (Elsevier, 2003).

165. Swinehart, D. F. The Beer-Lambert Law. *J. Chem. Educ.* **39**, 333 (1962).

166. Lathrop, K. D. Use of Discrete-Ordinates Methods for Solution of Photon Transport Problems. *Nucl. Sci. Eng.* **24**, 381–388 (1966).

167. Fiveland, W. A. Three-dimensional radiative heat-transfer solutions by the discrete-ordinates method. *J. Thermophys. Heat Transf.* **2**, 309–316 (1988).

168. Aillet, T. Conception et mise en œuvre de réacteurs photochimiques intensifiés. (2014).

169. Chai, J. C., Lee, H. S. & Patankar, S. V. Ray effect and false scattering in the Discrete Ordinates Method. *Numer. Heat Transf. Part B Fundam.* **24**, 373–389 (1993).

170. Schuster, A. Radiation Through a Foggy Atmosphere. *Astrophys. J.* **21**, 1 (1905).

171. Schwarzschild, K. & K. On the equilibrium of the Sun's atmosphere. *Nachrichten von der Königlichen Gesellschaft der Wissenschaften zu Göttingen. Math.-phys. Klasse, 195, p. 41-53* **195**, 41–53 (1906).

172. Siegel, R. & Howell, J. R. *Thermal Radiation Heat Transfer*. (Taylor & Francis, 2002).

173. van Noort, M., Hubeny, I. & Lanz, T. Multidimensional Non-LTE Radiative Transfer. I. A Universal Two-dimensional Short-Characteristics Scheme for Cartesian, Spherical, and Cylindrical Coordinate Systems. *Astrophys. J.* **568**, 1066–1094 (2002).

174. Cornet, J. F. Calculation of optimal design and ideal productivities of volumetrically lightened photobioreactors using the constructal approach. *Chem. Eng. Sci.* **65**, 985–998 (2010).

175. Chandrasekhar, S. *Radiative Transfer*. (Dover Publications, 1960). doi:10.1888/0333750888/2102.

176. Imoberdorf, G. & Mohseni, M. Modeling and experimental evaluation of vacuum-UV photoreactors for water treatment. *Chem. Eng. Sci.* **66**, 1159–1167 (2011).

177. Knowles, J. P., Elliott, L. D. & Booker-Milburn, K. I. Flow photochemistry: Old light through new windows. *Beilstein J. Org. Chem.* **8**, 2025–2052 (2012).

178. Gilmore, K. & Seeberger, P. H. Continuous flow photochemistry. *Chem. Rec.* **14**, 410–418 (2014).

179. Muramoto, Y., Kimura, M. & Nouda, S. Development and future of ultraviolet light-emitting diodes: UV-LED will replace the UV lamp. *Semicond. Sci. Technol.* **29**, 084004 (2014).

180. Sender, M. & Ziegenbalg, D. Light sources for photochemical processes–estimation of technological potentials. *Chemie Ing. Tech.* **89**, 1159–1173 (2017).

181. Albini, A. & Germani, L. *Handbook of Synthetic Photochemistry*. (WILEY-VCH Verlag, 2010).

182. Griesbeck, A. G., Maptue, N., Bondock, S. & Oelgemöller, M. The excimer radiation system: A powerful tool for preparative organic photochemistry. A technical note. *Photochem. Photobiol. Sci.* **2**, 450–451 (2003).

183. Lowry, E. F. The Physical Properties of Mercury Improtant in Electronics. *Ann. N. Y. Acad. Sci.* **65**, 417–426 (1957).

184. Heering, W. UV Sources - Basics, Properties and Applications. *Int. Ultrav. Assoc. Inc News* **6**, (2004).

185. Sosnin, E. A., Oppenländer, T. & Tarasenko, V. F. Applications of capacitive and barrier discharge excilamps in photoscience. *J. Photochem. Photobiol. C Photochem. Rev.* **7**, 145–163 (2006).

186. DeLaney, E. N. et al. A laboratory-scale annular continuous flow reactor for UV photochemistry using excimer lamps for discrete wavelength excitation and its use in a wavelength study of a photodecarboxlyative cyclisation. *Green Chem.* **19**, 1431–1438 (2017).

187. Optical Radiation Laboratory. *Institute of High Current Electronics*. (2014).

188. Syed, A. & Früh, W. G. Modelling of mixing in a Taylor-Couette reactor with axial flow. in *Journal of Chemical Technology and Biotechnology* vol. 78 227–235 (John Wiley & Sons, Ltd, 2003).

189. Giordano, R. L. C., Giordano, R. C., Prazeres, D. M. F. & Cooney, C. L. Analysis of a Taylor-Poiseuille vortex flow reactor -- II: Reactor modeling and performance assessment using glucose-fructose isomerization as test reaction. *Chem. Eng. Sci.* **55**, 3611–3626 (2000).

190. Taylor, G. I. Stability of a Viscous Liquid Contained between Two Rotating Cylinders. *Philos. Trans. R. Soc. A Math. Phys. Eng. Sci.* **223**, 289–343 (1923).

191. Zhou, F., Hearne, Z. & Li, C. J. Water—the greenest solvent overall. *Current Opinion in Green and Sustainable Chemistry* vol. 18 118–123 (2019).

192. Hughes, G. & Lewis, J. C. Introduction: Biocatalysis in Industry. *Chemical Reviews* vol. 118 1–3 (2018).

193. Akiya, N. & Savage, P. E. Roles of water for chemical reactions in high-temperature water. *Chem. Rev.* **102**, 2725–50 (2002).

194. Brill, T. B. Geothermal Vents and Chemical Processing: The Infrared Spectroscopy of Hydrothermal Reactions. *J. Phys. Chem. A* **104**, 4343–4351 (2000).

195. Siskin, M. & Katritzky, A. Reactivity of Organic Compounds in Hot Water: Geochemical and Technological Implications. *Science (80-.).* **254**, 231 LP – 237 (1991).

196. Simoneit, B. R. . Aqueous high-temperature and high-pressure organic geochemistry of hydrothermal vent systems. *Geochim. Cosmochim. Acta* **57**, 3231–3243 (1993).

197. Savage, P. E., Gopalan, S., Mizan, T. I., Martino, C. J. & Brock, E. E. Reactions at supercritical conditions: Applications and fundamentals. *AIChE J.* **41**, 1723–1778 (1995).

198. Savage, P. E. Organic Chemical Reactions in Supercritical Water. *Chem. Rev.* **99**, 603–621 (1999).

199. An, J., Bagnell, L., Cablewski, T., Strauss, C. R. & Trainor, R. W. Applications of High-Temperature Aqueous Media for Synthetic Organic Reactions. *J. Org. Chem.* **62**, 2505–2511 (1997).

200. Katritzky, A. R., Allin, S. M. & Siskin, M. Aquathermolysis: Reactions of Organic Compounds with Superheated Water. *Acc. Chem. Res.* **29**, 399–406 (1996).

201. Siskin, M. & Katritzky, A. A Review of the Reactivity of Organic Compounds with Oxygen-containing Functionality in Superheated Water. *J. Anal. Appl. Pyrolysis* **54**, 193–214 (2000).

202. Mizan, T. I., Savage, P. E. & Ziff, R. M. *Temperature Dependence of Hydrogen Bonding in*

Supercritical Water. https://pubs.acs.org/sharingguidelines (1996).

203. Rebert, C. J. & Kay, W. B. The phase behavior and solubility relations of the benzene-water system. *AIChE J.* **5**, 285–289 (1959).

204. Connolly, J. F. Solubility of Hydrocarbons in Water near the Critical Solution Temperatures. *J. Chem. Eng. Data* **11**, 13–16 (1966).

205. Krau, C. I., Kuhn, D. & Schulenberg, T. Heat Transfer Phenomena of Supercritical Fluids. in *Proceedings of the International Youth Nuclear Congress 2008* 352.2 (Institute for Nuclear and Energy Technologies, 2008).

206. Ramayya, S., Brittain, A., DeAlmeida, C., Mok, W. & Antal, M. J. Acid-catalysed dehydration of alcohols in supercritical water. *Fuel* **66**, 1364–1371 (1987).

207. Wang, X., Gron, L. U., Klein, M. T. & Brill, T. B. The influence of high-temperature water on the reaction pathways of nitroanilines. *J. Supercrit. Fluids* **8**, 236–249 (1995).

208. Belsky, A. J., Maiella, P. G. & Brill, T. B. Spectroscopy of Hydrothermal Reactions 13. Kinetics and Mechanisms of Decarboxylation of Acetic Acid Derivatives at 100-260 °C under 275 bar. *J. Phys. Chem. A* **103**, 4253–4260 (1999).

209. Bertrán, J., Lluch, J. M., González-Lafont, A., Dillet, V. & Pérez, V. Transition-State Structures. in *Structure and Reeactivity in Aqueuous Solution: Characterization of Chemical and Biological Systems* 168–180 (1994). doi:10.1021/bk-1994-0568.ch012.

210. Howie, R. A. Metal-organic frameworks: towards greener synthesis. (University of Nottingham, 2017).

211. Kirschning, A., Monenschein, H. & Wittenberg, R. Functionalized polymers - Emerging versatile tools for solution-phase chemistry and automated parallel synthesis. *Angewandte Chemie - International Edition* vol. 40 650–679 (2001).

212. Reichardt, C. & Welton, T. *Solvents and Solvent Effects in Organic Chemistry*. (Wiley, 2011).

213. Pardalos, P. M. & Rosen, J. Ben. *Constrained Global Optimization: Algorithms and Applications*. *Constrained Global Optimization: Algorithms and Applications* vol. 268 (Springer-Verlag, 1987).

214. Lange, H. et al. A breakthrough method for the accurate addition of reagents in multi-step segmented flow processing. *Chem. Sci.* **2**, 765–769 (2011).

215. Jolliffe, H. G. & Gerogiorgis, D. I. Technoeconomic Optimization of a Conceptual Flowsheet for Continuous Separation of an Analgaesic Active Pharmaceutical Ingredient (API). *Ind. Eng. Chem. Res.* **56**, 4357–4376 (2017).

216. Hangos, K. M. & Cameron, I. T. *Process modelling and model analysis*. vol. 4 (Academic press London, 2001).

217. Laidler, K. J. The development of the arrhenius equation. *J. Chem. Educ.* **61**, 494–498 (1984).

218. Schmidt, L. D. *The Engineering of Chemical Reactions*. (Oxford University Press, 1998).

219. Levenspiel, O. *Chemical Reaction Engineering*. (John Wiley & Sons, 1998).

220. Leibniz, G. W. The Art of Discovery. (1685).

221. Mendel, J. M. *Discrete Techniques of Parameter Estimation: The Equation Error Formulation*. (M. Dekker, 1973).

222. Box, G. E. P. Robustness in the Strategy of Scientific Model Building. in *Robustness in Statistics* 201–236 (Elsevier, 1979). doi:10.1016/b978-0-12-438150-6.50018-2.

223. Greeff, D. J. & Aldrich, C. Empirical modelling of chemical process systems with evolutionary programming. *Comput. Chem. Eng.* **22**, 995–1005 (1998).

224. Piepel, G. F. Empirical Model Building. *Technometrics* **32**, 353–353 (1990).

225. Bequette, B. W. Operability analysis of an exothermic semi-batch reactor. *Comput. Chem. Eng.* **20**, (1996).

226. Duarte, B., Saraiva, P. M. & Pantelides, C. C. Combined mechanistic and empirical modelling. *Int. J. Chem. React. Eng.* **2**, (2004).

227. Psichogios, D. C. & Ungar, L. H. A hybrid neural network-first principles approach to process modeling. *AIChE J.* **38**, 1499–1511 (1992).

228. Ullmann, F. *Ullmann's Chemical Engineering and Plant Design*. (John Wiley & Sons, 2005).

229. Levenspiel, O. *Chemical Reaction Engineering*. (John Wiley & Sons, Inc., 1998).

230. Nayfeh, A. H. & Balachandran, B. *Applied nonlinear dynamics: analytical, computational, and experimental methods*. (John Wiley & Sons, 2008).

231. Kittrell, J. R. Mathematical Modeling of Chemical Reactions. *Adv. Chem. Eng.* **8**, 97–183 (1970).

232. Lapidus, L. & Pinder, G. F. *Numerical solution of partial differential equations in science and engineering*. (John Wiley & Sons, 2011).

233. Moon, P. & Spencer, D. E. *Field theory handbook: including coordinate systems, differential equations and their solutions*. (Springer, 2012).

234. Zwillinger, D. *CRC standard mathematical tables and formulae*. (Chapman and Hall/CRC, 2002).

235. Evans, L. C. *Partial Differential Equations*. (American Mathematical Society, 1998).

236. Perrot, P. *A to Z of Thermodynamics*. (Oxford University Press, 1998).

237. Clapeyron, E. Mémoire sur la puissance motrice de la chaleur. *J. l'École Polytech.* **XIV**, 153–190 (1834).

238. Wilczek-Vera, G. & Vera, J. H. Understanding cubic equations of state: A search for the hidden clues of their success. *AIChE J.* **61**, 2824–2831 (2015).

239. Van der Waals, J. D. *Over de Continuiteit van den Gas-en Vloeistoftoestand*. vol. 1 (Sijthoff, 1873).

240. Berg, H. J., D, R. I., Peng, D.-Y. & Robinson, D. B. A New Two-Constant Equation of State. *J. Ind. fng. Chem. J. Phys. Chem. Ind. fng. Chem.. Fundam. J. Agric. Sci. Van Stralen, S. J. 0.. lnt. J. Heat Mass Transf. I O* **51**, 385–1082 (1972).

241. Soave, G. Equilibrium constants from a modified Redlich-Kwong equation of state. *Chem. Eng. Sci.* **27**, 1197–1203 (1972).

242. Economou, I. G. Statistical Associating Fluid Theory: A Successful Model for the Calculation of Thermodynamic and Phase Equilibrium Properties of Complex Fluid Mixtures. *Ind. Eng. Chem. Res.* **41**, 953–962 (2002).

243. Wertheim, M. S. Fluids with highly directional attractive forces. I. Statistical thermodynamics. *J. Stat. Phys.* **35**, 19–34 (1984).

244. Wertheim, M. S. Fluids with highly directional attractive forces. II. Thermodynamic perturbation theory and integral equations. *J. Stat. Phys.* **35**, 35–47 (1984).

245. Wertheim, M. S. Fluids with highly directional attractive forces. III. Multiple attraction sites. *J. Stat. Phys.* **42**, 459–476 (1986).

246. Wertheim, M. S. Fluids with highly directional attractive forces. IV. Equilibrium polymerization. *J. Stat. Phys.* **42**, 477–492 (1986).

247. I. Sandier, S. & Orbey, H. Mixing and combining rules. *Exp. Thermodyn.* **5**, 321–357 (2000).

248. Gao, G., Daridon, J.-L., Saint-Guirons, H., Xans, P. & Montel, F. A simple correlation to evaluate binary interaction parameters of the Peng-Robinson equation of state: binary light hydrocarbon systems. *Fluid Phase Equilib.* **74**, 85–93 (1992).

249. Gao, W., Robinson, R. L. & Gasem, K. A. M. Alternate equation of state combining rules and interaction parameter generalizations for asymmetric mixtures. *Fluid Phase Equilib.* **213**, 19–37 (2003).

250. Behrens, D., Stephan, K. & Hildwein, H. *Chemistry data series. IV, Recommended data of selected compounds and binary mixtures*. (DECHEMA).

251. Ely, J. F. & Hanley, H. J. M. Prediction of Transport Properties. 1. Viscosity of Fluids and Mixtures. *Ind. Eng. Chem. Fundam.* **20**, 323–332 (1981).

252. Ely, J. F. & Hartley, H. J. M. Prediction of Transport Properties. 2. Thermal Conductivity of Pure Fluids and Mixtures. *Ind. Eng. Chem. Fundam.* **22**, 90–97 (1983).

253. Huber, M. L. *NIST Thermophysical properties of hydrocarbon mixtures database (SUPERTRAPP), version 3.2*. (2007).

254. Pedersen, K. S., Fredenslund, A. & Thomassen, P. *Properties of oils and natural gases*. (Gulf Pub. Co., Book Division, 1989).

255. Lohrenz, J., Bray, B. G. & Clark, C. R. Calculating viscosities of reservoir fluids from their compositions. *J. Pet. Technol.* **16**, 1–171 (1964).

256. Lhner, R. *Applied Computational Fluid Dynamics Techniques*. (John Wiley & Sons, Ltd, 2008). doi:10.1002/9780470989746.

257. Zawawi, M. H. et al. A review: Fundamentals of computational fluid dynamics (CFD). in *AIP Conference Proceedings* vol. 2030 020252 (AIP Publishing LLC , 2018).

258. Marchisio, D. L. & Barresi, A. A. CFD simulation of mixing and reaction: The relevance of the micro- mixing model. *Chem. Eng. Sci.* **58**, 3579–3587 (2003).

259. Sczechowski, J. G. et al. Continuous Photo-Oxidation in a Vortex Reactor: Efficient Operations Using Air Drawn from the Laboratory. *Org. Process Res. Dev.* **21**, 1042–1050 (2017).

260. Fick, A. Ueber Diffusion. *Ann. Phys.* **170**, 59–86 (1855).

261. Bailyn, M. & Baierlein, R. A Survey of Thermodynamics. *Am. J. Phys.* **64**, 94–95 (1996).

262. Kays, W. M. & Crawford, M. E. *Convective heat and mass transfer*. (New York : McGraw-Hill, 1993).

263. Newton, I. *Philosophiæ Naturalis Principia Mathematica (Latin)*. *Philosophical Studies* (1687).

264. Clay Institute. Navier-Stokes Equation. https://www.claymath.org/millennium-problems/navier–stokes-equation (2000).

265. Gary Leal, L. *Laminar Flow and Convective Transport Processes*. (Butterworth-Heinemann, 1992).

266. Sieder, E. N. & Tate, G. E. Heat transfer and pressure drop of liquids in tubes. *Ind. Eng. Chem.* **28**, 1429–1435 (1936).

267. Reynolds, O. An experimental investigation of the circumstances which determine whether the motion of water shall be direct or sinuous, and of the law of resistance in parallel channels. *Proc. R. Soc. London* **35**, 84–99 (1883).

268. Moody, L. F. Friction Factor for Pipe Flow. *Trans. ASME* **66**, 671–684 (1944).

269. Churchill, S. W. Friction factor equation spans all fluid-flow regimes. *Chem. Eng.* **84**, 91–92 (1977).

270. Von Kármán, T. *Mechanische Ähnlichkeit und Turbulenz*. (Weidmannsche Buchh., 1930).

271. Colebrook, C. F. & White, C. M. Experiments with Fluid Friction in Roughened Pipes. *Proc. R. Soc. London. Ser. A - Math. Phys. Sci.* **161**, 367 LP – 381 (1937).

272. Massey, B. S. *Mechanics of fluids*. (Chapman & Hall, 1989).

273. Bezzo, F., Bernardi, R., Cremonese, G., Finco, M. & Barolo, M. Using process simulators for steady-state and dynamic plant analysis: An industrial case study. *Chem. Eng. Res. Des.* **82**, 499–512 (2004).

274. Matzopoulos, M., Georgiadis, M. C., Banga, J. R. & Pistikopoulos, E. N. *Dynamic Process Modeling Edited*. *Process Systems Engineering* vol. 7 (2011).

275. Süli, E. & Mayers, D. F. *An introduction to numerical analysis*. (Cambridge university press, 2003).

276. Runge, C. Ueber die numerische Auflösung von Differentialgleichungen. *Math. Ann.* **46**, 167–178 (1895).

277. Kutta, W. Beitrag zur näherungsweisen Integration totaler Differentialgleichungen. *Zeitschrift für Math. und Phys.* **46**, 435–453 (1901).

278. Euler, L. Methodus inveniendi lineas curvas maximi minimive proprietate gaudentes, sive solutio problematis isoperimetrici latissimo sensu accepti, additamentum {II} (1744). in *Opera omnia* (Orell Füssli Turici, 1744).

279. Löhner, R. *Applied computational fluid dynamics techniques : an introduction based on finite element methods*. (John Wiley & Sons, 2008).

280. Raol, J. R., Girija, G. & Singh, J. *Modelling and Parameter Estimation of Dynamic Systems*. (Institution of Engineering and Technology, 2004).

281. Fisher, R. A. On the Mathematical Foundations of Theoretical Statistics. *Philos. Trans. R. Soc. A Math. Phys. Eng. Sci.* **222**, 309–368 (1922).

282. Fisher, R. A. Contributions to mathematical statistics. (1950).

283. Åström, K. J. Maximum likelihood and prediction error methods. *Automatica* **16**, 551–574 (1980).

284. Stanford Encylopedia of Philosophy. Bayes' Theorem.

https://plato.stanford.edu/entries/bayes-theorem/ (2003).

285. StatQuest with Josh Starmer. *StatQuest: Maximum Likelihood, clearly explained*. (2017).

286. Pfeiffer, P. E. Covariance, Correlation, and Linear Regression. in 371–391 (1990). doi:10.1007/978-1-4615-7676-1_20.

287. Bard, Y. *Nonlinear Parameter Estimation*. (Academic Press, 1974).

288. Schwaab, M. & Pinto, J. C. Optimum reference temperature for reparameterization of the Arrhenius equation. Part 1: Problems involving one kinetic constant. *Chem. Eng. Sci.* **62**, 2750–2764 (2007).

289. Schwaab, M., Lemos, L. P. & Pinto, J. C. Optimum reference temperature for reparameterization of the Arrhenius equation. Part 2: Problems involving multiple reparameterizations. *Chem. Eng. Sci.* **63**, 2895–2906 (2008).

290. Agarwal, A. K. & Brisk, M. L. Sequential experimental design for precise parameter estimation. 1. Use of reparameterization. *Ind. Eng. Chem. Process Des. Dev.* **24**, 203–207 (1985).

291. Pritchard, D. J. & Bacon, D. W. Statistical assessment of chemical kinetic models. *Chem. Eng. Sci.* **30**, 567–574 (1975).

292. Rimensberger, T. & Rippin, D. W. T. Comments on "Sequential Experimental Design for Precise Parameter Estimation. 1. Use of Reparameterization". *Ind. Eng. Chem. Process Des. Dev.* **25**, 1042–1044 (1986).

293. Bernstein, D. S. *Matrix mathematics: Theory, facts, and formulas (second edition)*. *Matrix Mathematics: Theory, Facts, and Formulas (Second Edition)* (Princeton University Press, 2009).

294. Griffiths, L. Towards the automatic analysis of1H NMR spectra: Part 2. Accurate integrals and stoichiometry. *Magn. Reson. Chem.* **39**, 194–202 (2001).

295. Grob, R. L. & Barry, E. F. *Modern practice of gas chromatography*. vol. 2 (Wiley Online Library, 1977).

296. Malz, F. & Jancke, H. Validation of quantitative NMR. *J. Pharm. Biomed. Anal.* **38**, 813–823 (2005).

297. Himmelblau, D. M. *Process Analysis by Statistical Methods*. (Wiley, 1970).

298. Rossi, R. J. *Mathematical Statistics: An Introduction to Likelihood Based Inference*. (John Wiley & Sons, 2018).

299. Pearson, K. X. On the criterion that a given system of deviations from the probable in the case of a correlated system of variables is such that it can be reasonably supposed to have arisen from random sampling. *London, Edinburgh, Dublin Philos. Mag. J. Sci.* **50**, 157–175 (1900).

300. Cochran, W. G. The X2 Test of Goodness of Fit. *Ann. Math. Stat.* **23**, 315–345 (1952).

301. Box, J. F. Guinness, gosset, fisher, and small samples. *Stat. Sci.* **2**, 45–54 (1987).

302. Welch, B. L. The generalisation of student's problems when several different population variances are involved. *Biometrika* **34**, 28–35 (1947).

303. Biegler, L. T., Grossmann, I. E. & Westerberg, A. W. Systematic methods for chemical process design. (1997).

304. Saltelli, A. & Tarantola, S. On the relative importance of input factors in mathematical

models: safety assessment for nuclear waste disposal. *J. Am. Stat. Assoc.* **97**, 702–709 (2002).

305. Morris, M. D. Factorial sampling plans for preliminary computational experiments. *Technometrics* **33**, 161–174 (1991).

306. Campolongo, F., Cariboni, J. & Saltelli, A. An effective screening design for sensitivity analysis of large models. *Environ. Model. Softw.* **22**, 1509–1518 (2007).

307. Arioli, M., Demmel, J. W. & Duff, I. S. Solving sparse linear systems with sparse backward error. *SIAM J. Matrix Anal. Appl.* **10**, 165–190 (1989).

308. Martín, M. M. *Introduction to Software for Chemical Engineers, Second Edition*. (CRC Press, 2019).

309. Jarvis, R. B. Robust dynamic simulation of Chemical Engineering Processes. (University of London, 1993).

310. Friedler, F. Process integration, modelling and optimisation for energy saving and pollution reduction. *Appl. Therm. Eng.* **30**, 2270–2280 (2010).

311. Büchi, G., Inman, C. G. & Lipinsky, E. S. Light-catalyzed Organic Reactions. I. The Reaction of Carbonyl Compounds with 2-Methyl-2-butene in the Presence of Ultraviolet Light. *J. Am. Chem. Soc.* **76**, 4327–4331 (1954).

312. Thompson, M. P., Agger, J. & Wong, L. S. Paternò–Büchi Reaction as a Demonstration of Chemical Kinetics and Synthetic Photochemistry Using a Light Emitting Diode Apparatus. *J. Chem. Educ.* **92**, 1716–1720 (2015).

313. Bach, T. Stereoselective intermolecular [2+ 2]-photocycloaddition reactions and their application in synthesis. *Synthesis (Stuttg).* **1998**, 683–703 (1998).

314. Tom, S. & Sakurai, H. *Kinetic Studies of the Photoreaction of Benzophenone with Furan*. https://www.journal.csj.jp/doi/pdf/10.1246/bcsj.40.2885.

315. Storey, C. & Rosenbrock, H. H. *Computational Techniques for Chemical Engineers: International Series of Monographs in Chemical Engineering*. (Pergamon Press, 1996).

316. Van Wyk, R. Variable mesh multistep methods for ordinary differential equations. *J. Comput. Phys.* **5**, 244–264 (1970).

317. ANSYS. ANSYS Fluent. (2018).

318. DeLaney, E. N. Photochemistry and Electrochemistry in Continuous Flow Toward Integrated Processes. (University of Nottingham, 2018).

319. Cussler, E. L. *Diffusion: Mass Transfer in Fluid Systems.* (Cambridge University Press, 1997). doi:10.1086/415398.

320. Takahashi, T., Korenaga, T. & Shen, F. *A Numerical Solution for the Dispersion in Laminar Flow Through a Circular Tube*. https://onlinelibrary.wiley.com/doi/pdf/10.1002/cjce.5450680202 (1953).

321. Matsushima, R. & Terada, K. Photoreactions of Alkylated 2-Pyridones. *J. Chem. Soc., Perkin Trans. 2* 1445–1448 (1985).

322. Herzfeld, K. F. *Theory of Light Absorption in Simple Aromatic Compounds*. *Source: Proceedings of the American Philosophical Society* vol. 82 (1940).

323. Oelgemöller, M., Cygon, P., Lex, J. & G. Griesbeck, A. The Photodecarboxylative Addition of

Carboxylates to Phthalimides: Scope and Limitations. *Heterocycles* **59**, 669 (2003).

324. Oelgemöller, M. & Griesbeck, A. G. Photoinduced electron transfer chemistry of phthalimdes: An efficient tool for C-C-bond formation. *Journal of Photochemistry and Photobiology C: Photochemistry Reviews* vol. 3 109–127 (2002).

325. Griesbeck, A. G., Henz, A., Peters, K., Peters, E.-M. & von Schnering, H. G. Photo Electron Transfer Induced Macrocyclization ofN-Phthaloyl-ω-aminocarboxylic Acids. *Angew. Chemie Int. Ed. English* **34**, 474–476 (1995).

326. Griesbeck, A. G., Kramer, W. & Lex, J. Diastereo- and Enantioselective Synthesis of Pyrrolo[1,4]benzodiazepines through Decarboxylative Photocyclization. *Angew. Chemie Int. Ed.* **40**, 577–579 (2001).

327. Hatoum, F., Gallagher, S., Baragwanath, L., Lex, J. & Oelgemöller, M. Photodecarboxylative benzylations of phthalimides. *Tetrahedron Lett.* **50**, 6335–6338 (2009).

328. Griesbeck, A. G., Nazarov, N., Neudörfl, J. M. & Heffen, M. Intermolecular photodecarboxylation of electron-deficient substrates by phthalimides in water: efficiency, selectivity and online monitoring. *Green Chem.* **14**, 3004 (2012).

329. Griesbeck, A. G. et al. Synthesis of Medium- and Large-Ring Compounds Initiated by Photochemical Decarboxylation of ω-Phthalimidoalkanoates. *Helv. Chim. Acta* **80**, 912–933 (1997).

330. Axel G. Griesbeck, *, Frank Nerowski, 1 and & Lex, J. Decarboxylative Photocyclization: Synthesis of Benzopyrrolizidines and Macrocyclic Lactones. (1999) doi:10.1021/JO990390B.

331. Griesbeck, A. G., Henz, A., Peters, K., Peters, E.-M. & von Schnering, H. G. Photo Electron Transfer Induced Macrocyclization ofN-Phthaloyl-ω-aminocarboxylic Acids. *Angew. Chemie Int. Ed. English* **34**, 474–476 (1995).

332. Elliott, L. D. et al. Batch versus flow photochemistry: A revealing comparison of yield and productivity. *Chem. - A Eur. J.* **20**, 15226–15232 (2014).

333. Clark, C. A., Lee, D. S., Pickering, S. J., Poliakoff, M. & George, M. W. UV PhotoVap: Demonstrating How a Simple and Versatile Reactor Based on a Conventional Rotary Evaporator Can Be Used for UV Photochemistry. *Org. Process Res. Dev.* **22**, 595–599 (2018).

334. Bodenstein, M. Eine theorie der photochemischen reaktionsgeschwindigkeiten. *Zeitschrift für Phys. Chemie* **85**, 329–397 (1913).

335. Darko, A. et al. Conformationally strained trans-cyclooctene with improved stability and excellent reactivity in tetrazine ligation. *Chem. Sci.* **5**, 3770–3776 (2014).

336. Boger, D. L. Diels-Alder reactions of heterocyclic aza dienes. Scope and applications. *Chem. Rev.* **86**, 781–793 (1986).

337. Maksim Royzen, Glenn P. A. Yap, and & Fox*, J. M. A Photochemical Synthesis of Functionalized trans-Cyclooctenes Driven by Metal Complexation. (2008) doi:10.1021/JA8001919.

338. Svatunek, D. et al. Efficient low-cost preparation of trans-cyclooctenes using a simplified flow setup for photoisomerization. *Monatshefte fur chemie* **147**, 579–585 (2016).

339. Blanco-Ania, D., Maartense, L. & Rutjes, F. P. J. T. Rapid Production of *trans* -Cyclooctenes in Continuous Flow. *ChemPhotoChem* **2**, 898–905 (2018).

340. Inoue, Y., Takamuku, S. & Sakurai, H. Direct and sensitized cis-trans photoisomerization of cyclooctene. Effects of spin multiplicity and vibrational activation of excited states on the photostationary trans/cis ratio. *J. Phys. Chem.* **81**, 7–11 (1977).

341. Inoue, Y., Takamuku, S., Kunitomi, Y. & Sakurai, H. Singlet photosensitization of simple alkenes. Part 1. cis–trans-Photoisomerization of cyclo-octene sensitized by aromatic esters. *J. Chem. Soc., Perkin Trans. 2* 1672–1677 (1980) doi:10.1039/P29800001672.

342. Inoue, Y., Takamuku, S. & Sakurai, H. An anomalously high trans: Cis photostationary ratio on the direct photoisomerization of cyclo-octene. *J. Chem. Soc. Chem. Commun.* 423–424 (1976).

343. Srinivasan, R. & Brown, K. H. Organic Photochemistry with High Energy (6.7 eV) Photons: Cis⇌Trans Isomerism in Cyclooctene. *Journal of the American Chemical Society* vol. 100 2589–2590 (1978).

344. Inoue, Y., Takamuku, S. & Sakurai, H. Direct and sensitized cis-trans photoisomerization of cyclooctene. Effects of spin multiplicity and vibrational activation of excited states on the photostationary trans/cis ratio. *J. Phys. Chem.* **81**, 7–11 (1977).

345. Cussler, E. L. *Diffusion: Mass Transfer in Fluid Systems.* (Cambridge University Press, 1997). doi:10.1086/415398.

346. Taylor, G. I. Stability of a Viscous Liquid Contained between Two Rotating Cylinders. *Philos. Trans. R. Soc. A Math. Phys. Eng. Sci.* **223**, 289–343 (1923).

347. Sczechowski, J. G., Koval, C. A. & Noble, R. D. A Taylor vortex reactor for heterogeneous photocatalysis. *Chem. Eng. Sci.* **50**, 3163–3173 (1995).

348. Charpentier, J.-C. The triplet “molecular processes–product–process” engineering: the future of chemical engineering ? *Chem. Eng. Sci.* **57**, 4667–4690 (2002).

349. Cohen, S. & David Moalem, M. Analysis of a rotating annular reactor in the vortex flow regime. *Chem. Eng. Sci.* **46**, 123–134 (1991).

350. Pudjiono, P. I., Tavare, N. S., Garside, J. & Nigam, K. D. P. Residence time distribution from a continuous Couette flow device. *Chem. Eng. J.* **48**, 101–110 (1992).

351. Nagy, K. D., Shen, B., Jamison, T. F. & Jensen, K. F. Mixing and Dispersion in Small-Scale Flow Systems. (2012) doi:10.1021/op200349f.

352. Ramart-Lucas, P. & Guilmart, T. Sur les variations d’absorption dans les series homologues. *Bull. Soc. Chim. Fr.* **17**, 405–411 (1950).

353. Kormányos, A., Endrődi, B., Ondok, R., Sápi, A. & Janáky, C. Controlled Photocatalytic Synthesis of Core–Shell SiC/Polyaniline Hybrid Nanostructures. *Materials (Basel).* **9**, 201 (2016).

354. Lillacci, G. & Khammash, M. Parameter estimation and model selection in computational biology. *PLoS Comput. Biol.* **6**, 1000696 (2010).

355. Ralph, M. J., Harrowven, D. C., Gaulier, S., Ng, S. & Booker-Milburn, K. I. The profound effect of the ring size in the electrocyclic opening of cyclobutene-fused bicyclic systems. *Angew. Chemie - Int. Ed.* **54**, 1527–1531 (2015).

356. Wiberg, K. B. The concept of strain in organic chemistry. *Angew. Chemie Int. Ed. English* **25**, 312–322 (1986).

357. Bach, T. & Hehn, J. P. Photochemical reactions as key steps in natural product synthesis.

Angew. Chemie Int. Ed. **50**, 1000–1045 (2011).

358. Kandyala, R., Raghavendra, S. P. & Rajasekharan, S. Xylene: An overview of its health hazards and preventive measures. *J. Oral Maxillofac. Pathol.* **14**, 1 (2010).

359. Hu, Y. et al. Sustainable Production of o-Xylene from Biomass-Derived Pinacol and Acrolein. *ChemSusChem* **10**, 2880–2885 (2017).

360. Seban, R. A. & McLaughlin, E. F. Heat transfer in tube coils with laminar and turbulent flow. *Int. J. Heat Mass Transf.* **6**, 387–395 (1963).

361. Dean, W. R. LXXII. The stream-line motion of fluid in a curved pipe (Second paper). *London, Edinburgh, Dublin Philos. Mag. J. Sci.* **5**, 673–695 (1928).

362. Aris, R. On the dispersion of a solute in a fluid flowing through a tube. in *Process Systems Engineering* vol. 1 109–120 (1999).

363. Incropera, F. P. & DeWitt, D. P. *Fundamentals of Heat and Mass Transfer*. (Wiley, 1990).

364. van den Berg, J. H. & Deelder, R. S. Measurement of axial dispersion in laminar flow through coiled capillary tubes. *Chem. Eng. Sci.* **34**, 1345–1347 (1979).

365. Iyer, R. N. Laminar dispersion in helical coils. *Chem. Eng. Sci.* **36**, 1104–1105 (1981).

366. Gelhausen, M. G., Kurt, S. K. & Kockmann, N. Mixing and Heat Transfer in Helical Capillary Flow Reactors With Alternating Bends. in *ASME 2014 12th International Conference on Nanochannels, Microchannels and Minichannels* V001T13A001 (ASME, 2014). doi:10.1115/icnmm2014-21779.

8. Appendix

8.1. Appendix I – Introduction to photochemistry and HTW

8.1.1. Definitions of quantum yield

The quantum yield of a reaction is a measure of the efficiency the reaction has compared to the number of photons it has absorbed. However, there are a number of different definitions in the literature regarding quantum yield which are outlined below.

Apparent Integral Quantum Yield

$$\Phi_i = \frac{\Delta N_i}{N_{h\nu}} = \frac{C_i(t) - C_{i,0}}{\int_0^t I_T \, dt} \tag{107}$$

The *apparent integral quantum yield,* defined in Equation 107, is the ratio between the photochemical reaction and the total light absorbed by the whole system; where ΔN_i is the number of moles of reactant i that react in time t and $N_{h\nu}$ is number of light quanta (moles/einsteins) absorbed by the whole system in time t. $C_i(t)$ and $C_{i,0}$ are the concentrations of i at time t and $t = 0$, respectively. I_T is the total amount of light absorbed by the whole system, not just the molecule in question, i.

True Integral Quantum Yield

$$\Phi_i^A = \frac{\Delta N_i}{N_{h\nu,i}} = \frac{C_i(t) - C_{i,0}}{\int_0^t I_i \, dt} \tag{108}$$

The *true integral quantum yield,* defined in Equation 108, is reactant specific and looks at the ratio between the reactions happening to i compared to the amount of light i has absorbed. $N_{h\nu,i}$ is the amount of light i has absorbed in time t.

The integral based quantum yields above are conceptually easy to understand and often can be measured experimentally; however, some assumptions are needed. For example, if a quantum yield is measured relative to the starting material it has to be assumed that said starting material only reacts photochemically. A similar assumption has to be taken with quantum yields that are taken relative to

the production of a product; it has to be assumed to only be formed photochemically. Also, care needs to be taken with what we see as a desired quantum yield – one reaction may have a high quantum yield (which is often seen as good) because once it absorbs light it is likely to go onto react, but it could be reacting to form an unwanted side product. These assumptions are likely to be true simple reactions at low temperature but would need to be considered for more complex reactions.

Time independent quantum yields

The previous quantum yields are useful for understanding an overall reaction scheme but are integrated over time and hence cannot be used in a program that predicts over time. Time independent quantum yields are therefore generally preferred for this computational approach.

Apparent Differential Quantum Yield

$$\Phi'_{a,i} = \frac{\dot{C}_\iota}{I_T} \tag{109}$$

The *apparent differential quantum yield,* defined in Equation 109, is a measure that looks at an infinitesimal small change, with $\dot{C}_i$ being the change in the concentration of i with time, with I_T being the total amount of light absorbed per unit volume in the infinitesimal time step.

True Differential Quantum Yield

$$\Phi'_i = \frac{\dot{C}_\iota}{I_i} \tag{110}$$

The *true differential quantum yield,* defined in Equation 110, is the simplest method for mathematical treatment of the kinetics as it treats just the individual molecule that both absorbs and goes onto react. This is therefore useful for mixtures where there is more than one species present that absorbs the light. This in combination with the Bodenstein assumption thus allows it to be treated as one photochemical step.

The quantum yield used in the subsequent work is the **true differential quantum yield** as the code is built up with differential equations and the rates are based within the time steps of the calculations, along with the amount of light that has been absorbed by the photoreactive species.

8.1.2. RTE section

The derivation of an absorbing and scattering medium is shown below for the discrete ordinate method and two-flux approximation.

DOM derivation

The Discrete Ordinate Method (DOM) discretises the angular space into a finite number ($\boldsymbol{N_d}$) of directions ($\boldsymbol{u_i}$). The RTE is then replaced by a system of partial differentials and integrals that are solved by digital quadrature. The integrals therefore become a weighted summation of all the $\boldsymbol{N_d}$ directions, as defined in Equation 111.

$$\frac{\xi}{4\pi}\int_{\Omega'=4\pi} B(\mathbf{u}' \rightarrow \mathbf{u}) v \, d\Omega' = \frac{\xi}{4\pi}\sum_{j=1}^{N_d} w_j B\left(\mathbf{u_j'} \rightarrow \mathbf{u_j}\right) L\left(s, \mathbf{u_j}\right) \tag{111}$$

The overall RTE can then be written as:

$$\begin{cases} \mathbf{u_1} \cdot \nabla I = -(\alpha+\xi) I(s,\mathbf{u_1}) + \alpha I^0(T) + \dfrac{\xi}{4\pi}\displaystyle\sum_{j=1}^{\mathbf{N_d}} w_j B(\mathbf{u_j}' \rightarrow \mathbf{u_1})\, I(s,\mathbf{u_j}) \\ \vdots \\ \mathbf{u_{N_d}} \cdot \nabla I = -(\alpha+\xi) I(s,\mathbf{u_{N_d}}) + \alpha I^0(T) + \dfrac{\xi}{4\pi}\displaystyle\sum_{j=1}^{\mathbf{N_d}} w_j B(\mathbf{u_j}' \rightarrow \mathbf{u_{N_d}})\, I(s,\mathbf{u_{N_d}}) \end{cases}$$

Where w_j are the quadrature weights corresponding to the direction $\boldsymbol{u_i}$. These equations are then solved using quadratures (S_N) or Fiveland quadrature (F_N).

The above equations need boundary conditions specifying the luminance leaving the boundaries of the domain for each direction. For an isotropic surface, the luminance leaving the border at point P_0 in the direction $\boldsymbol{u_i}$, where $\boldsymbol{u_i} \cdot \boldsymbol{n_{P_0}}$ where $\boldsymbol{n_{P_0}}$ is the normal vector of the surface at point P_0 directed towards the middle, is defined in Equation 112.

$$I(s,\mathbf{u_i}) = I^{Wall}(s,\boldsymbol{u_i}) + \epsilon I^0(T) + \frac{1-\varepsilon-t}{\pi} \sum_{j=1\left(\boldsymbol{u_i}\cdot\boldsymbol{n_{P_0}}<0\right)}^{\boldsymbol{N_d/2}} w_j I\left(\boldsymbol{s},\boldsymbol{u_j}\right)\left|\boldsymbol{u_j}\cdot\boldsymbol{n_{P_0}}\right| \qquad (112)$$

Where ϵ and t are the emission and transmission coefficients of the wall, with the term $1-\varepsilon-t$ representing the reflectivity coefficient r.

The solution to the above equations is then solved numerically. Caution should be taken with non-uniform grids as this method was developed for uniform grids. They should be solved at the same resolution as hydrodynamics, but as hydrodynamic grids are often non-uniform the solutions become much more complex. There has been a number of developments in this area to extend the DOM method to non-uniform meshes.

Simplification for absorbing only medium

For a medium that only absorbs the RTE is simplified to Equation 15, as defined previously.

$$\frac{dI}{ds} = -\alpha I(s,\boldsymbol{u}) \qquad (15)$$

For the Discrete Ordinates Method (DOM) the angular space is discretised in N_d directions, obtaining these equations:

$$\begin{cases} \mathbf{u_1}\cdot\nabla I &= -\alpha I(s,\mathbf{u_1}) \\ &\vdots \\ \mathbf{u_{N_d}}\cdot\nabla I &= -\alpha I(s,\mathbf{u_{N_d}}) \end{cases}$$

For purely absorbing mediums the RTE can be solved using a finite volume method, with a step diagram. The total irradiance can be obtained by summing the irradiances from each direction and multiplying it by the weight (w_j) of the associated light, as defined previously in Equation 16.

$$I_{total}(s) = \int_{\Omega'=4\pi} I(s,\mathbf{u})d\Omega = \sum_{j=1}^{\mathbf{N_d}} w_j I\left(s,\mathbf{u_j}\right) \qquad (16)$$

Collimated radiation

For purely collimated radiation with u perpendicular to the surface, the energy flux density is equal to luminance.

$$F_0 = I_0$$

Technically the units are different as F (eins·cm^{-2}·s^{-1}) whereas I (eins·cm^{-2}·s^{-1}·sr^{-1}), however as the light is collimated this is not considered.

Isotropic Radiation

For isotropic radiation where irradiance is independent of the direction of the light the Energy Flux Density at the wall (F_0) is defined in Equation 113.

$$F_0 = 2\pi \int_{\mathbf{u_i}\cdot\mathbf{n}_{P_0}<0} I_0(\mathbf{s}=0,\mathbf{u_i})|\mathbf{u_i}\cdot\mathbf{n}|d\Omega \tag{113}$$

Two-flux approximation derivation

For the two-flux approximation the angular space is separated into two hemispheres, where the luminance is assumed to be constant but different in each hemisphere. This model was first developed by Schuster et al. and used the following assumptions:

- Rectangular 1D geometry
- Isotropic phase function
- Luminance independent of the incident angle

Cornet et al. proposed an extension of this method to cylindrical and spherical geometries in one dimension but also taking into account an anisotropic radiation field, depending on the angular dependence of the radiation. The Radiative Transfer Equation (RTE) for an absorbing, scattering and emission free medium is defined in Equation 114.

$$\frac{dI}{ds} = -(\alpha+\xi)I(s,\boldsymbol{u}) + \frac{\vartheta}{4\pi}\int_{\Omega'=4\pi} F_P(\boldsymbol{u}'\rightarrow\boldsymbol{u})I(s,\boldsymbol{u}')d\Omega' \tag{114}$$

Where F_P is the phase function and s is the curvilinear coordinate related to the direction $\boldsymbol{u}$ of the light beam. α is the Naperian linear absorption coefficient and ξ is the linear scattering coefficient. This can also be written as shown in Equation 115.

$$\frac{1}{\beta_T}\frac{dI}{ds} = -I(s,\boldsymbol{u}) + \frac{\vartheta}{4\pi}\int_{\Omega'=4\pi} F_P(\boldsymbol{u}' \to \boldsymbol{u}) I(s,\boldsymbol{u}') d\Omega' \tag{115}$$

Where β_T and ω are the extinction coefficient and the albedo, respectively, defined below, where β_T is the extinction coefficient (a sum of the absorption and scattering coefficients) and ϑ is the albedo of the fluid which defines how absorbing or reflective the medium is.

$$\beta_T = \alpha + \xi \; ; \;\; \vartheta = {}^{\xi}/_{\beta_T}$$

The two-flux approximation splits the irradiance into two hemispheres (+/–), with the irradiance at position c_1 defined in Equation 116, where the +/- signs indicate the *positive* and *negative* hemispheres, respectively. The irradiance is a function of five parameters, the coordinates and both the zenith (γ) angle and azimuthal (φ) angle, as shown in Figure 35.

$$\begin{cases} (+) = \int_{\Omega^+} d\,\Omega = 2\pi \int_0^{\pi/2} \sin\gamma \;\, d\gamma \;\; = 2\pi \int_0^1 dZ \,, (Z = \cos\gamma) \\ (-) = \int_{\Omega^-} d\,\Omega = 2\pi \int_{\pi/2}^{\pi} \sin\gamma \;\, d\gamma \;\; = 2\pi \int_{-1}^0 dZ \,, (Z = \cos\gamma) \end{cases} \tag{116}$$

For most cases the RTE cannot be solved analytically and hence numerical methods have to be applied. However, certain assumptions can be made to simplify the problem:

- A single direction is chosen for reference (y axis in cartesian and r axis in the cylindrical coordinates)
- The luminance is considered symmetrical about the axis of choice, so that it does not only depend on the zenith (γ) angle.
- The solid angle is expressed as $d\Omega \;=\; 2\pi \sin\gamma \, d\gamma$

Considering these assumptions, the equation for the variation in irradiance with position for the curvilinear coordinates in the Cartesian and cylindrical systems is defined in Equation 117.

$$\frac{dI}{ds} = \cos\gamma \, \frac{dI}{dc_1} \tag{117}$$

In order to consider varying luminance with the zenith angle (γ) Cornet introduced an angular dependence as defined in Equation 118, where n is the degree of collimation (n→0 luminance is independent of zenith angle and hence isotropic; n→∞ luminance will tend to 0 in all directions except for γ = 0 and hence fully collimated).

$$I(c_1, \gamma) = I^{\pm}(c_1)|\cos^n\gamma| = I^{\pm}(c_1)|Z^n| \tag{118}$$

Where $Z = cos\,\gamma$. This formula, therefore, allows for calculations with varying degrees of collimation between collimated and isotropic, which is expected for differing lamps and equipment. Equations 115 and 118 are combined using the assumptions described above, giving the RTE defined in Equation 119.

$$\frac{1}{\beta_T} Z \frac{dI}{dc_1} = -I + \frac{\vartheta}{2}\left(\int_{-1}^{0} I\, B(Z', Z)\left|Z'^n\right| dZ' \; + \; \int_{0}^{1} I\, B(Z', Z)\left|Z'^n\right| dZ'\right) \tag{119}$$

Equation 119 is the integrated over the solid angle, which gave Equation 120 corresponding to the two hemispheres.

$$\begin{aligned}
\frac{1}{\beta_T}\frac{d\int_0^1 I\,|Z^n|Z\,dZ}{dc_1} &= -\int_0^1 I\,dZ \; + \frac{\vartheta}{2}\left(\int_{-1}^{0}\int_{0}^{1} IB(Z', Z)\left|Z'^n\right| dZdZ' + \int_0^1\int_0^1 IB(Z', Z)\left|Z'^n\right| dZdZ' \right) \\
\frac{1}{\beta_T}\frac{d\int_{-1}^0 I\,|Z^n|Z\,dZ}{dc_1} &= -\int_{-1}^0 I\,dZ \; + \frac{\vartheta}{2}\left(\int_{-1}^{0}\int_{-1}^{0} IB(Z', Z)\left|Z'^n\right| dZdZ' + \int_0^1\int_{-1}^0 IB(Z', Z)\left|Z'^n\right| dZdZ' \right)
\end{aligned} \tag{120}$$

The following constants are then introduced where b^{-+} is the fraction of the luminance which is back diffused by the diffusion effect, whilef^{--} corresponds to the fraction of the luminance that is pre-diffused, b^{+-} is the fraction of the luminance that is back-diffused and f^{++} is the fraction of the luminance that is pre-diffused.

$$b^{-+} = \frac{1}{2(n+1)L^{-}} \int_{-1}^{0} \int_{0}^{1} IB(Z', Z) \left| Z'^{n} \right| dZ dZ'$$

$$f^{++} = \frac{1}{2(n+1)L^{+}} \int_{0}^{1} \int_{0}^{1} IB(Z', Z) \left| Z'^{n} \right| dZ dZ'$$

$$b^{+-} = \frac{1}{2(n+1)L^{+}} \int_{0}^{1} \int_{-1}^{0} IB(Z', Z) \left| Z'^{n} \right| dZ dZ'$$

$$f^{--} = \frac{1}{2(n+1)L^{-}} \int_{-1}^{0} \int_{-1}^{0} IB(Z', Z) \left| Z'^{n} \right| dZ dZ'$$

For this part the phase function is symmetrical, such that the fraction of the outbound direction depends only on the angle formed between the incident light direction and the outbound direction. Mathematically this equivalence is represented as:

$$\begin{cases} f^{++} = f^{--} = f \\ b^{-+} = b^{+-} = b \end{cases}$$

The property of normalisation of the phase function allows f to be presented as:

$$f = 1 - b$$

From:

$$\begin{aligned} \frac{1}{\beta_T k_H} \frac{dI^{+}}{dc_1} &= -(1 - \vartheta f) I + \vartheta \mathrm{b} I^{-} \\ \frac{1}{\beta_T k_H} \frac{dI^{-}}{dc_1} &= +(1 - \vartheta f) I^{-} - \vartheta \mathrm{b} I^{+} \end{aligned} \tag{121}$$

Where k_H is the collimation factor as defined by $k_H = \frac{n+2}{n+1}$

The summation of Equation 121 gives Equation 122 for both hemispheres.

$$\frac{d(I^{+} + I^{-})}{dc_1} = -\beta_T k_H \big(1 - \omega(1 - 2b)\big)[I^{+} - I^{-}] \tag{122}$$

The photon flux density vector (F) and spherical irradiance (E) express themselves as:

$$F = 2\pi\left(I^{+}\int_{0}^{1}|Z^{n+1}|\,dZ - I^{-}\int_{-1}^{0}|Z^{n+1}|\,dZ\right) = \frac{2\pi}{n+2}(I^{+}-I^{-}) = F^{+}-F^{-}$$
$$E = 2\pi\left(I^{+}\int_{0}^{1}|Z^{n}|\,dZ - I^{-}\int_{-1}^{0}|Z^{n}|\,dZ\right) = \frac{2\pi}{n+1}(I^{+}-I^{-}) = E^{+}+E^{-} \quad (123)$$

Using these definitions and the assumptions stated above the balanced radiation equation can be combined into Equation 124.

$$\frac{d(I^{+}-I^{-})}{dc_1} + \frac{\psi}{c_1}(I^{+}-I^{-}) + \beta_T k_H(1-\vartheta)(I^{+}+I^{-}) = 0 \quad (124)$$

Where m is a parameter depending on the coordinate system: ψ = 0 – cartesian; ψ = 1 – cylindrical coordinates and ψ = 3 – spherical coordinates.

By combining the differential of Equation 122 with Equation 124, a one-dimensional two-flux approximation RTE is formed for any coordinate system, as shown in Equation 125.

$$\frac{d^2(I^{+}+I^{-})}{dc_1^2} + \frac{\psi}{c_1}\frac{d(I^{+}+I^{-})}{dc_1} - {\beta_T}^2 k_H^2(1-\vartheta)\big(1-\vartheta(1-2b)\big)(I^{+}+I^{-}) = 0 \quad (125)$$

8.2. Appendix II – Photochemical chapter

8.2.1. Decarboxylative cyclisation

A comparison of the Aillet calculations used in the decarboxylative cyclisation is discussed in this section, followed by a discussion of the estimated quantum yields using both methods.

Aillet calculations

The 'Aillet method' was used to estimate the quantum yield of the decarboxylative cyclisation. The following three Figures show the 'Aillet Graph' so the gradient can be calculated for 308 nm, 282 nm and 222 nm excimer flow reactors. For 282 nm and 222 nm, the method becomes invalidated but the calculations are still carried out, with it also explaining the great uncertainty in the values for the experiments with a higher residence times. The gradients and subsequent calculated values are then shown in Table 78, where Δc is equal to 0.0121 cm.

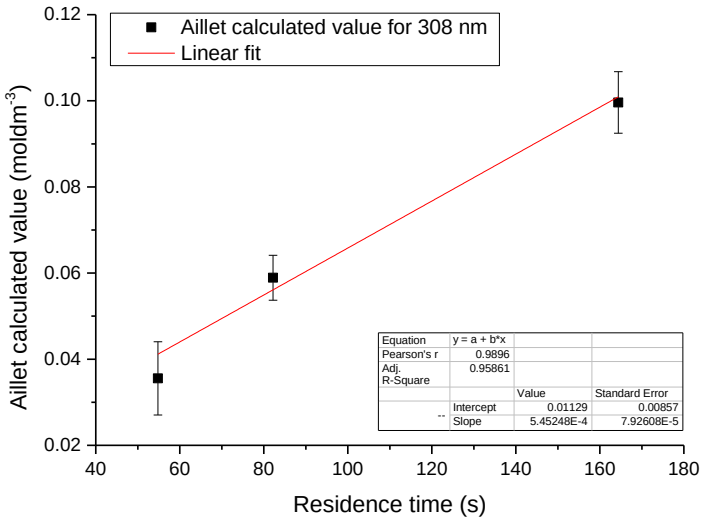


Figure 132 – The Aillet graph for the decarboxylative cyclisation at 308 nm, with the error bar one standard deviation of the measurements each way.

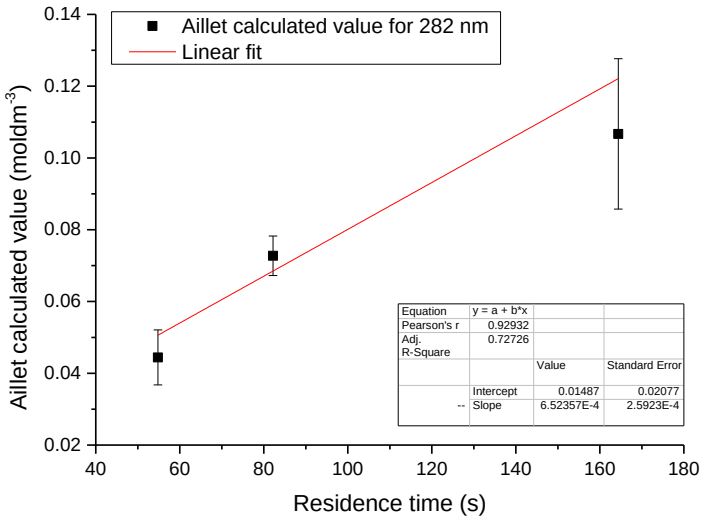


Figure 133 - The Aillet graph for the decarboxylative cyclisation at 282 nm, with the error bar one standard deviation of the measurements each way. The Aillet method becomes invalidated at 282 nm due to the multiple absorbing species.

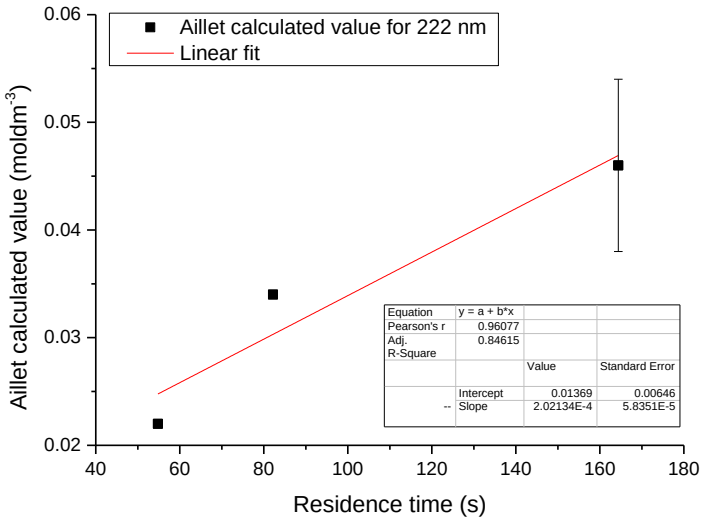


Figure 134 - The Aillet graph for the decarboxylative cyclisation at 222 nm, with the error bar one standard deviation of the measurements each way. The Aillet method becomes invalidated at 222 nm due to the multiple absorbing species and high absorbing values.

Table 78 – The Aillet gradient calculated using the Aillet graphs presented above, with the light intensity from the manufacturer's specification and the estimated quantum yield.

Wavelength (nm)	Aillet gradient value (±std. er., $mol \cdot dm^{-3} \cdot s^{-1}$)	Light intensity ($eins \cdot cm^{-2} \cdot s^{-1}$)	Quantum yield (±std. er., %)	Aillet method valid?
308	5.45 (±0.793) x 10^{-4}	1.26 x 10^{-7}	5.24 (±0.76)	Yes
282	6.52 (±2.59) x 10^{-4}	8.49 x 10^{-8}	9.30 (±3.69)	No
222	2.02 (±0.584) x 10^{-4}	3.90 x 10^{-8}	6.28 (±1.81)	No

Statistical significance of the quantum yield estimations

As the quantum yield estimations were assumed to be normally distributed for the estimation, a comparison of the different methods are shown in Figure 135, Figure 136 and Figure 137 for 308 nm, 282 nm and 222 nm, respectively. A summary of the overlapping probability density is shown in Table 79, where the high degree of overlap is shown when the Aillet method is valid (308 nm) and a reducing amount of overlap as Aillet's assumptions are no longer true (282 nm and 222 nm).

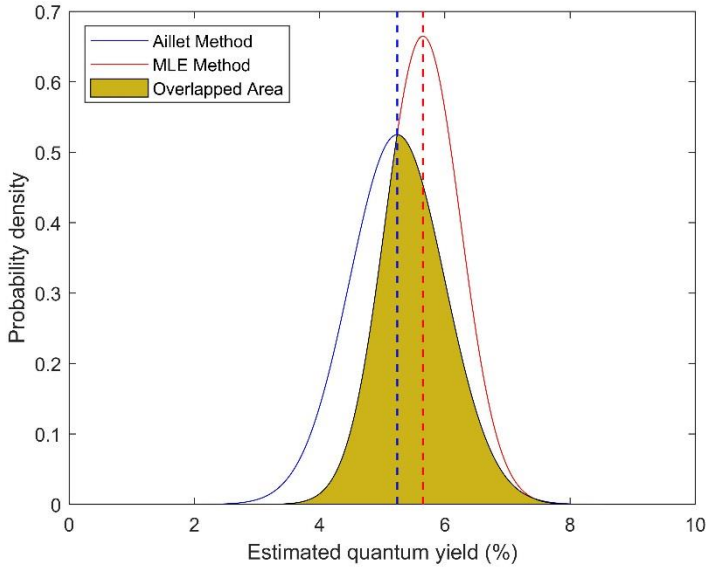


Figure 135 - The overlap of probability density functions of the estimated quantum yields, shown in yellow, using Aillet's method (—) and gPROMS' MLE method (—) at 308 nm. This is the equivalent of P = 73.4 % showing good agreement as Aillet's assumptions are valid. The dashed lines indicate the estimated value.

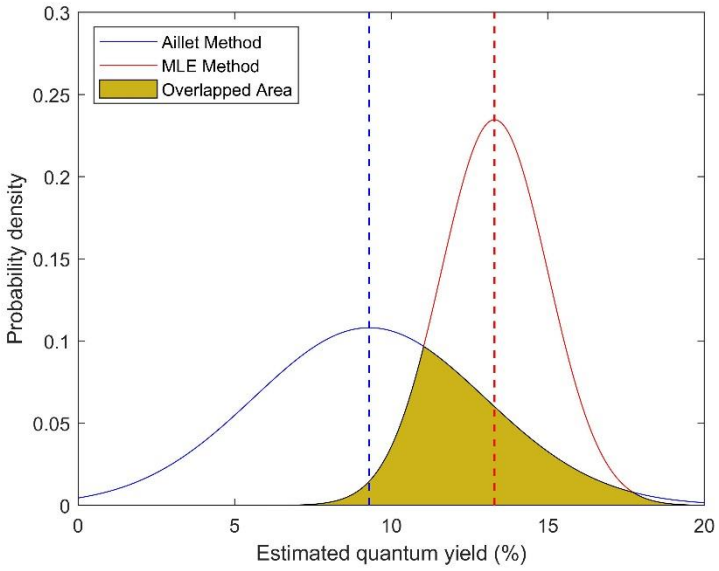


Figure 136 - The overlap of probability density functions of the estimated quantum yields, shown in yellow, using Aillet's method (—) and gPROMS' MLE method (—) at 282 nm. This is the equivalent of P = 40.2 % showing more than likely to not be equivalent when Aillet's assumptions are not valid. The dashed lines indicate the estimated value.

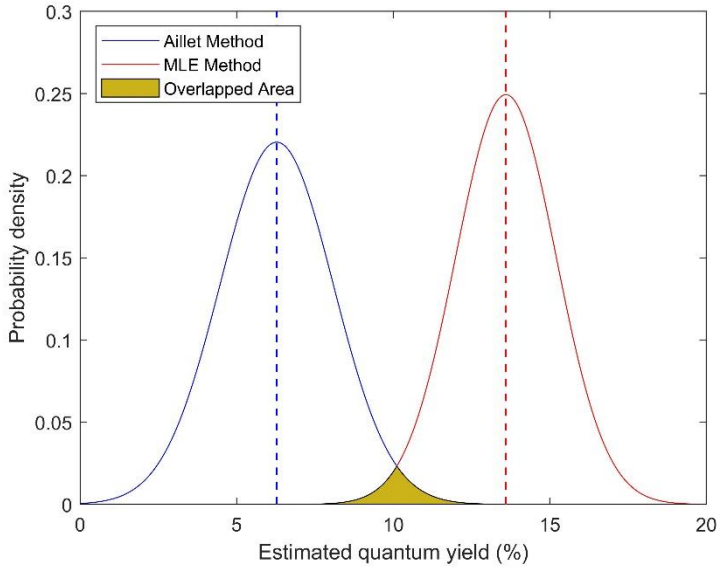


Figure 137 - The overlap of probability density functions of the estimated quantum yields, shown in yellow, using Aillet's method (—) and gPROMS' MLE method (—) at 222 nm. This is the equivalent of P = 3.38 % showing highly likely to not be equivalent when Aillet's assumptions are not valid. The dashed lines indicate the estimated value.

Table 79 - The Aillet gradient calculated using the Aillet graphs presented above, with the light intensity from the manufacturer's specification and the estimated quantum yield.

Wavelength (nm)	Aillet method ϕ (±SD, %)	MLE method ϕ (±SD, %)	Overlapped probability density (%)	Aillet method valid?
308	5.24 (±0.76)	5.65 (±0.57)	73.4	Yes
282	9.30 (±3.69)	13.3 (±1.69)	40.2	No
222	6.28 (±1.81)	13.6 (±1.64)	3.38	No

8.2.2. Cookson's dione Aillet calculations

A comparison of the Aillet calculations used in the Cookson's dione reactions is presented in this section, with the Aillet gradient shown in Figure 138, alongside the subsequent calculations shown in Table 80.

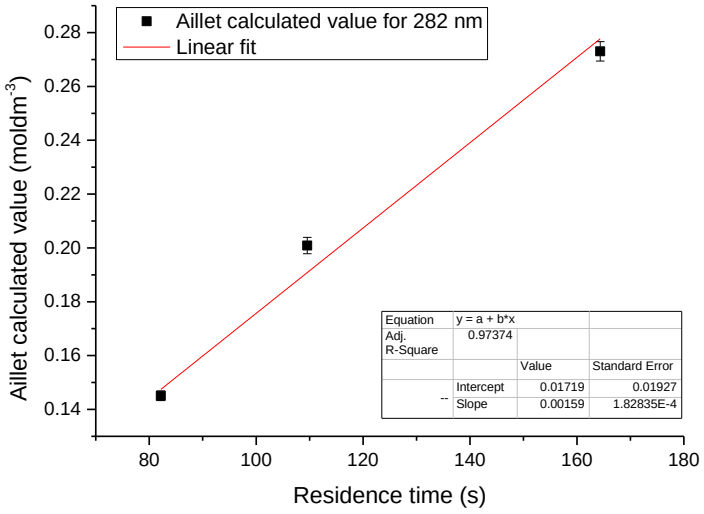


Figure 138 - The Aillet graph for Cookson's dione at 282 nm, with the error bar one standard deviation of the measurements each way. The Aillet method is valid for these conditions.

Table 80 - The Aillet gradient calculated using the Aillet graphs presented above, with the light intensity from the manufacturer's specification and the estimated quantum yield.

Wavelength (nm)	Aillet gradient value (±std. er., mol·dm^{-3}·s^{-1})	Light intensity (eins·cm^{-2}·s^{-1})	Quantum yield (±std. er., %)	Aillet method valid?
282	15.9 (±1.83) x 10^{-4}	8.49 x 10^{-8}	22.7 (±2.59)	Yes

8.2.3. Bodenstein-like assumption for quantum yield

A Bodenstein-like assumption was used to simplify the kinetic schemes of photoreactions that used photosensitisers, as the production of the excited photosensitiser was often assumed to be much faster than the production rate of the product. A symbolic reaction scheme of three consecutive reactions (i, ii and iii) is presented below, where A and B are the starting material and products, respectively, while PS is the photosensitiser and * symbolises the excited state.

$$(i)\ PS + h\nu \rightarrow PS*;\quad (ii)\ PS* + A \rightarrow B;\quad (iii)\ PS* \rightarrow PS$$

The intermediate steps presented here are assumed to be rapid compared to the overall rate of production of B. A Bodenstein-like assumption is made for the excited photosensitiser as it is not used

up in the reaction and within the control volume can be assumed to be of constant concentration, hence the rate of production of PS* is equal to the rate of consumption of PS*.

$$\Phi_1 \, LVRPA_{PS} \; = \; k_2[PS^*] \; + \; k_3[TXO^*][A]$$

$$[PS^*] \; = \; \frac{\Phi_1 \, LVRPA_{PS}}{k_2 \; + \; k_3[A]}$$

$$\frac{d[B]}{dt} \; = \; \frac{k_3[A] \, \Phi_1 \, LVRPA_{PS}}{k_2 \; + \; k_3[A]}$$

The reaction to form the product was assumed to be much slower than the photoexcitation and the relaxation of the photosensitiser, meaning the rate of formation of B can be rewritten, as defined in Equation 126.

$$\frac{d[B]}{dt} = \Phi' LVRPA_{PS}[A]; \Phi' = \frac{k_3 \Phi_1}{k_2} \tag{126}$$

8.2.4. Experimental results for the THPAA cyclisation

The experimental results used in the THPAA quantum kinetic parameter estimation are shown in Table 81, Table 82, Table 83 and Table 84, with the different conditions explained in the captions for each.

Table 81 – The experimental results for the cyclisation of THPAA at 282 nm and 308 nm and 0.1 mol·dm-3 of starting material, without any photosensitiser.

282 nm, without TXO, 0.1 mol·dm^{-3} SM					308 nm, without TXO, 0.1 mol·dm^{-3} SM				
	Yield/Recovery (%)					Yield/Recovery (%)			
Time (min)	**Bridged**	**Non-bridged**	**Recovery**	**Mass Bal.**	**Time (min)**	**Bridged**	**Non-bridged**	**Recovery**	**Mass Bal.**
0	0	0	97	97	**0**	0	0	100	100
15	21	6	77	104					
30	40	11	37	88	**30**	60	16	19	95
60	68	17	3	88	**60**	67	15	3	85
90	65	12	2	79	**90**	60	12	3	75
120	57	9	2	68					
150	61	9	2	72	**150**	71	12	3	86
180	58	7	2	67	**180**	61	9	3	73

Table 82 - The experimental results for the cyclisation of THPAA using the 282 nm and 308 nm excimer batch reactor and 0.1 mol·dm^{-3} of starting material, with 1 % TXO photosensitiser.

282 nm, 1% TXO, 0.1 mol·dm^{-3} SM					308 nm, 1% TXO, 0.1 mol·dm^{-3} SM				
	Yield/Recovery (%)					Yield/Recovery (%)			
Time (min)	Bridged	Non-bridged	Recovery	Mass Bal.	Time (min)	Bridged	Non-bridged	Recovery	Mass Bal.
0	0	0	93	93	**0**	0	0	96	96
15	22	7	70	99	**15**	36	10	48	94
30	45	12	35	96	**30**	65	17	4	86
60	66	16	2	84	**60**	55	13	3	71
90	64	13	1	78					
120	56	11	1	68	**120**	60	11	3	74
150	48	8	1	57	**150**	53	9	3	65
180	60	9	1	70	**180**	58	9	3	70

Table 83 - The experimental results for the cyclisation of THPAA using the 282 nm and 308 nm excimer flow reactor and 0.1 mol·dm^{-3} of starting material, without photosensitiser.

282 nm, without TXO, 0.1 mol·dm^{-3} SM					308 nm, without TXO, 0.1 mol·dm^{-3} SM				
	Yield/Recovery (%)					Yield/Recovery (%)			
Flowrate (ml/min)	Bridged	Non-bridged	Recovery	Mass Bal.	Flowrate (ml/min)	Bridged	Non-bridged	Recovery	Mass Bal.
5	5	1	85	91	**5**	5	1	85	91
2.5	8	2	82	92	**2.5**	8	2	82	92
1	17	5	73	95	**1**	17	5	73	95
0.5	23	6	51	80	**0.5**	23	6	51	80
0.25	31	8	27	66	**0.25**	31	8	27	66

Table 84 - The experimental results for the cyclisation of THPAA using the 308 nm excimer flow reactor and 0.1 mol·dm^{-3} of starting material, with 1 % of TXO photosensitiser.

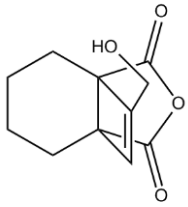
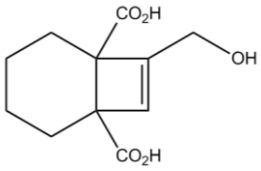
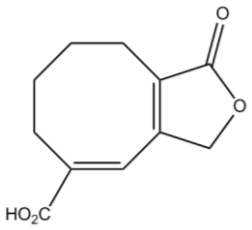
308 nm, 1 % TXO, 0.1 mol·dm^{-3} SM				
	Yield/Recovery (%)			
Flowrate (ml/min)	Bridged	Non-bridged	Recovery	Mass Bal.
5	6	2	94	102
2.5	11	3	77	91
1	23	6	52	81
0.5	43	11	36	90
0.25	64	16	8	88

8.3. Appendix III – High temperature water chapter

8.3.1. Enthalpy of reaction and temperature change in reactor

To understand how the enthalpy change of both reactions could affect the reactor temperature, the enthalpy of formation of both molecules was estimated using the gSAFT γ-Mie EoS. The benefit of using this EoS was that as it was developed from understanding functional groups effect on properties, the functional groups present in each molecule could be inputted into the programme. The estimated values for the enthalpy of formation of each molecule are shown in Table 85.

Table 85 – The estimated enthalpy of formation for each molecule used in this reaction as predicted by SAFT-γ Mie.

Molecule			
Enthalpy of formation (kJ·mol^{-1})	-841.3	-1012	-768.5

Hess's law was then used to estimate the enthalpy of reaction, as shown in Table 86, which was then used along with the estimated heat capacity of the solvent to understand the possible change in temperature of the reaction fluid.

Table 86 – The enthalpy of reaction for the reaction steps used in this work as calculated by using Hess's law.

Reaction	**Enthalpy of reaction (kJ·mol^{-1})**
Hydrolysis	-170.7
Ring-opening	243.5
Overall process	72.8

The effect on the temperature was calculated using properties such as heat capacity and density predicted by the gSAFT γ-Mie EoS. A concentration of 0.1 mol·dm^{-3} was assumed as it was towards the top of the values used to estimate the kinetics and would be towards the maximum temperature change expected from the reaction. For simplicity and understanding the calculations were also

carried out for a batch reaction; the majority of the flow reactor is at near constant conditions too apart from the initial entry section (*ca.* 5 % of reactor). The calculations can be followed in Table 87, with the final temperature change of the fluid considered for endothermic and exothermic reactions.

Table 87 – The calculations used to estimate the increase in temperature of a reaction mixture as predicted by the SAFT-γ Mie EoS, showing only a small increase in temperature with the reaction fluid.

	Hydrolysis	Ring opening	Multi-step process
Enthalpy of reaction ($kJ \cdot mol^{-1}$)	-170.7	243.5	72.80
Density of solvent at 230 °C 15MPa ($kgdm^{-3}$)	0.53	0.53	0.53
Concentration of compound ($molkg^{-1}$)	0.19	0.19	0.19
Enthalpy of reaction ($kJkg^{-1}$)	-31.97	45.60	13.63
Heat capacity of solvent ($kJkg^{-1}K^{-1}$)	4.60	4.60	4.60
Temperature change to solvent (°C)	6.95	-9.91	-2.96

The overall temperature change for the multi-step reaction was a reduction in temperature of 2.96 °C, which was considered negligible enough to not be considered within the model. The assumptions made regarding the heat transfer and uncertainty in the EoS's physical properties used to calculate the heating rate were also expected to be greater than the estimated temperatures from the heat of reaction.

8.3.2. Effect of dispersion

The values from the reactor model and predicted physical properties used to estimate the effective dispersion coefficient. Two conditions are shown to highlight that even towards the lower end of the conditions used the effective dispersion coefficient is still significant and hence the plug-flow like assumption made was valid. In Table 88 are the values for the larger reactor and in Table 89 the values for the smaller reactor are shown, using Equation 106. [365]

$$\kappa = 1.65 - 0.863\log\left(\mathrm{De}\sqrt{\mathrm{Sc}}\right) + \left[0.113\left(\log\sqrt{\mathrm{Sc}}\right)\right]^2 \qquad (106)$$

Table 88 – The values used in the calculation of the dispersion ratio for the larger reactor, with the effective dispersion coefficient large enough such that the plug-flow assumption made was valid.

	215 °C, 175 bar	245 °C, 125 bar
Flowrate ($ml \cdot min^{-1}$)	11.5	34
Fluid velocity ($m \cdot s^{-1}$)	2.62×10^{-3}	7.75×10^{-3}
Dynamic viscosity ($kg \cdot m^{-1}s^{-1}$)	1.14×10^{-5}	9.54×10^{-5}
Density ($kg \cdot m^{-3}$)	578	478
Mol. Diffusion Coefficient ($m^2 \cdot s^{-1}$)	1.00×10^{-9}	1.00×10^{-9}
Tube diameter (m)	3.05×10^{-3}	3.05×10^{-3}
Coil diameter (m)	0.07	0.07
Reynolds number	405	118
Dean number	84.6	24.7
Schmidt number	19.7	200
$DeSc^{0.5}$	376	349
$\log_{10}(DeSc^{0.5})$	2.58	2.54
Dispersion ratio	0.177	0.186
Effective dispersion coefficient ($cm^2 \cdot s^{-1}$)	**0.590**	**5.42**

Table 89 - The values used in the calculation of the dispersion ratio for the smaller reactor, with the effective dispersion coefficient large enough such that the plug-flow assumption made was valid.

	215 °C, 175 bar	245 °C, 125 bar
Flowrate ($ml \cdot min^{-1}$)	0.1	3.2
Fluid velocity ($m \cdot s^{-1}$)	6.54×10^{-3}	2.09×10^{-3}
Dynamic viscosity ($kg \cdot m^{-1} \cdot s^{-1}$)	1.14×10^{-5}	9.54×10^{-5}
Density ($kg \cdot m^3$)	578	478
Mol. Diffusion Coefficient ($m^2 \cdot s^{-1}$)	1.00×10^{-9}	1.00×10^{-9}
Tube diameter (m)	5.07×10^{-4}	5.07×10^{-4}
Coil diameter (m)	0.025	0.025
Reynolds number	168	531
Dean number	23.9	75.7
Schmidt number	19.7	200
$DeSc^{0.5}$	106	1070
$\log_{10}(DeSc^{0.5})$	2.03	3.03
Dispersion ratio	0.365	0.0727
Effective dispersion coefficient ($cm^2 \cdot s^{-1}$)	**0.209**	**42.6**

8.3.3. Raman method for calculating yield of smaller reactor yields

The initial yields for each experiment carried out in the smaller reactor were calculated by ^{1}H NMR yield, giving the results shown in Table 90.

Table 90 – The yields, calculated using ^{1}H NMR, of the ring-opened product and the intermediate formed from the hydrolysis step, carried out in the smaller reactor.

Flow rate ($ml \cdot min^{-1}$)	Estimated residence time (min)	Yield of ring opened product (%)	Yield of hydrolysis product (%)
0.1	8	95	-
0.2	4	97	-
0.266	3	97	3
0.4	2	92	8
0.53	1.5	84	15
0.8	1	67	28
1.06	0.75	56	44
1.6	0.5	40	58
3.2	0.25	13	70

The samples used to calculate the 1H NMR were also measured using a Raman probe to explore future possibilities of in-line spectroscopic analysis. The spectra, displayed in Figure 139, show an obvious increase in a product formation *ca.* 1650 cm^{-1}, with the spectra colour changing from blue (0.25 minutes) to yellow (8 minutes) with residence time. The spectra have also been normalised using this product peak which allowed the formation of the product to be tracked and compared to the ^{1}H NMR results.

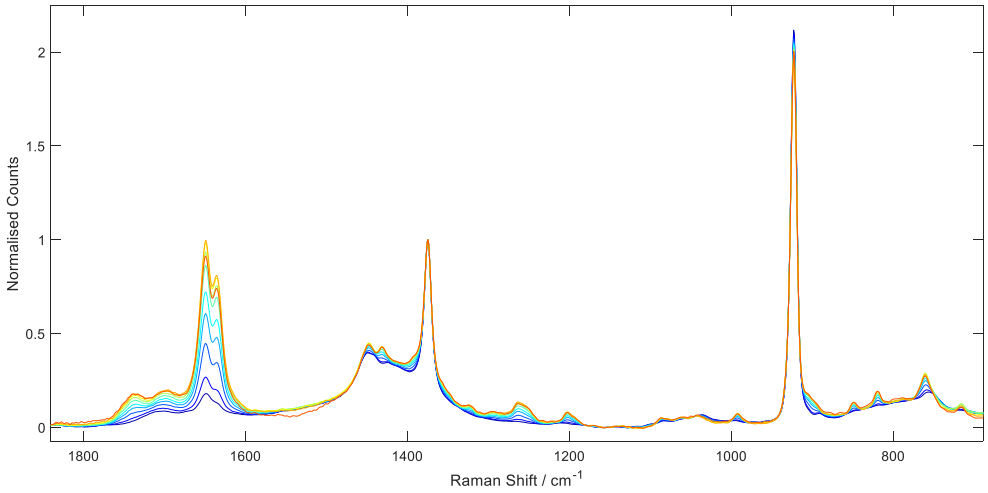


Figure 139 - The normalised spectra of the reactor output for the combined hydrolysis and ring-opening reactions in the smaller reactor. It should be noted that the spectra have been normalised at *ca.* 1650 cm^{-1}.

The normalised product peak values were then plotted against residence time, as shown in Figure 140, which agree well with the values shown in Table 90. Therefore, this Raman method showed good potential for future work involving online analysis of this reaction.

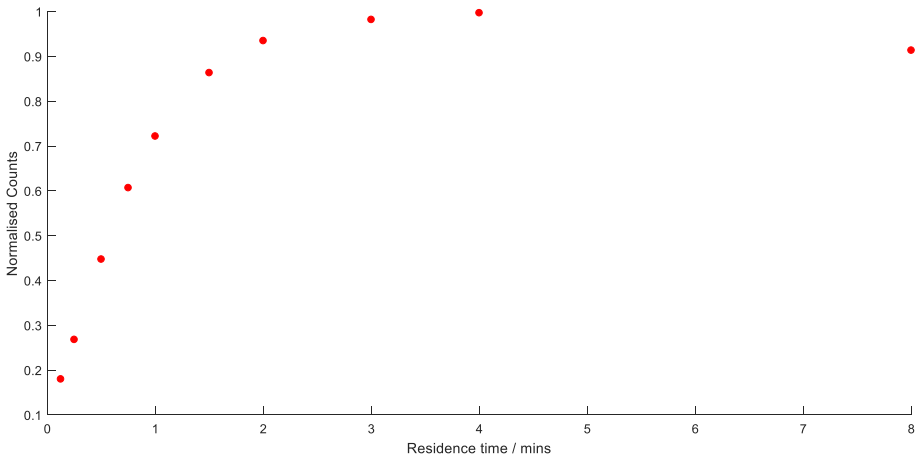


Figure 140 – The normalised counts for the ring-opened product peak plotted against residence time showing the formation of the ring-opened product in the smaller reactor. These normalised values show good agreement with the yield values calculated using ^{1}H NMR.